

NAVAL POSTGRADUATE SCHOOL

Monterey, California



THESIS

HEAT TRANSFER, ADIABATIC EFFECTIVENESS AND
INJECTANT DISTRIBUTIONS DOWNSTREAM OF
SINGLE AND DOUBLE ROWS OF FILM-COOLING
HOLES WITH COMPOUND ANGLES

by

James Michael Wigle

DECEMBER 1991

Thesis Advisor:

Phillip M. Ligrani

Approved for public release: Distribution is unlimited

T259289

REPORT DOCUMENTATION PAGE				Form Approved OMB No 0704-0188	
1a. REPORT SECURITY CLASSIFICATION Unclassified			1b. RESTRICTIVE MARKINGS		
2a. SECURITY CLASSIFICATION AUTHORITY			3. DISTRIBUTION/AVAILABILITY OF REPORT Approved for public release: Distribution is unlimited		
2b. DECLASSIFICATION/DOWNGRADING SCHEDULE					
4. PERFORMING ORGANIZATION REPORT NUMBER(S)			5. MONITORING ORGANIZATION REPORT NUMBER(S)		
6a. NAME OF PERFORMING ORGANIZATION Naval Postgraduate School		6b. OFFICE SYMBOL (If applicable) ME	7a. NAME OF MONITORING ORGANIZATION Naval Postgraduate School		
6c. ADDRESS (City, State and ZIP Code) Monterey, CA 93943-5000			7b. ADDRESS (City, State, and ZIP Code) Monterey, CA 93943-5000		
8a. NAME OF FUNDING/SPONSORING ORGANIZATION Naval Sea Systems Command		8b. OFFICE SYMBOL (If applicable) 56X3	9. PROCUREMENT INSTRUMENT IDENTIFICATION NUMBER RGPLG		
8c. ADDRESS (City, State, and ZIP Code) Dr. Dan Groghan Naval Sea Systems Command Code 56X3 Washington, D.C. 20352			10. SOURCE OF FUNDING NUMBER		
			PROGRAM ELEMENT NO. LG2LG	PROJECT NO.	TASK NO.
11. TITLE (Include Security Classification) HEAT TRANSFER, ADIABATIC EFFECTIVENESS AND INJECTANT DISTRIBUTIONS DOWNSTREAM OF SINGLE AND DOUBLE ROWS OF FILM-COOLING HOLES WITH COMPOUND ANGLES					
12. PERSONAL AUTHORS JAMES MICHAEL WIGLE					
13a. TYPE OF REPORT Master's Thesis		13b. TIME COVERED FROM _____ TO _____	14. DATE OF REPORT (Year, Month, Day) DECEMBER 1991		15. PAGE COUNT 265
16. SUPPLEMENTARY NOTATION The views expressed are those of the author and do not reflect the official policy or position of the Department of Defense or the U.S. Government					
17. COSATI CODES			18. SUBJECT TERMS (Continue on reverse if necessary and identify by block numbers) compound angle injection, film-cooling, turbulent boundary layer		
FIELD	GROUP	SUB-GROUP			
19. ABSTRACT (Continue on reverse if necessary and identify by block numbers) Experimental results are presented which describe the development and structure of flow downstream of one row and downstream of two staggered rows of film-cooling holes with compound angle orientations. Results presented include distributions of iso-energetic Stanton number ratios, and adiabatic film-cooling effectiveness deduced from Stanton numbers using superposition. Also presented are plots showing the streamwise development of injectant distributions and streamwise development of mean velocity distributions. Spanwise averaged values of the adiabatic film-cooling effectiveness are highest for blowing ratio $m=0.5$ and decrease as blowing ratio increases for x/d less than 20. At farther downstream positions, spanwise averaged effectiveness values increase with blowing ratio, except for data obtained downstream of two rows of holes with a blowing ratio of 3.0 and data obtained downstream of two rows of holes with a blowing ratio of 3.0 and data obtained downstream of one row of holes with a blowing ratio of 4.0, where severe lift-off of injectant occurs. Spanwise averaged iso-energetic Stanton number ratios range between 1.0 and 1.4 and show little variation as x/d increases for each value of blowing ratio, however for each x/d , values increase with increasing blowing ratio.					
20. DISTRIBUTION/AVAILABILITY OF ABSTRACT XX UNCLASSIFIED/UNLIMITED SAME AS RPT DTIC USERS			21. ABSTRACT SECURITY CLASSIFICATION unclassified		
22a. NAME OF RESPONSIBLE INDIVIDUAL Phillip M. Ligrani			22b. TELEPHONE (Include Area Code) (408) 646-3382		22c. OFFICE SYMBOL ME/Li

Approved for public release; distribution is unlimited.

**Heat Transfer, Adiabatic Effectiveness and Injectant
Distributions Downstream of Single and Double Rows of Film-
Cooling Holes with Compound Angles**

by

**James Michael Wigle
Lieutenant Commander, United States Navy
B.S., Pennsylvania State University, 1978**

Submitted in partial fulfillment of the requirements
for the degree of

**MASTER OF SCIENCE IN MECHANICAL
ENGINEERING**

from the

**NAVAL POSTGRADUATE SCHOOL
December 1991**

ABSTRACT

Experimental results are presented which describe the development and structure of flow downstream of one row and downstream of two staggered rows of film-cooling holes with compound angle orientations. Results presented include distributions of iso-energetic Stanton number ratios, and adiabatic film-cooling effectiveness deduced from Stanton numbers using superposition. Also presented are plots showing the streamwise development of injectant distributions and streamwise development of mean velocity distributions. Spanwise averaged values of the adiabatic film-cooling effectiveness are highest for blowing ratio $m=0.5$ and decrease as blowing ratio increases for x/d less than 20. At farther downstream positions, spanwise averaged effectiveness values increase with blowing ratio, except for data obtained downstream of two rows of holes with a blowing ratio of 3.0 and data obtained downstream of two rows of holes with a blowing ratio of 3.0 and data obtained downstream of one row of holes with a blowing ratio of 4.0, where severe lift-off of injectant occurs. Spanwise averaged iso-energetic Stanton number ratios range between 1.0 and 1.4 and show little variation as x/d increases for each value of blowing ratio, however for each x/d , values increase with increasing blowing ratio.

7/26/13
14/58375
C.1

TABLE OF CONTENTS

I.	INTRODUCTION	1
A.	BACKGROUND/THEORY	1
B.	PRESENT STUDY	5
C.	EXPERIMENTAL OUTLINE	6
D.	THESIS ORGANIZATION	6
II.	EXPERIMENTAL APPARATUS AND PROCEDURES	8
A.	WIND TUNNEL AND COORDINATE SYSTEM	8
B.	INJECTION HOLE CONFIGURATION	9
C.	INJECTION SYSTEM	10
D.	HEAT TRANSFER SURFACE	11
E.	STANTON NUMBER MEASUREMENTS	12
1.	Energy Balance	12
2.	Thermal Contact Resistance	13
3.	Conduction Heat Transfer	14
4.	Radiation Heat Transfer	14
5.	Spanwise/Streamwise Conduction Heat Transfer	16
F.	TEMPERATURE MEASUREMENTS	18
G.	STREAMWISE MEAN VELOCITY MEASUREMENTS	20
H.	BASELINE DATA MEASUREMENTS	21
III.	EXPERIMENTAL RESULTS	22
A.	PLATE 3, COMPOUND ANGLE, ONE ROW OF FILM-COOLING HOLES	23
1.	Heat Transfer Measurements	23
a.	m=0.5	23
b.	m=1.0	24
c.	m=1.5	24
d.	m=2.0	25
e.	m=3.0	25
f.	m=4.0	26
2.	Injectant Distributions	27
a.	m=1.5	27
b.	m=2.0	27
c.	m=3.0	28
d.	m=4.0	28
3.	Streamwise Mean Velocity Surveys	28
a.	m=1.5	28
b.	m=2.0	29

c.	m=3.0	29
d.	m=4.0	30
B.	PLATE 3, COMPOUND ANGLE, TWO STAGGERED ROWS OF FILM-COOLING HOLES	30
1.	Heat Transfer Measurements	30
a.	m=2.0	30
b.	m=3.0	31
2.	Injectant Distributions	32
a.	m=2.0	32
b.	m=3.0	32
3.	Streamwise Mean Velocity Surveys	32
a.	m=2.0	33
b.	m=3.0	33
C.	COMPARISON OF RESULTS FROM SIMPLE ANGLE AND COMPOUND ANGLE FILM-COOLING HOLES	34
D.	CORRELATIONS OF ADIABATIC FILM-COOLING EFFECTIVENESS DATA	37
IV.	SUMMARY AND CONCLUSIONS	38
	APPENDIX A FIGURES	41
	APPENDIX B DATA ACQUISITION, PROCESSING AND PLOTTING PROGRAMS	221
	APPENDIX C DATA FILE DIRECTORY	226
	REFERENCES	242
	INITIAL DISTRIBUTION LIST	244

LIST OF FIGURES

Figure 1.	Test Section Coordinate System, Configuration 3, Compound Angle	42
Figure 2.	Top View Schematic of Wind Tunnel Test Section, Configuration 3, Compound Angle	43
Figure 3.	Injection Hole Configuration, Configuration 3, Compound Angle	44
Figure 4.	Coefficient of Discharge (C_d) Versus Reynolds Number (Re) for Injection System, Bishop [Ref. 7]	45
Figure 5.	Injectant Temperature Versus Plenum Temperature, Bishop [Ref. 7]	46
Figure 6.	Side View Schematic of Thermocouple Control Volume for Energy Balance Analysis	47
Figure 7.	Top View Schematic of Thermocouple Control Volume Showing Spanwise and Streamwise Conduction	48
Figure 8.	Baseline Stanton Number Versus x/d , Comparison Between Correlation and Experimental Measurements	49
Figure 9.	Baseline Stanton Number Versus Reynolds Number, Comparison Between Correlation and Experimental Measurements	50
Figure 10.	St/St_0 Versus θ , Compound Angle, 1 row, $m=0.5$, $x/d=6.8$, $Z=-1.27$ cm	51
Figure 11.	St/St_0 Versus θ , Compound Angle, 1 Row, $m=0.5$, $x/d=17.6$, $Z=-1.27$ cm	52
Figure 12.	St/St_0 Versus θ , Compound Angle, 1 Row, $m=0.5$, $x/d=33.8$, $Z=-1.27$ cm	53
Figure 13.	St/St_0 Versus θ , Compound Angle, 1 row, $m=0.5$, $x/d=55.5$, $Z=-1.27$ cm	54
Figure 14.	St/St_0 Versus θ , Compound Angle, 1 Row, $m=0.5$, $x/d=77.1$, $Z=-1.27$ cm	55
Figure 15.	St/St_0 Versus θ , Compound Angle, 1 Row, $m=0.5$, $x/d=98.7$, $Z=-1.27$ cm	56

Figure 16.	$\bar{\eta}$ Versus x/d , Compound Angle, 1 Row, $m=0.5$, Spanwise Average	57
Figure 17.	$\overline{St_f/St_o}$ Versus x/d , Compound Angle, 1 Row, $m=0.5$, Spanwise Average	58
Figure 18.	Spanwise Averaged Stanton Number Versus Reynolds Number, Comparison of Different θ Values and Baselines, 1 Row, $m=0.5$	59
Figure 19.	Spanwise Variation of η , Compound Angle, 1 Row, $m=0.5$.	60
Figure 20.	Spanwise Variation of St_f/St_o , Compound Angle, 1 Row, $m=0.5$	61
Figure 21.	Spanwise Variation of St/St_o , Compound Angle, 1 Row, $m=0.5$, $\theta=1.39$	62
Figure 22.	St/St_o Versus θ , Compound Angle, 1 Row, $m=1.0$, $x/d=6.8$, $Z=-1.27$ cm	63
Figure 23.	St/St_o Versus θ , Compound Angle, 1 Row, $m=1.0$, $x/d=17.6$, $Z=-1.27$ cm	64
Figure 24.	St/St_o Versus θ , Compound Angle, 1 Row, $m=1.0$, $x/d=33.8$, $Z=-1.27$ cm	65
Figure 25.	St/St_o Versus θ , Compound Angle, 1 Row, $m=1.0$, $x/d=55.5$, $Z=-1.27$ cm	66
Figure 26.	St/St_o Versus θ , Compound Angle, 1 Row, $m=1.0$, $x/d=77.1$, $Z=-1.27$ cm	67
Figure 27.	St/St_o Versus θ , Compound Angle, 1 Row, $m=1.0$, $x/d=98.7$, $Z=-1.27$ cm	68
Figure 28.	$\bar{\eta}$ Versus x/d , Compound Angle, 1 Row, $m=1.0$, Spanwise Average	69
Figure 29.	$\overline{St_f/St_o}$ Versus x/d , Compound Angle, 1 Row, $m=1.0$, Spanwise Average	70
Figure 30.	Spanwise Averaged Stanton Number Versus Reynolds Number, Comparison of Different θ Values and Baselines, 1 Row, $m=1.0$	71
Figure 31.	Spanwise Variation of η , Compound Angle, 1 Row, $m=1.0$.	72
Figure 32.	Spanwise Variation of St_f/St_o , Compound Angle, 1 Row, $m=1.0$	73

Figure 33.	Spanwise Variation of St_t/St_o , Compound Angle, 1 Row, $m=1.0$, $\theta=1.16$	74
Figure 34.	St/St_o Versus θ , Compound Angle, 1 Row, $m=1.5$, $x/d=6.8$, $Z=-1.27$ cm	75
Figure 35.	St/St_o Versus θ , Compound Angle, 1 Row, $m=1.5$, $x/d=17.6$, $Z=-1.27$ cm	76
Figure 36.	St/St_o Versus θ , Compound Angle, 1 Row, $m=1.5$, $x/d=33.8$, $Z=-1.27$ cm	77
Figure 37.	St/St_o Versus θ , Compound Angle, 1 Row, $m=1.5$, $x/d=55.5$, $Z=-1.27$ cm	78
Figure 38.	St/St_o Versus θ , Compound Angle, 1 Row, $m=1.5$, $x/d=77.1$, $Z=-1.27$ cm	79
Figure 39.	St/St_o Versus θ , Compound Angle, 1 Row, $m=1.5$, $x/d=98.7$, $Z=-1.27$ cm	80
Figure 40.	$\bar{\eta}$ Versus x/d , Compound Angle, 1 Row, $m=1.5$, Spanwise Average	81
Figure 41.	$\overline{St_t/St_o}$ Versus x/d , Compound Angle, 1 Row, $m=1.5$, Spanwise Average	82
Figure 42.	Spanwise Averaged Stanton Number Versus Reynolds Number, Comparison of Different θ Values and Baselines, 1 Row, $m=1.5$	83
Figure 43.	Spanwise Variation of η , Compound Angle, 1 Row, $m=1.5$.	84
Figure 44.	Spanwise Variation of St_t/St_o , Compound Angle, 1 Row, $m=1.5$	85
Figure 45.	Spanwise Variation of St_t/St_o , Compound Angle, 1 Row, $m=1.5$, $\theta=1.30$	86
Figure 46.	St/St_o Versus θ , Compound Angle, 1 Row, $m=2.0$, $x/d=6.8$, $Z=-2.54$ cm	87
Figure 47.	St/St_o Versus θ , Compound Angle, 1 Row, $m=2.0$, $x/d=17.6$, $Z=-2.54$ cm	88
Figure 48.	St/St_o Versus θ , Compound Angle, 1 Row, $m=2.0$, $x/d=33.8$, $Z=-2.54$ cm	89
Figure 49.	St/St_o Versus θ , Compound Angle, 1 Row, $m=2.0$, $x/d=55.5$, $Z=-2.54$ cm	90
Figure 50.	St/St_o Versus θ , Compound Angle, 1 Row, $m=2.0$, $x/d=77.1$, $Z=-2.54$ cm	91

Figure 51.	St/St_0 Versus θ , Compound Angle, 1 Row, $m=2.0$, $x/d=98.7$, $Z=-2.54$ cm	92
Figure 52.	$\bar{\eta}$ Versus x/d , Compound Angle, 1 Row, $m=2.0$, Spanwise Average	93
Figure 53.	$\overline{St_f/St_0}$ Versus x/d , Compound Angle, 1 Row, $m=2.0$, Spanwise Average	94
Figure 54.	Spanwise Averaged Stanton Number Versus Reynolds Number, Comparison of Different θ Values and Baselines, 1 Row, $m=2.0$	95
Figure 55.	Spanwise Variation of η , Compound Angle, 1 Row, $m=2.0$.	96
Figure 56.	Spanwise Variation of St_f/St_0 , Compound Angle, 1 Row, $m=2.0$	97
Figure 57.	Spanwise Variation of St_f/St_0 , Compound Angle, 1 Row, $m=2.0$, $\theta=1.28$	98
Figure 58.	St/St_0 Versus θ , Compound Angle, 1 Row, $m=3.0$, $x/d=6.8$, $Z=-2.54$ cm	99
Figure 59.	St/St_0 Versus θ , Compound Angle, 1 Row, $m=3.0$, $x/d=17.6$, $Z=-2.54$ cm	100
Figure 60.	St/St_0 Versus θ , Compound Angle, 1 Row, $m=3.0$, $x/d=33.8$, $Z=-2.54$ cm	101
Figure 61.	St/St_0 Versus θ , Compound Angle, 1 Row, $m=3.0$, $x/d=55.5$, $Z=-2.54$ cm	102
Figure 62.	St/St_0 Versus θ , Compound Angle, 1 Row, $m=3.0$, $x/d=77.1$, $Z=-2.54$ cm	103
Figure 63.	St/St_0 Versus θ , Compound Angle, 1 Row, $m=3.0$, $x/d=98.7$, $Z=-2.54$ cm	104
Figure 64.	$\bar{\eta}$ Versus x/d , Compound Angle, 1 Row, $m=3.0$, Spanwise Average	105
Figure 65.	$\overline{St_f/St_0}$ Versus x/d , Compound Angle, 1 Row, $m=3.0$, Spanwise Average	106
Figure 66.	Spanwise Averaged Stanton Number Versus Reynolds Number, Comparison of Different θ Values and Baselines, 1 Row, $m=3.0$	107
Figure 67.	Spanwise Variation of η , Compound Angle, 1 Row, $m=3.0$	108

Figure 68.	Spanwise Variation of St_t/St_o , Compound Angle, 1 Row, $m=3.0$	109
Figure 69.	Spanwise Variation of St_t/St_o , Compound Angle, 1 Row, $m=3.0, \theta=1.76$	110
Figure 70.	St/St_o Versus θ , Compound Angle, 1 Row, $m=4.0, x/d=6.8, Z=-7.62$ cm	111
Figure 71.	St/St_o Versus θ , Compound Angle, 1 Row, $m=4.0, x/d=17.6, Z=-7.62$ cm	112
Figure 72.	St/St_o Versus θ , Compound Angle, 1 Row, $m=4.0, x/d=33.8, Z=-7.62$ cm	113
Figure 73.	St/St_o Versus θ , Compound Angle, 1 Row, $m=4.0, x/d=55.5, Z=-7.62$ cm	114
Figure 74.	St/St_o Versus θ , Compound Angle, 1 Row, $m=4.0, x/d=77.1, Z=-7.62$ cm	115
Figure 75.	St/St_o Versus θ , Compound Angle, 1 Row, $m=4.0, x/d=98.7, Z=-7.62$ cm	116
Figure 76.	$\bar{\eta}$ Versus x/d , Compound Angle, 1 Row, $m=4.0$, Spanwise Average	117
Figure 77.	$\overline{St_t/St_o}$ Versus x/d , Compound Angle, 1 Row, $m=4.0$, Spanwise Average	118
Figure 78.	Spanwise Averaged Stanton Number Versus Reynolds Number, Comparison of Different θ Values and Baselines, 1 Row, $m=4.0$	119
Figure 79.	Spanwise Variation of η , Compound Angle, 1 Row, $m=4.0$	120
Figure 80.	Spanwise Variation of St_t/St_o , Compound Angle, 1 Row, $m=4.0$	121
Figure 81.	Spanwise Variation of St_t/St_o , Compound Angle, 1 Row, $m=4.0, \theta=1.56$	122
Figure 82.	Streamwise Injectant Distribution, Compound Angle, 1 Row, $m=1.5, x/d=9.9$	123
Figure 83.	Streamwise Injectant Distribution, Compound Angle, 1 Row, $m=1.5, x/d=44.3$	124
Figure 84.	Streamwise Injectant Distribution, Compound Angle, 1 Row, $m=1.5, x/d=86.3$	125
Figure 85.	Streamwise Injectant Distribution, Compound Angle, 1 Row, $m=2.0, x/d=9.9$	126

Figure 86.	Streamwise Injectant Distribution, Compound Angle, 1 Row, $m=2.0$, $x/d=44.3$	127
Figure 87.	Streamwise Injectant Distribution, Compound Angle, 1 Row, $m=2.0$, $x/d=86.3$	128
Figure 88.	Streamwise Injectant Distribution, Compound Angle, 1 Row, $m=3.0$, $x/d=9.9$	129
Figure 89.	Streamwise Injectant Distribution, Compound Angle, 1 Row, $m=3.0$, $x/d=44.3$	130
Figure 90.	Streamwise Injectant Distribution, Compound Angle, 1 Row, $m=3.0$, $x/d=86.3$	131
Figure 91.	Streamwise Injectant Distribution, Compound Angle, 1 Row, $m=4.0$, $x/d=9.9$	132
Figure 92.	Streamwise Injectant Distribution, Compound Angle, 1 Row, $m=4.0$, $x/d=44.3$	133
Figure 93.	Streamwise Injectant Distribution, Compound Angle, 1 Row, $m=4.0$, $x/d=86.3$	134
Figure 94.	Streamwise Velocity Field, Compound Angle, 1 Row, $m=1.5$, $x/d=9.9$	135
Figure 95.	Streamwise Velocity Field, Compound Angle, 1 Row, $m=1.5$, $x/d=44.3$	136
Figure 96.	Streamwise Velocity Field, Compound Angle, 1 Row, $m=1.5$, $x/d=86.3$	137
Figure 97.	Streamwise Pressure Field, Compound Angle, 1 Row, $m=1.5$, $x/d=9.9$	138
Figure 98.	Streamwise Pressure Field, Compound Angle, 1 Row, $m=1.5$, $x/d=44.3$	139
Figure 99.	Streamwise Pressure Field, Compound Angle, 1 Row, $m=1.5$, $x/d=86.3$	140
Figure 100.	Streamwise Velocity Field, Compound Angle, 1 Row, $m=2.0$, $x/d=9.9$	141
Figure 101.	Streamwise Velocity Field, Compound Angle, 1 Row, $m=2.0$, $x/d=44.3$	142
Figure 102.	Streamwise Velocity Field, Compound Angle, 1 Row, $m=2.0$, $x/d=86.3$	143
Figure 103.	Streamwise Pressure Field, Compound Angle, 1 Row, $m=2.0$, $x/d=9.9$	144

Figure 104.	Streamwise Pressure Field, Compound Angle, 1 Row, $m=2.0$, $x/d=44.3$	145
Figure 105.	Streamwise Pressure Field, Compound Angle, 1 Row, $m=2.0$, $x/d=86.3$	146
Figure 106.	Streamwise Velocity Field, Compound Angle, 1 Row, $m=3.0$, $x/d=9.9$	147
Figure 107.	Streamwise Velocity Field, Compound Angle, 1 Row, $m=3.0$, $x/d=44.3$	148
Figure 108.	Streamwise Velocity Field, Compound Angle, 1 Row, $m=3.0$, $x/d=86.3$	149
Figure 109.	Streamwise Pressure Field, Compound Angle, 1 Row, $m=3.0$, $x/d=9.9$	150
Figure 110.	Streamwise Pressure Field, Compound Angle, 1 Row, $m=3.0$, $x/d=44.3$	151
Figure 111.	Streamwise Pressure Field, Compound Angle, 1 Row, $m=3.0$, $x/d=86.3$	152
Figure 112.	Streamwise Velocity Field, Compound Angle, 1 Row, $m=4.0$, $x/d=9.9$	153
Figure 113.	Streamwise Velocity Field, Compound Angle, 1 Row, $m=4.0$, $x/d=44.3$	154
Figure 114.	Streamwise Velocity Field, Compound Angle, 1 Row, $m=4.0$, $x/d=86.3$	155
Figure 115.	Streamwise Pressure Field, Compound Angle, 1 Row, $m=4.0$, $x/d=9.9$	156
Figure 116.	Streamwise Pressure Field, Compound Angle, 1 Row, $m=4.0$, $x/d=44.3$	157
Figure 117.	Streamwise Pressure Field, Compound Angle, 1 Row, $m=4.0$, $x/d=86.3$	158
Figure 118.	St/St_0 Versus θ , Compound Angle, 2 Rows, $m=2.0$, $x/d=6.8$, $Z=-2.54$ cm	159
Figure 119.	St/St_0 Versus θ , Compound Angle, 2 Rows, $m=2.0$, $x/d=17.6$, $Z=-2.54$ cm	160
Figure 120.	St/St_0 Versus θ , Compound Angle, 2 Rows, $m=2.0$, $x/d=33.8$, $Z=-2.54$ cm	161
Figure 121.	St/St_0 Versus θ , Compound Angle, 2 Rows, $m=2.0$, $x/d=55.5$, $Z=-2.54$ cm	162

Figure 122.	St/St_o Versus θ , Compound Angle, 2 Rows, $m=2.0$, $x/d=77.1$, $Z=-2.54$ cm	163
Figure 123.	St/St_o Versus θ , Compound Angle, 2 Rows, $m=2.0$, $x/d=98.7$, $Z=-2.54$ cm	164
Figure 124.	$\bar{\eta}$ Versus x/d , Compound Angle, 2 Rows, $m=2.0$, Spanwise Average	165
Figure 125.	$\overline{St_f/St_o}$ Versus x/d , Compound Angle, 2 Rows, $m=2.0$, Spanwise Average	166
Figure 126.	Spanwise Averaged Stanton Number Versus Reynolds Number, Comparison of Different θ Values and Baselines, 2 Rows, $m=2.0$	167
Figure 127.	Spanwise Variation of η , Compound Angle, 2 Rows, $m=2.0$	168
Figure 128.	Spanwise Variation of St_f/St_o , Compound Angle, 2 Rows, $m=2.0$	169
Figure 129.	Spanwise Variation of St_f/St_o , Compound Angle, 2 Rows, $m=2.0$, $\theta=1.67$	170
Figure 130.	St/St_o Versus θ , Compound Angle, 2 Rows $m=3.0$, $x/d=6.8$, $Z=-1.27$ cm	171
Figure 131.	St/St_o Versus θ , Compound Angle, 2 Rows, $m=3.0$, $x/d=17.6$, $Z=-1.27$ cm	172
Figure 132.	St/St_o Versus θ , Compound Angle, 2 Rows, $m=3.0$, $x/d=33.8$, $Z=-1.27$ cm	173
Figure 133.	St/St_o Versus θ , Compound Angle, 2 Rows, $m=4.0$, $x/d=55.5$, $Z=-1.27$ cm	174
Figure 134.	St/St_o Versus θ , Compound Angle, 2 Rows, $m=3.0$, $x/d=77.1$, $Z=-1.27$ cm	175
Figure 135.	St/St_o Versus θ , Compound Angle, 2 Rows, $m=3.0$, $x/d=98.7$, $Z=-1.27$ cm	176
Figure 136.	$\bar{\eta}$ Versus x/d , Compound Angle, 2 Rows, $m=3.0$, Spanwise Average	177
Figure 137.	$\overline{St_f/St_o}$ Versus x/d , Compound Angle, 2 Rows, $m=3.0$, Spanwise Average	178
Figure 138.	Spanwise Averaged Stanton Number Versus Reynolds Number, Comparison of Different θ Values and Baselines, 2 Rows, $m=3.0$	179

Figure 139.	Spanwise Variation of η , Compound Angle, 2 Rows, $m=3.0$	180
Figure 140.	Spanwise Variation of St_i/St_o , Compound Angle, 2 Rows, $m=3.0$	181
Figure 141.	Spanwise Variation of St_i/St_o , Compound Angle, 2 Rows, $m=3.0$, $\theta=1.67$	182
Figure 142.	Streamwise Injectant Distribution, Compound Angles, 2 Rows, $m=2.0$, $x/d=9.9$	183
Figure 143.	Streamwise Injectant Distribution, Compound Angles, 2 Rows, $m=2.0$, $x/d=44.3$	184
Figure 144.	Streamwise Injectant Distribution, Compound Angles, 2 Rows, $m=2.0$, $x/d=86.3$	185
Figure 145.	Streamwise Injectant Distribution, Compound Angles, 2 Rows, $m=3.0$, $x/d=9.9$	186
Figure 146.	Streamwise Injectant Distribution, Compound Angles, 2 Rows, $m=3.0$, $x/d=44.3$	187
Figure 147.	Streamwise Injectant Distribution, Compound Angles, 2 Rows, $m=3.0$, $x/d=86.3$	188
Figure 148.	Streamwise Velocity Field, Compound Angle, 2 Rows, $m=2.0$, $x/d=9.9$	189
Figure 149.	Streamwise Velocity Field, Compound Angle, 2 Rows, $m=2.0$, $x/d=44.3$	190
Figure 150.	Streamwise Velocity Field, Compound Angle, 2 Rows, $m=2.0$, $x/d=86.3$	191
Figure 151.	Streamwise Pressure Field, Compound Angle, 2 Rows, $m=2.0$, $x/d=9.9$	192
Figure 152.	Streamwise Pressure Field, Compound Angle, 2 Rows, $m=2.0$, $x/d=44.3$	193
Figure 153.	Streamwise Pressure Field, Compound Angle, 2 Rows, $m=2.0$, $x/d=86.3$	194
Figure 154.	Streamwise Velocity Field, Compound Angle, 2 Rows, $m=3.0$, $x/d=9.9$	195
Figure 155.	Streamwise Velocity Field, Compound Angle, 2 Rows, $m=3.0$, $x/d=44.3$	196
Figure 156.	Streamwise Velocity Field, Compound Angle, 2 Rows, $m=3.0$, $x/d=86.3$	197
Figure 157.	Streamwise Pressure Field, Compound Angle, 2 Rows, $m=3.0$, $x/d=9.9$	198

Figure 158.	Streamwise Pressure Field, Compound Angle, 2 Rows, $m=3.0$, $x/d=44.3$	199
Figure 159.	Streamwise Pressure Field, Compound Angle, 2 Rows, $m=3.0$, $x/d=86.3$	200
Figure 160.	Spanwise Averaged $\bar{\eta}$ Versus x/d , Comparison of Configuration 1 to Configuration 2, $m=0.5, 1.0$, and 1.5 , 1 Row	201
Figure 161.	Spanwise Averaged $\overline{St_f/St_o}$ Versus x/d , Comparison of Configuration 1 to Configuration 2, $m=0.5, 1.0$, and 1.5 , 1 Row	202
Figure 162.	Spanwise Averaged $\bar{\eta}$ Versus x/d , Comparison of Configuration 1 to Configuration 2, $m=0.5, 1.0$, and 1.5 , 2 Rows	203
Figure 163.	Spanwise Averaged $\overline{St_f/St_o}$ Versus x/d , Comparison of Configuration 1 to Configuration 2, $m=0.5, 1.0$, and 1.5 , 2 Rows	204
Figure 164.	Spanwise Averaged $\bar{\eta}$ Versus x/d , Comparison of Configuration 1 to Configuration 3, $m=0.5, 1.0$, and 1.5 , 1 Row	205
Figure 165.	Spanwise Averaged $\overline{St_f/St_o}$ Versus x/d , Comparison of Configuration 1 to Configuration 3, $m=0.5, 1.0$, and 1.5 , 1 Row	206
Figure 166.	Spanwise Averaged $\bar{\eta}$ Versus x/d , Comparison of Configuration 1 to Configuration 3, $m=0.5, 1.0$, and 1.5 , 2 Rows	207
Figure 167.	Spanwise Averaged $\overline{St_f/St_o}$ Versus x/d , Comparison of Configuration 1 to Configuration 3, $m=0.5, 1.0$, and 1.5 , 2 Rows	208
Figure 168.	Spanwise Averaged $\bar{\eta}$ Versus x/d , Comparison of Configuration 2 to Configuration 3, $m=0.5, 1.0$, and 1.5 , 1 Row	209

Figure 169.	Spanwise Averaged $\overline{St_f/St_o}$ Versus x/d , Comparison of Configuration 2 to Configuration 3, $m=0.5, 1.0$, and 1.5 , 1 Row	210
Figure 170.	Spanwise Averaged $\bar{\eta}$ Versus x/d , Comparison of Configuration 2 to Configuration 3, $m=0.5, 1.0$, and 1.5 , 2 Rows	211
Figure 171.	Spanwise Averaged $\overline{St_f/St_o}$ Versus x/d , Comparison of Configuration 2 to Configuration 3, $m=0.5, 1.0$, and 1.5 , 2 Rows	212
Figure 172.	Spanwise Averaged $\bar{\eta}$ Versus x/d , Comparison of Different Blowing Ratios for Configuration 3, 1 Row	213
Figure 173.	Spanwise Averaged $\overline{St_f/St_o}$ Versus x/d , Comparison of Different Blowing Ratios for Configuration 3, 1 Row	214
Figure 174.	Spanwise Averaged $\bar{\eta}$ Versus x/d , Comparison of Different Blowing Ratios for Configuration 3, 2 Rows	215
Figure 175.	Spanwise Averaged $\overline{St_f/St_o}$ Versus x/d , Comparison of Different Blowing Ratios for Configuration 3, 2 Rows	216
Figure 176.	$\bar{\eta}/m$ Versus $x*I/s$, Correlation Plot of Configurations 1, 2, and 3, All Blowing Ratios, 1 Row and 2 Rows	217
Figure 177.	$\bar{\eta}/I$ Versus $x*I/s$, Correlation Plot of Configurations 1, 2, and 3, All Blowing Ratios, 1 Row and 2 Rows	218
Figure 178.	$\bar{\eta}/m$ Versus $x*I/s$, Correlation Plot of Configurations 1, 2, and 3, $m=0.5, 1.0$ and 1.5 , 1 Row and 2 Rows	219
Figure 179.	$\bar{\eta}/I$ Versus $x*I/s$, Correlation Plot of Configurations 1, 2, and 3, $m=0.5, 1.0$, and 1.5 , 1 Row and 2 Rows	220

LIST OF SYMBOLS

A	- heat transfer surface area
C_d	- coefficient of discharge
C_p	- specific heat
d	- injection hole diameter (0.925 cm)
F_{ij}	- radiation view factor
h	- heat transfer coefficient with film injection
h_o	- baseline heat transfer coefficient, no film injection
h_f	- iso-energetic heat transfer coefficient with film injection
I	- momentum flux ratio, $\rho_c U_c^2 / \rho_\infty U_\infty^2$
K	- thermal conductivity, W/m ⁰ K
m	- blowing ratio, $\rho_c U_c / \rho_\infty U_\infty$
q	- heat flux
Re	- Reynolds number
s	- equivalent slot width
St	- Stanton number with film injection
St_o	- baseline Stanton number, no film injection
St_f	- iso-energetic Stanton number with film injection
$\overline{St_f}$	- spanwise-averaged iso-energetic Stanton number with film injection
T	- static temperature
T_{amb}	- ambient temperature
T_{plate}	- average plate temperature
T_c	- coolant temperature

T_{inj}	- injectant temperature
T_{plenum}	- plenum temperature
T_w	- wall temperature
T_{∞}	- freestream temperature
T_{aw}	- adiabatic wall temperature
U	- streamwise mean (time-averaged) velocity
X	- streamwise distance measured from the leading edge of the boundary layer trip
x	- streamwise distance measured from the downstream edges of the injection holes
x/d	- dimensionless streamwise distance
Y	- distance normal to the test surface
Z	- spanwise distance measured from the test surface centerline
α	- thermal diffusivity, $K/\rho C_p$
β_1	- complete beta function
β_{u1}	- incomplete beta function
ϵ	- radiation emissivity
σ	- Stefan-Boltzman constant
ξ	- unheated starting length
η	- adiabatic film cooling effectiveness, $(T_{aw} - T_{\infty})/(T_c - T_{\infty})$
$\bar{\eta}$	- spanwise-averaged adiabatic film cooling effectiveness
ρ	- density
θ	- non-dimensional injection temperature, $(T_c - T_{\infty})/(T_w - T_{\infty})$
Ω	- injection hole angles with respect to the test surface as projected into the streamwise/normal plane

β - injection hole angle with respect to the test surface as projected into the spanwise/normal plane.

Subscripts

aw - adiabatic wall
c - injectant at exits of injection holes
o - stagnation
w - wall
 ∞ - freestream
cond - conduction heat transfer
conv - convection heat transfer
rad - radiation heat transfer

Superscripts

—
time-average

ACKNOWLEDGMENTS

This research was sponsored by Naval Sea Systems Command, Code 56X3, Washington, D.C. Program monitor was Dr. Dan Groghan.

I wish to express my deep appreciation to Professor Phillip Ligrani who was a very influential and important driving force behind this study. Dr. Chelakara Subramanian was extremely helpful with his Knowledge of computer programming and technical familiarity with all laboratory procedures employed. I wish to thank both Professor Phillip Ligrani and Dr. Subramanian for their patience, guidance and enthusiasm for this study.

In addition, I wish to thank the entire staff of the NPS Department of Mechanical Engineering, especially Thomas H. McCord, Thomas Christian, James T. Schofield, and Mardo Blanco who were always willing to assist in the manufacture and repair of equipment. Last, but not least, I am deeply appreciative of my wife, Jackie, whose support and understanding was an asset throughout this research.

I. INTRODUCTION

A. BACKGROUND/THEORY

The need for greater efficiency in gas turbine engines has resulted in higher turbine inlet temperatures approaching 2000 K. These extreme temperatures, in combination with the high rotational speeds, result in large stress magnitudes on component materials, especially on the blades of the first turbine stage. Efficient means of cooling these components is thus a necessity if such stresses are to be minimized, and the safety, reliability and operating lifetimes of gas turbines are to be maximized. Film cooling is one method of thermal protection of gas turbine component surfaces which is used extensively in commercial and military applications, particularly on turbine blades, turbine endwalls, combustion chamber linings, and afterburner linings. In the past, the most common film cooling arrangement employed holes with simple angle orientations. Simple angle injection refers to orientations in which the film is injected from holes inclined to the test surface such that injectant is issued from the holes at an angle with respect to the test surface when viewed in the streamwise/normal plane and approximately in the direction of the mainstream flow when viewed in the streamwise/spanwise plane.

Recently, gas turbine components have been manufactured with film cooling holes using compound angle orientations. The compound angle injection is believed to produce injectant distributions with better protection and higher film effectivenesses than injectant from holes with simple angle orientations. Compound angle orientations are ones in which the film is injected with holes

inclined to the test surface such that the injectant is issued with a spanwise velocity component relative to the mainstream flow (when viewed in the streamwise/spanwise plane). Although film-cooling from compound angle holes is now quite common on gas turbine components, little data is available in the archival literature on heat transfer and boundary layer behavior downstream of film cooling holes with compound angle orientations.

In the present study, Stanton number, iso-energetic Stanton number, adiabatic film cooling effectiveness, mean velocity, mean total pressure, and injectant distribution data are presented and analyzed for the compound angle configuration first used by Jackson [Ref. 1]. Adiabatic film cooling effectiveness values are determined using linear superposition theory applied to Stanton number ratios measured at different injection temperatures. This is possible since the three-dimensional energy equation which describes the flow field is linear and homogeneous in its dependent variable, temperature, for constant property flow. This equation is of the form:

$$\alpha \left(\frac{\partial^2 T}{\partial x^2} + \frac{\partial^2 T}{\partial y^2} + \frac{\partial^2 T}{\partial z^2} \right) = u \frac{\partial T}{\partial x} + v \frac{\partial T}{\partial y} + w \frac{\partial T}{\partial z} \quad (\text{Equation 1.1})$$

where $\alpha = \frac{k}{\rho c}$. (Equation 1.2)

The technique of superposition was first applied to film cooling by Metzger, Carper and Swank [Ref. 2]. In a comment on this paper, E.R.G. Eckert showed how local heat transfer coefficient ratios for different injection temperatures can be used to deduce the adiabatic wall temperature, T_{aw} , and the iso-energetic

heat transfer coefficient, h_f . The adiabatic wall temperature is defined as the temperature which the film cooled wall assumes when the heat flux is zero. The iso-energetic heat transfer coefficient is defined as the heat transfer coefficient obtained under iso-energetic conditions in which the freestream and injectant recovery temperatures are the same. With these parameters, the heat flux with film cooling is given by :

$$q = h_f (T_w - T_{aw}) \quad (\text{Equation 1.3})$$

The same heat flux may also be expressed in terms of the difference between the actual wall temperature and the freestream recovery temperature using the equation given by :

$$q = h (T_w - T_\infty) \quad (\text{Equation 1.4})$$

Equating these two then produces an equation having the form :

$$h = h_f \frac{(T_w - T_{aw})}{(T_w - T_\infty)} \quad (\text{Equation 1.5})$$

or, after rearrangement;

$$h = h_f \left[1 - \frac{(T_{aw} - T_\infty)}{(T_w - T_\infty)} \right] \quad (\text{Equation 1.6})$$

This equation is then equivalent to :

$$h = h_f (1 - \theta \eta) \quad (\text{Equation 1.7})$$

where;

$$\theta = \frac{(T_c - T_\infty)}{(T_w - T_\infty)} \quad (\text{Equation 1.8})$$

and;

$$\eta = \frac{(T_{aw} - T_\infty)}{(T_c - T_\infty)} \quad (\text{Equation 1.9})$$

θ is defined as the non-dimensional temperature and η is the definition of the adiabatic film-cooling effectiveness. Dividing each side of equation 1.7 by h_o , the heat transfer coefficient without film cooling, and then expressing heat transfer coefficients in terms of Stanton numbers then produces the form of this equation employed in the present study :

$$\frac{St}{St_o} = \frac{St_f}{St_o} (1 - \theta \eta) \quad (\text{Equation 1.10})$$

A plot of St/St_o versus θ , where θ is varied by changing the injection temperature, thus gives a straight line with a vertical axis intercept of iso-energetic Stanton number ratio St_f/St_o , and a horizontal axis intercept of the inverse of the adiabatic film cooling effectiveness $1/\eta$. This approach applies

only so long as temperature variations are small enough that fluid properties are reasonably invariant as θ is changed, and as long as fluid properties are reasonably invariant with respect to all three coordinate directions (Ligrani and Camci, [Ref. 3], and Ligrani, [ref. 4]).

B. PRESENT STUDY

Experimental results are presented which describe the development and structure of flow downstream of film-cooling holes with compound angle orientations. Results are given which were measured both downstream of one row of holes and downstream of two staggered rows of holes. Holes are inclined at 35 degrees with respect to the test surface when projected into the streamwise/normal plane, and 30 degrees with respect to the test surface when projected into the spanwise/normal plane. Within each row, holes are spaced $6.0d$ apart, where d is the hole diameter. This gives $3.0d$ spacing between adjacent holes when two staggered rows are employed. Results presented include distributions of surface Stanton numbers, adiabatic film cooling effectiveness deduced from heat transfer coefficients using superposition, iso-energetic Stanton numbers, and injectant distributions. The Stanton number data are presented for θ values ranging from 0 to 4.0 at x/d ratios of 6.8, 17.6, 33.8, 55.5, 77.1, and 98.7. Blowing ratios m range from 0.5 to 4.0 for one row of film cooling holes and 2.0 to 3.0 for two rows of holes. Also presented are plots showing the streamwise development of distributions of mean streamwise velocity.

C. EXPERIMENTAL OUTLINE

Three different types of measurements are made in the present study:

1. Stanton numbers, Stanton number ratios and adiabatic film cooling effectiveness values at 21 spanwise locations at x/d ratios of 6.8, 17.6, 33.8, 55.5, 77.1, and 98.7.

2. Mean velocity and total pressure surveys in Y-Z planes at x/d values of 9.9, 44.3, and 86.3.

3. Mean temperature $(T - T_{\infty})$ surveys in Y - Z planes at x / d values of 9.9, 44.3, and 86.3 to provide information on injectant distributions. These data are obtained for eight different injection configurations as well as with no film-cooling: (1) one row of compound angle film-cooling holes with a blowing ratio of $m=0.5$, (2) one row of compound angle film-cooling holes with a blowing ratio of $m=1.0$, (3) one row of compound angle film-cooling holes with a blowing ratio of $m=1.5$, (4) one row of compound angle film-cooling holes with a blowing ratio of $m=2.0$, (5) one row of compound angle film-cooling holes with a blowing ratio of $m=3.0$, (6) one row of compound angle film-cooling holes with a blowing ratio of $m=4.0$, (7) two staggered rows of compound angle film-cooling holes with a blowing ratio of $m=2.0$, (8) two staggered rows of compound angle film-cooling holes with a blowing ratio of $m=3.0$, and (9) no film-cooling.

D. THESIS ORGANIZATION

The remainder of this thesis is organized as follows. Chapter II discusses the experimental apparatus and procedures. Chapter III contains experimental results. Chapter IV then presents a summary and conclusions. Appendix A

contains all of the figures. Appendix B discusses all of the data acquisition programs, processing programs and plotting programs developed and used for this study. Appendix C contains a data file directory which gives the names of all data files contained on micro floppy disks.

II. EXPERIMENTAL APPARATUS AND PROCEDURES

A. WIND TUNNEL AND COORDINATE SYSTEM.

The wind tunnel is the same one used in the experiments of Ligrani, et al. [Refs. 5 and 6]. The facility is open-circuit, subsonic, and located in the laboratories of the Department of Mechanical Engineering of the Naval Postgraduate School. A centrifugal blower is located at the upstream end, followed by a diffuser, a header containing a honeycomb and three screens, and then a 16 to 1 contraction ratio nozzle. The nozzle leads to the test section which is a rectangular duct 3.05 m long and 0.61 m wide, with a topwall having adjustable height to permit a zero pressure gradient to be set along the length of the test section (without the film cooling) to within 0.01 inches of water differential pressure. The initial duct height at the nozzle exit is 0.203 m. The freestream velocity is 10 m/s and the freestream turbulence intensity is approximately 0.13 percent based on the same velocity. The boundary layer is tripped using a 2 mm high spanwise uniform strip of tape near the nozzle exit 1.072 m upstream of the constant heat flux transfer surface.

Figure 1 shows the side view, and figure 2 shows the top view of the wind tunnel test section when the compound angle film-cooling arrangement (configuration 3) is installed. Locations of the boundary layer trip, the film cooling holes, the heat transfer test surface, and the thermocouple rows are labelled in figure 1 and in figure 2. With this arrangement, an unheated starting length exists when the heat transfer surface is at an elevated temperature. Thus, the direction of heat transfer is from the wall to the gas. In regard to the

coordinate system, Z is the spanwise coordinate measured from the test section spanwise centerline, X is measured from the upstream edge of the boundary layer trip, and Y is measured normal to the test surface. x is measured from the downstream edge of the injection holes and generally presented as x/d .

B. INJECTION HOLE CONFIGURATION

A schematic showing the compound angle film hole geometry (configuration 3) along the test surface is shown in figure 3. Here, holes are arranged in two rows which are staggered with respect to each other, with spanwise spacings between adjacent holes of $3.0d$. Centerlines of holes in separate rows are separated by $4.0d$ in the streamwise direction. When only one row of holes is employed, it is the downstream one located closest to the heat flux surface. With this arrangement, spanwise hole spacing is $6.0d$. Each row of holes contains five injection cooling holes with a nominal inside diameter of 0.925 cm. The centerline of the middle hole of the downstream row is located on the spanwise centerline ($Z=0.0$ cm) of the test surface. The compound angle holes are employed with $\Omega=35$ degrees and $\beta=30$ degrees, where Ω is the angle of the injection holes with respect to the test surface as projected into the streamwise/normal plane, and β is the angle of the injection holes with respect to the test surface as projected into the spanwise/normal plane. Thus, as shown in figure 3, holes are oriented so that the spanwise components of injectant velocity are directed in the negative- Z direction. The plane of each injection hole is angled at 50.5 degrees from the streamwise/normal (X - Y) plane. Within the plane of each hole, hole centerlines are oriented at angles of 24 degrees from the plane of the test surface (X - Z).

C. INJECTION SYSTEM.

The injection system is described by Ligrani, et al. [Ref. 6]. Air for the injection system originates either in two 1.5 horsepower DR513 Rotron Blowers capable of producing 30 cfm at 2.5 psig, or in one Spencer vortex blower VB-037-E capable of producing 100 cfm at 3.0 psig. From the blowers, air flows through a regulating valve, a Fisher and Porter rotometer, a diffuser, and finally into the injection heat exchanger and plenum chamber. The exchanger provides the means to heat the injectant above ambient temperature. With this system and test plate heating, the non-dimensional injection temperature parameter θ is maintained at values ranging from 0.0 to 4.0, which includes values within the range of gas turbine component operation. The upper surface of the plenum chamber is connected to the injection tubes which are 9.4 cm long, giving a length to diameter ratio of about 10.

Injection system performance was checked by measuring discharge coefficients at different Reynolds numbers based on injection hole diameter and mean injectant velocity. The results of these performance checks are presented in figure 4. They compare favorably with ones from Bishop [Ref. 7] who also gives procedures to measure discharge coefficients and blowing ratios.

All film cooling parameters, such as the blowing ratio, are calculated based on the temperature at the exits of the injection holes, (T_{inj}). This temperature T_{inj} is related to the injection plenum temperature, T_{plenum} , as shown by the results in figure 5, which are represented by an equation given by [Ref. 7]:

$$T_{inj}(\text{°C}) = 2.2907 + 0.85948 \times T_{plenum}(\text{°C}) \quad (\text{Equation 2.1})$$

This equation represents an empirical fit to experimental data for blowing ratios ranging from 0 to 1.5 and for injection temperatures from 0 to 100 degrees Celsius. With this arrangement, injection temperatures may be determined from measurements of the plenum temperature.

When one row of holes is employed, the downstream row of injection holes is used. With this arrangement the upstream holes are plugged and covered with cellophane tape.

D. HEAT TRANSFER SURFACE

The heat transfer surface is designed to provide a constant heat flux over its area. The test surface is inserted into the bottom wall of the wind tunnel next to the airstream. The upper face of this test surface is maintained level with the bottom of the wind tunnel using height adjustment screws mounted in the plexiglass support frame. The test surface is made of stainless steel foil painted flat black, with dimensions of 1.3 m x 0.476 m x 0.20 mm. Copper-constantan thermocouples are attached to the underside of the stainless steel foil in six rows of 21 thermocouples per row, with a spanwise spacing of 1.27 cm between individual thermocouples. Thermocouple lead wires are embedded in grooves cut into a triple sheet of 0.254 mm thick double sided tape. RTV epoxy is then used to fill spaces around thermocouple lead wires within these grooves. Electrobond epoxy is used to attach a wire wound heater, with dimensions of 1.0 mm x 1.118 m x 0.438 m and manufactured by Marchi Associates, to the underside of the double sided tape. The heater is rated at 120 volts and 1500 watts, and designed to maintain uniform dissipation of heat over its entire

surface. The dimensions and manufacturer of the heater are incorrectly noted in thesis by Jackson [Ref. 1], Bishop [Ref. 7], Ciriello [Ref. 8], and Ortiz [Ref. 9]. Located below the heater are several layers of insulating materials including Lexan sheets, foam insulation, styrofoam and balsa wood. A plexiglass support frame then encases the bottom portion of the heat transfer test surface and provides support. This frame is then mounted on the underside of the wind tunnel. Surface temperature levels and convective heat transfer rates are controlled by adjusting power into the heater using a Standard Electric Co. Variac, type 3000B.

After the surface was completed, a variety of qualification tests were conducted to check the performance of the heat transfer test surface. These are described in detail by Ligrani, [Ref. 5], Bishop [Ref. 7], and Ciriello [Ref. 8], along with additional details on the measurement of local Stanton numbers.

E. STANTON NUMBER MEASUREMENTS

1. Energy Balance

In previous studies, local Stanton numbers were calculated based on local temperature measurements and global convective heat flux levels. The global convective heat flux levels were determined from a global energy balance which accounts for radiation, conduction and convection from the entire test surface. In the present study, this analysis is refined to also include energy balances for control volumes around individual thermocouples which account for local spanwise and streamwise conduction along the test surface. Figure 6 illustrates these local energy balances based on control volumes around each thermocouple. The corresponding energy balance equation is given by :

$$q_{\text{conv}} = q_{\text{in}} - q_{\text{rad}} - q_{\text{cond}} - q_{\text{spanwise}} - q_{\text{streamwise}} \quad (\text{Equation 2.2})$$

The local heat transfer coefficient is then given by :

$$h = \frac{q_{\text{conv}}}{(T - T_{\infty})} \quad (\text{Equation 2.3})$$

The resulting Stanton number equation is :

$$St = \frac{h}{\rho U_{\infty} C_p} \quad (\text{Equation 2.4})$$

where $q_{\text{in}} = I \cdot V$, which is the power into the heater. q_{rad} is a global radiation heat flux from the test surface. q_{cond} is a global conduction heat flux from the bottom and sides of the test surface. q_{spanwise} is the local spanwise conduction between the thermocouple of interest and the adjacent thermocouples. $q_{\text{streamwise}}$ is the local streamwise conduction between the row of the thermocouple of interest and the adjacent rows of thermocouples. q_{in} , q_{rad} , and q_{cond} are global heat fluxes, and as such, are averaged over the heat transfer surface using the surface area of the heater which is 0.4897 m^2 .

2. Thermal Contact Resistance

During the heat transfer tests, temperatures measured by the thermocouples are greater than ones at the surface of the test plate, due to thermal contact resistance between the thermocouples and the surface of the test plate. This thermal contact resistance is estimated from the convective heat flux

measurements, from thermocouple measurements, and from measurements from calibrated liquid crystals on the surface of the test plate. The temperature difference is then correlated as a function of global convection heat flux through the test surface. The thermal contact resistance is 0.016 K/Watt based on measurements by Joseph [Ref.10]. This value was later verified by Williams [Ref.11] in a repeat of the original test.

3. Conduction Heat Transfer

To determine the heat loss by conduction from the bottom and sides of the heat transfer test surface, an energy balance was performed by Ortiz [Ref. 9]. This was accomplished by insulating the top of the test surface (which is normally exposed to the airstream) and measuring the conduction loss from the bottom as it is dependent upon the temperature difference between the test surface and the surrounding ambient air. The resulting equation fitted to the data is given by :

$$q_{\text{cond}} = 0.683 + 0.954 \times T_{\text{diff}} - 0.016 \times T_{\text{diff}}^2 \quad (\text{Equation 2.5})$$

Where $T_{\text{diff}} = T_w - T_{\text{amb}}$.

4. Radiation Heat Transfer

Radiation losses from the top of the test surface were analytically estimated using equations given by:

$$q_{ij} = \frac{\sigma (T_w^4 - T_{\text{amb}}^4)}{\left(\frac{1 - \epsilon_i}{\epsilon_i A_i} + \frac{1}{A_i F_{ij}} + \frac{1 - \epsilon_j}{\epsilon_j A_j} \right)} \quad (\text{Equation 2.6})$$

and

$$q_{\text{rad}} = \sum_{j=1}^n q_{ij} \quad (\text{Equation 2.7})$$

where ϵ is the emissivity of the surface, A is the surface area of the surface of interest, and F_{ij} is the view factor. The subscript i stands for the heat transfer test surface in this application, and the subscript j stands for other surfaces inside of the wind tunnel. ϵ is estimated to be 0.8 for the test surface, based on the value for a stainless steel plate painted flat black. ϵ is estimated to be 0.59 for the side walls of the wind tunnel, for a combination of galvanized gray zinc and plexiglass. ϵ is estimated to be 0.9 for the top of the wind tunnel, based on the value for plexiglass. All emissivity values are estimated from the ranges of values given in Appendix A of [Ref. 12]. The inside dimensions of the wind tunnel test section are 1.118 m x 0.21 m x 0.61 m for length, height, and width, respectively. View factors, F_{ij} for the top and each of the side walls are estimated to be 0.54 and 0.23, respectively, using Figure 13.4 of [Ref. 12] and the summation rule given by :

$$\sum_{j=1}^n F_{ij} = 1 \quad (\text{Equation 2.8})$$

After including the numerical values for all these parameters, the resulting equation for radiation heat transfer is given by :

$$q_{\text{rad}} = 2.169 \times 10^{-8} (T_w^4 - T_{\text{amb}}^4) \quad (\text{Equation 2.9})$$

Where T_w is the surface temperature of the plate, calculated using the average thermocouple temperature for the entire plate (average of all 126 thermocouples) after correction for thermal contact resistance. The software used to determine Stanton numbers, first calculates the average surface temperature in an iterative manner. This is necessary because the convective heat flux is required for the thermal contact resistance correction factor, and because the radiation heat loss is required in order to calculate the convection heat loss (see energy balance).

5. Spanwise/Streamwise Conduction Heat Transfer

A schematic of the control volume employed to account for spanwise and streamwise conduction from one thermocouple is shown in figure 7. This view of the control volume is oriented looking in the negative Y direction. The i index in the figure denotes the thermocouple row number (1 through 6), and the j index denotes the thermocouple position in each row (1 through 21).

The control volume used to analyze spanwise and streamwise conduction for each thermocouple is 1.27 cm x 1.27 cm x 0.2 mm. For each thermocouple, Fourier's law for heat conduction in one dimension is used to calculate the spanwise and streamwise conduction heat transfer. The equation is given by :

$$q = -K_f \frac{dT}{dZ} \quad (\text{Equation 2.10})$$

where $K_f = 14.25 \text{ Watts/m} \cdot ^\circ\text{K}$ [Ref. 13]. In order to evaluate dT/dZ , a temperature equation in polynomial form is first determined to describe the local variation of temperature in the vicinity of each thermocouple. This is accomplished using a least squares polynomial fit program [Ref. 14] to calculate a third order polynomial using four data points (thermocouple temperatures). The data points employed for each calculation are T_{j-2} , T_{j-1} , T_j and T_{j+1} . At the end of each row of thermocouples, the four thermocouples closest to the thermocouple of interest are employed. After the polynomial temperature equation is determined, it is then differentiated with respect to Z and evaluated at $\pm 0.3175 \text{ cm}$ from the Z position of the thermocouple of interest. The derivative is evaluated at these locations because the polynomial fit of the temperature field is a better representation of the physical model when it was evaluated closer to the thermocouple of interest instead of, for example, at the midpoint between two thermocouples ($\pm 0.635 \text{ cm}$). After determination of dT/dZ , it is then used in Fourier's law for conduction to calculate the spanwise conduction.

Streamwise conduction is evaluated in a similar manner except conduction heat transfer is calculated from thermocouple row to thermocouple row using an average thermocouple temperature for each row. Magnitudes of streamwise conduction calculated this way are thus the same for each thermocouple in a particular row. When applied to the energy balance equation, magnitudes of the spanwise and streamwise conduction heat flux are multiplied by the conduction area for the thermocouple ($1.27 \text{ cm} \times 0.2 \text{ mm}$) and divided by the surface area of the thermocouple control volume ($1.27 \text{ cm} \times 1.27 \text{ cm}$).

F. TEMPERATURE MEASUREMENTS

All temperature measurements are made using calibrated copper-constantan thermocouples. These include heat transfer surface temperatures, the freestream temperature, local boundary layer temperatures, and the injection plenum temperature. The calibration equation used for the heat transfer surface temperatures is given by Ortiz [Ref. 9]. These are connected to channels 1 to 126 of the data acquisition system. The calibration equation for the test surface thermocouples is given by :

$$T(^{\circ}\text{C}) = 0.018205 + 0.025846 \times E - 0.000000581 \times E^2$$

(Equation 2.11)

where E is in microvolts.

The calibration equation used for the freestream thermocouple is given by Williams [Ref. 11]. This thermocouple is connected to data acquisition channel 147. Its calibration equation is given by :

$$T(^{\circ}\text{C}) = -2.602912 + 32.177745 \times E - 5.483059 \times E^2 + 1.24739 \times E^3$$

(Equation 2.12)

where E is in millivolts.

Thermocouples employed in the plenum chamber, used to measure film injectant temperatures in the boundary layer, were calibrated by Bishop [Ref. 7]. From this calibration, the polynomial representing temperature as a function of thermocouple output voltage is given by :

$$T(^{\circ}\text{C}) = 0.0858454 + 26017.4569 \times E - 740382.8 \times E^2 + 35639480 \times E^3$$

(Equation 2.13)

where E is in volts/1000. Two thermocouples of this type are used on channels 149 and 150 for measurement of plenum temperature. One of these same thermocouples is also used on channel 153 when boundary layer temperatures are measured to determine injection distributions.

Temperature surveys to determine injectant distributions are performed using a thermocouple traversed through the boundary layer in conjunction with a thermocouple measuring freestream temperature. For these tests, freestream temperature is maintained at ambient temperature while injectant is heated to 50 degrees Celsius in the injection plenum, with no power applied to the heat transfer test plate. For each survey, local temperatures are taken at 800 (20 x 40) locations in the Y-Z plane at a particular x/d location. The spatial resolution between sampling points is 0.508 cm in each direction (Y and Z), and the overall sampling plane dimensions are 10.2 cm x 20.3 cm.

The traversing device consists of spanwise and vertical traversing blocks allowing two degrees of freedom. Each block is mounted on a separate assembly consisting of two steel case hardened support shafts and a 20 thread per inch pitch drive screw. Separate M092-FD310 stepping motors are used to drive each

of the two shafts. A two-axis Motion Controller(MITAS), equipped with 2K bytes of memory and a MC68000 16 bit microprocessor controls a motor drive which runs the motors. The motors, controller, and the drive are manufactured by the Superior Electric Company. Software within a Hewlett-Packard Series 9000 Model 310 computer provides instructions which control operation of the controller and traversing device.

A Hewlett-Packard 3497A Data Acquisition/Control Unit with a Hewlett-Packard 3498A Extender is used to collect all voltages from the thermocouples used. These units are also controlled by a Hewlett-Packard Series 9153C computer.

G. STREAMWISE MEAN VELOCITY MEASUREMENTS.

The streamwise mean velocity is measured using a five-hole pressure probe with a conical tip manufactured by United Sensors Corporation. Celesco transducers and Carrier Demodulators are used to sense pressures when connected to probe output ports. The same automated traverse used for injectant surveys was used to obtain these surveys. With this device, the pressure probe was traversed over 10.2 cm by 20.3 cm spanwise/normal planes at 800 locations spaced 0.51 cm apart in each direction. At each location, 50 samples of the output from each of the five pressure ports are aquisitioned for later processing. These devices, measurement procedures employed, as well as data acquisition equipment and procedures used are further detailed by Ligrani, et al. [Ref. 5 and 6], Bishop [Ref. 7], and Ciriello [Ref. 8].

H. BASELINE DATA MEASUREMENTS.

To provide a baseline data check, Stanton numbers, measured without film injection present, are compared to an empirical relationship given by Kays and Crawford [Ref. 15]. This relationship represents turbulent boundary layer flow in a zero pressure gradient over a constant heat flux surface just downstream of an unheated starting length. The equation is given by :

$$\text{StPr}^{0.4} = 0.03\text{Re}^{-0.2} \times \frac{\beta_1\left(\frac{1}{9}, \frac{10}{9}\right)}{\beta_{u1}\left(\frac{1}{9}, \frac{10}{9}\right)} \quad (\text{Equation 2.14})$$

Here, β_1 and β_{u1} are the Beta function and the incomplete Beta function, respectively. The term u_1 is defined as :

$$u_1 = 1 - \left(\frac{\xi_1}{x}\right)^{\frac{9}{10}} \quad (\text{Equation 2.15})$$

Figures 8 and 9 compare the exact solution given by equation 2.2 to baseline data obtained when either 4 amps $\{(T_{\text{plate}} - T_{\infty}) = 9.6\}$ or 6 amps $\{(T_{\text{plate}} - T_{\infty}) = 21.6\}$ of current are applied to the heat transfer test surface. Figure 8 is a plot of Stanton numbers versus x/d which shows that experimental data agree with the correlation for x/d greater than about 17. Figure 9 shows a plot of Stanton numbers versus Reynolds numbers with trends which are similar to the ones in figure 8.

III. EXPERIMENTAL RESULTS

Experimental results are presented for the compound angle angle injection configuration 3. Heat transfer data, injectant temperature distributions, and mean velocity/ total pressure surveys are presented from measurements downstream of both one row of film-cooling holes, and two staggered rows of film-cooling holes at various blowing ratios. For one row of film-cooling holes with blowing ratios $m=0.5$ and $m=1.0$, heat transfer data only are presented. For each blowing ratio, the first heat transfer data presented are the plots of St/St_0 vs θ for $x/d=6.8, 17.6, 33.8, 55.5, 77.1$, and 98.7 at a particular spanwise location. These data demonstrate the linearity of the St/St_0 vs θ data. The linearity of the data is important because it validates the use of the linear superposition technique to deduce the iso-energetic Stanton number ratio (St_f/St_0) and the adiabatic film-cooling effectiveness (η).

The next figures presented are plots of spanwise averaged adiabatic film-cooling effectiveness ($\bar{\eta}$) and iso-energetic Stanton number ratio ($\overline{St_f / St_0}$) vs x/d . Stanton number data are also given as a function of Reynolds number for various values of non-dimensional temperature (θ). The next three figures are three-dimensional plots showing the spanwise variation of adiabatic film-cooling effectiveness (η), iso-energetic Stanton number ratio (St_f/St_0), and Stanton number ratio (St/St_0) for a particular θ . Temperature surveys and mean velocity and total pressure surveys are subsequently presented for three different spanwise normal planes at streamwise locations of $x/d=9.9, 44.3$, and 86.3 for each blowing ratio.

A. PLATE 3, COMPOUND ANGLE, ONE ROW OF FILM-COOLING HOLES.

1. Heat Transfer Measurements

a. $m=0.5$

Figures 10 - 15 present St/St_0 vs θ results for $x/d=6.8, 17.6, 33.8, 55.5, 77.1,$ and 98.7 at a spanwise location of $Z=-1.27$ cm for $m=0.5$. The data presented for these six x/d locations demonstrate the linearity of the St/St_0 vs θ data. Figure 16 is a plot of spanwise-averaged $\bar{\eta}$ vs x/d and shows that $\bar{\eta}$ is largest at $x/d=6.8$ and that it decreases as x/d increases. Figure 17 is a plot of spanwise-averaged $\overline{St_f / St_0}$ vs x/d and shows that the values range between 1.0 and 1.1 and are generally independent of x/d . In figure 18, spanwise-averaged Stanton number data are given as a function of Reynolds number for $\theta = -0.036, 0.96, 1.39, 2.79,$ and 3.07 . Also included are the baseline curves with no film-cooling for 4 amp and 6 amp heater current levels. In general, at each Reynolds number, Stanton numbers decrease as θ increases, and at a particular θ , Stanton number values generally decrease with increasing Reynolds number, such that all sets of data show similar qualitative trends. The baseline Stanton number data are generally higher than all θ value curves with the exception of $\theta=-0.036$ data. Figures 19, 20, and 21 show streamwise and spanwise variations of η , St_f/St_0 , and St/St_0 for $\theta=1.39$, respectively. The plots of η at $x/d=6.8$ and $x/d=17.6$ in figure 19 show spanwise periodicity which becomes less pronounced with streamwise development. The spanwise periodicity of η is due to deficits (low η) and accumulations (high η) of injectant. The plots of St_f/St_0 and St/St_0 are spanwise periodic such that the higher values correspond to areas of high near-

wall mixing, and the lower values correspond to areas of higher concentrations of injectant.

b. $m=1.0$

Figures 22 - 27 present St/St_0 vs θ results for $x/d=6.8, 17.6, 33.8, 55.5, 77.1,$ and 98.7 at a spanwise location of $Z=-1.27$ cm for $m=1.0$. Figure 28 is a plot of spanwise-averaged $\bar{\eta}$ vs x/d . Figure 29 is a plot of spanwise-averaged $\overline{St_f / St_0}$ vs x/d . In figure 30, spanwise-averaged Stanton number data are given as a function of Reynolds number for $\theta = 0.062, 1.16, 1.90, 2.45,$ and 3.23 . Also included are the baseline curves with no film-cooling for 4 amp and 6 amp heater current levels. Figures 31, 32, and 33 show streamwise and spanwise variations of η , St_f/St_0 and St/St_0 for $\theta=1.16$, respectively. The trends of the plots are qualitatively similar to ones present for $m=0.5$. Quantitative magnitudes of spanwise averaged $\bar{\eta}$ and local η are somewhat lower than similar data for $m=0.5$. Spatially resolved St_f/St_0 and St/St_0 distributions show larger spanwise periodic variations than the results for $m=0.5$.

c. $m=1.5$

Figures 34 - 39 present St/St_0 vs θ results for $x/d=6.8, 17.6, 33.8, 55.5, 77.1,$ and 98.7 at a spanwise location of $Z=-1.27$ cm for $m=1.5$. Figure 40 is a plot of spanwise-averaged $\bar{\eta}$ vs x/d . Figure 41 is a plot of spanwise-averaged $\overline{St_f / St_0}$ vs x/d . In figure 42, spanwise-averaged Stanton number data are given as a function of Reynolds number for $\theta = 0.116, 0.938, 1.30, 2.00, 2.71,$ and 3.37 . Also included are the baseline curves with no film-cooling for 4 amp and 6 amp heater current levels. Figures 43, 44, and 45 show streamwise and spanwise variations of η , St_f/St_0 and St/St_0 for $\theta=1.30$, respectively. The trends of the plots are qualitatively somewhat similar to ones present for $m=0.5$

and $m=1.0$. Quantitative magnitudes of spanwise averaged $\bar{\eta}$ and local η are lower than similar results at $m=0.5$ and $m=1.0$ for x/d less than 60. Quantitative magnitudes of $\overline{St_f / St_0}$ are higher than similar data for $m=0.5$ and $m=1.0$, and spatially resolved plots of St_f/St_0 and St/St_0 show larger spanwise periodic variations than St_f/St_0 and St/St_0 data for $m=0.5$ and $m=1.0$.

d. $m=2.0$

Figures 46 - 51 present St/St_0 vs θ results for $x/d=6.8, 17.6, 33.8, 55.5, 77.1$, and 98.7 at a spanwise location of $Z=-2.54$ cm for $m=2.0$. Figure 52 is a plot of spanwise-averaged $\bar{\eta}$ vs x/d . Figure 53 is a plot of spanwise-averaged $\overline{St_f / St_0}$ vs x/d . In figure 54, spanwise-averaged Stanton number data are given as a function of Reynolds number for $\theta = 0.35, 0.94, 1.30, 1.83, 2.29$, and 2.71 . Also included are the baseline curves with no film-cooling for 4 amp and 6 amp heater current levels. Figures 55, 56, and 57 show streamwise and spanwise variations of η , St_f/St_0 and St/St_0 for $\theta=1.28$, respectively. Quantitative magnitudes of spanwise averaged $\bar{\eta}$ and local η are lower than similar results at lower blowing ratios for x/d less than 40. At larger x/d , $\bar{\eta}$ are slightly higher. Quantitative magnitudes of $\overline{St_f / St_0}$ are higher than data at the lower blowing ratios, and spatially resolved plots of St_f/St_0 and St/St_0 show larger amplitude variations than are evident in data obtained with lower m .

e. $m=3.0$

Figures 58 - 63 present St/St_0 vs θ results for $x/d=6.8, 17.6, 33.8, 55.5, 77.1$, and 98.7 at a spanwise location of $Z=-2.54$ cm for $m=3.0$. Figure 64 is a plot of spanwise-averaged $\bar{\eta}$ vs x/d . Figure 65 is a plot of spanwise-averaged $\overline{St_f / St_0}$ vs x/d . In figure 66, spanwise-averaged Stanton number data

are given as a function of Reynolds number for $\theta = 0.55, 1.37, 1.78, 2.58, 3.24,$ and 3.74 . Also included are the baseline curves with no film-cooling for 4 amp and 6 amp heater current levels. Figures 67, 68, and 69 show streamwise and spanwise variations of η , St_f/St_0 and St/St_0 for $\theta=1.76$, respectively. Quantitative magnitudes of spanwise averaged $\bar{\eta}$ and local η are lower than results for lower blowing ratios for x/d less than 40 due to injectant lift-off. At larger x/d , the values of $\bar{\eta}$ are slightly higher due to greater amounts of injectant over the test surface. Quantitative magnitudes of $\overline{St_f / St_0}$ are higher than data at lower blowing ratios, and spatially resolved plots of St_f/St_0 and St/St_0 show larger periodic amplitude variations across the span of the test surface than are present at lower m .

f. $m=4.0$

Figures 70 - 75 present St/St_0 vs θ results for $x/d=6.8, 17.6, 33.8, 55.5, 77.1,$ and 98.7 at a spanwise location of $Z=-7.62$ cm for $m=4.0$. Figure 76 is a plot of spanwise-averaged $\bar{\eta}$ vs x/d . Figure 77 is a plot of spanwise-averaged $\overline{St_f / St_0}$ vs x/d . In figure 78, spanwise-averaged Stanton number data are given as a function of Reynolds number for $\theta = 1.04, 1.57, 2.07, 3.12$ and 4.01 . Also included are the baseline curves with no film-cooling for 4 amp and 6 amp heater current levels. Figures 79, 80, and 81 show streamwise and spanwise variations of η , St_f/St_0 and St/St_0 for $\theta=1.56$, respectively. Quantitative magnitudes of spanwise averaged $\bar{\eta}$ and local η are lower for x/d less than 40 and slightly higher at larger x/d , compared to results at lower m . The quantitative magnitudes of $\overline{St_f / St_0}$ are higher than data at the lower blowing ratios, and the spatially resolved plots of St_f/St_0 and St/St_0 show larger

amplitude variations across the span of the test surface than are present at lower m .

2. Injectant Distributions

a. $m=1.5$

Figures 82 - 84 present mean temperature survey results which provide information on injectant distributions for $m=1.5$ for streamwise locations of $x/d=9.9$, 44.3, and 86.3. At the first streamwise location of $x/d=9.9$, the injectant distribution is spanwise periodic such that higher temperature regions correspond to accumulations of injectant. Individual accumulations of injectant are skewed and not symmetrical with respect to the spanwise direction. As the injectant is convected downstream, it becomes more diffuse at streamwise locations of $x/d=44.3$ and $x/d=86.3$. The injectant distribution is still spanwise periodic at $x/d=44.3$ but concentrations of injectant are moved farther from the wall. At $x/d=86.3$, the injectant is more spanwise uniform, especially 2 - 4 cm from the wall, with increasing spanwise periodicity closer to the wall.

b. $m=2.0$

Figures 85 - 87 present injectant distributions for $m=2.0$ for streamwise locations of $x/d=9.9$, 44.3, and 86.3. Qualitative trends are similar to surveys for m of 1.5. Injectant distributions are spanwise periodic at $x/d=9.9$ and become more diffuse as the injectant is convected downstream to $x/d=44.3$ and $x/d=86.3$. In addition, the survey at $x/d=86.3$ shows spanwise uniformity 3 - 5 cm from the wall. The injectant in figures 85 - 87 is farther away from the test surface at all three streamwise survey locations by about 0.5 cm compared to results for $m=1.5$.

c. $m=3.0$

Figures 88 - 90 show injectant distributions for $m=3.0$ for $x/d=9.9$, 44.3, and 86.3. Qualitative trends show some similarity to ones observed at lower m . In this case, injectant distributions begin to show spanwise uniformity at $x/d=44.3$ especially 3 -5 cm from the wall. At $x/d=86.3$, there is spanwise uniform behavior 3 - 6 cm from the wall, and evidence of skewed injectant accumulations on the left side of the tunnel. Compared to results for the lower blowing ratios, injectant is pushed farther from the test surface at all three streamwise locations investigated. In particular, significant injectant lift-off is evident at $x/d=9.9$.

d. $m=4.0$

The $m=4.0$ results in figures 91 - 93 are somewhat similar to the $m=3.0$ surveys. In both cases, injectant distributions begin to show spanwise uniform behavior at $x/d=44.3$, especially 3 - 6 cm from the wall. There is also spanwise uniform behavior at $x/d=86.3$, 2 - 6 cm from the wall at Z from 8 cm to -4 cm. At smaller Z , some skewing of the injectant is evident as a consequence of accumulations of injectant near the wind tunnel side wall.

3. Streamwise Mean Velocity Surveys

The five hole pressure probe is used to obtain distributions of streamwise mean velocity and total mean pressure. These two types of distributions are qualitatively very similar for all experimental conditions examined.

a. $m=1.5$

Figures 94 - 96 present streamwise velocity distributions and figures 97 - 99 present total pressure distributions for $m=1.5$ for streamwise

locations $x/d=9.9$, 44.3, and 86.3. Distributions for the first streamwise location at $x/d=9.9$ are spanwise periodic near the wall. Accumulations of injectant correspond to streamwise velocity deficits at spanwise locations $Z=-7$ cm to -8 cm, -2 cm to -3 cm, and 3 cm to 4 cm. Individual deficits are also skewed such that they are not symmetrical with respect to the spanwise direction. The downstream survey locations at $x/d=44.3$ and $x/d=86.3$ also show spanwise periodicity and thicker boundary layers with smaller quantitative variations near the wall compared to the survey at $x/d=9.9$.

b. $m=2.0$

Figures 100 - 102 present streamwise velocity distributions and figures 103 - 105 present total pressure distributions for $m=2.0$ for streamwise locations $x/d=9.9$, 44.3, and 86.3. These results are qualitatively similar to ones for a blowing ratio $m=1.5$.

c. $m=3.0$

Figures 106 - 108 present streamwise velocity distributions and figures 109 - 111 present total pressure distributions for $m=3.0$ for streamwise locations $x/d=9.9$, 44.3, and 86.3. Distributions for the first streamwise location at $x/d=9.9$ are spanwise periodic with high velocity regions corresponding to injectant accumulations, located at spanwise locations $Z=-7$ cm to -9 cm, -2 cm to -4 cm, and 2 cm to 4 cm. This behavior is different from results for lower blowing ratios due to the high injection velocities associated with this blowing ratio. Results for $x/d=9.9$ additionally show severe lift-off effects since the injectant appears to be about 1 cm above the wall. Velocity distributions at $x/d=44.3$ and $x/d=86.3$ also show spanwise periodicity due to velocity deficits which correspond to accumulations of injectant.

d. m=4.0

Figures 112 - 114 present streamwise velocity distributions and figures 115 - 117 present total pressure distributions for $m=4.0$ for streamwise locations $x/d=9.9, 44.3,$ and 86.3 . These results are qualitatively similar to ones for a blowing ratio $m=3.0$. Here, spanwise periodic high velocity regions are located at spanwise locations $Z=-7$ cm to -11 cm, -2 cm to -5 cm, and 0 cm to 4 cm. These accumulations of injectant are different from ones for $m=3.0$ since they are much larger and extend farther away from the wall as a consequence of more severe injectant lift-off associated with the higher blowing ratio.

B. PLATE 3, COMPOUND ANGLE, TWO STAGGERED ROWS OF FILM-COOLING HOLES

1. Heat Transfer Measurements

a. m=2.0

Figures 118 - 123 present St/St_0 vs θ results for $x/d=6.8, 17.6, 33.8, 55.5, 77.1,$ and 98.7 at a spanwise location of $Z=-2.54$ cm for $m=2.0$. The data presented for these six x/d locations demonstrate the linearity of the St/St_0 vs θ data. Figure 124 is a plot of spanwise-averaged $\bar{\eta}$ vs x/d and shows that $\bar{\eta}$ is largest at $x/d=6.8$ and decreases as x/d increases. Figure 125 is a plot of spanwise-averaged $\overline{St_f / St_0}$ vs x/d and shows that the values range between 1.30 and 1.40 and are generally independent of x/d . In figure 126, spanwise-averaged Stanton number data are given as a function of Reynolds number for $\theta = 0.96, 1.30, 1.68, 2.58,$ and 2.97 . Also included are the baseline curves with no film-cooling for 4 amp and 6 amp heater current levels. In general, at each Reynolds number, Stanton numbers decrease as θ increases, and at a particular θ , Stanton

number values generally decrease with increasing Reynolds number, such that all sets of data show similar qualitative trends. The baseline Stanton number data are generally higher than all θ value curves with the exception of the $\theta=0.96$ data. Figures 127, 128, and 129 show spanwise variations of η , St_f/St_0 , and St/St_0 for $\theta=1.67$, respectively. The plots of η at $x/d=6.8$ in figure 127 show spanwise periodicity which becomes less pronounced with streamwise development. Measurements of η at larger x/d show spanwise uniformity with slight skewing in the negative Z direction due to injectant accumulation on the left side of the tunnel looking downstream. The plots of St_f/St_0 and St/St_0 in figures 128 and 129 are spanwise periodic with peaks which are amplified compared to results measured downstream of one row of film-cooling holes.

b. $m=3.0$

Figures 130 - 135 present St/St_0 vs θ results for $x/d=6.8, 17.6, 33.8, 55.5, 77.1$, and 98.7 at a spanwise location of $Z=-1.27$ cm for $m=3.0$. Figure 136 is a plot of spanwise-averaged $\bar{\eta}$ vs x/d . Figure 137 is a plot of spanwise-averaged $\overline{St_f/St_0}$ vs x/d . Figure 138 presents spanwise-averaged Stanton number data as a function of Reynolds number for $\theta = 1.67, 1.82, 3.03, 3.32$, and 3.61 . Also included are the baseline curves with no film-cooling for 4 amp and 6 amp heater current levels. Figures 139, 140, and 141 show streamwise and spanwise variations of η , St_f/St_0 and St/St_0 for $\theta=1.67$, respectively. The trends shown by data in these plots are qualitatively similar to trends observed for $m=2.0$. However, quantitative magnitudes of spanwise averaged $\bar{\eta}$ and local η are lower than results for $m=2.0$ due to injectant lift-off which seems to influence boundary layer behavior at all streamwise locations

where measurements are available. Quantitative magnitudes of $\overline{St_f / St_0}$ are higher than $\overline{St_f / St_0}$ data for $m=2.0$ at all x/d .

2. Injectant Distributions

a. $m=2.0$

Figures 142 -144 present mean temperature survey results which provide information on injectant distributions for $m=2.0$ for streamwise locations of $x/d=9.9$, 44.3, and 86.3. At $x/d=9.9$ individual injectant concentrations are non-circular and form a spanwise periodic pattern across the span of the measurement plane. As the injectant is convected downstream to $x/d=44.3$ and $x/d=86.3$, it is more diffuse and spanwise uniform, particularly 2 - 5 cm from the wall.

b. $m=3.0$

Figures 145 - 147 present injectant distributions for $m=3.0$ for streamwise locations of $x/d=9.9$, 44.3, and 86.3. Qualitative trends are similar to the $m=2.0$ surveys. In both cases, injectant distributions are spanwise periodic at $x/d=9.9$ and become more diffuse and spanwise uniform as the injectant is convected downstream to $x/d=44.3$ and $x/d=86.3$. Extra accumulations of injectant on the left side of tunnel (looking downstream) are evident at $x/d=86.3$, as a consequence of spanwise convection of the injectant in the negative Z direction.

3. Streamwise Mean Velocity Surveys

The five hole pressure probe is used to obtain distributions of streamwise mean velocity and total mean pressure. These two types of distributions are qualitatively very similar for all experimental conditions examined.

a. $m=2.0$

Figures 148 - 150 present streamwise mean velocity distributions and figures 151 - 153 present total mean pressure distributions for $m=2.0$ for streamwise locations $x/d=9.9, 44.3$, and 86.3 . Velocity distributions for the first streamwise location at $x/d=9.9$ are spanwise periodic with high velocity regions located at spanwise locations $Z=-8$ cm to -10 cm, -2 cm to -4 cm, and 1.5 cm to 3.5 cm which correspond to locations where injectant from the downstream row of holes accumulates. Nearby velocity deficits correspond to accumulations of injectant which originated in the upstream row of holes. Results for $x/d=9.9$ also show severe lift-off effects since the injectant from the downstream row of holes appears to be about 1 cm above the wall. Velocity distributions at $x/d=44.3$ and $x/d=86.3$ show spanwise periodicity which results because injectant from the upstream row of holes merges and coalesces with injectant from the downstream row of holes.

b. $m=3.0$

Figures 154 - 156 present streamwise mean velocity distributions and figures 157 - 159 present mean total pressure distributions for $m=3.0$ for streamwise locations $x/d=9.9, 44.3$, and 86.3 . Velocity distributions at $x/d=9.9$ are spanwise periodic with high velocity regions which correspond to injectant accumulations located at spanwise locations $Z=-8$ cm to -12 cm, -3 cm to -7 cm, -2 cm to 3 cm, and 4 cm to 8 cm. These accumulations of injectant are different from ones for $m=2.0$ since they are larger and seem to result from merging of injectant from the upstream and downstream rows. The injectant accumulations are also different from the $m=2.0$ results because they extend farther from the

wall as a consequence of greater injectant lift-off associated with the higher blowing ratio.

C. COMPARISON OF RESULTS FROM SIMPLE ANGLE AND COMPOUND ANGLE FILM-COOLING HOLES

Experimental results for the compound angle injection systems, configuration 1 and configuration 3, and for the simple angle injection system, configuration 2, are compared in this section. To quantify the orientations of the film-cooling holes for the different configurations, angles Ω and β are employed. Ω is the angle of the injectant holes with respect to the test surface as projected into the streamwise/normal plane, and β is the angle of the injection holes with respect to the test surface as projected into the spanwise/normal plane. Configuration one is a compound angle injection arrangement with $\Omega=35^\circ$, $\beta=30^\circ$, and a hole spacing of 7.8d for one row of holes, and a hole spacing of 3.9d for two rows of holes. Configuration two is a simple angle injection arrangement with $\Omega=35^\circ$, $\beta=90^\circ$, and a hole spacing of 6.0d for one row of holes and a hole spacing of 3.0d for two rows of holes. Configuration three is a compound angle injection arrangement with $\Omega=35^\circ$, $\beta=30^\circ$, and a hole spacing of 6.0d for one row of holes and a hole spacing of 3.0d for two rows of holes.

Changes resulting from different blowing ratios and streamwise positions (x/d) on spanwise-averaged values of adiabatic film-cooling effectiveness ($\overline{\eta}$) and on spanwise-averaged values of the iso-energetic Stanton number ratio ($\overline{St_f / St_o}$) are now discussed. To accomplish this, summary graphs of results from all three film-cooling configurations are presented which were measured downstream of one row of holes and downstream of two staggered rows of

holes. Figures 160 to 163 present data from compound angle configuration one and simple angle configuration two. Spanwise-averaged $\bar{\eta}$ and spanwise-averaged $\overline{St_f / St_o}$ vs x/d data for one row of film-cooling holes are given in figures 160 and 161. Similar data for two staggered rows of film-cooling holes are given in figures 162 and 163. Figures 164 - 167 present data from configurations one and three. Of these figures, 164 and 165 give spanwise averaged $\bar{\eta}$ and spanwise averaged $\overline{St_f / St_o}$ data vs x/d for one row of holes, and figures 166 and 167 present results obtained downstream of two staggered rows of holes. Figures 168 - 171 present data from configurations two and three. Spanwise-averaged $\bar{\eta}$ and spanwise-averaged $\overline{St_f / St_o}$ vs x/d data for one row of film-cooling holes are given in figures 168 and 169. Similar data for two staggered rows of film-cooling holes are given in figures 170 and 171. Figures 172 and 173 present results from configuration three only. These give spanwise averaged $\bar{\eta}$ and spanwise averaged $\overline{St_f / St_o}$ data for blowing ratios of 0.5, 1.0, 1.5, 2.0, 3.0, and 4.0 as measured downstream of one row of film-cooling holes. Figures 174 - 175 then present similar data measured downstream of two staggered rows of configuration three film-cooling holes.

After examining these graphs, it is evident that, for a given blowing ratio, for all configurations tested, spanwise averaged $\bar{\eta}$ values are generally greatest at low x/d and decrease with increasing x/d as injectant is diffused and convected downstream. In addition, spanwise averaged $\bar{\eta}$ values decrease with increasing blowing ratio for x/d less than 20 - 40 due to injectant lift-off effects. This trend reverses at higher x/d because effectiveness is mostly dependent upon the amount of injectant along the test surface, and at lower blowing ratios smaller amounts of injectant are spread across the test surface. One exception to these trends is

evident in data measured downstream of two staggered rows of holes with a blowing ratio m of 3.0 since temperature, mean velocity and total pressure distributions show that lift-off effects are prevalent at all streamwise locations.

Spanwise averaged iso-energetic Stanton number ratios ($\overline{St_f / St_o}$) downstream of one row of holes and downstream of two staggered rows of holes generally range between 1.0 and 1.4 and show little variation with x/d for each blowing ratio tested. The trend at any given x/d shows increasing $\overline{St_f / St_o}$ with blowing ratio.

Spanwise-averaged values of $\bar{\eta}$ measured downstream of two staggered rows of holes are higher than data measured downstream of one row of holes when compared at any given blowing ratio since twice as much injectant is present per unit test surface area. Figures 164 and 166 also show that spanwise averaged $\bar{\eta}$ data for any given blowing ratio downstream of configuration three holes are as much as 40 percent higher than results measured downstream of configuration one holes because of smaller spanwise hole spacing. Figures 168 and 170 compare spanwise averaged data for configuration two and configuration three with the same spanwise hole spacing, downstream of one row of holes and downstream of two staggered rows of film-cooling holes. Compound angle injection data for configuration three are higher by as much as 100 percent for x/d of 6 - 8 for any given blowing ratio. As x/d increases, these differences decrease as the influences of the spanwise velocity component from compound angle injection diminish.

D. CORRELATIONS OF ADIABATIC FILM-COOLING EFFECTIVENESS DATA

Figure 176 shows a log-log plot of xI/s vs $\bar{\eta}/m$ with data of all blowing ratios tested on each configuration. Figure 177 shows the same data in a log-log plot of xI/s vs $\bar{\eta}/l$. In each plot, the data are presented for both the one row of holes and for two staggered rows of film-cooling holes. The data in the plot of xI/s vs $\bar{\eta}/m$ collapse according to spanwise hole spacing and overall, show the least scatter. The data in the plot of xI/s vs $\bar{\eta}/l$ seem to collapse according to blowing ratio. Results presented in figures 178 and 179 are the same as the ones in figures 176 and 177, except data for blowing ratios of 2.0, 3.0, and 4.0 are not included.

IV. SUMMARY AND CONCLUSIONS

Experimental results are presented which describe the development and structure of flow downstream of a single row and two staggered rows of film-cooling holes with compound angle orientations. With the configuration studied, holes are inclined at 35 degrees with respect to the test surface when projected into the streamwise/normal plane, and 30 degrees with respect to the test surface when projected into the spanwise/normal plane. Within each row, holes are spaced 6.0 hole diameters apart in the spanwise direction which gives 3.0d spacing between adjacent holes for the staggered row arrangement. Results presented include distributions of iso-energetic Stanton numbers, and adiabatic film cooling effectiveness deduced from Stanton numbers using superposition. Also presented are plots showing the streamwise development of injectant distributions and streamwise development of mean velocity distributions. The effects of blowing ratio, injectant temperature and downstream position are discussed. A new method is also implemented to account for local spanwise/streamwise conduction and radiation from the heat transfer test surface.

For the compound angle configuration, plate 3, results from eight different injection configurations are presented and discussed: (1) one row of film-cooling holes with a blowing ratio of $m=0.5$, (2) one row of film-cooling holes with a blowing ratio of $m=1.0$, (3) one row of film-cooling holes with a blowing ratio of $m=1.5$, (4) one row of film-cooling holes with a blowing ratio of $m=2.0$, (5) one row of film-cooling holes with a blowing ratio of $m=3.0$, (6) one row of film-cooling holes with a blowing ratio of $m=4.0$, (7) two staggered

rows of film-cooling holes with a blowing ratio of $m=2.0$, and (8) two staggered rows of film-cooling holes with a blowing ratio of $m=3.0$.

Spanwise averaged values of the adiabatic film-cooling effectiveness depend mostly on four parameters: hole angle orientation, spanwise hole spacing, number of rows of film-cooling holes (one or two), and blowing ratio. In general, for a given blowing ratio, spanwise averaged η values are greatest at low x/d and decrease with increasing x/d as injectant is diffused and convected downstream. In addition, spanwise averaged η values decrease with blowing ratio for x/d less than 20 - 40 due to injectant lift-off from the test surface. This trend generally reverses at higher x/d because smaller amounts of injectant are spread across the test surface as the blowing ratio decreases. Spanwise averaged iso-energetic Stanton number ratios downstream of one row of holes and two staggered rows of holes generally range between 1.0 and 1.4 and show little variation with x/d for each blowing ratio tested. At any given x/d , iso-energetic Stanton number ratios generally increase with increasing blowing ratio. Spanwise-averaged values of effectiveness measured downstream of two staggered rows of holes are higher than values measured downstream of one row of holes when compared at the same blowing ratio, because twice as much injectant covers the test surface.

Compound angle spanwise averaged adiabatic effectiveness values are as much as 100 percent higher than the simple angle data for x/d of 6 - 8. As the injectant is convected downstream to a larger x/d , these differences decrease until x/d near 100 when spanwise averaged values of effectiveness, for the same blowing ratio, are about the same for compound angle and simple angle configurations. Spanwise averaged effectiveness values decrease with blowing

ratio as blowing ratio is increased from 0.5 to 4.0 for x/d less than 40 - 60 downstream of one row of configuration 3 compound angle film-cooling holes. This is due to significant lift-off of the film injection jets from the test surface just downstream of the film holes. The same qualitative trend is observed for x/d less than 20 -25 downstream from two staggered rows of configuration 3 film-cooling holes.

APPENDIX A

Appendix A contains all of the figures generated for this thesis. The figures presented include: Test set-up; injection hole configuration, plots of spanwise-averaged adiabatic effectiveness and iso-energetic Stanton number ratios as dependent upon position; spatially resolved plots of local adiabatic effectiveness, iso-energetic Stanton number ratios, and Stanton number ratios for θ values near 1.5; and spanwise plots of mean velocity, total mean pressure and temperature for the eight configurations studied.

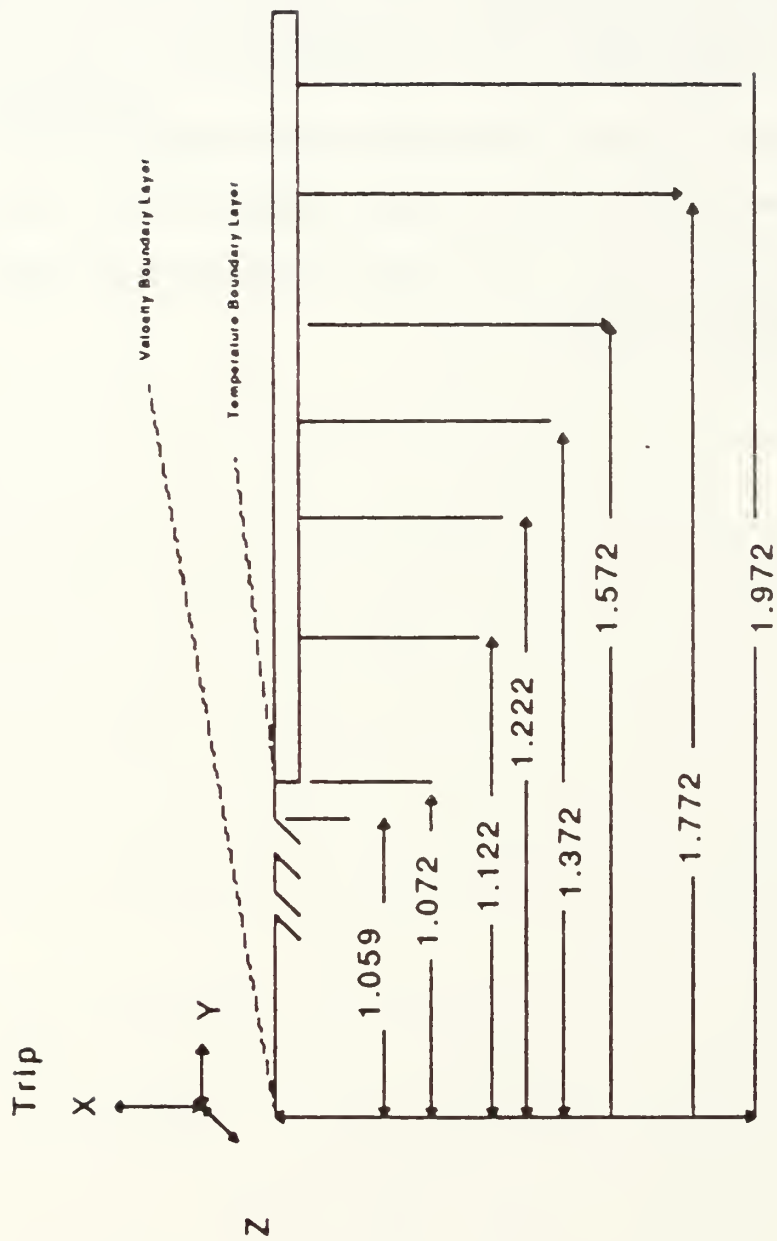


Figure 1. Test Section Coordinate System, Configuration 3, Compound Angle

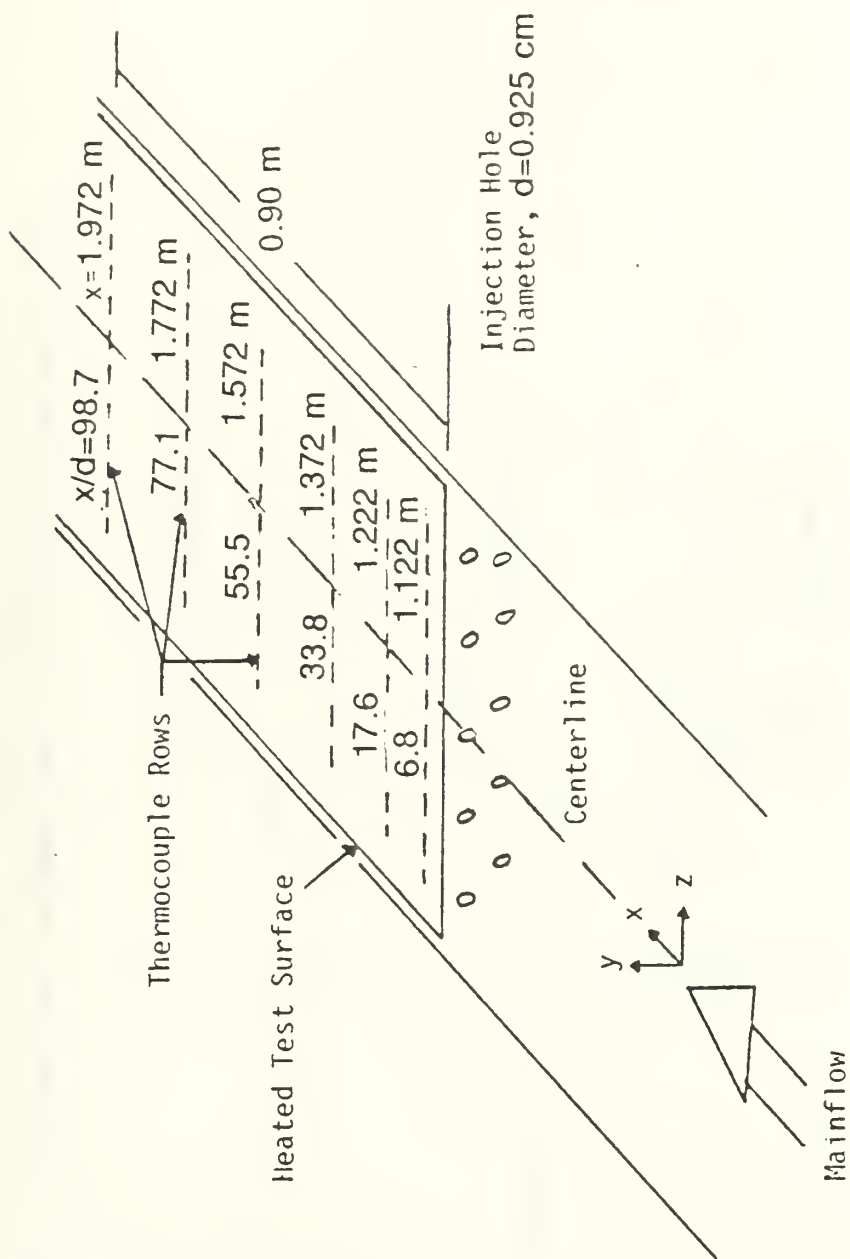


Figure 2. Top View Schematic of Wind Tunnel Test Section, Configuration 3, Compound Angle

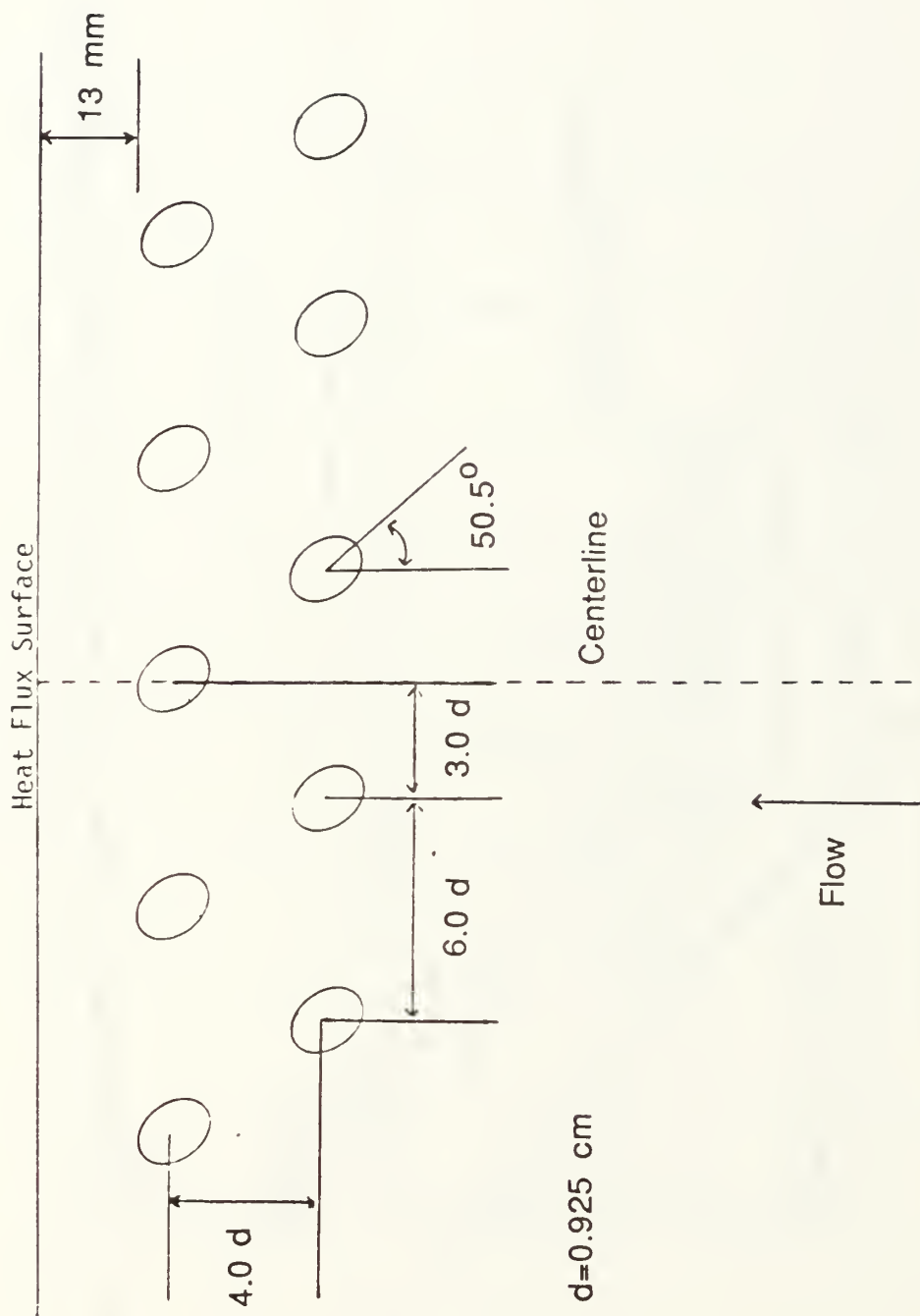


Figure 3. Injection Hole Configuration, Configuration 3, Compound Angle

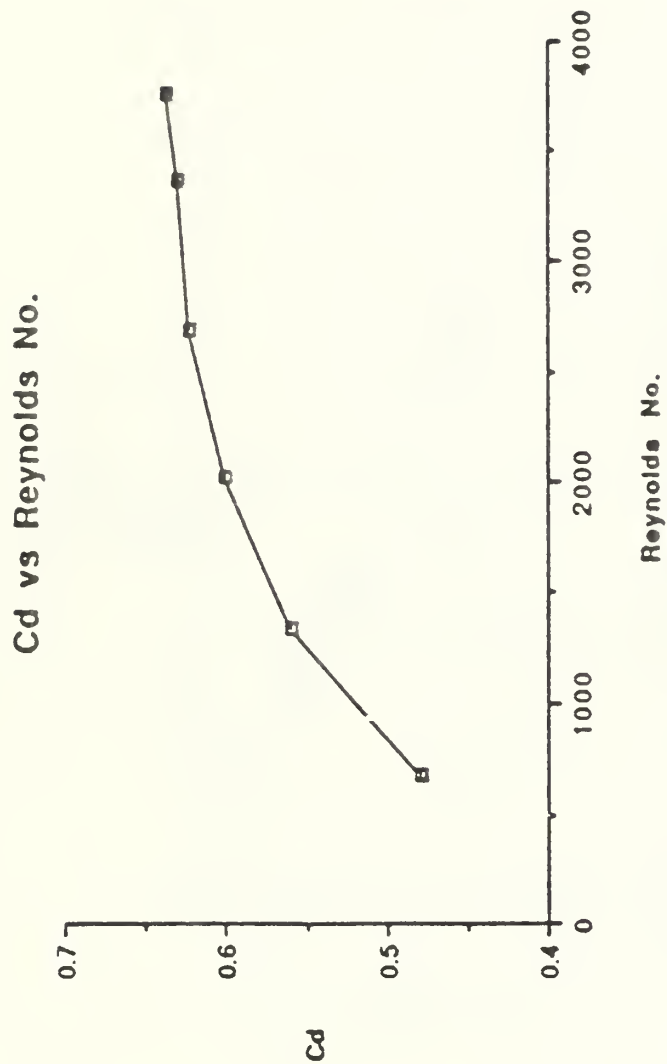


Figure 4. Coefficient of Discharge (C_d) Versus Reynolds Number (Re) for Injection System, Bishop [Ref. 7]

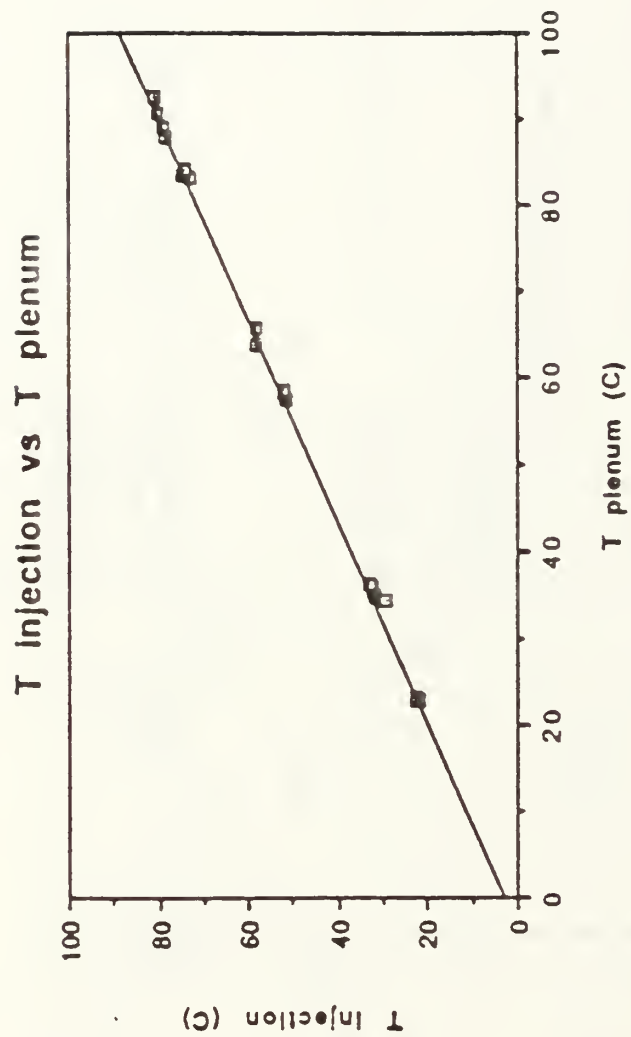


Figure 5. Injectant Temperature Versus Plenum Temperature, Bishop [Ref. 7]

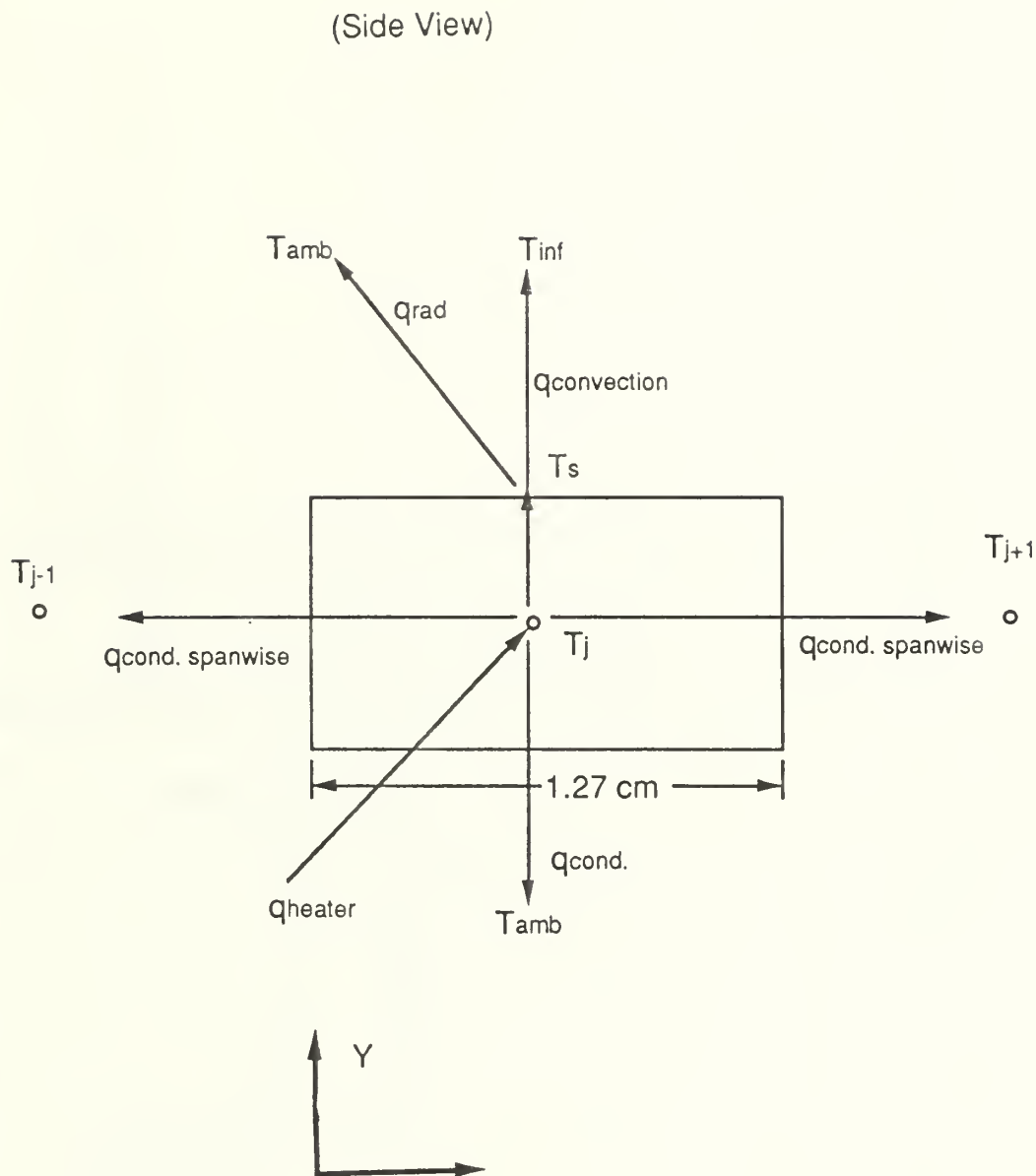


Figure 6. Side View Schematic of Thermocouple Control Volume for Energy Balance Analysis

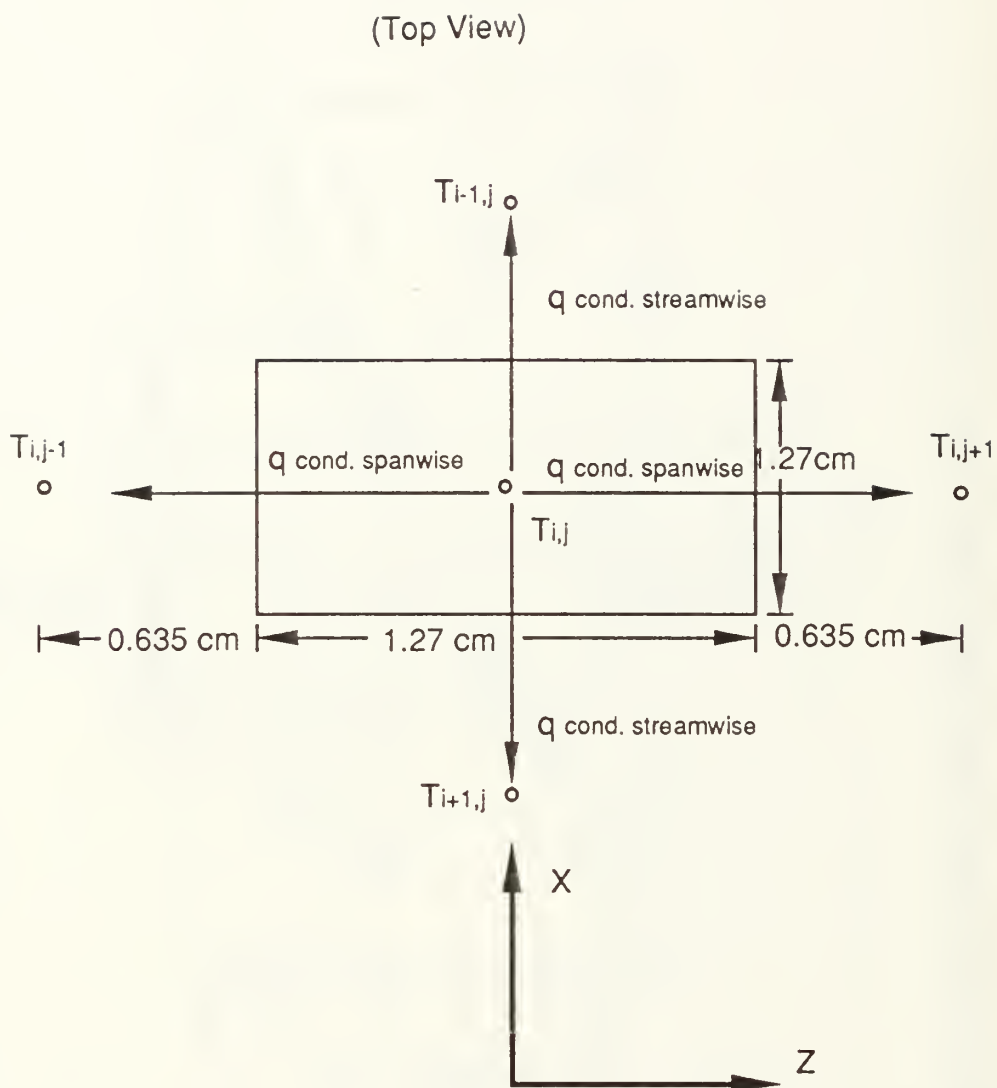


Figure 7. Top View Schematic of Thermocouple Control Volume Showing Spanwise and Streamwise Conduction

baseline plot of x/d vs avg. Stanton nr.

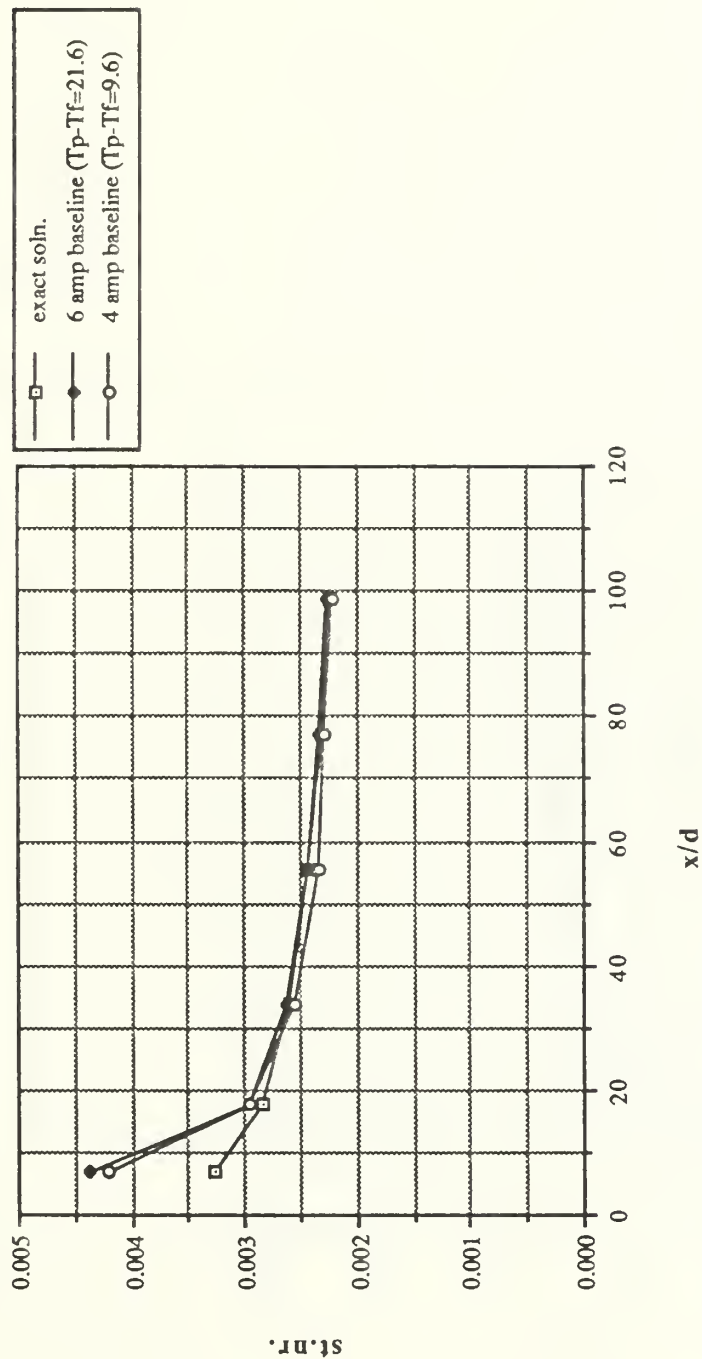


Figure 8. Baseline Stanton Number Versus x/d , Comparison Between Correlation and Experimental Measurements

baseline plot of reynolds nr. vs avg. stanton nr.

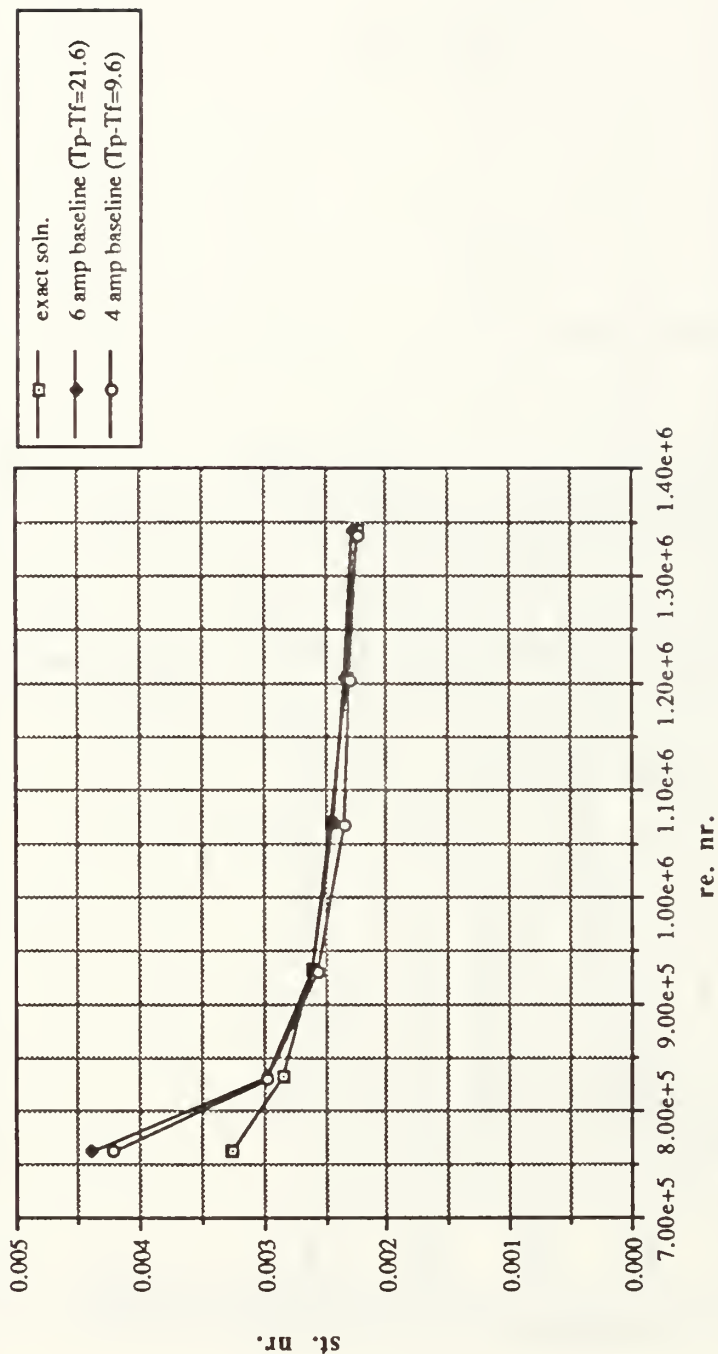


Figure 9. Baseline Stanton Number Versus Reynolds Number, Comparison Between Correlation and Experimental Measurements

1 row $m=0.5$ Theta vs St/St_0 for $z=-1.27$ cm

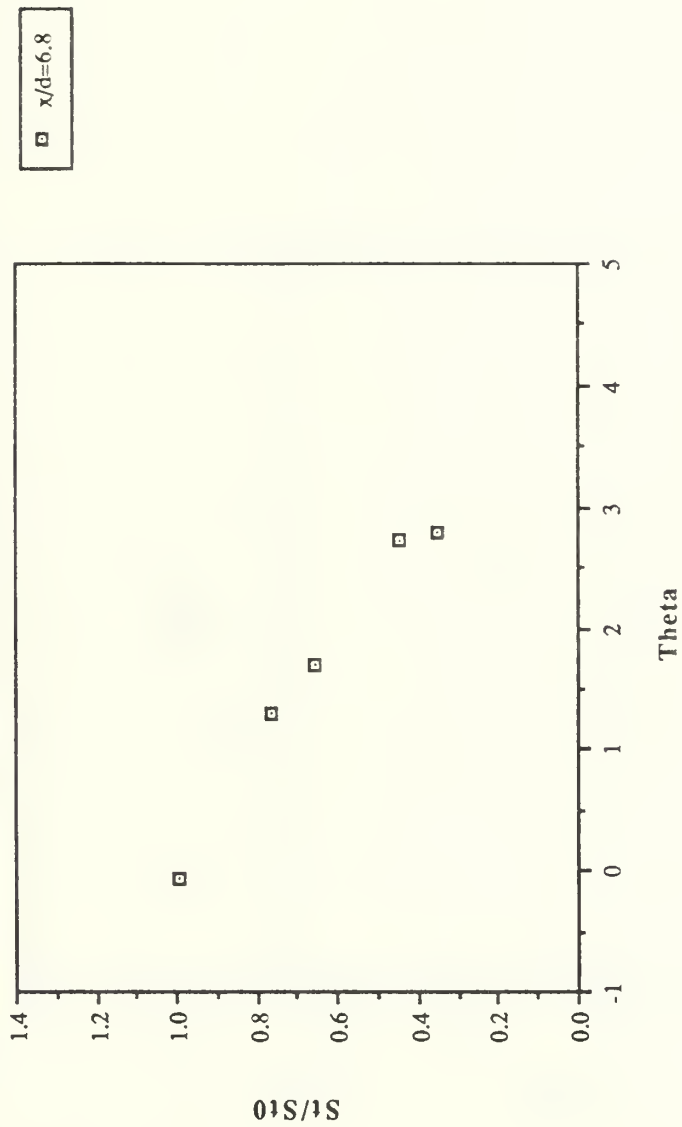


Figure 10. St/St_0 Versus θ , Compound Angle, 1 row, $m=0.5$, $x/d=6.8$, $Z=-1.27$ cm

1 row $m=0.5$ Theta vs St/St_0 for $z=-1.27$ cm



Figure 11. St/St_0 Versus θ , Compound Angle, 1 Row, $m=0.5$, $x/d=17.6$, $Z=-1.27$ cm

1 row $m=0.5$ Theta vs St/St_0 for $z=-1.27$ cm

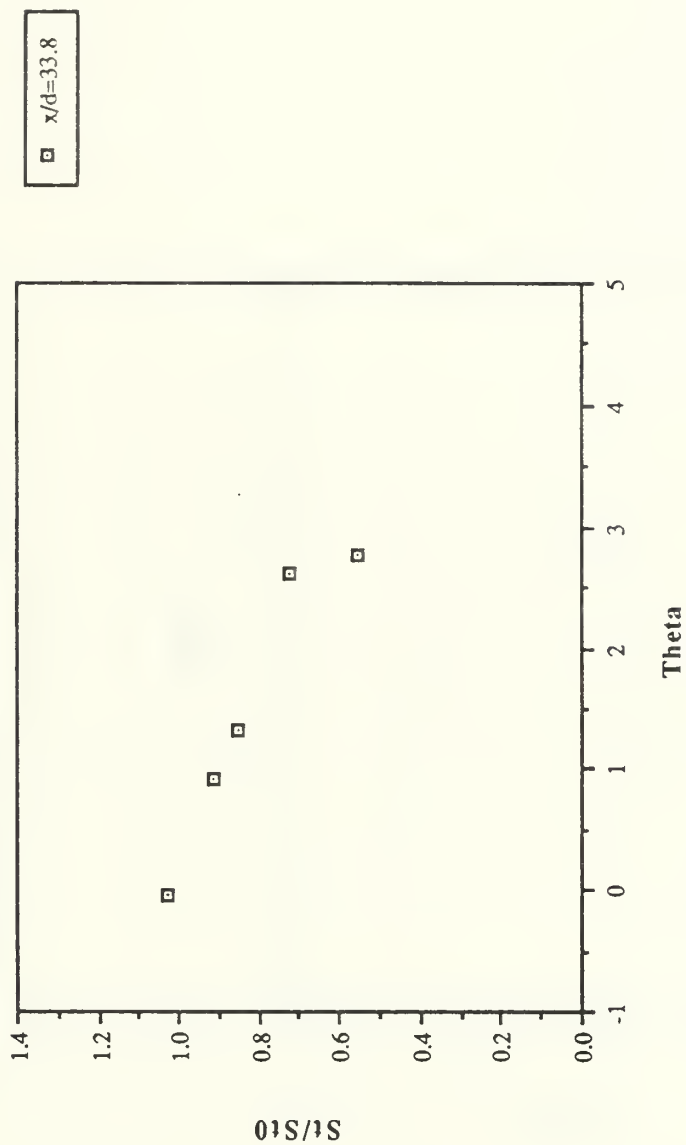


Figure 12. St/St_0 Versus θ , Compound Angle, 1 Row, $m=0.5$, $x/d=33.8$, $Z=-1.27$ cm

1 row $m=0.5$ Theta vs St/St_0 for $z=-1.27$ cm

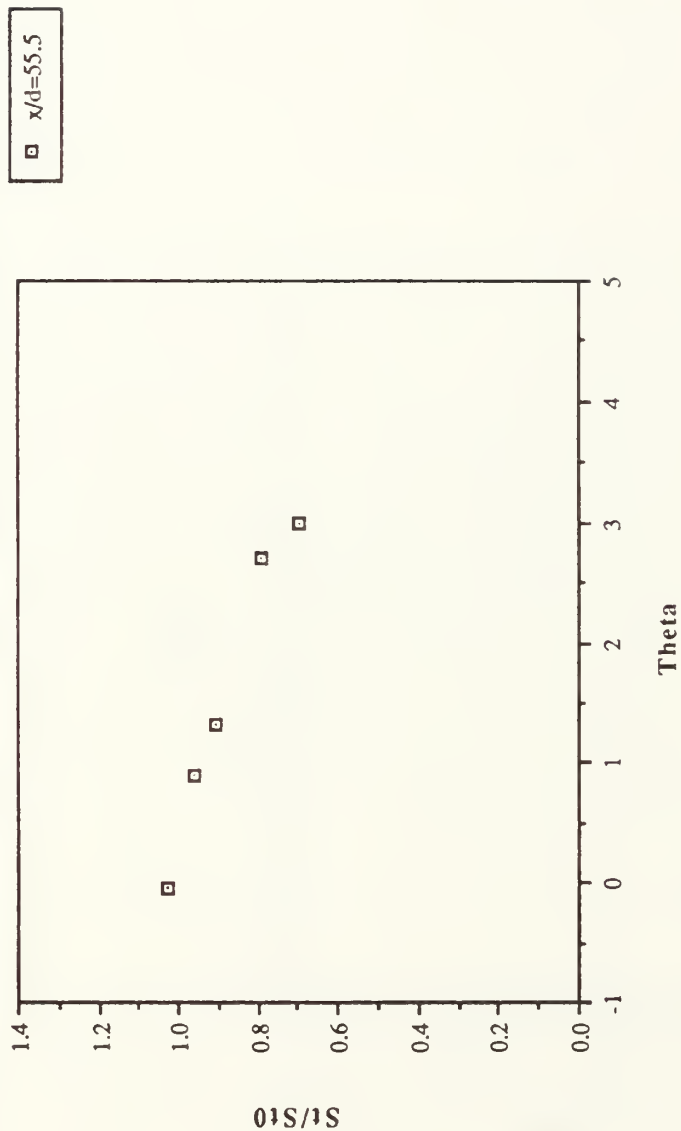


Figure 13. St/St_0 Versus θ , Compound Angle, 1 row, $m=0.5$, $x/d=55.5$, $z=-1.27$ cm

1 row $m=0.5$ Theta vs St/St_0 for $z=-1.27$ cm

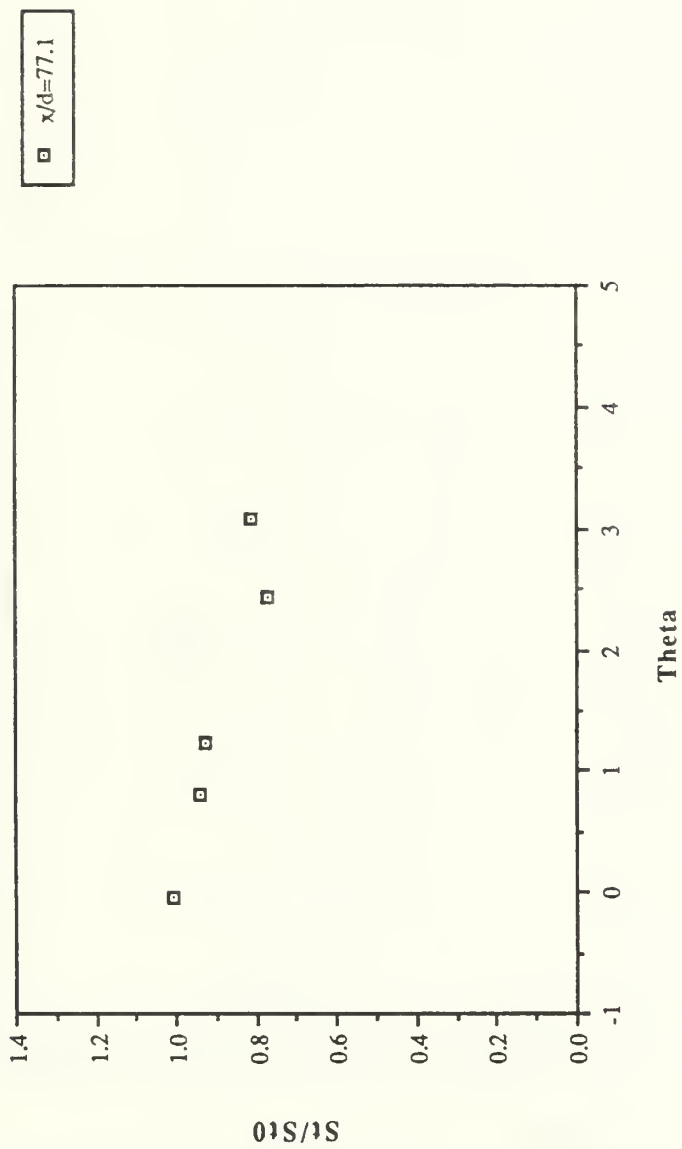


Figure 14. St/St_0 Versus θ , Compound Angle, 1 Row, $m=0.5$, $x/d=77.1$, $Z=-1.27$ cm

1 row $m=0.5$ Theta vs St/St_0 for $z=-1.27$ cm

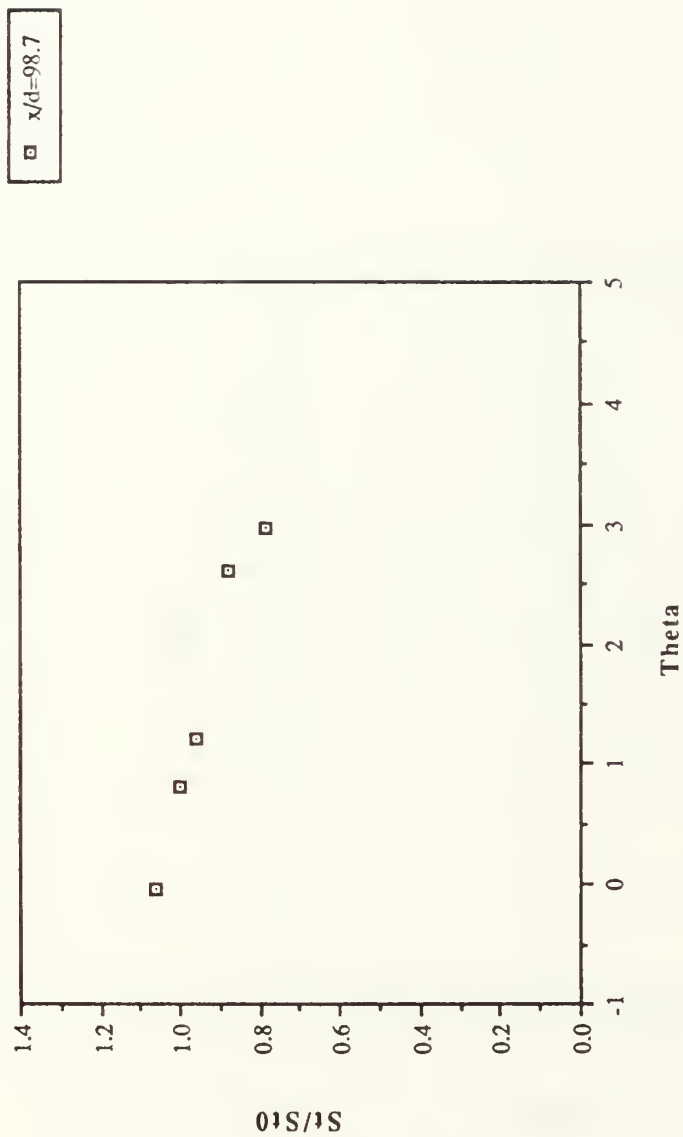


Figure 15. St/St_0 Versus θ , Compound Angle, 1 Row, $m=0.5$, $x/d=98.7$, $Z=-1.27$ cm

spanwise avg. eta vs x/d for 1 row m=0.5

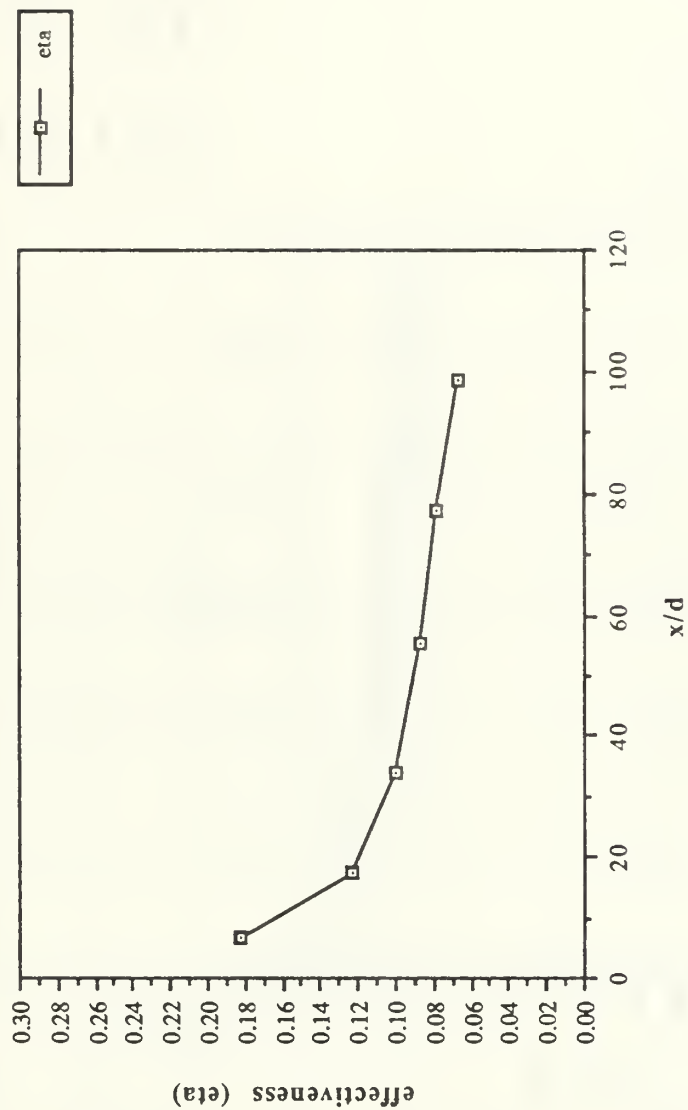


Figure 16. $\bar{\eta}$ Versus x/d , Compound Angle, 1 Row, $m=0.5$, Spanwise Average

spanwise avg. Stf/St0 vs x/d for 1 row m=0.5

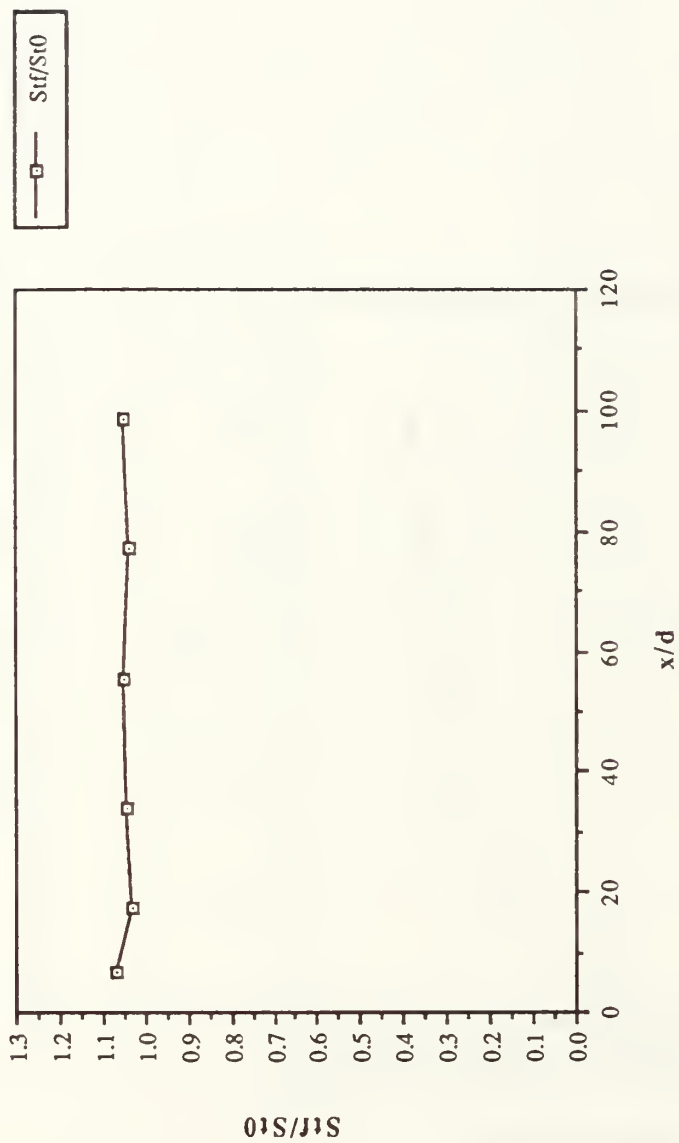


Figure 17. $\overline{St_f}/St_o$ Versus x/d , Compound Angle, 1 Row, $m=0.5$, Spanwise Average

Reynolds vs Stanton nr. for 1 row $m=0.5$

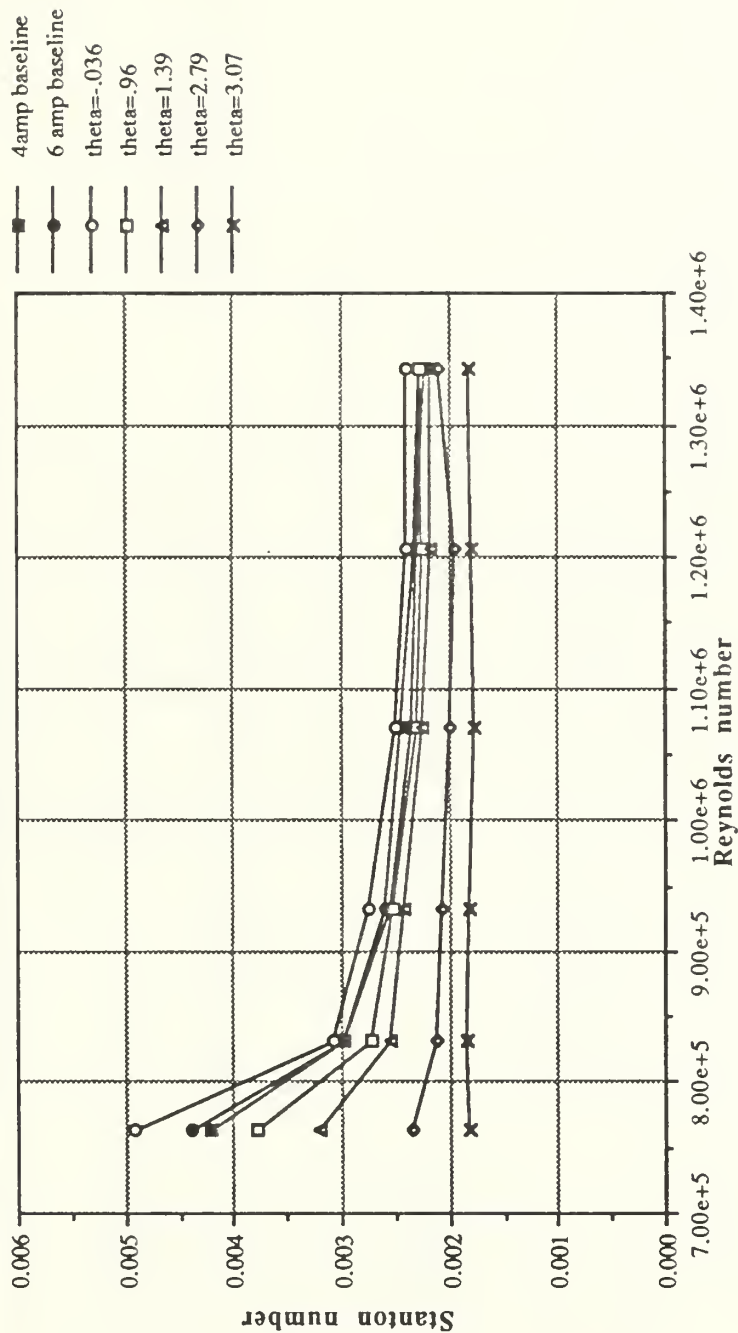


Figure 18. Spanwise Averaged Stanton Number Versus Reynolds Number, Comparison of Different θ Values and Baselines, 1 Row, $m=0.5$

FILM-COOLING EFFECTIVENESS

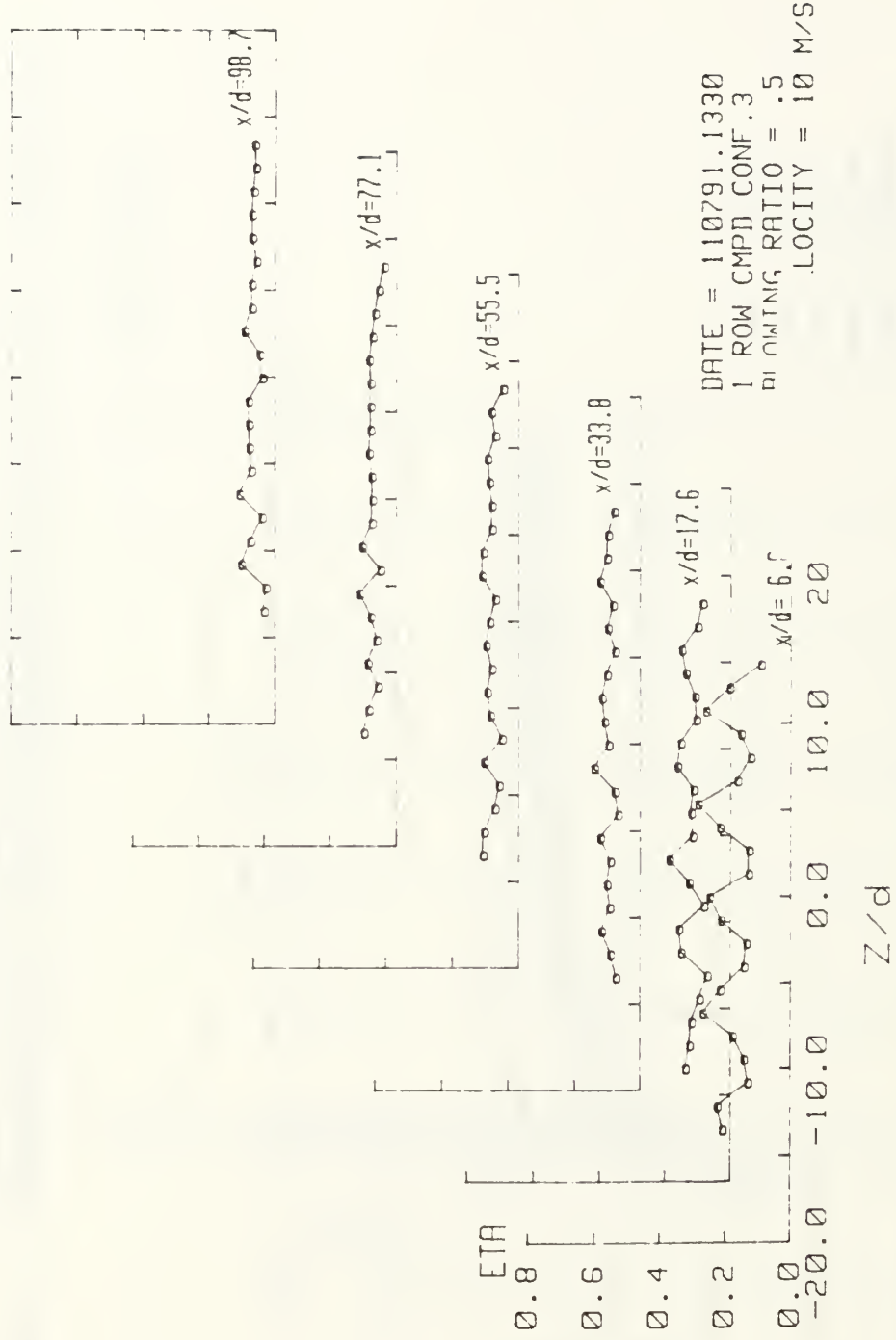


Figure 19. Spanwise Variation of η , Compound Angle, 1 Row, $m=0.5$

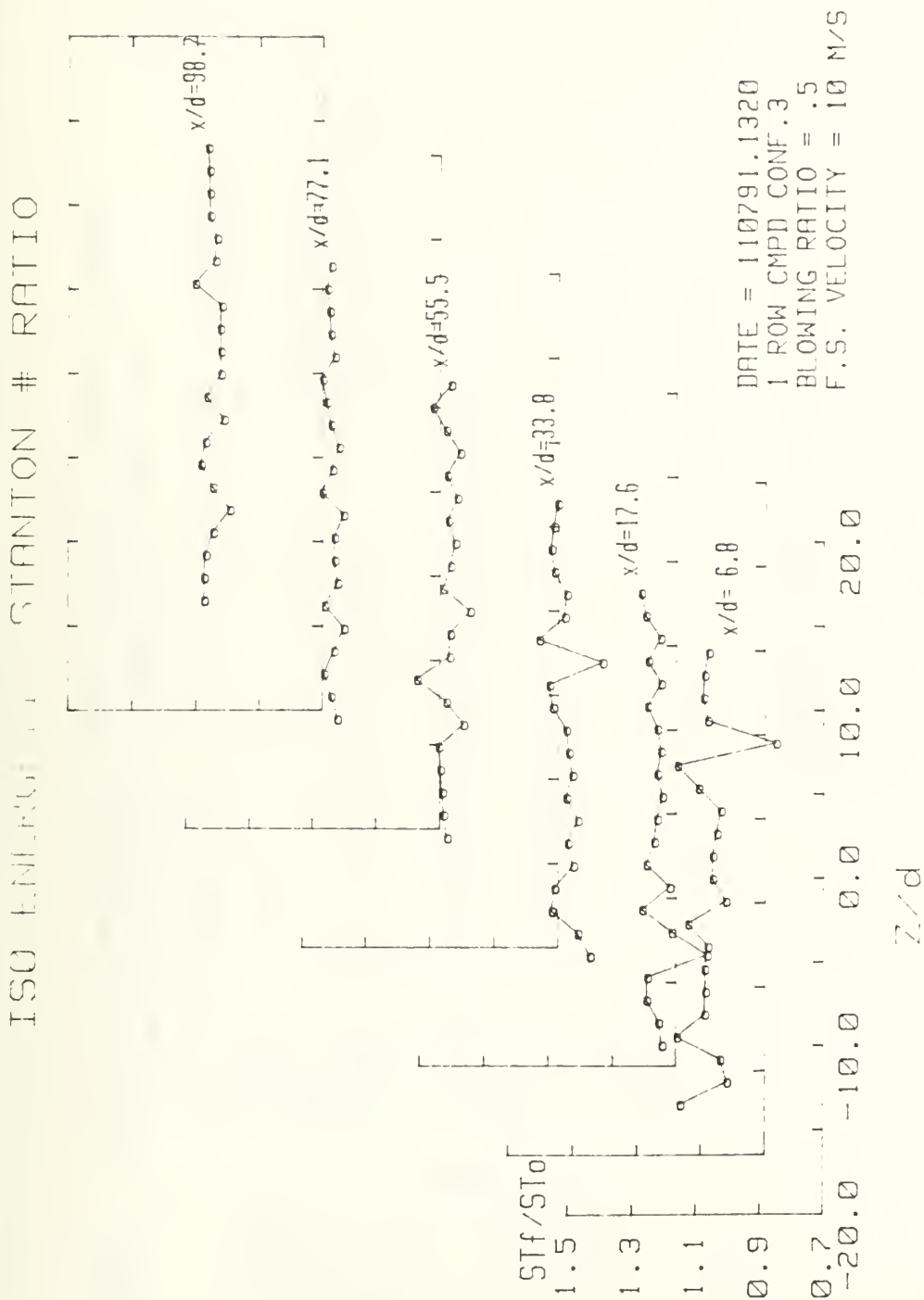


Figure 20. Spanwise Variation of St_f/St_0 , Compound Angle, 1 Row, $m=0.5$

STANTON NUMBER RATIOS

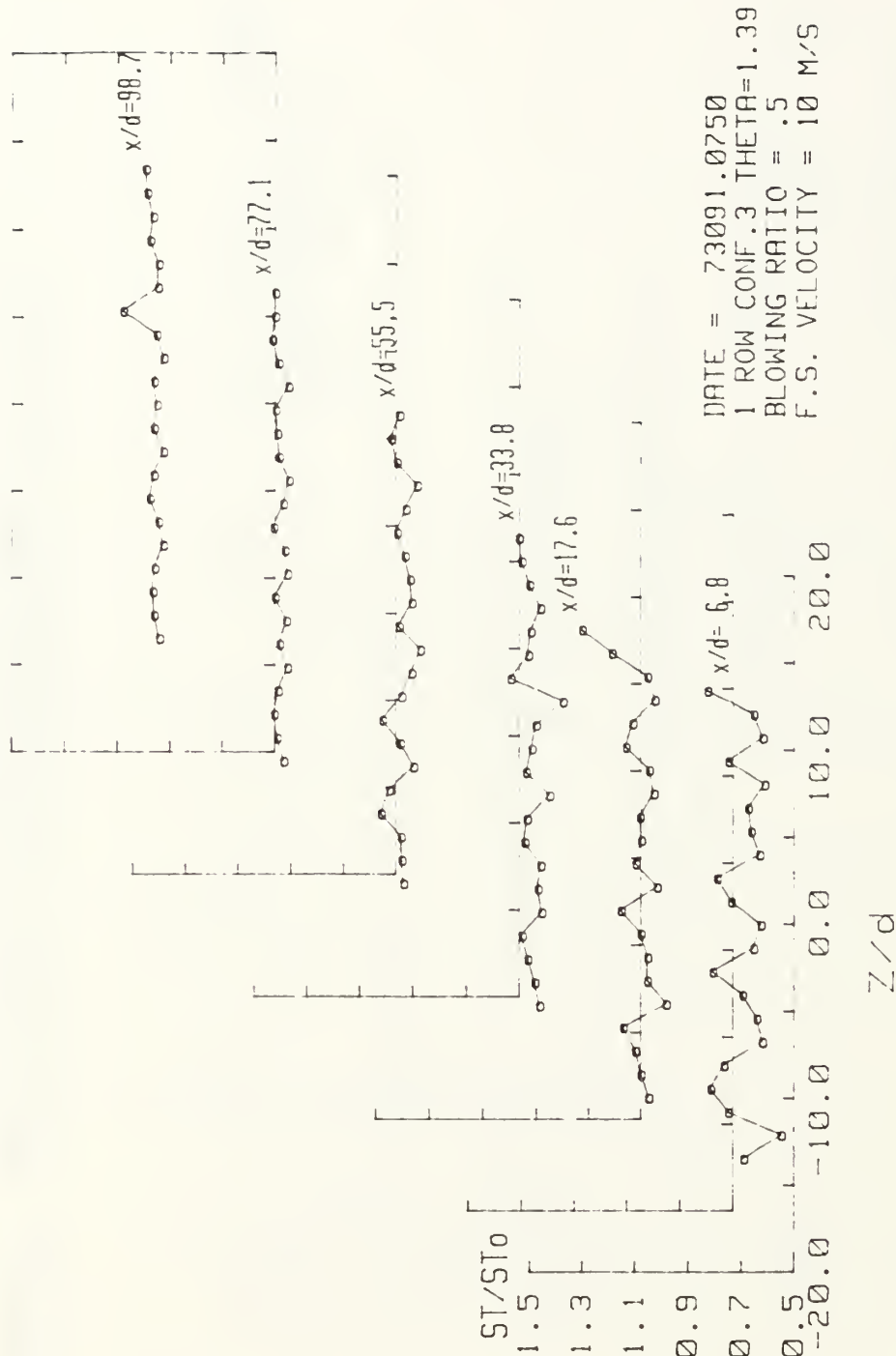


Figure 21. Spanwise Variation of St/St_0 Compound Angle, 1 Row, $m=0.5$, $\theta=1.39$

1 row $m=1.0$ Theta vs St/St_0 for $z=-1.27$ cm

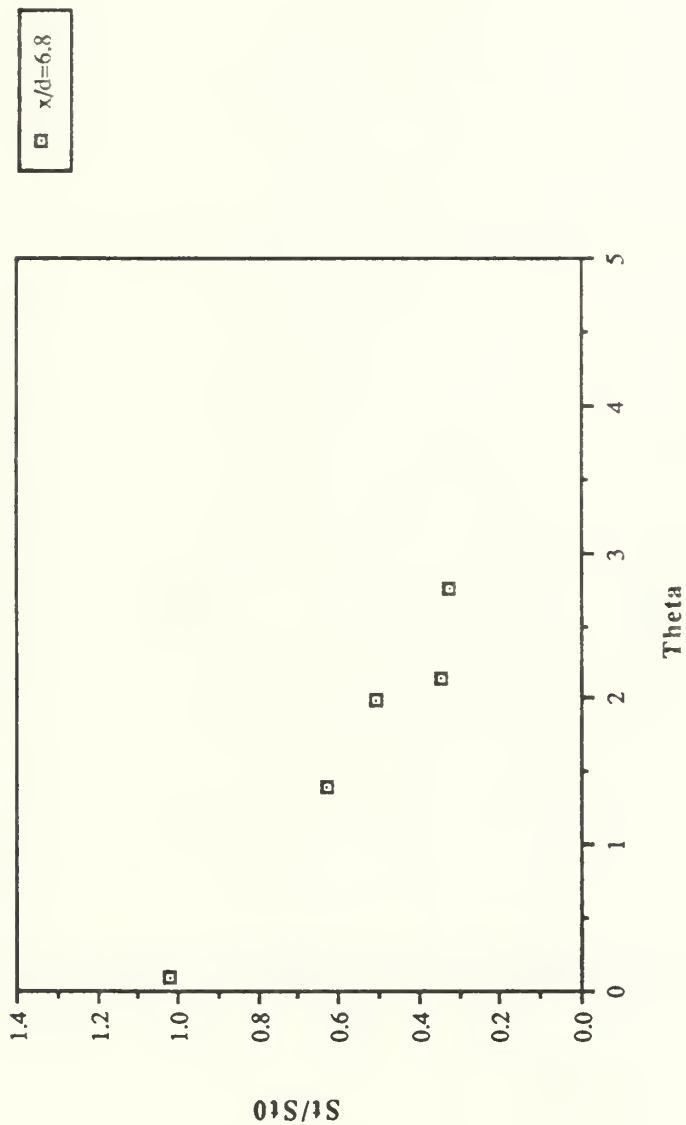


Figure 22. St/St_0 Versus θ , Compound Angle, 1 Row, $m=1.0$, $x/d=6.8$, $Z=-1.27$ cm

1 row $m=1.0$ Theta vs St/St_0 for $z=-1.27$ cm

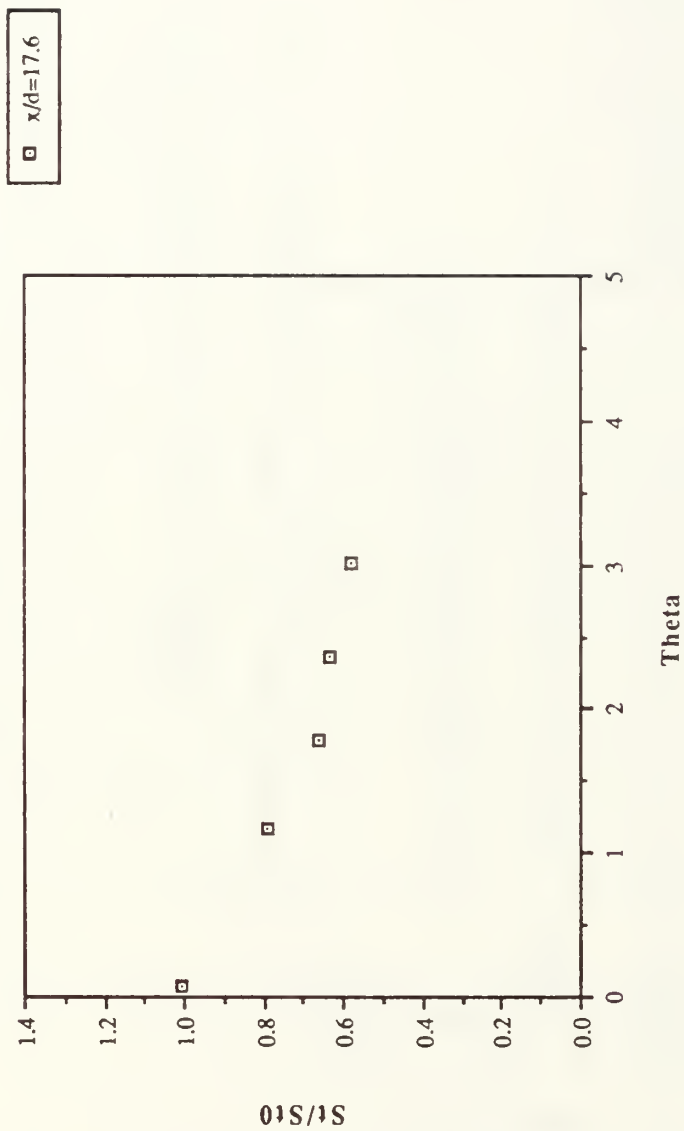


Figure 23. St/St_0 Versus θ , Compound Angle, 1 Row, $m=1.0$, $x/d=17.6$, $Z=-1.27$ cm

1 row $m=1.0$ Theta vs St/St_0 for $z=-1.27$ cm

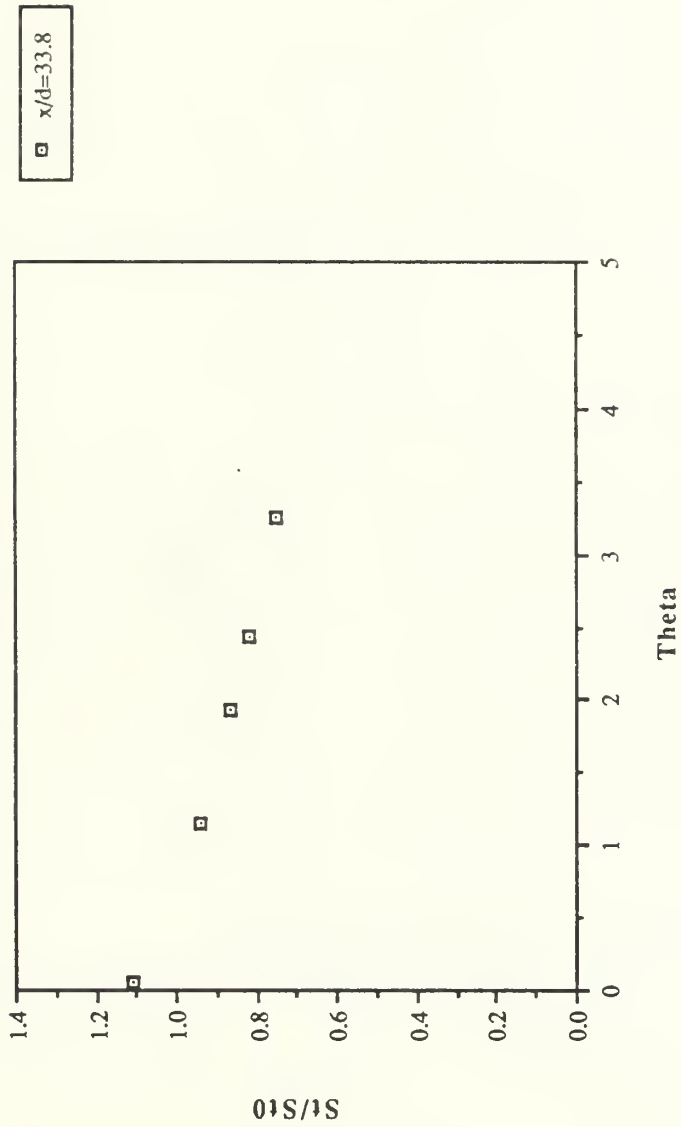


Figure 24. St/St_0 Versus θ , Compound Angle, 1 Row, $m=1.0$, $x/d=33.8$, $Z=-1.27$ cm

1 row $m=1.0$ Theta vs St/St_0 for $z=-1.27$ cm

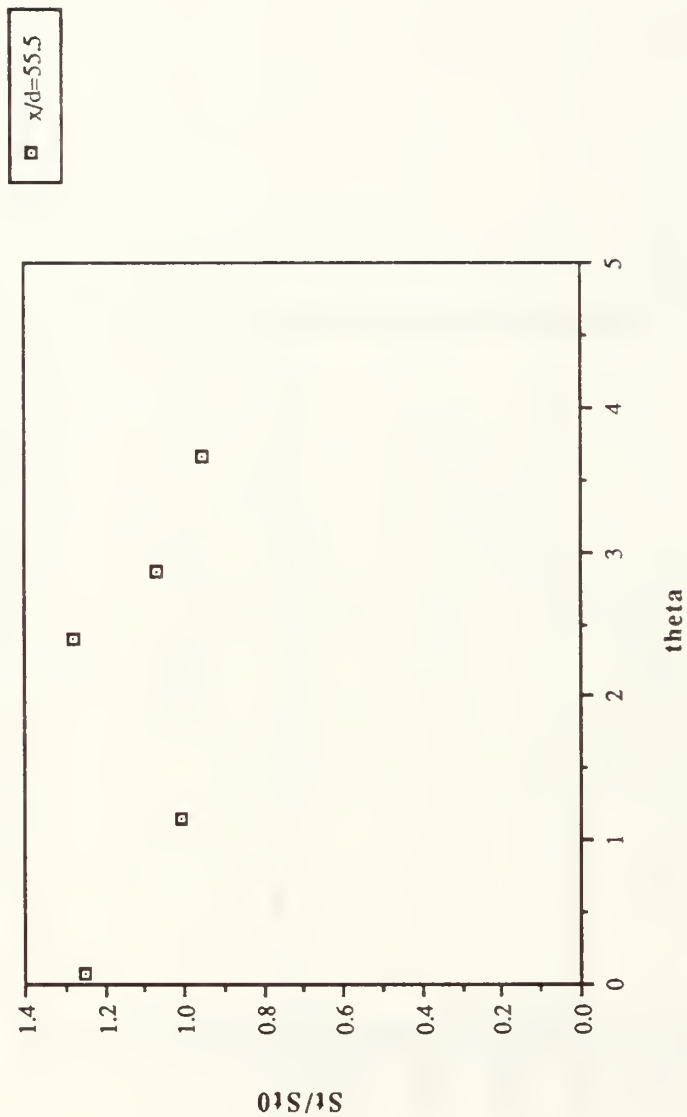


Figure 25. St/St_0 Versus θ , Compound Angle, 1 Row, $m=1.0$, $x/d=55.5$, $Z=-1.27$ cm

1 row $m=1.0$ Theta vs St/St_0 for $z=-1.27$ cm

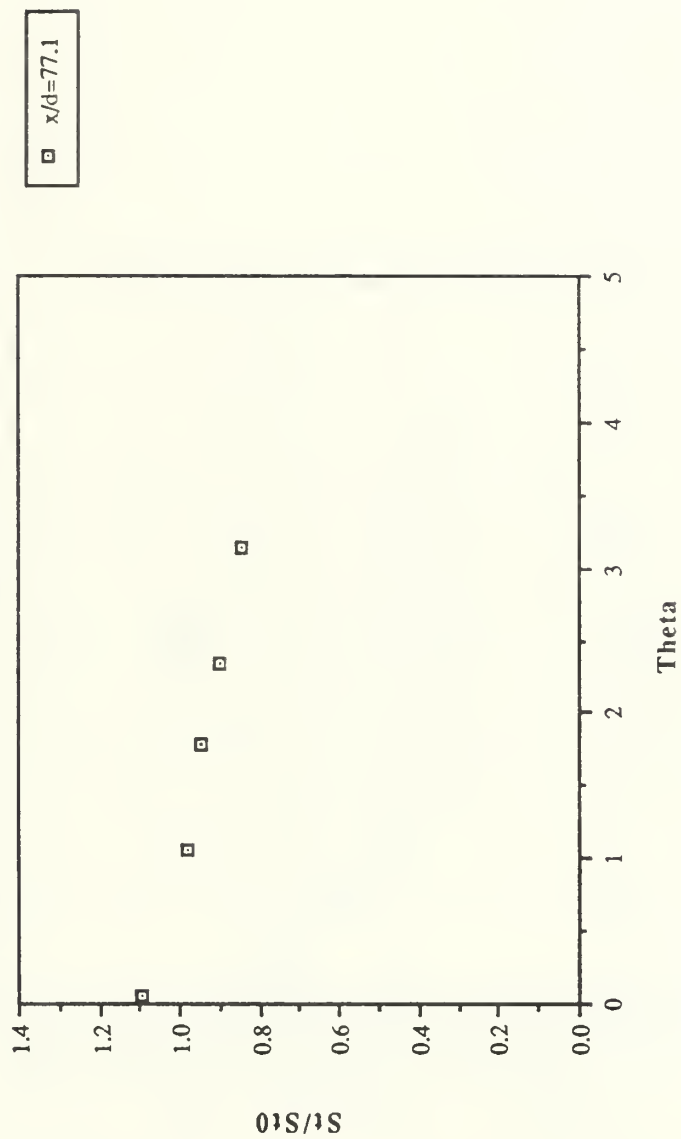


Figure 26. St/St_0 Versus θ , Compound Angle, 1 Row, $m=1.0$, $x/d=77.1$, $Z=-1.27$ cm

1 row $m=1.0$ Theta vs St/St_0 for $z=-1.27$ cm

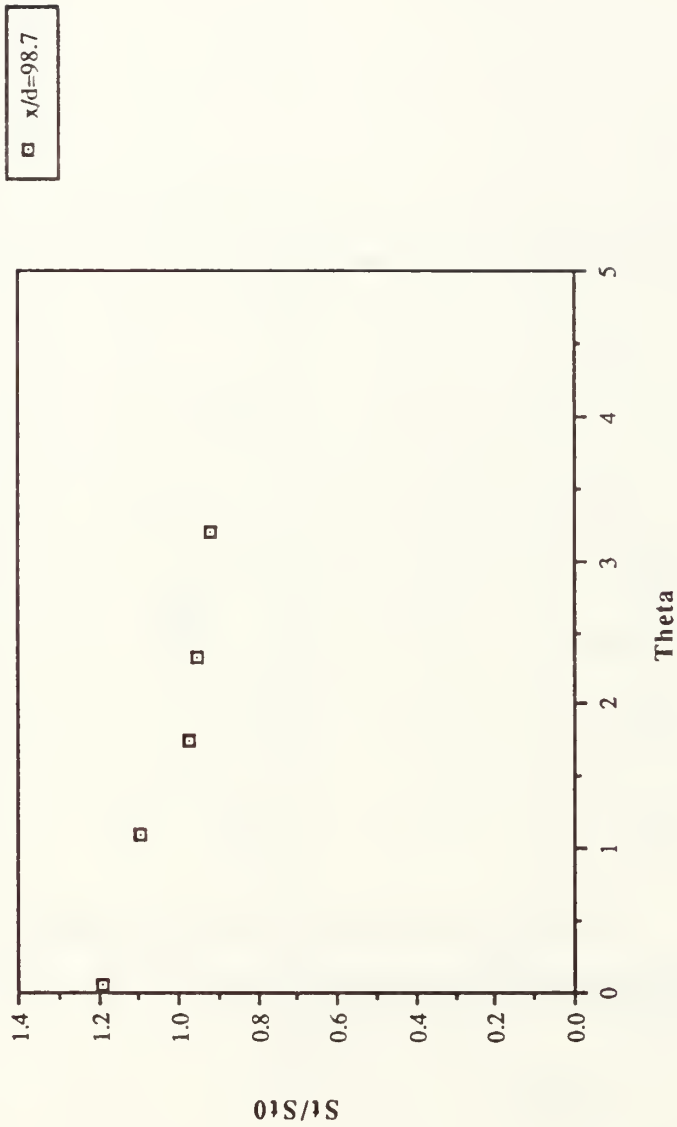


Figure 27. St/St_0 Versus θ , Compound Angle, 1 Row, $m=1.0$, $x/d=98.7$, $Z=-1.27$ cm

spanwise avg. eta vs x/d for 1 row m=1.0

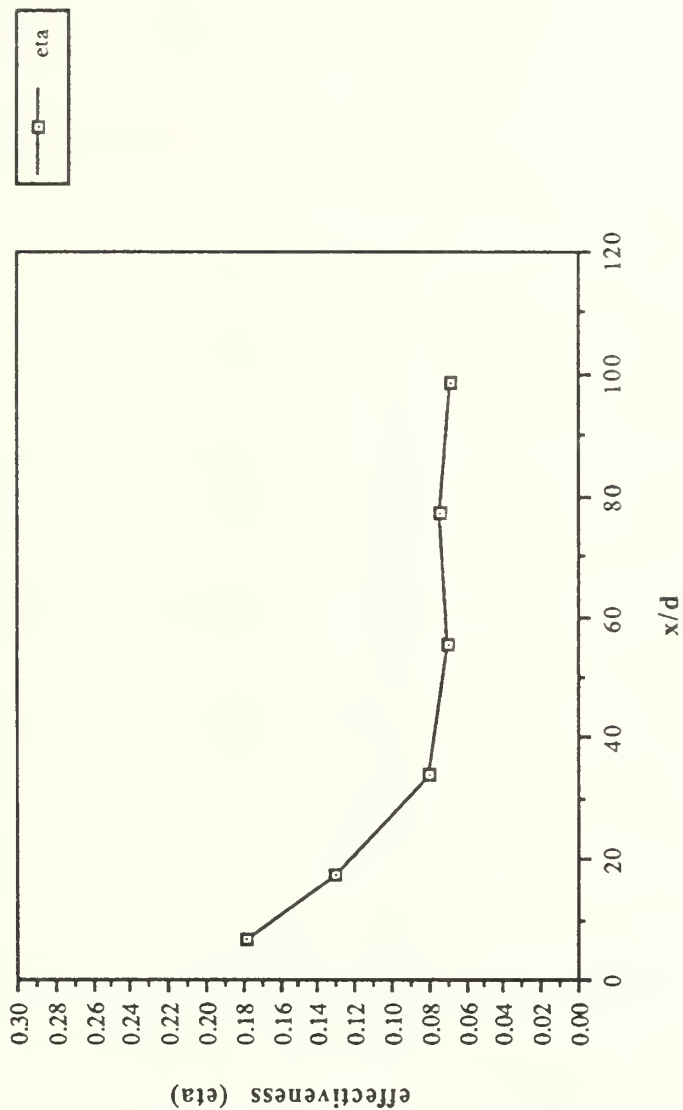


Figure 28. $\bar{\eta}$ Versus x/d , Compound Angle, 1 Row, $m=1.0$, Spanwise Average

spanwise avg. St_f/St_0 vs x/d for 1 row $m=1.0$

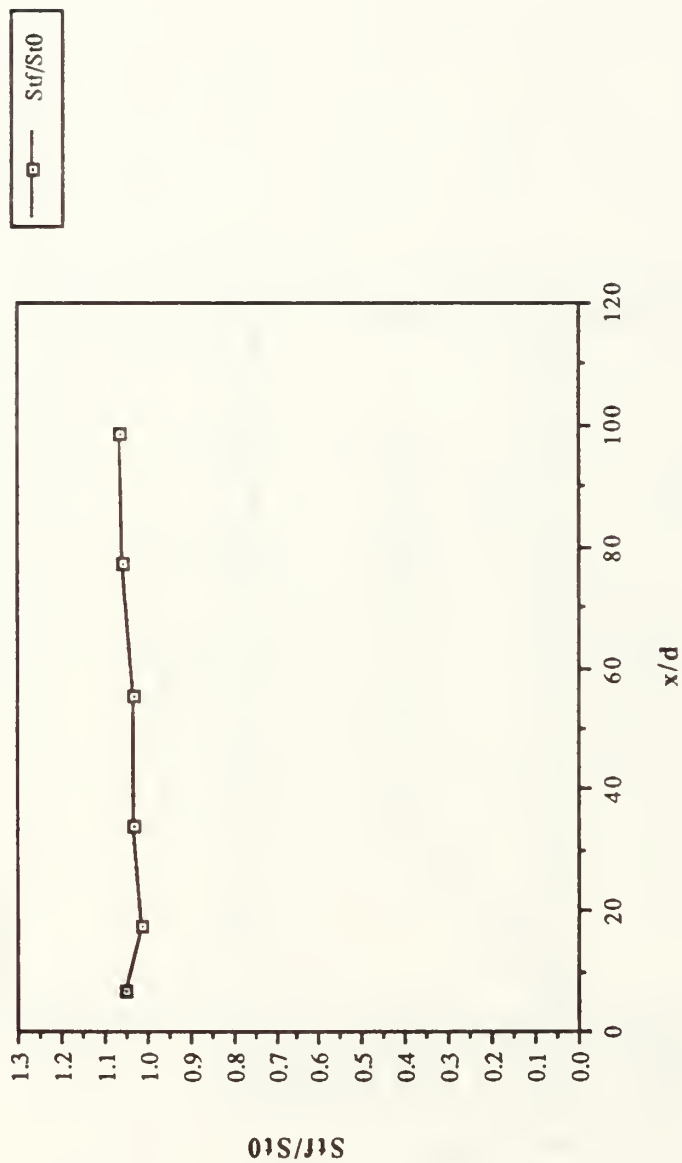


Figure 29. St_f/St_0 Versus x/d , Compound Angle, 1 Row, $m=1.0$, Spanwise Average

Reynolds vs Stanton nr. for 1 row $m=1.0$

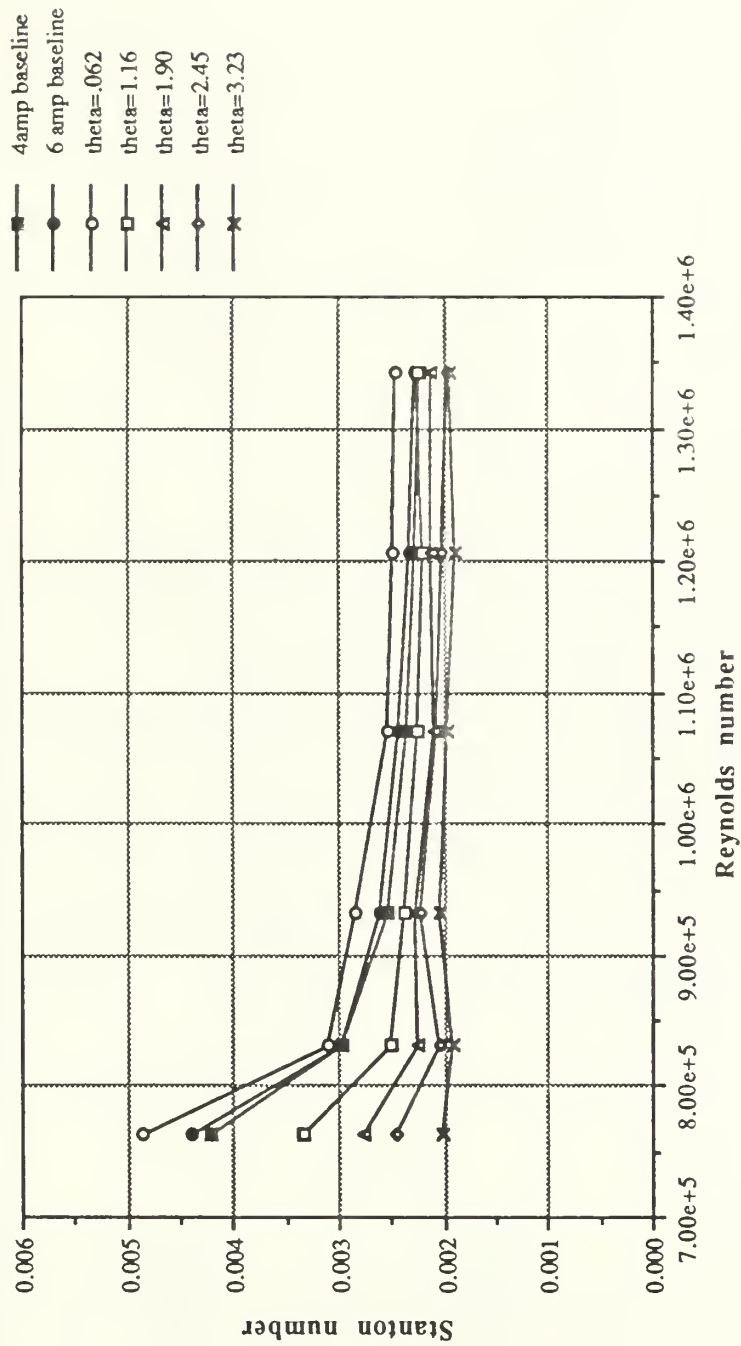


Figure 30. Spanwise Averaged Stanton Number Versus Reynolds Number, Comparison of Different θ Values and Baselines, 1 Row, $m=1.0$

FILM-COOLING EFFECTIVENESS

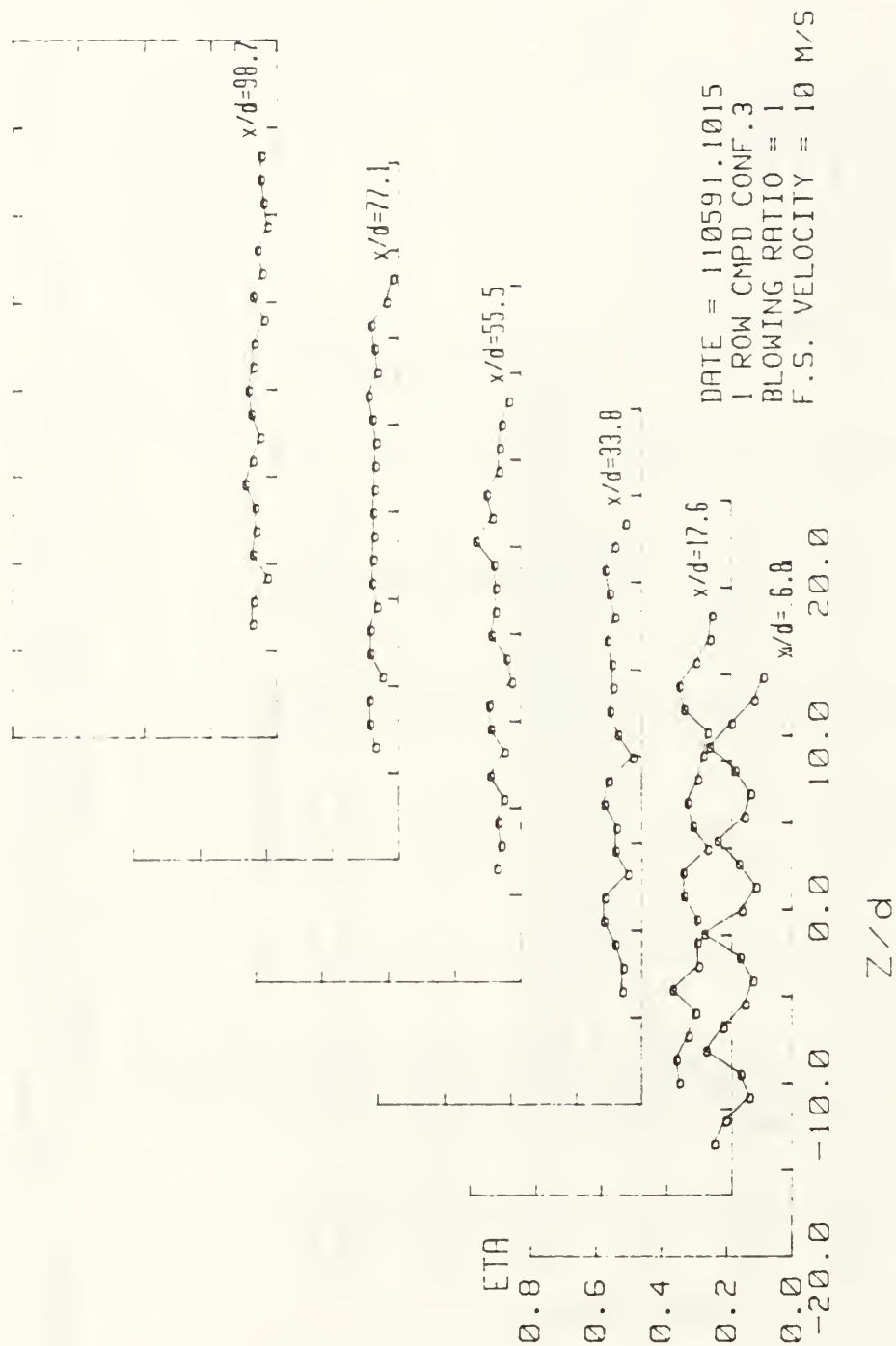


Figure 31. Spanwise Variation of η , Compound Angle, 1 Row, $m=1.0$

ISO-ENERGETIC STANTON # RATIO

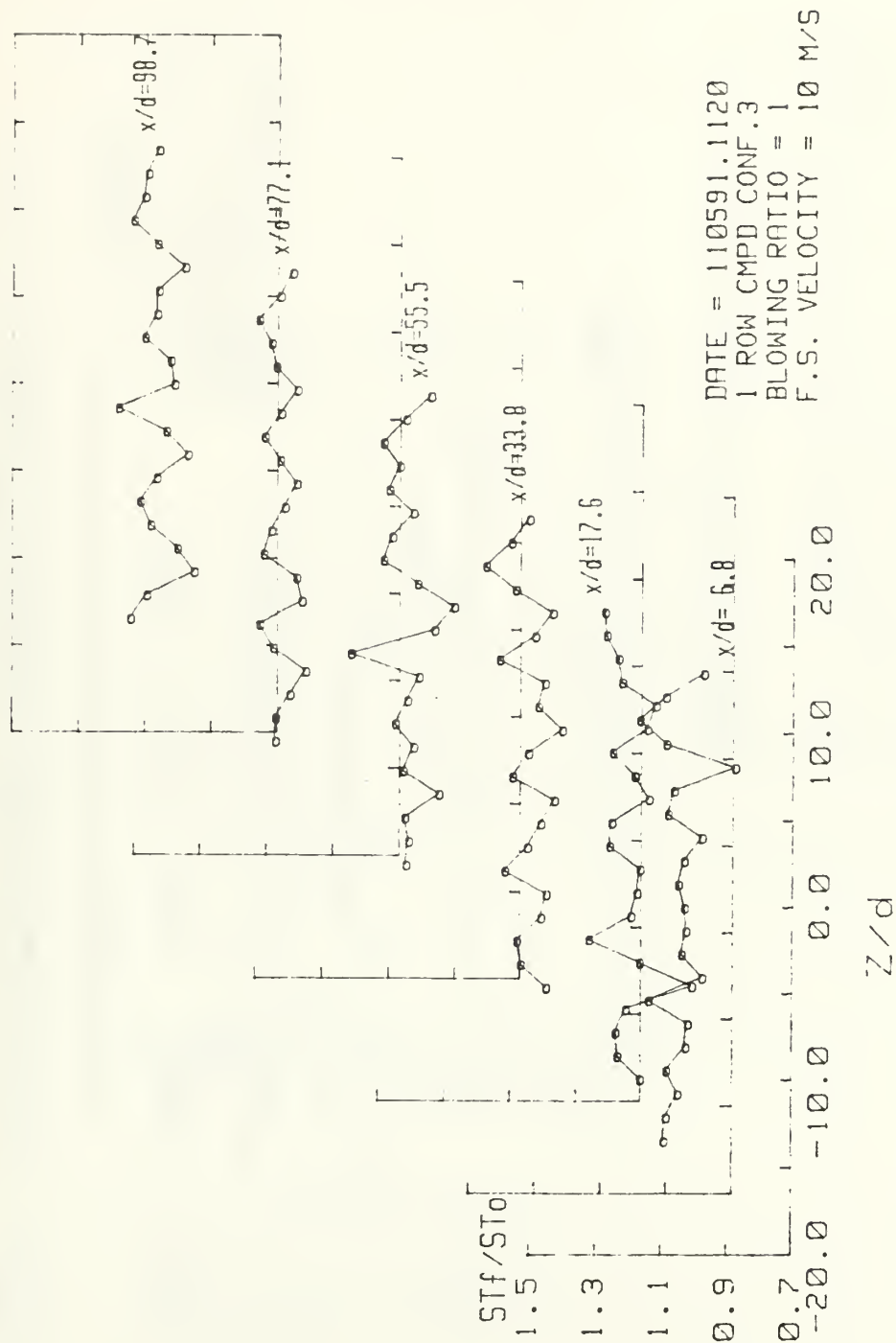


Figure 32. Spanwise Variation of St_f/St_0 , Compound Angle, 1 Row, $m=1.0$

STANTON NUMBER RATIOS

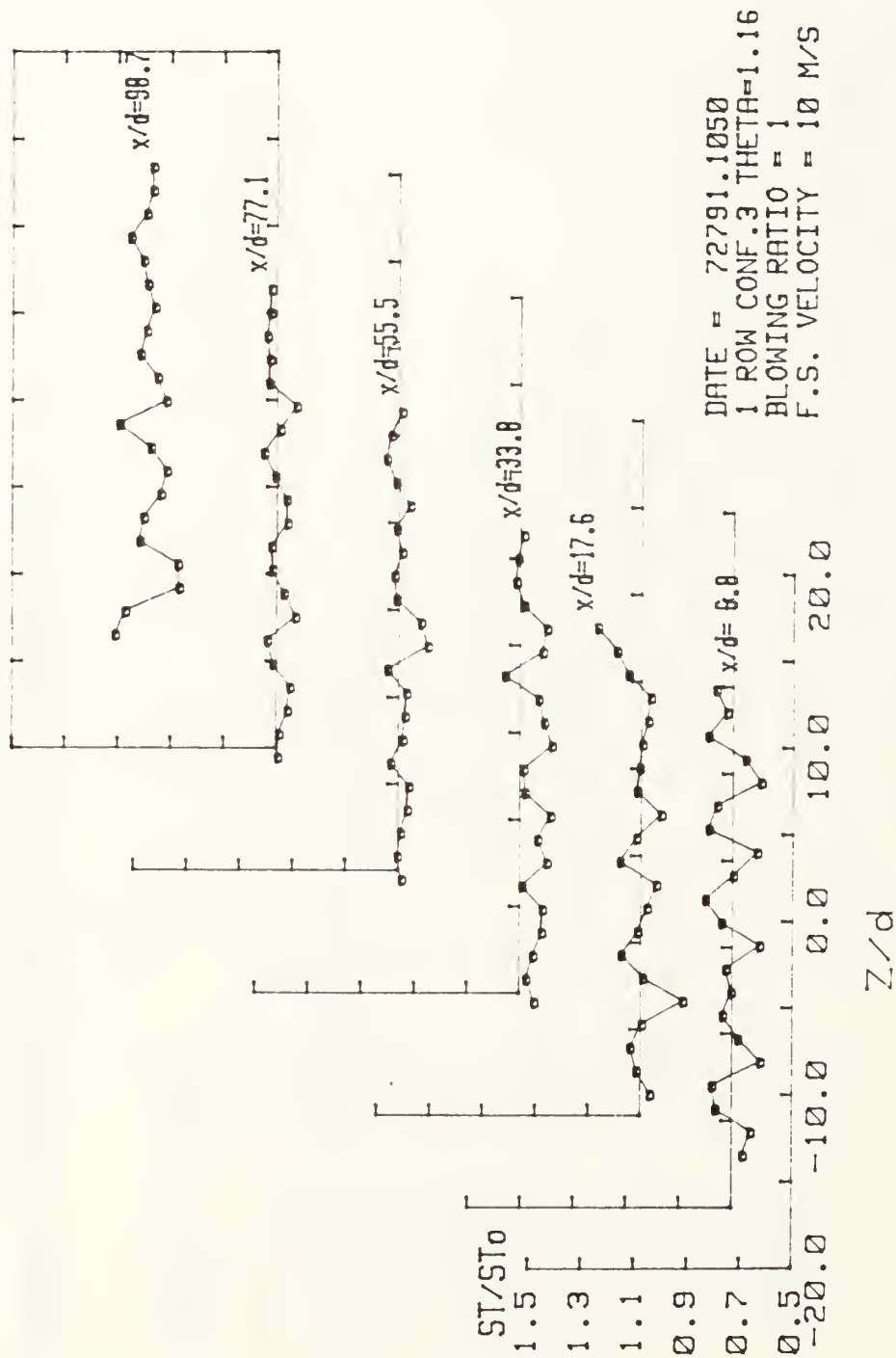


Figure 33. Spanwise Variation of St/St_0 , Compound Angle, 1 Row, $m=1.0$, $\theta=1.16$

1 row $m=1.5$ Theta vs St/St_0 for $z=-1.27$ cm

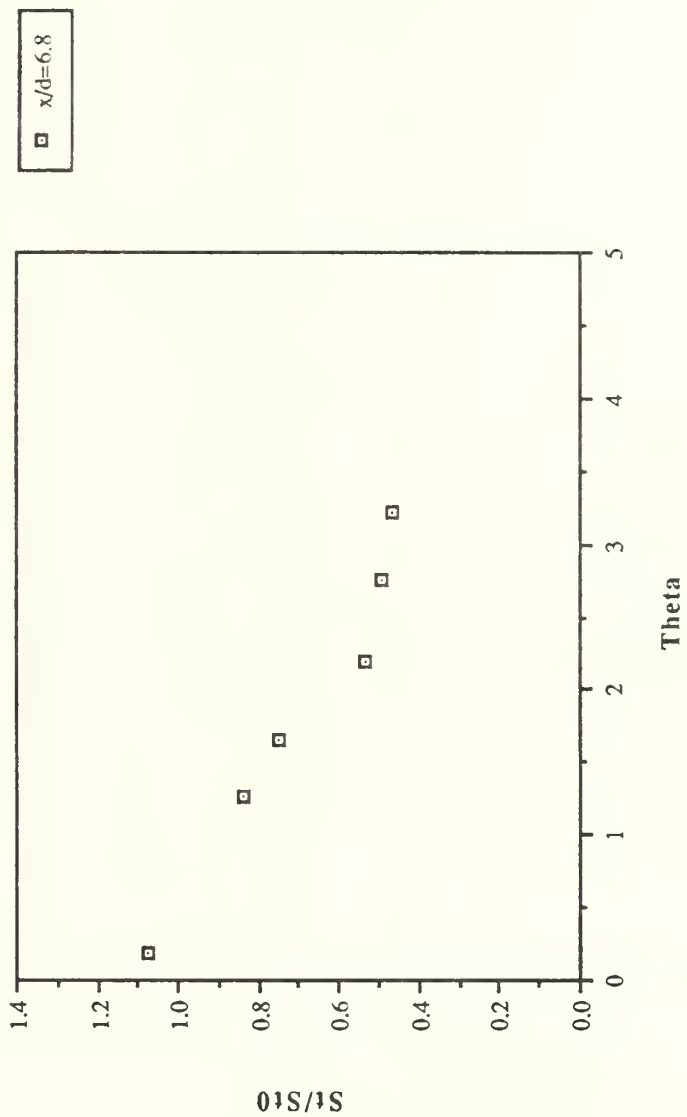


Figure 34. St/St_0 Versus θ , Compound Angle, 1 Row, $m=1.5$, $x/d=6.8$, $Z=-1.27$ cm

1 row $m=1.5$ Theta vs St/St_0 for $z=-1.27$ cm

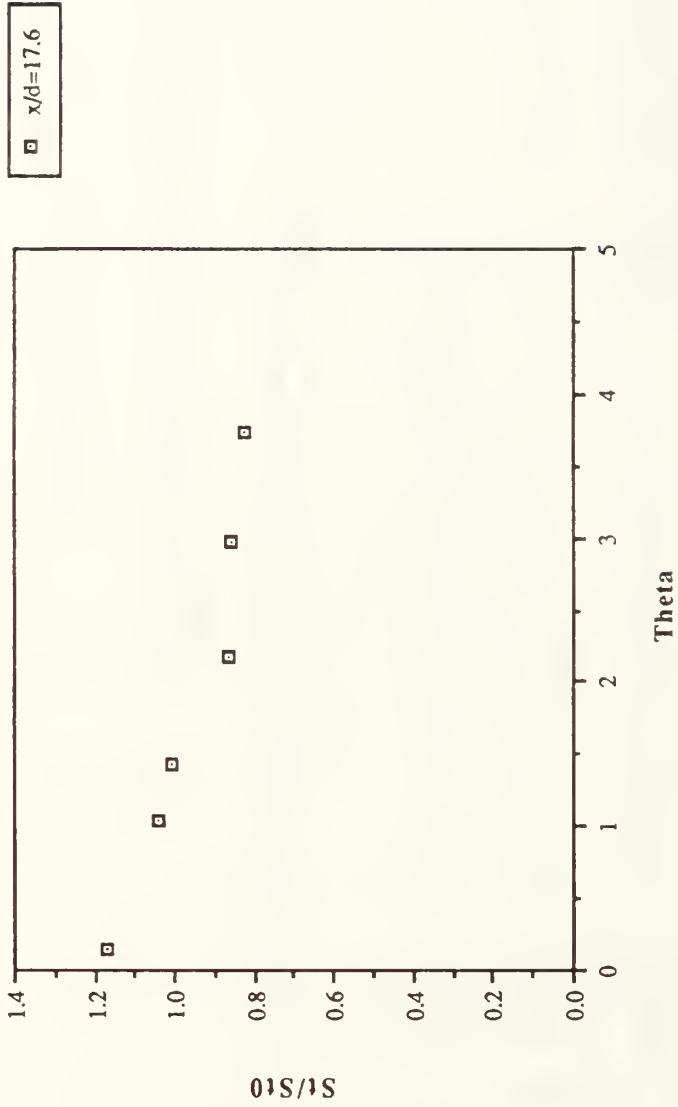


Figure 35. St/St_0 Versus θ , Compound Angle, 1 Row, $m=1.5$, $x/d=17.6$, $Z=-1.27$ cm

1 row $m=1.5$ Theta vs St/St_0 for $z=-1.27$ cm

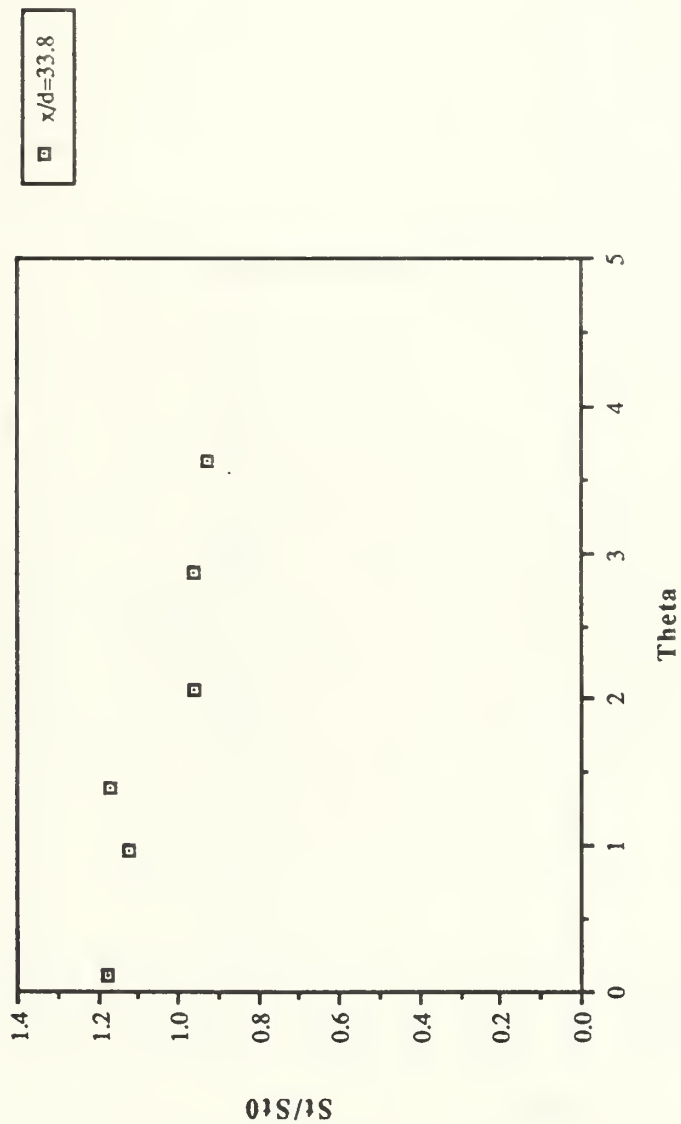


Figure 36. St/St_0 Versus θ , Compound Angle, 1 Row, $m=1.5$, $x/d=33.8$, $Z=-1.27$ cm

1 row $m=1.5$ Theta vs St/St_0 for $z=-1.27$ cm

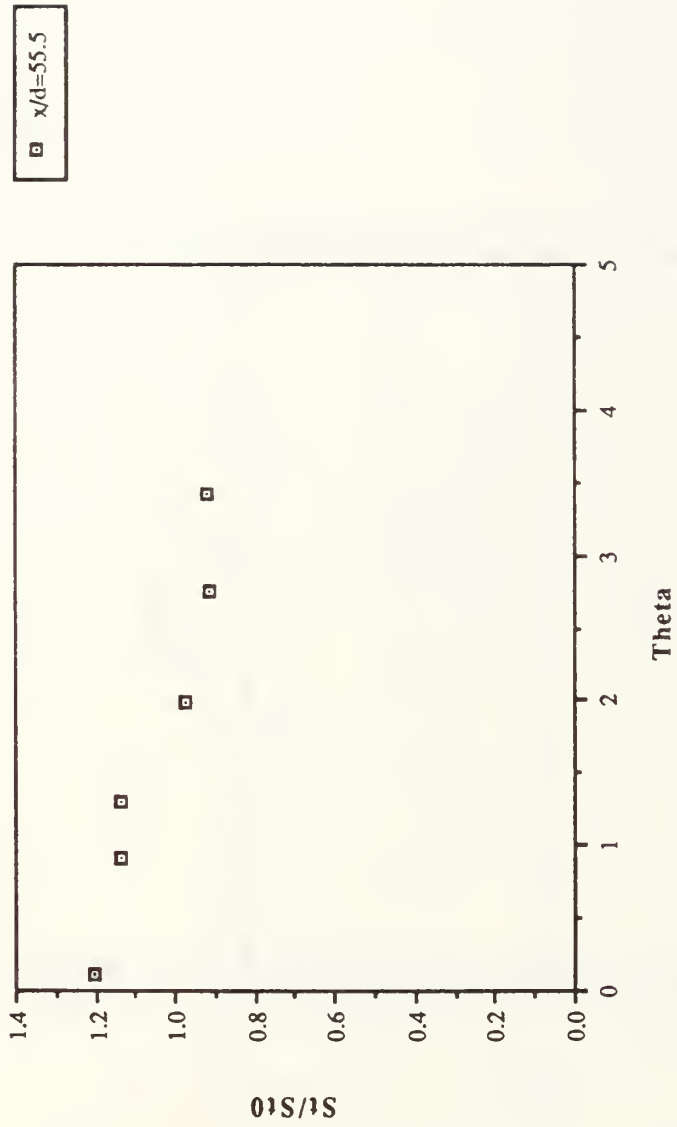


Figure 37. St/St_0 Versus θ , Compound Angle, 1 Row, $m=1.5$, $x/d=55.5$, $Z=-1.27$ cm

1 row $m=1.5$ Theta vs St/St_0 for $z=-1.27$ cm

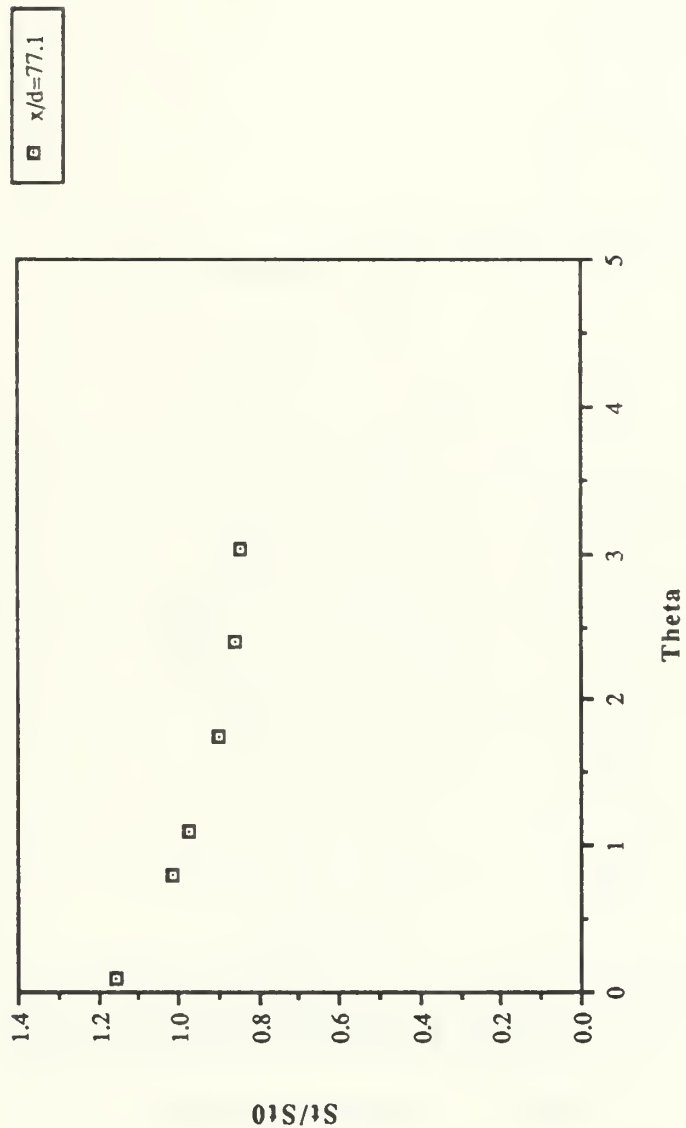


Figure 38. St/St_0 Versus θ , Compound Angle, 1 Row, $m=1.5$, $x/d=77.1$, $Z=-1.27$ cm

1 row $m=1.5$ Theta vs St/St_0 for $z=-1.27$ cm

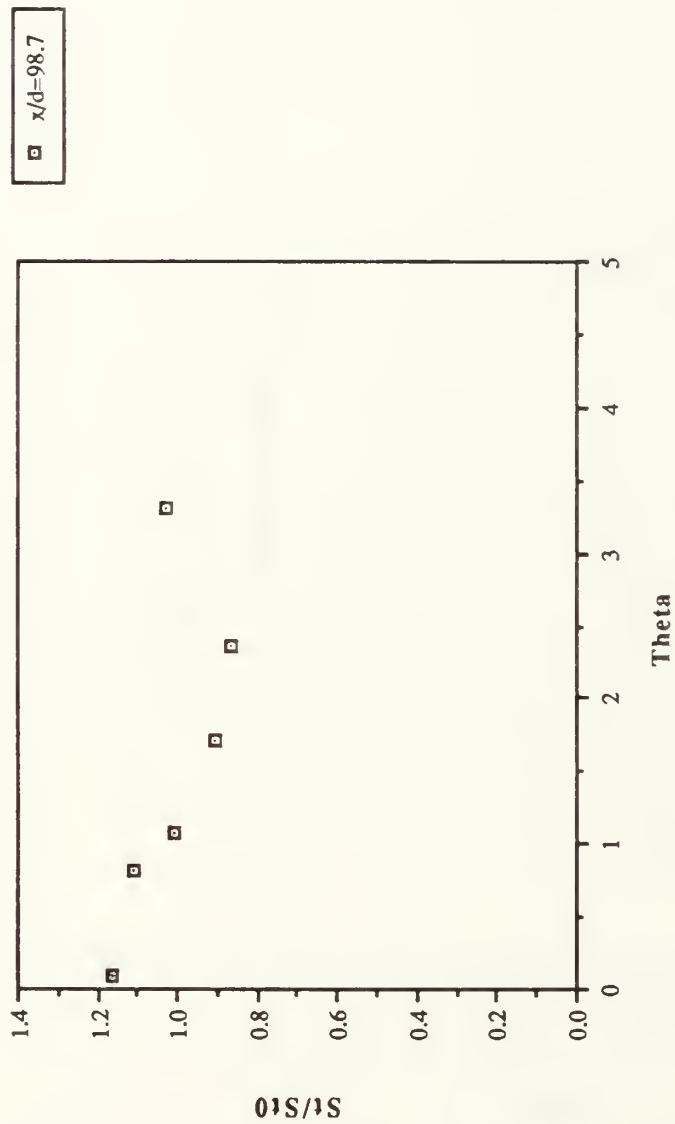


Figure 39. St/St_0 Versus θ , Compound Angle, 1 Row, $m=1.5$, $x/d=98.7$, $Z=-1.27$ cm

spanwise avg. η vs x/d for 1 row $m=1.5$

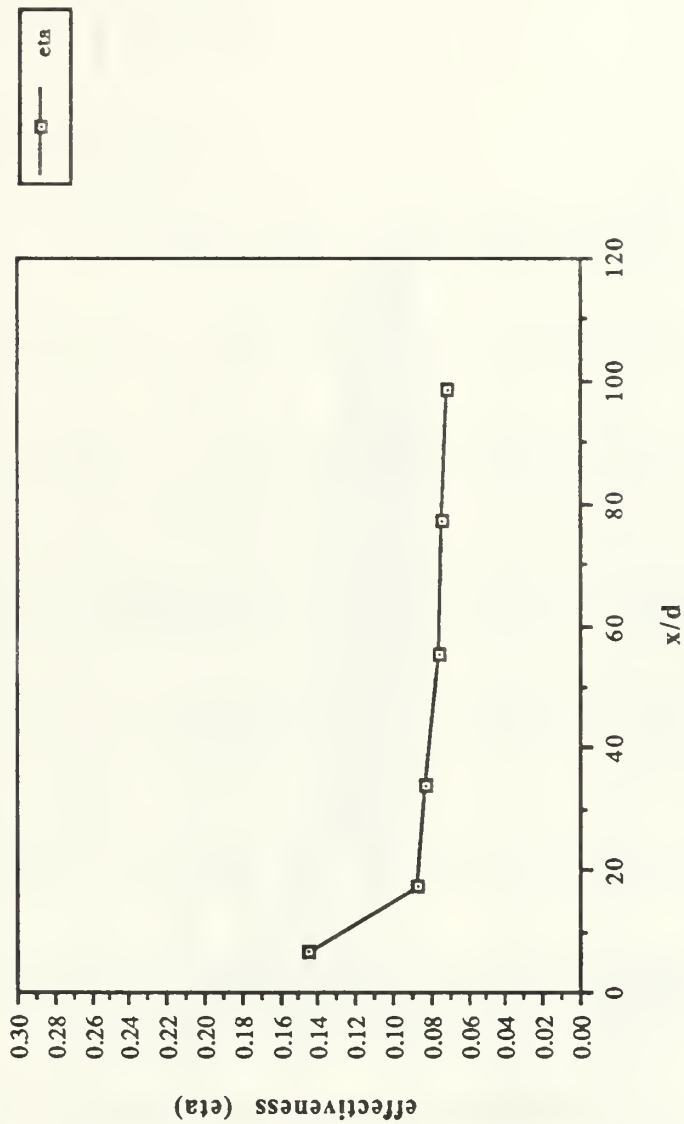


Figure 40. $\bar{\eta}$ Versus x/d , Compound Angle, 1 Row, $m=1.5$, Spanwise Average

spanwise avg. St_f/St_0 vs x/d for 1 row $m=1.5$

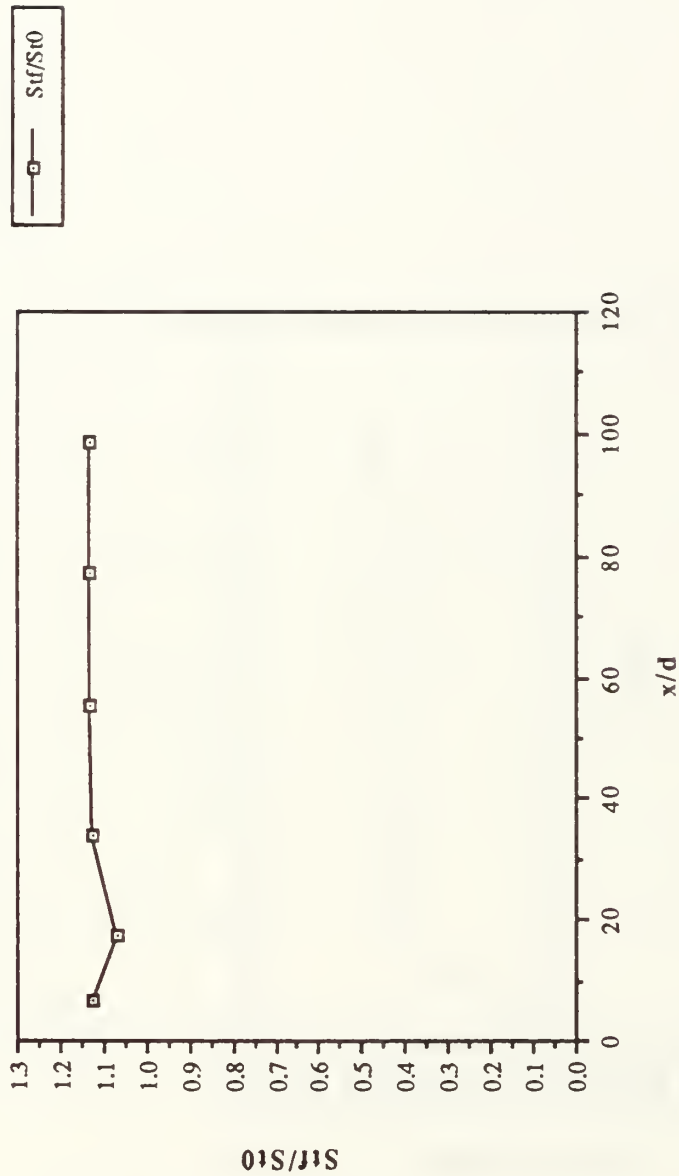


Figure 41. St_f/St_0 Versus x/d , Compound Angle, 1 Row, $m=1.5$, Spanwise Average

Reynolds vs Stanton nr. for 1 row $m=1.5$

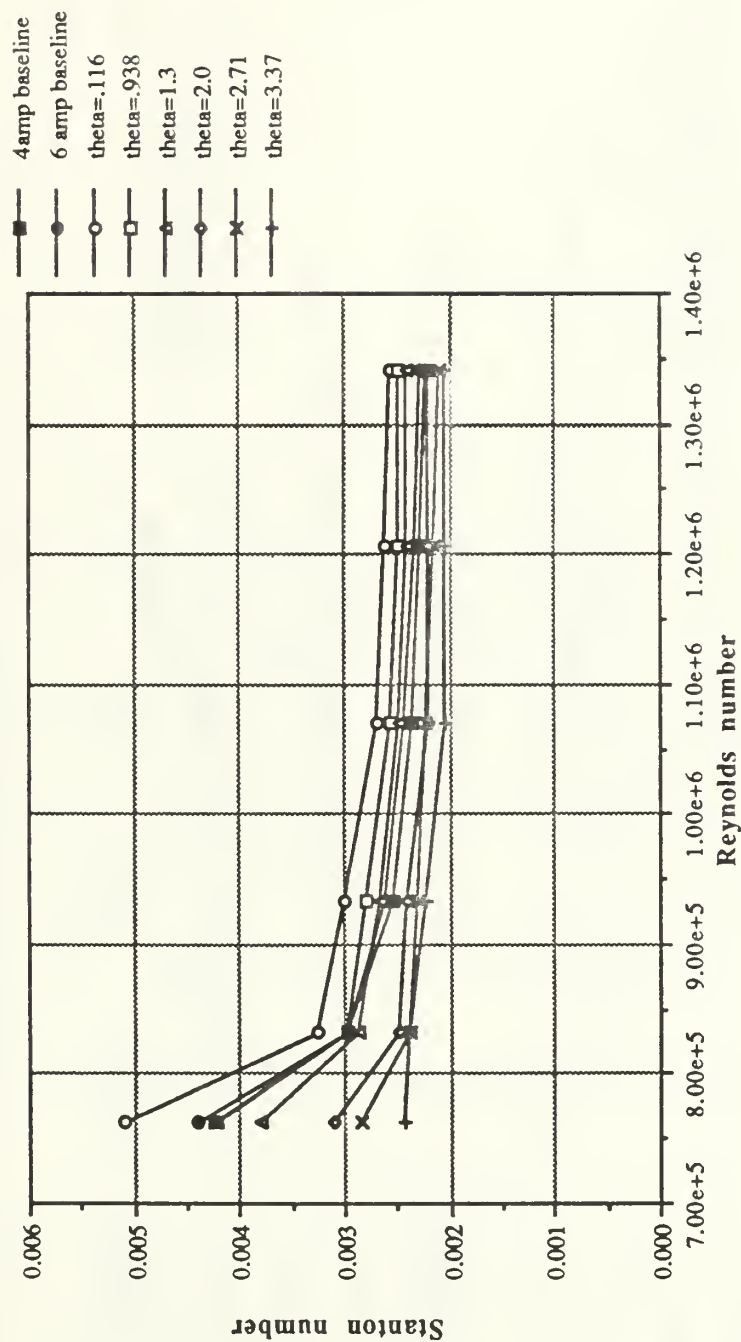


Figure 42. Spanwise Averaged Stanton Number Versus Reynolds Number, Comparison of Different θ Values and Baselines, 1 Row, $m=1.5$

FILM-COOLING EFFECTIVENESS

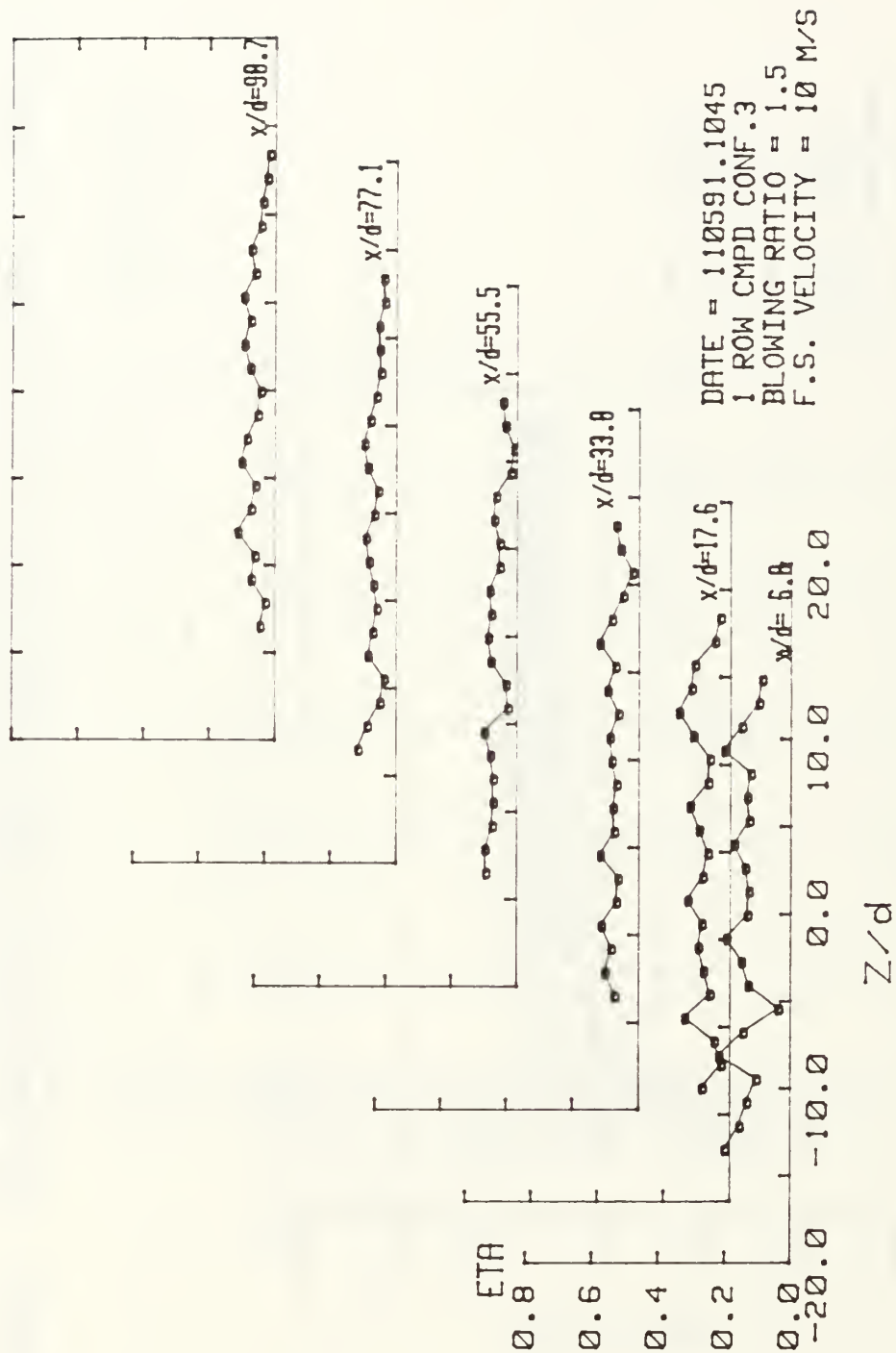


Figure 43. Spanwise Variation of η , Compound Angle, 1 Row, $m=1.5$

ISO-ENERGETIC STANTON # RATIO

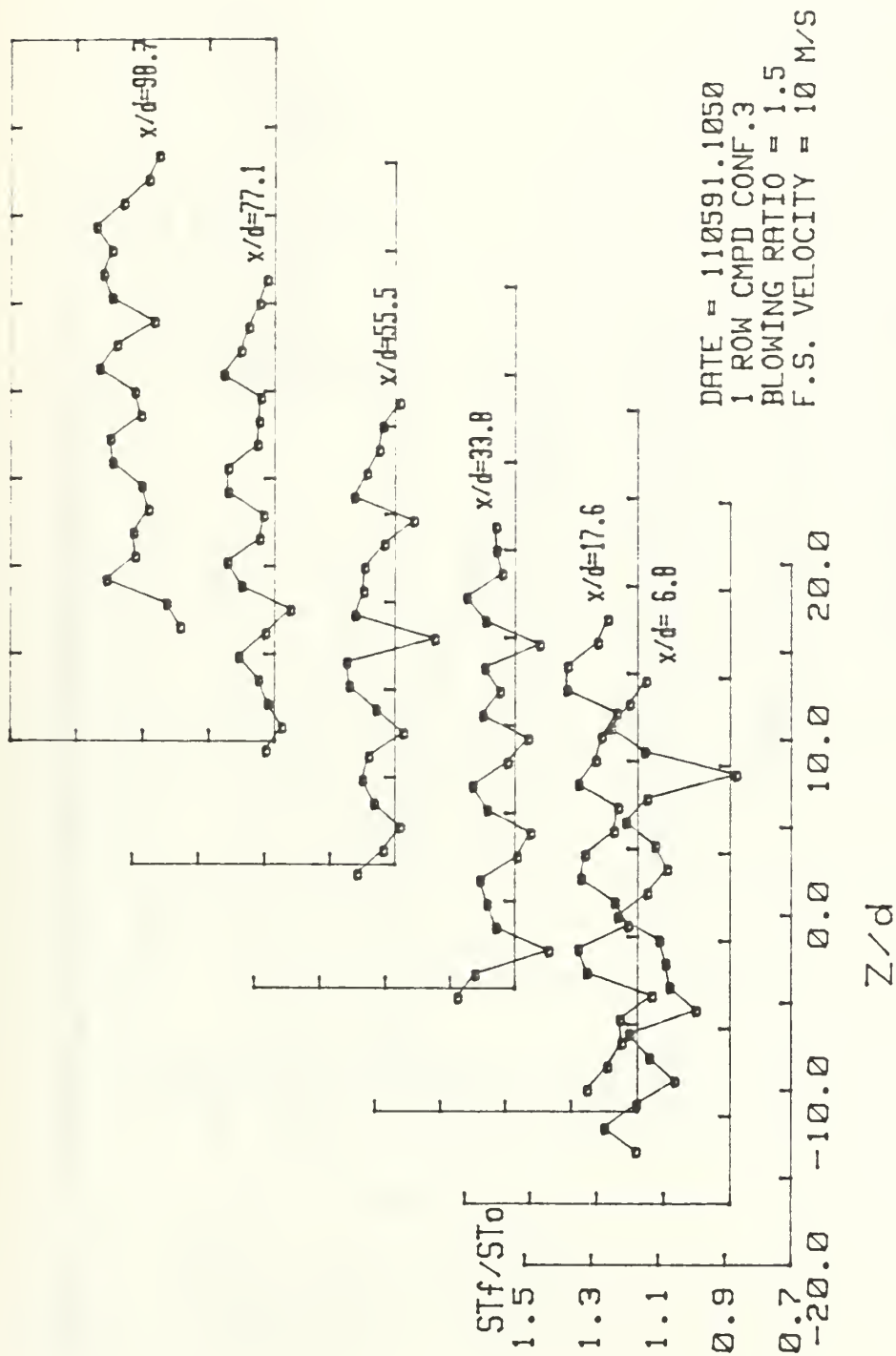


Figure 44. Spanwise Variation of St_f/St_0 , Compound Angle, 1 Row, $m=1.5$

STANTON NUMBER RATIOS

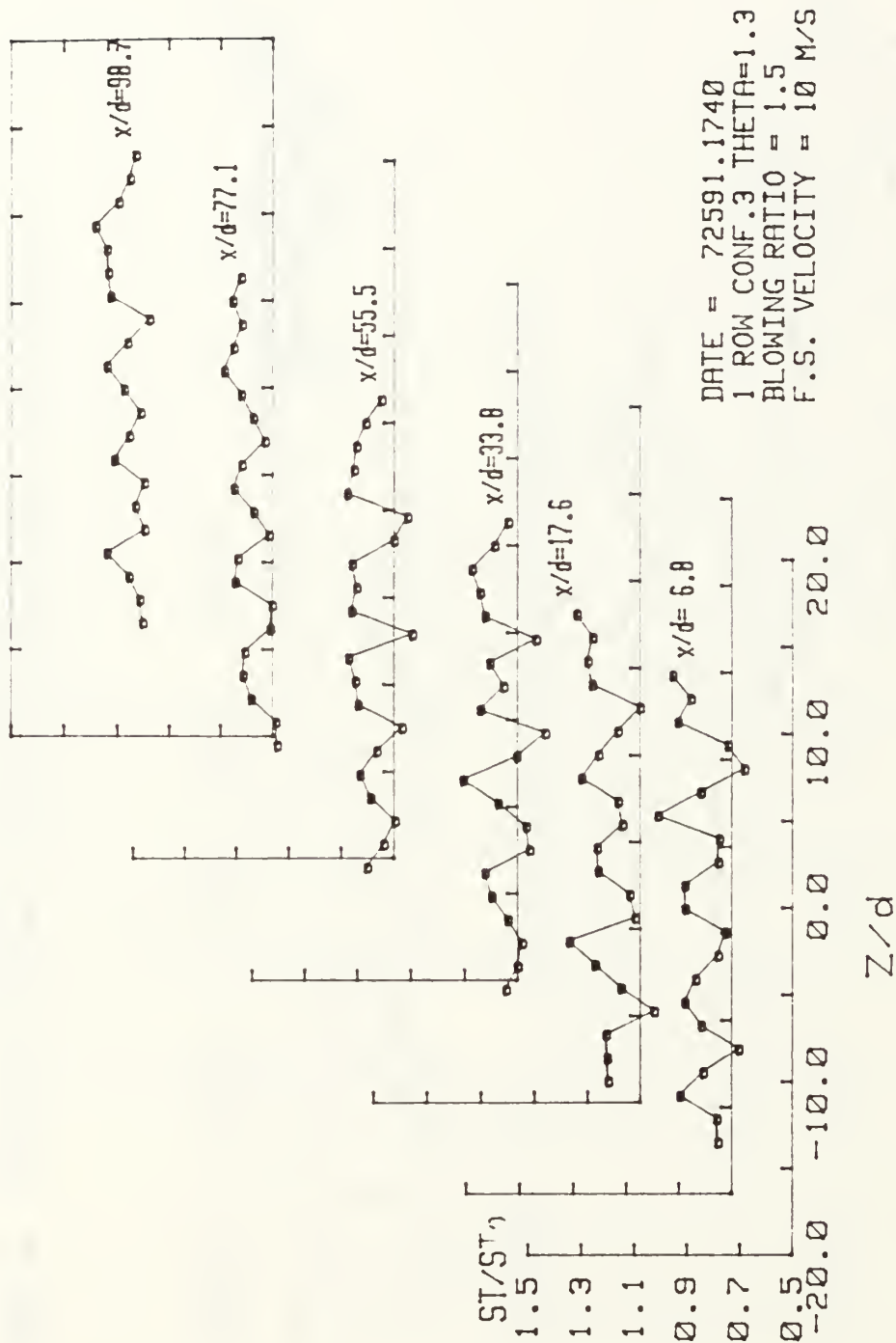


Figure 45. Spanwise Variation of St/St_w Compound Angle, 1 Row, $m=1.5$, $\theta=1.30$

1 row $m=2.0$ Theta vs St/St_0 for $z=-2.54$ cm



Figure 46. St/St_0 Versus θ , Compound Angle, 1 Row, $m=2.0$, $x/d=6.8$, $Z=-2.54$ cm

1 row $m=2.0$ Theta vs St/St_0 for $z=-2.54$ cm

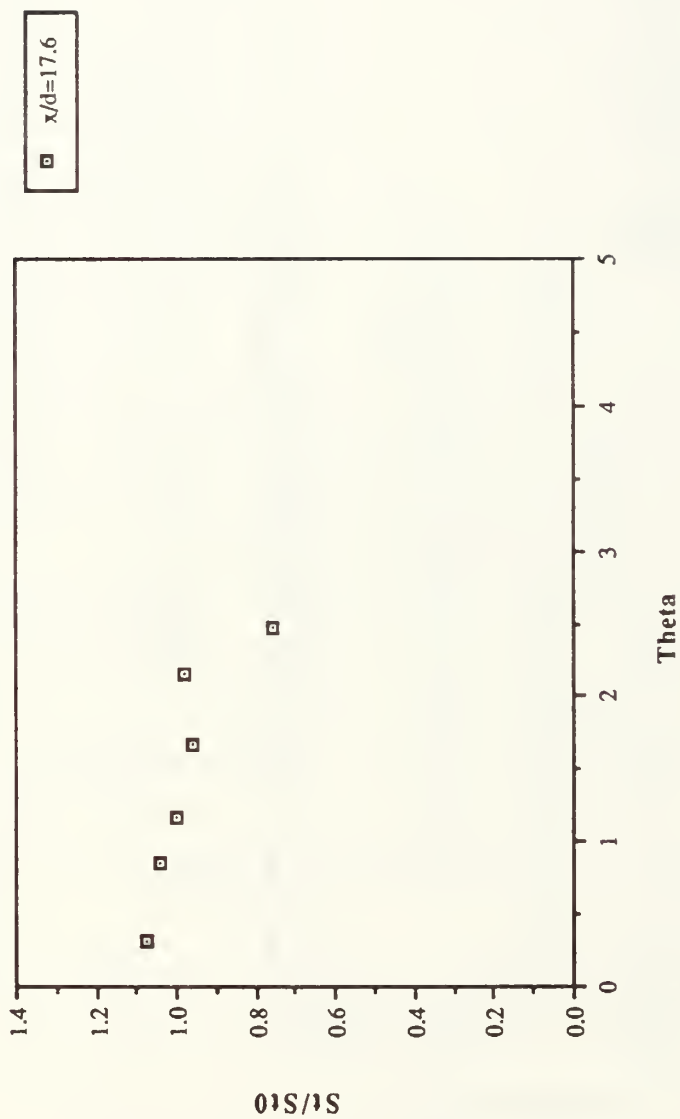


Figure 47. St/St_0 Versus θ , Compound Angle, 1 Row, $m=2.0$, $x/d=17.6$, $Z=-2.54$ cm

1 row $m=2.0$ Theta vs St/St_0 for $z=-2.54$ cm

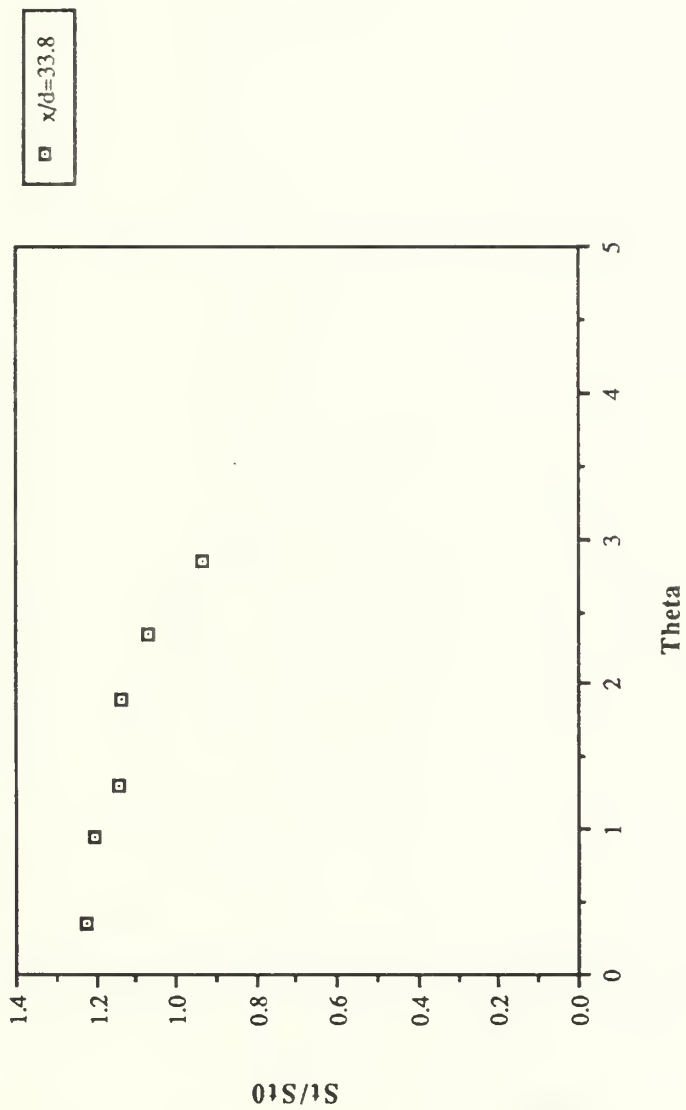


Figure 48. St/St_0 Versus θ , Compound Angle, 1 Row, $m=2.0$, $x/d=33.8$, $Z=-2.54$ cm

1 row $m=2.0$ Theta vs St/St_0 for $z=-2.54$ cm

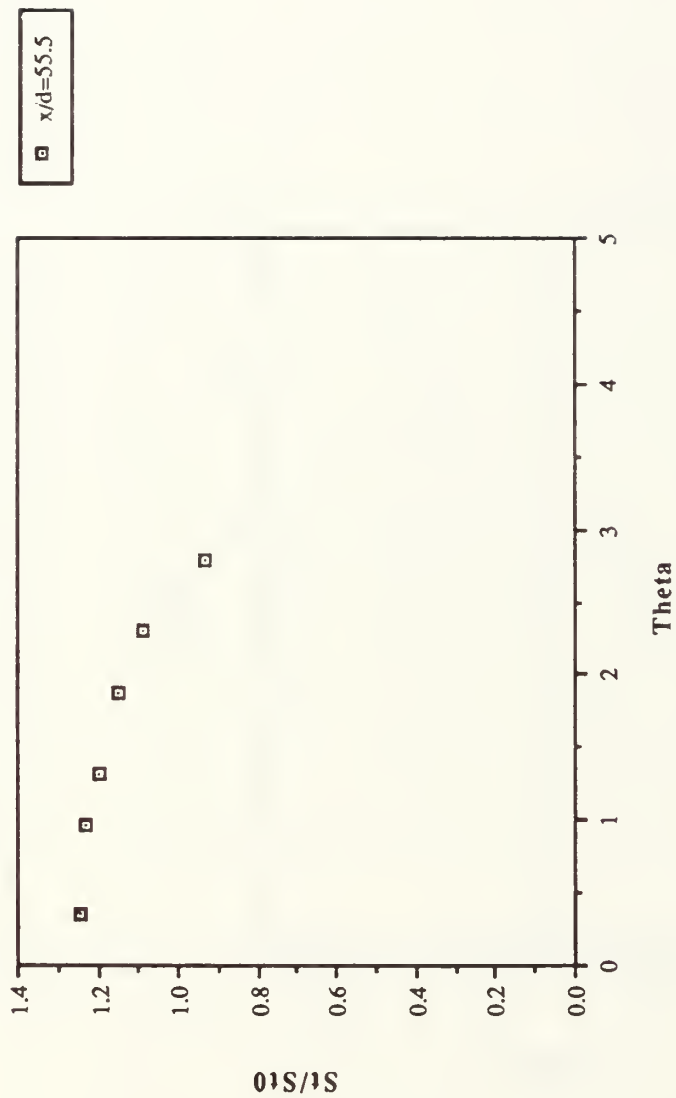


Figure 49. St/St_0 Versus θ , Compound Angle, 1 Row, $m=2.0$, $x/d=55.5$, $Z=-2.54$ cm

1 row $m=2.0$ Theta vs St/St_0 for $z=-2.54$ cm

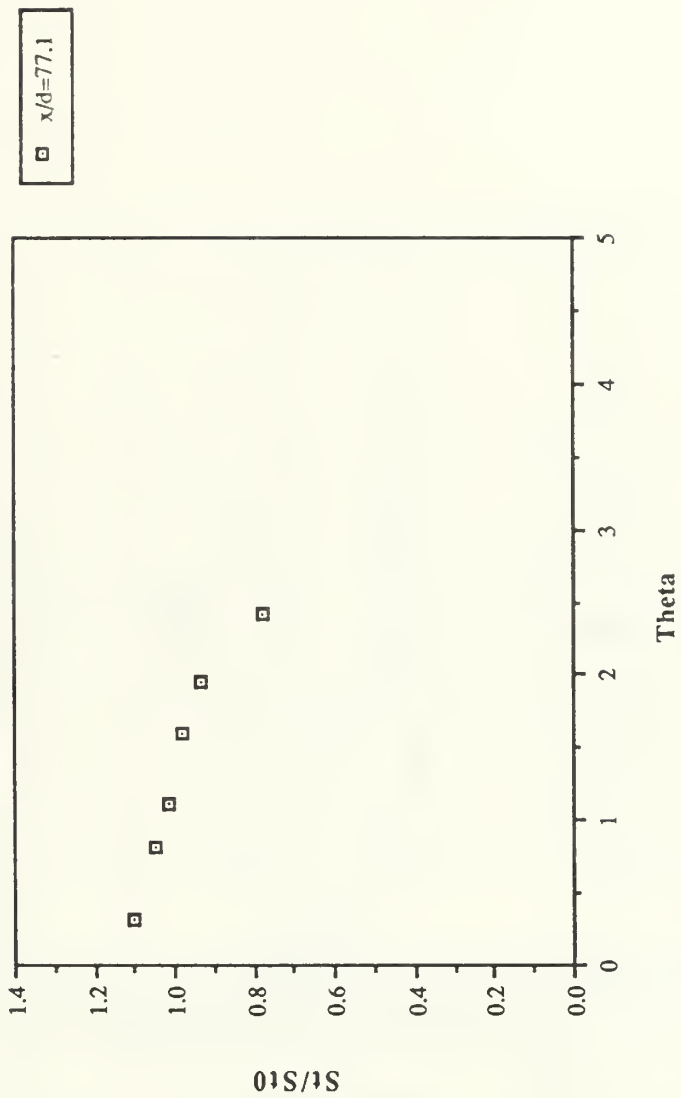


Figure 50. St/St_0 Versus θ , Compound Angle, 1 Row, $m=2.0$, $x/d=77.1$, $Z=-2.54$ cm

1 row $m=2.0$ Theta vs St/St_0 for $z=-2.54$ cm

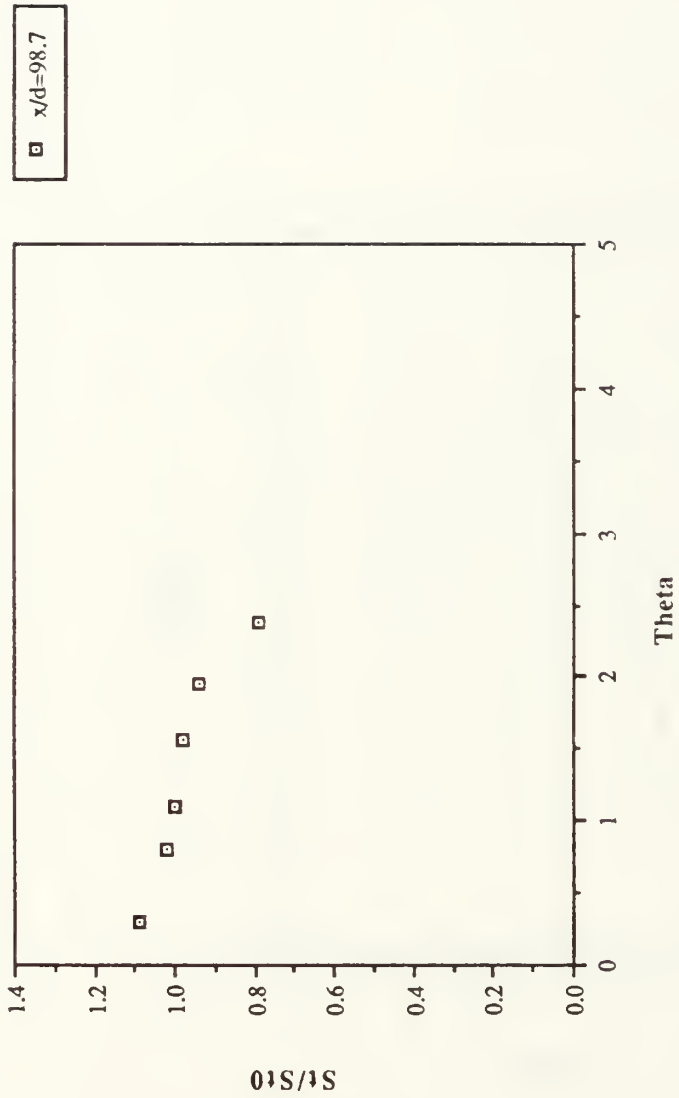


Figure 51. St/St_0 Versus θ , Compound Angle, 1 Row, $m=2.0$, $x/d=98.7$, $Z=-2.54$ cm

spanwise avg. η vs x/d for 1 row $m=2.0$

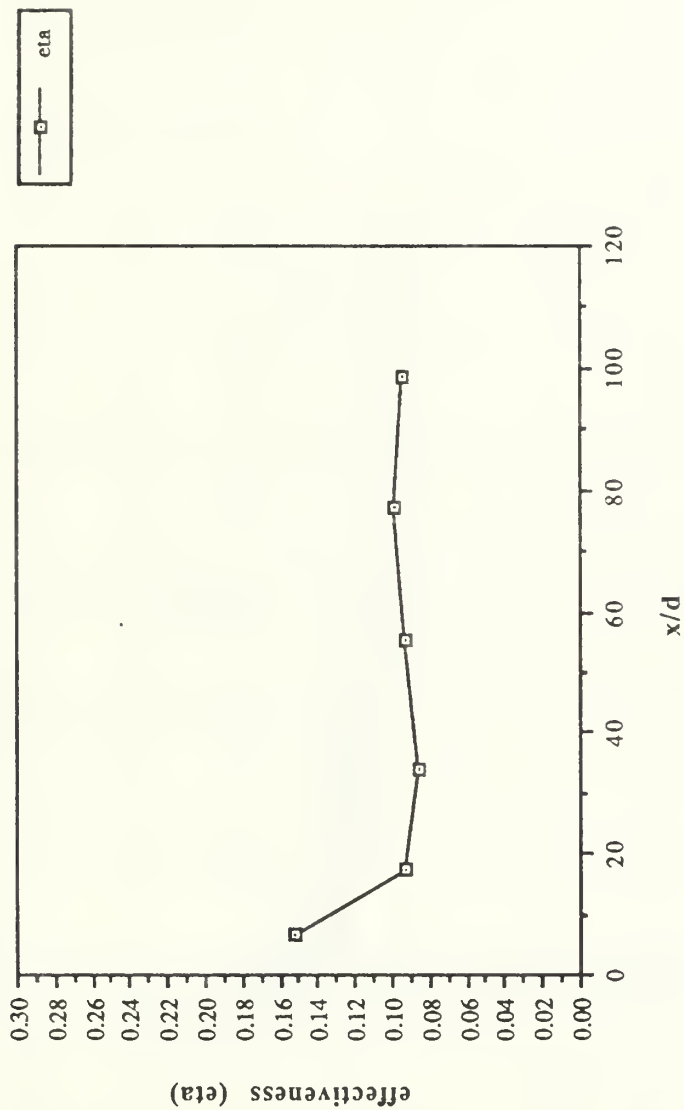


Figure 52. $\bar{\eta}$ Versus x/d , Compound Angle, 1 Row, $m=2.0$, Spanwise Average

Reynolds vs Stanton nr. for 1 row $m=2.0$

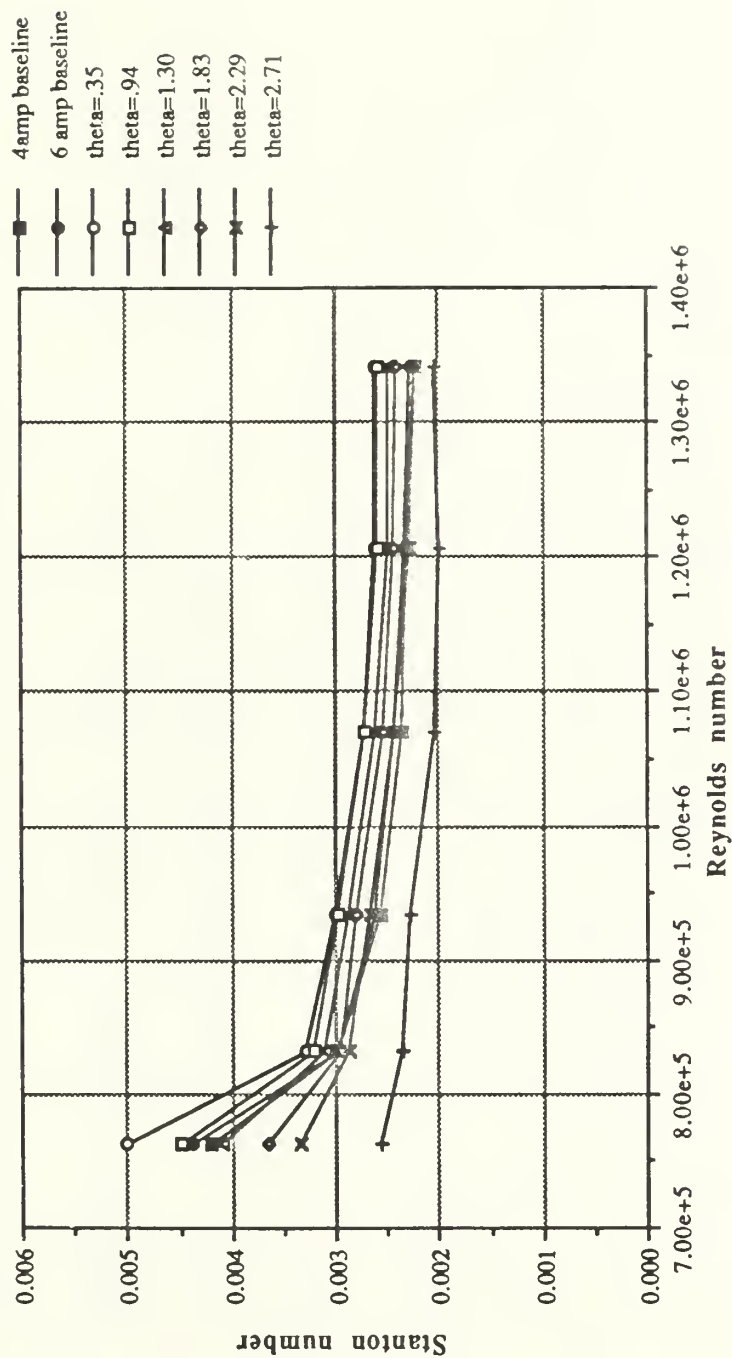


Figure 54. Spanwise Averaged Stanton Number Versus Reynolds Number, Comparison of Different θ Values and Baselines, 1 Row, $m=2.0$

FILM-COOLING EFFECTIVENESS

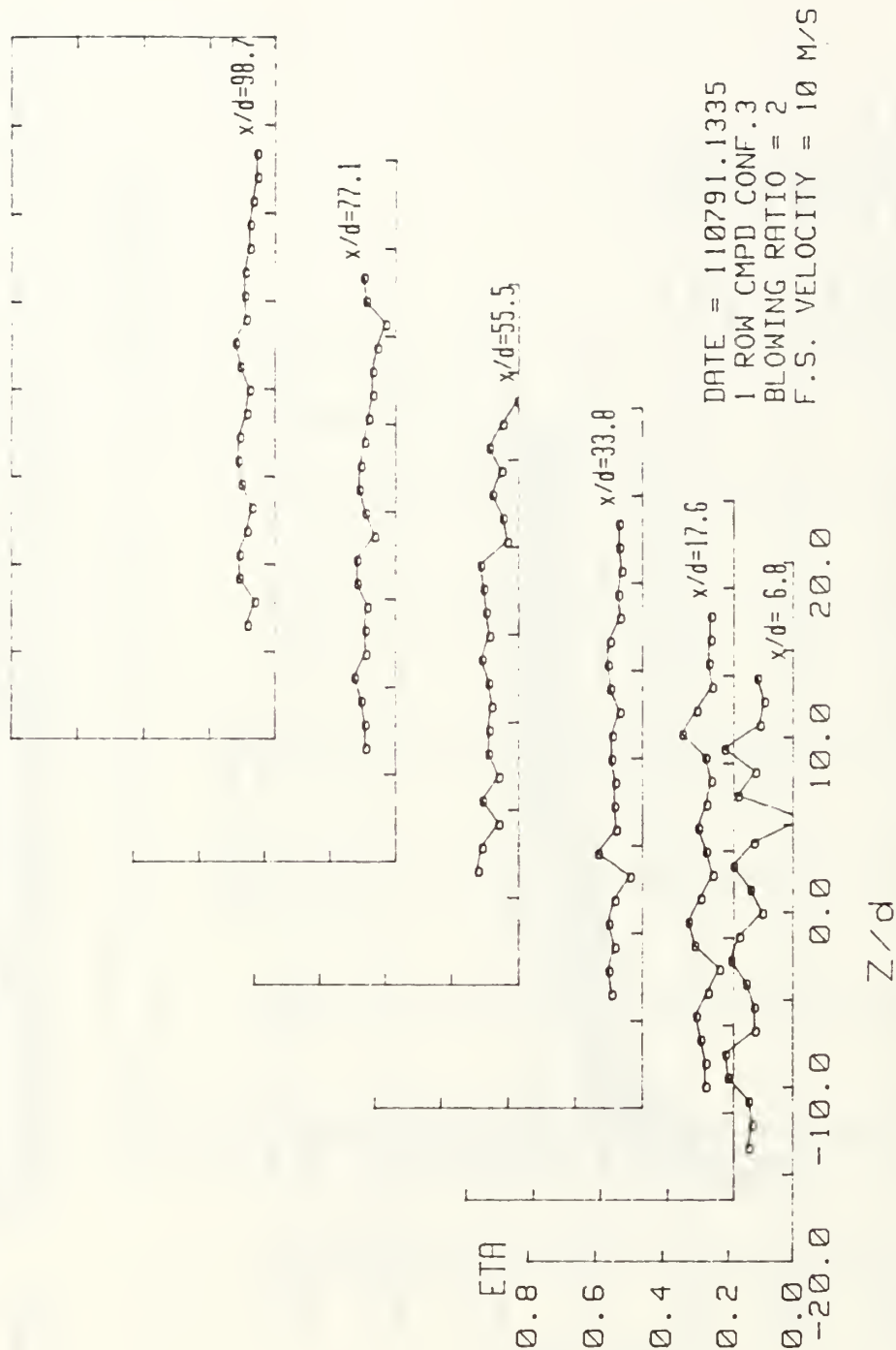


Figure 55. Spanwise Variation of η , Compound Angle, 1 Row, $m=2.0$

ISO-ENERGETIC STANTON # RATIO

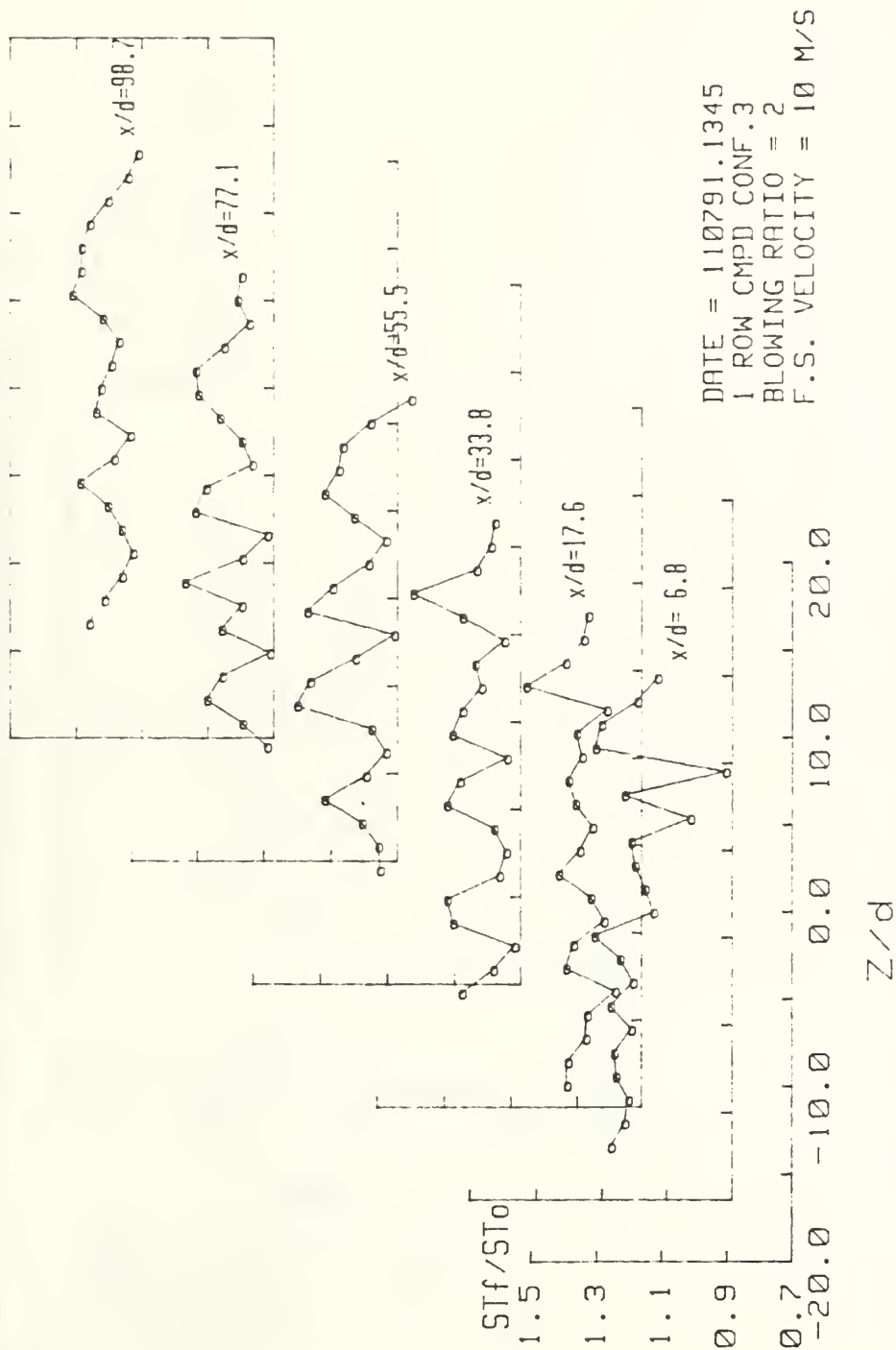


Figure 56. Spanwise Variation of St_f/St_0 , Compound Angle, 1 Row, $m=2.0$

STANTON NUMBER RATIOS

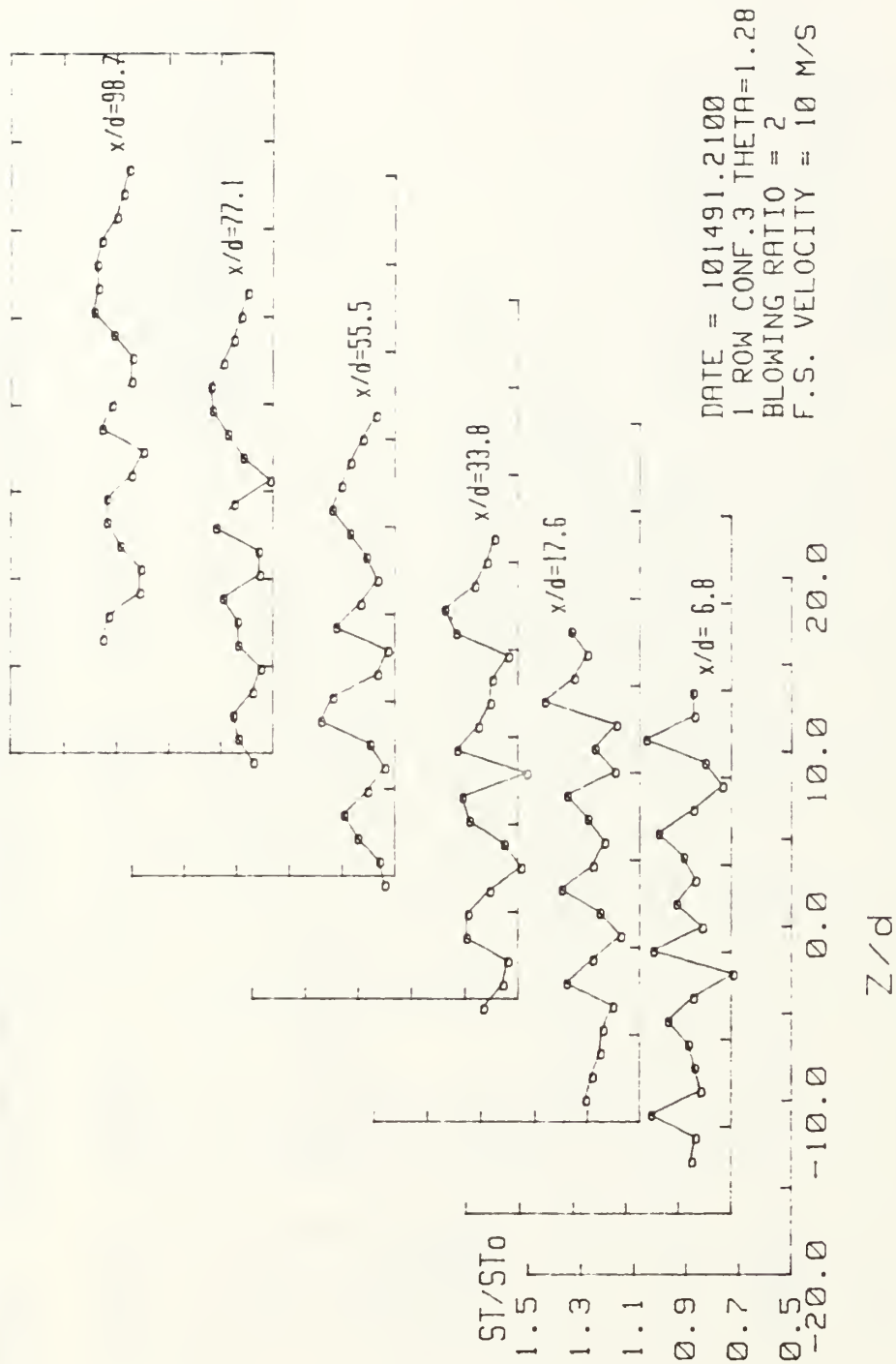


Figure 57. Spanwise Variation of St/St_0 , Compound Angle, 1 Row, $m=2.0$, $\theta=1.28$

1 row $m=3.0$ Theta vs St/St_0 for $z=-2.54$ cm

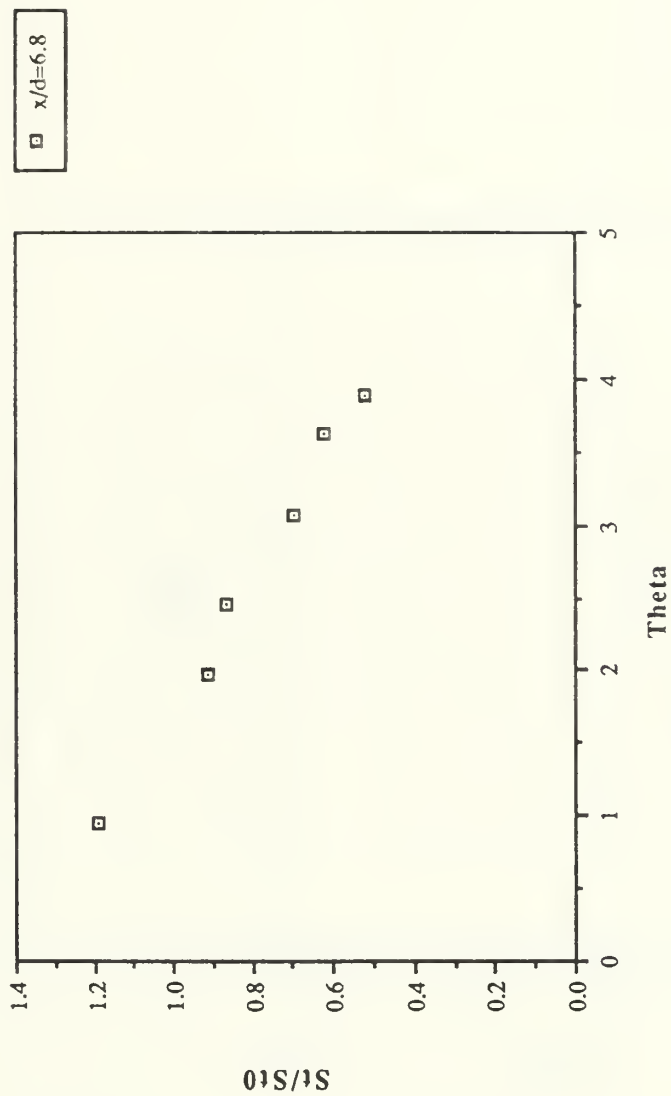


Figure 58. St/St_0 Versus θ , Compound Angle, 1 Row, $m=3.0$, $x/d=6.8$, $Z=-2.54$ cm

1 row $m=3.0$ Theta vs St/St_0 for $z=-2.54$ cm



Figure 59. St/St_0 Versus θ , Compound Angle, 1 Row, $m=3.0$, $x/d=17.6$, $Z=-2.54$ cm

1 row m=3.0 Theta vs St/St0 for z=-2.54 cm

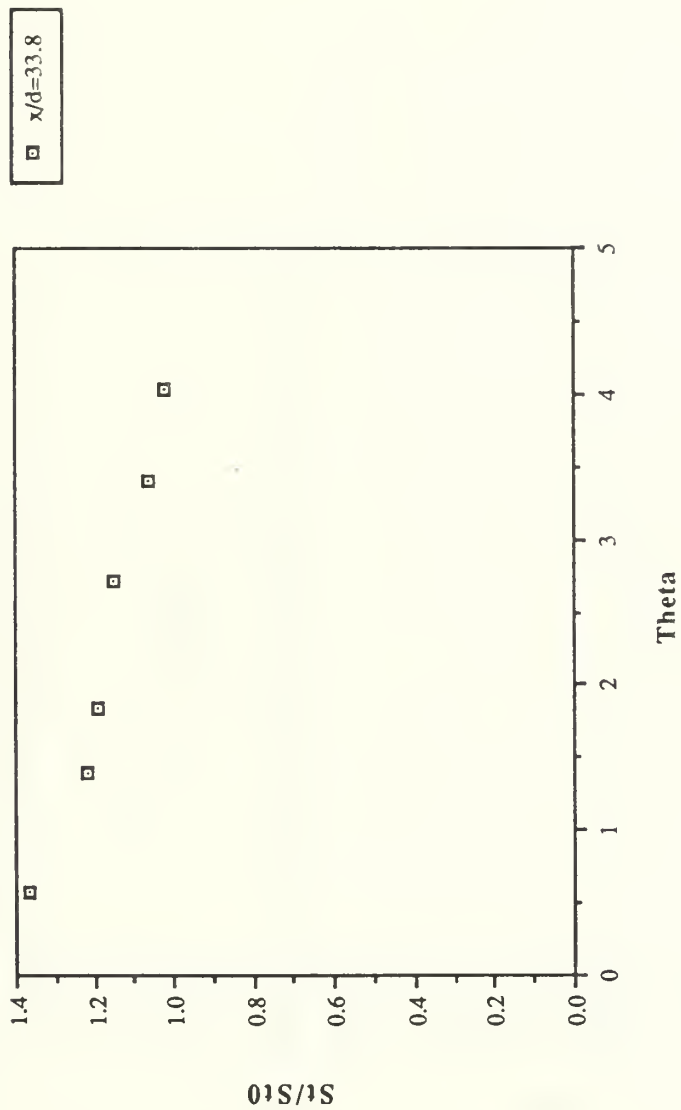


Figure 60. St/St_0 Versus θ , Compound Angle, 1 Row, $m=3.0$, $x/d=33.8$, $Z=-2.54$ cm

1 row $m=3.0$ Theta vs St/St_0 for $z=-2.54$ cm



Figure 61. St/St_0 Versus θ , Compound Angle, 1 Row, $m=3.0$, $x/d=55.5$, $Z=-2.54$ cm

1 row $m=3.0$ Theta vs St/St_0 for $z=-2.54$ cm

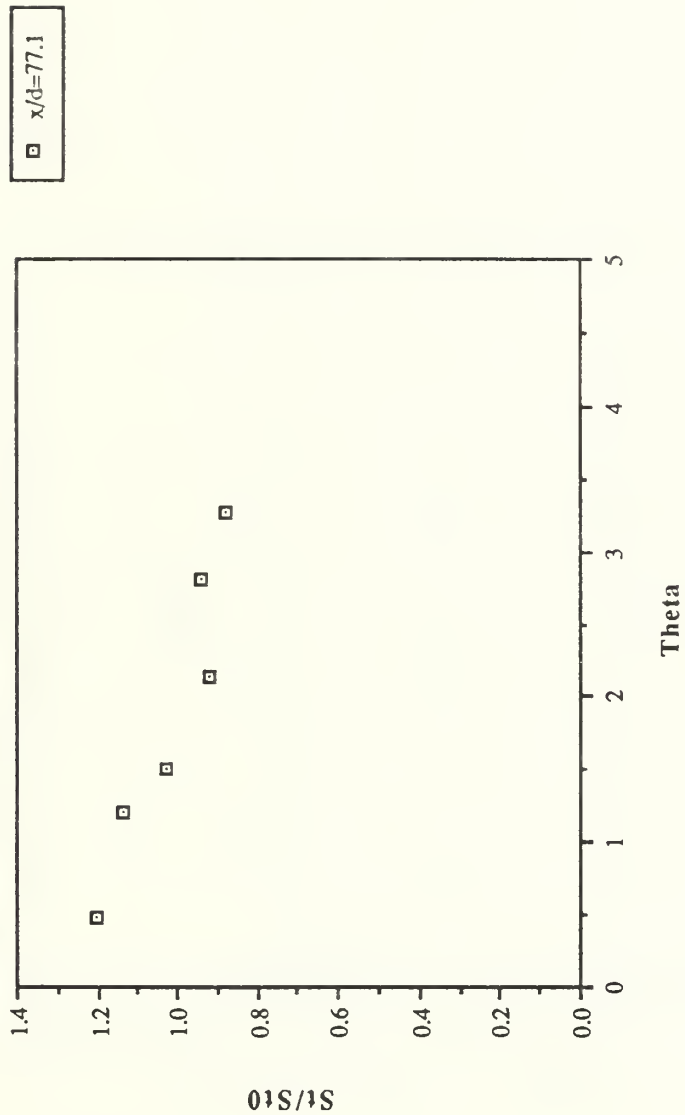


Figure 62. St/St_0 Versus θ , Compound Angle, 1 Row, $m=3.0$, $x/d=77.1$, $Z=-2.54$ cm

1 row $m=3.0$ Theta vs St/St_0 for $z=-2.54$ cm

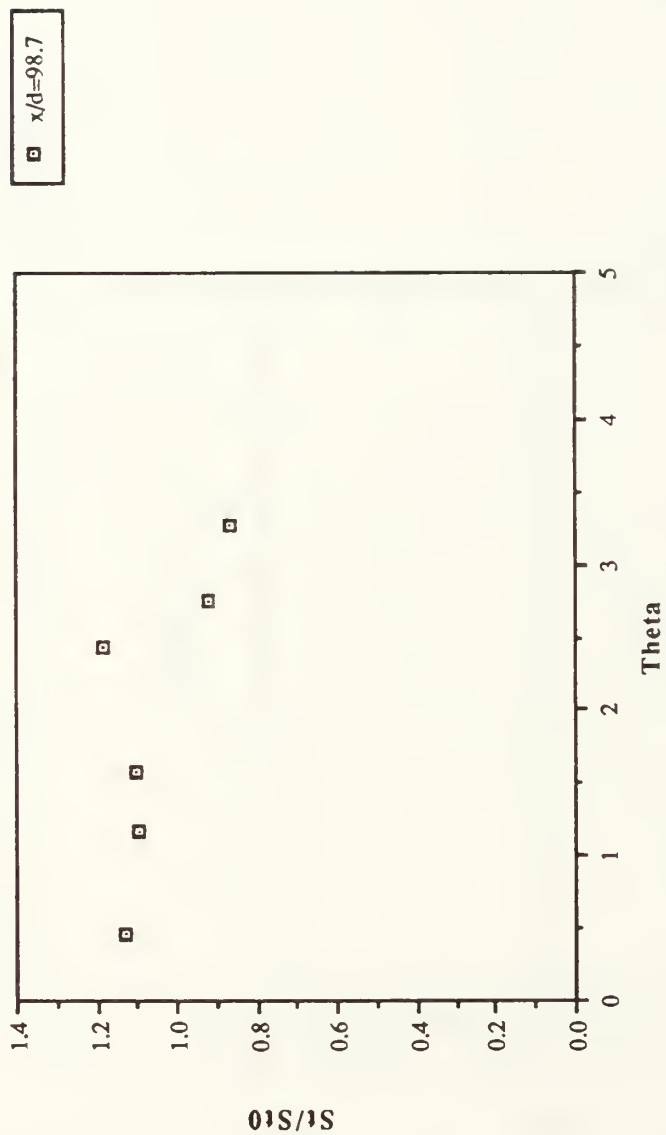


Figure 63. St/St_0 Versus θ , Compound Angle, 1 Row, $m=3.0$, $x/d=98.7$, $Z=-2.54$ cm

spanwise avg. η vs x/d for 1 row $m=3.0$

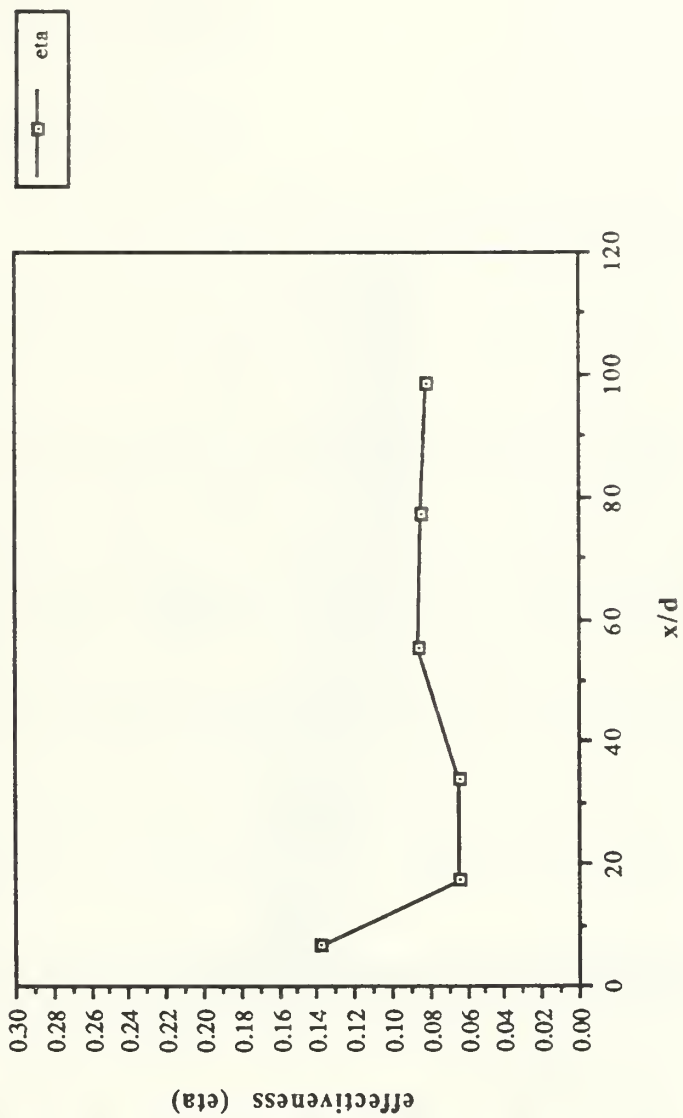


Figure 64. $\bar{\eta}$ Versus x/d , Compound Angle, 1 Row, $m=3.0$, Spanwise Average

spanwise avg. St_f/St_0 vs x/d for 1 row $m=3.0$

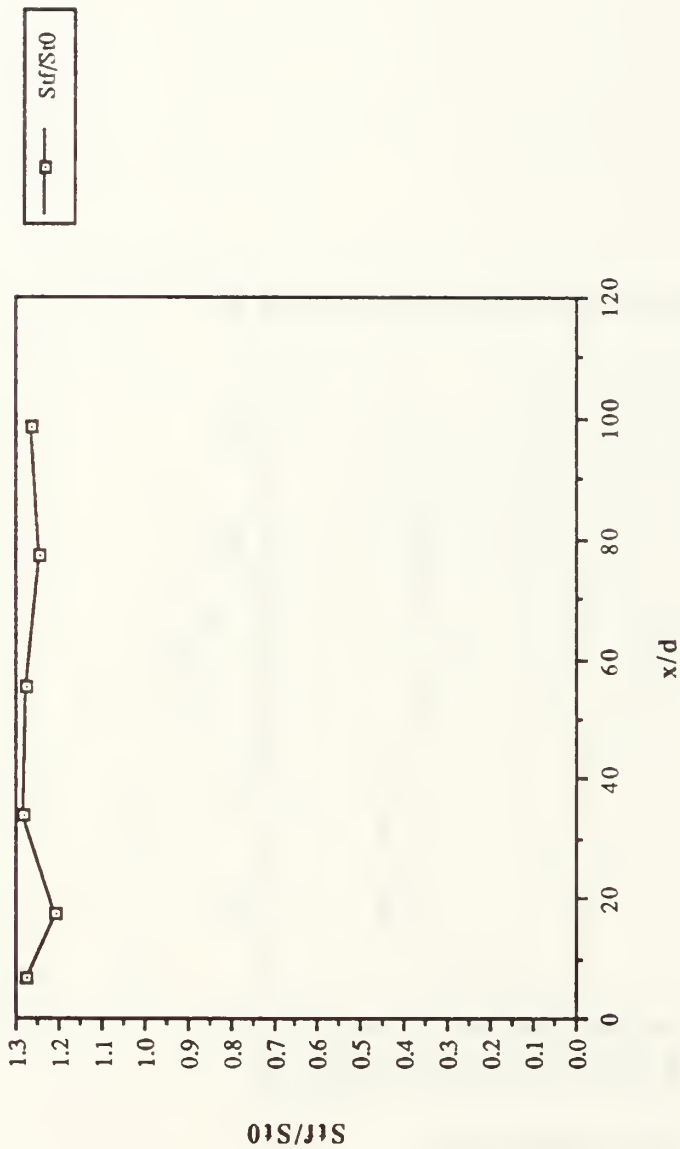


Figure 65. St_f/St_0 Versus x/d , Compound Angle, 1 Row, $m=3.0$, Spanwise Average

Reynolds vs Stanton nr. for 1 row $m=3.0$

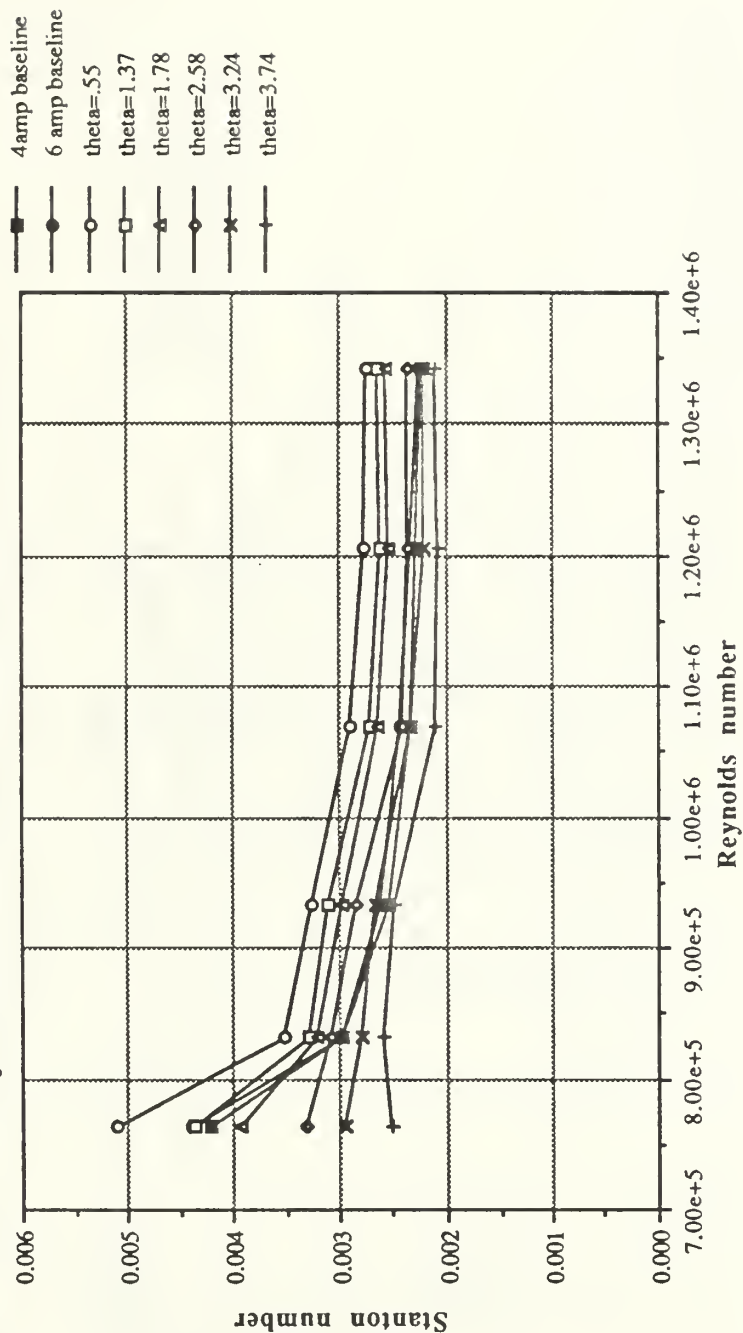


Figure 66. Spanwise Averaged Stanton Number Versus Reynolds Number, Comparison of Different θ Values and Baselines, 1 Row, $m=3.0$

FILM-COOLING EFFECTIVENESS

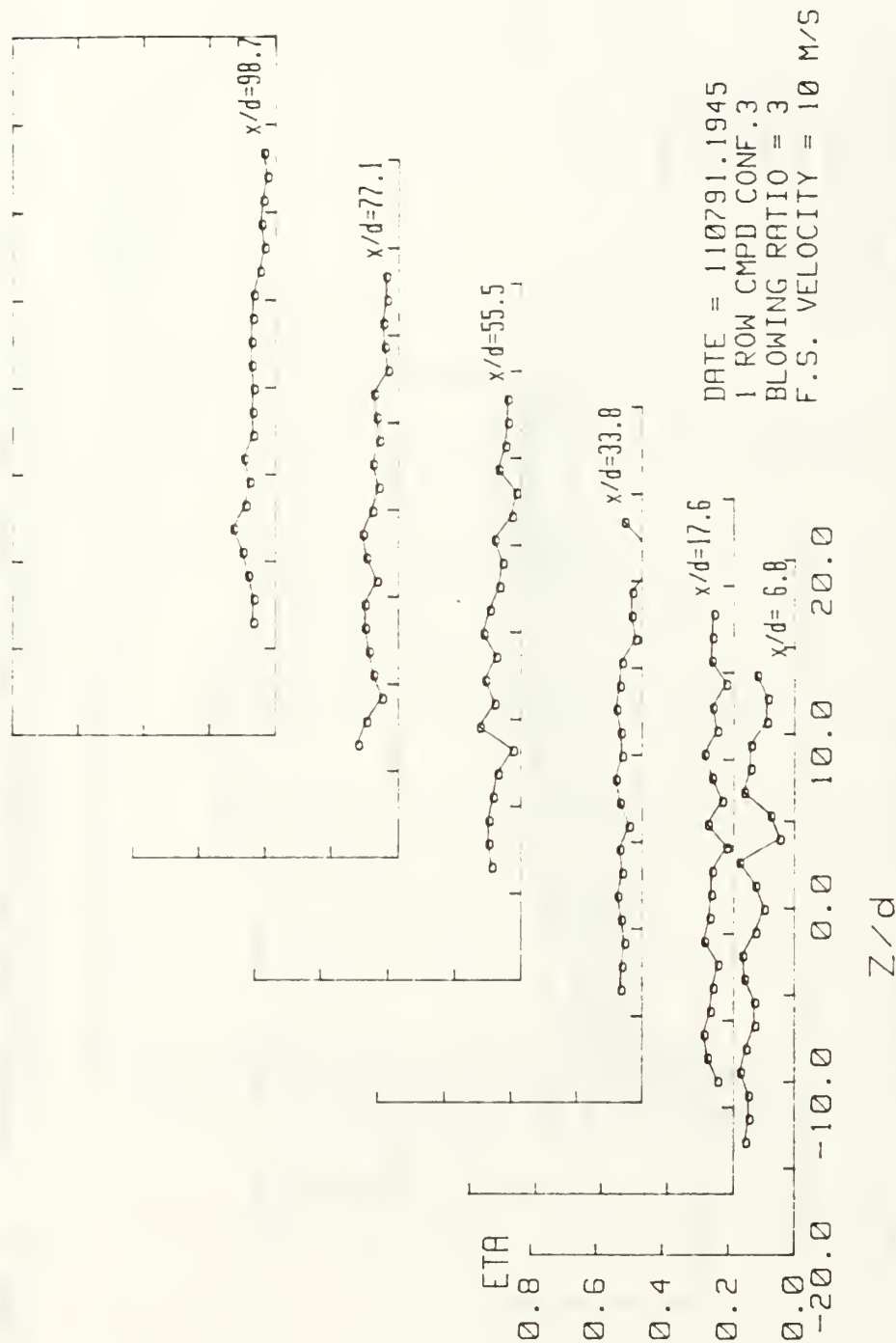


Figure 67. Spanwise Variation of η , Compound Angle, 1 Row, $m=3.0$

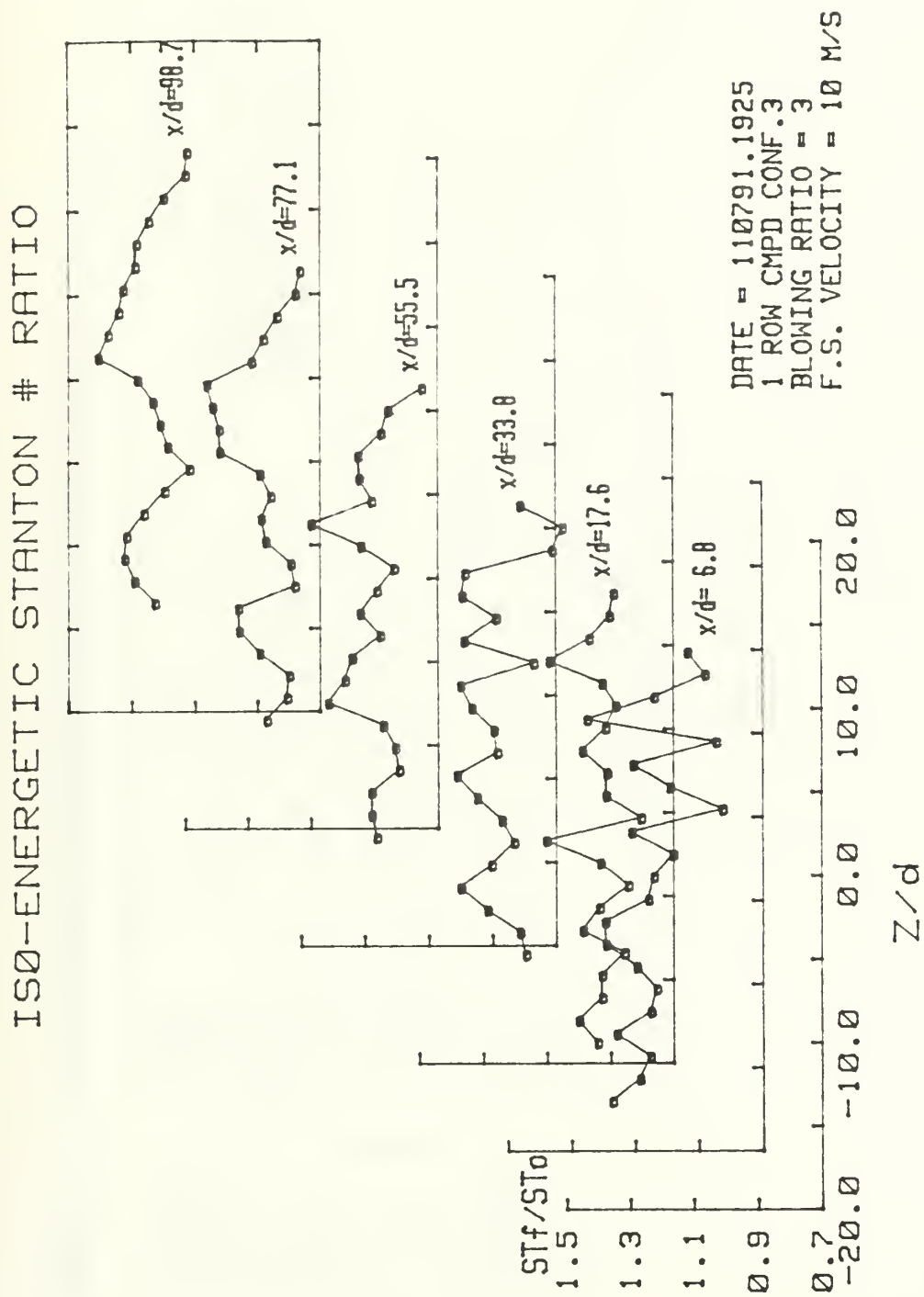


Figure 68. Spanwise Variation of St_f/St_0 , Compound Angle, 1 Row, $m=3.0$

STANTON NUMBER RATIOS

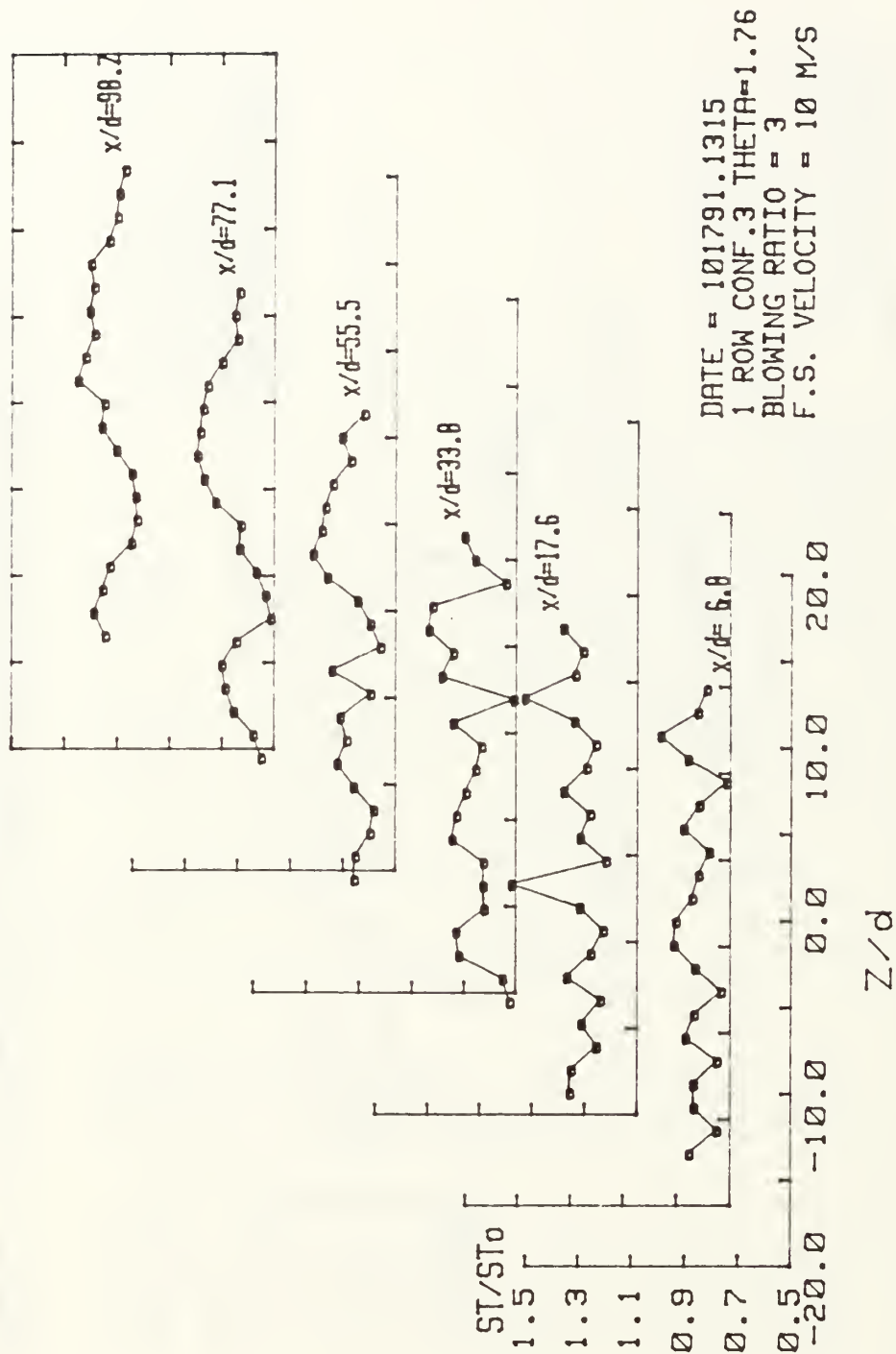


Figure 69. Spanwise Variation of St/St_0 , Compound Angle, 1 Row, $m=3.0$, $\theta=1.76$

1 row $m=4.0$ Theta vs St/St_0 for $z=-7.62$ cm

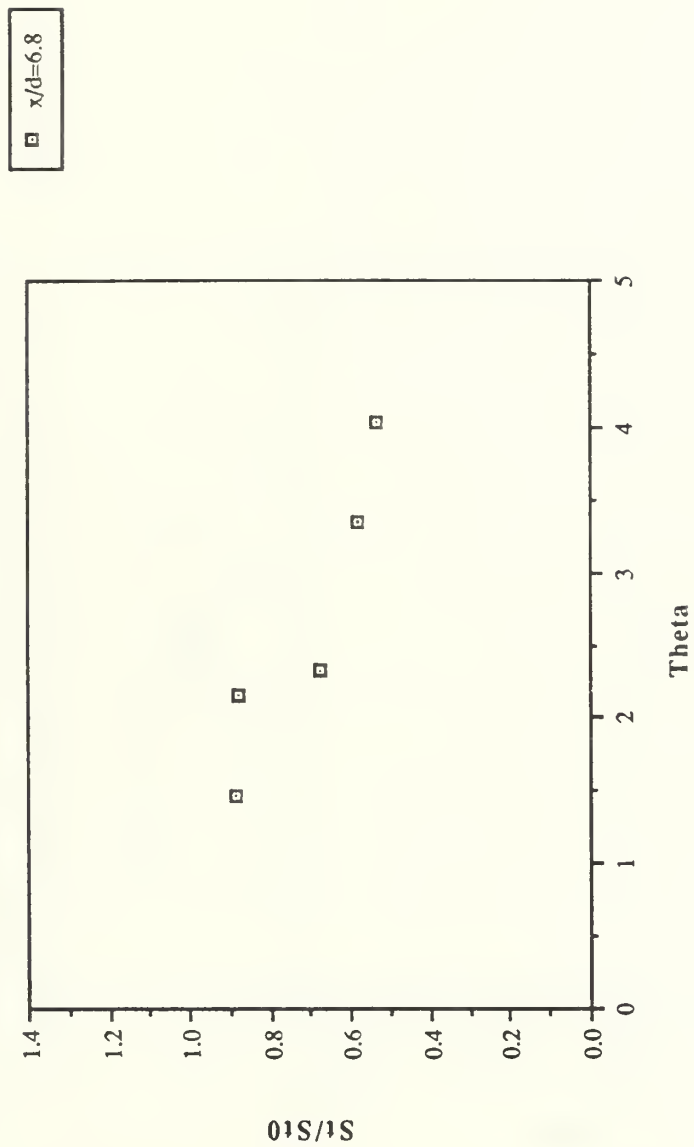


Figure 70. St/St_0 Versus θ , Compound Angle, 1 Row, $m=4.0$, $x/d=6.8$, $Z=-7.62$ cm

1 row $m=4.0$ Theta vs St/St_0 for $z=-7.62$ cm

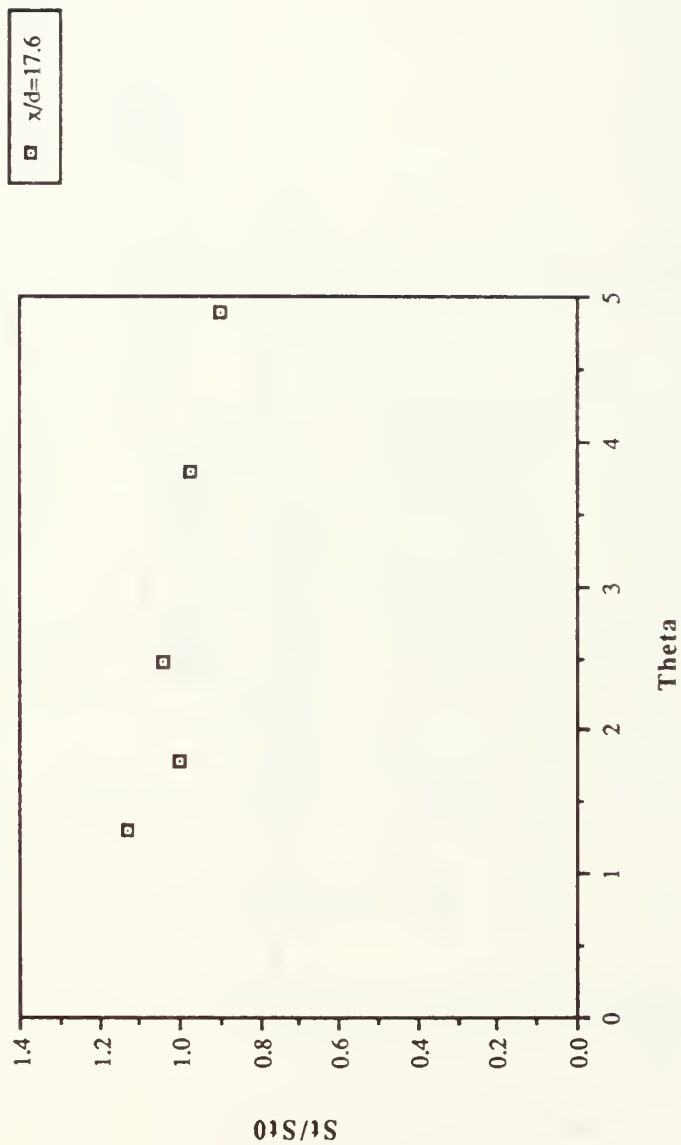


Figure 71. St/St_0 Versus θ , Compound Angle, 1 Row, $m=4.0$, $x/d=17.6$, $Z=-7.62$ cm

1 row $m=4.0$ Theta vs St/St_0 for $z=-7.62$ cm

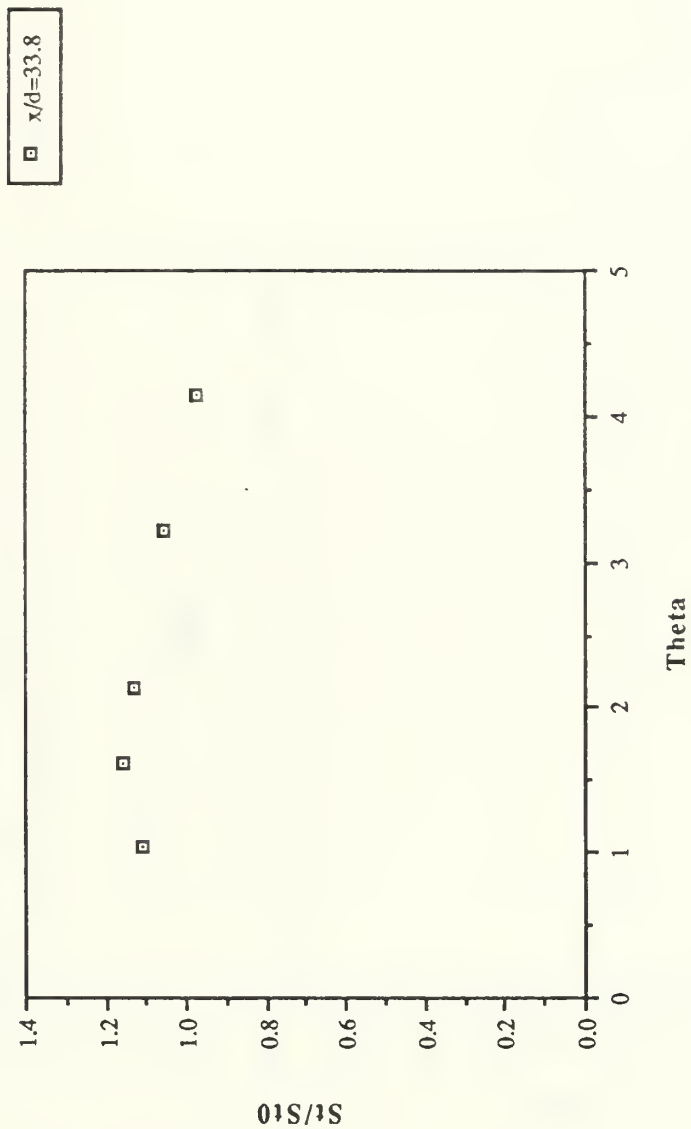


Figure 72. St/St_0 Versus θ , Compound Angle, 1 Row, $m=4.0$, $x/d=33.8$, $Z=-7.62$ cm

1 row $m=4.0$ Theta vs St/St_0 for $z=-7.62$ cm

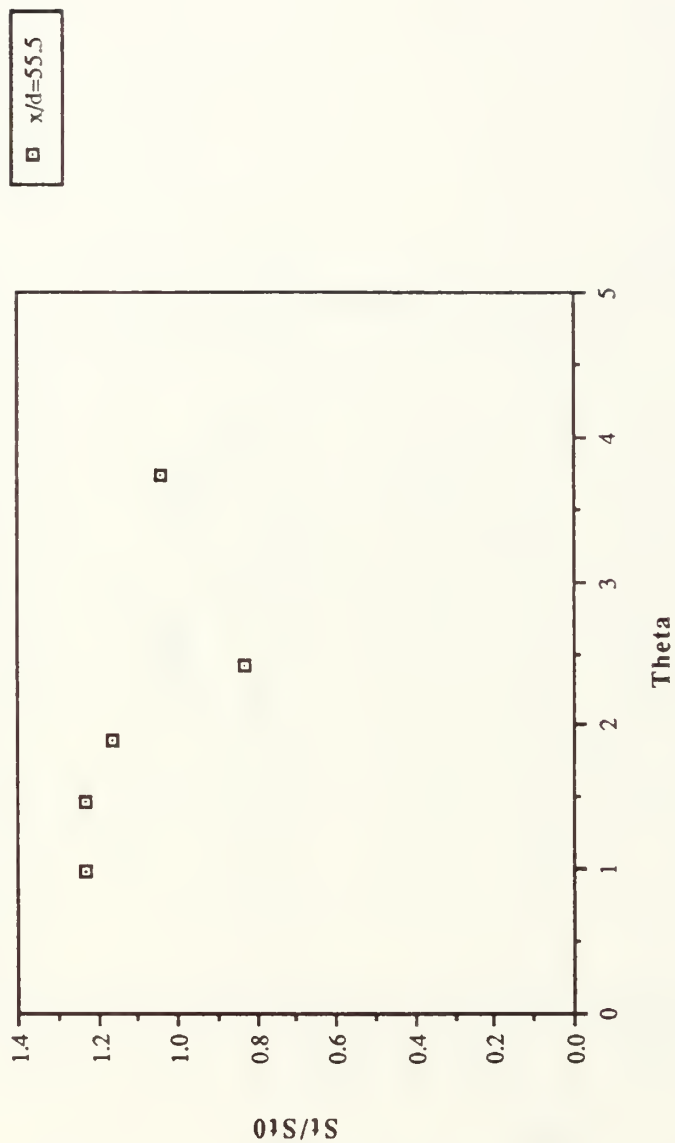


Figure 73. St/St_0 Versus θ , Compound Angle, 1 Row, $m=4.0$, $x/d=55.5$, $Z=-7.62$ cm

1 row $m=4.0$ Theta vs St/St_0 for $z=-7.62$ cm

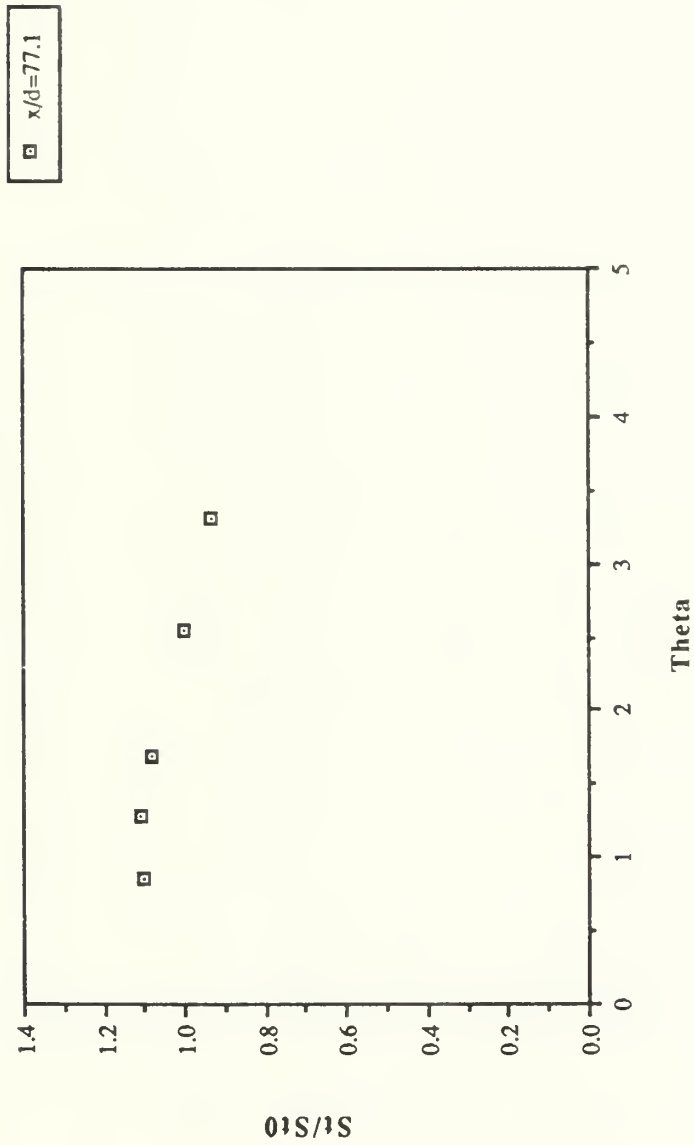


Figure 74. St/St_0 Versus θ , Compound Angle, 1 Row, $m=4.0$, $x/d=77.1$, $Z=-7.62$ cm

1 row $m=4.0$ Theta vs St/St_0 for $z=-7.62$ cm

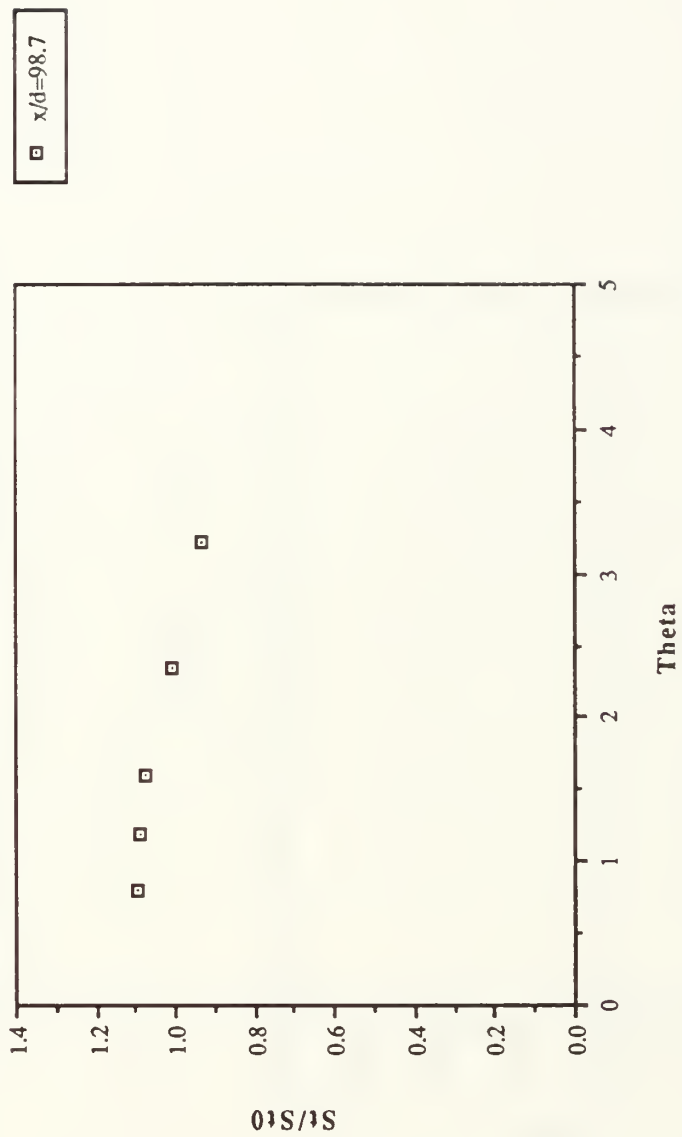


Figure 75. St/St_0 Versus θ , Compound Angle, 1 Row, $m=4.0$, $x/d=98.7$, $Z=-7.62$ cm

spanwise avg. η vs x/d for 1 row $m=4.0$

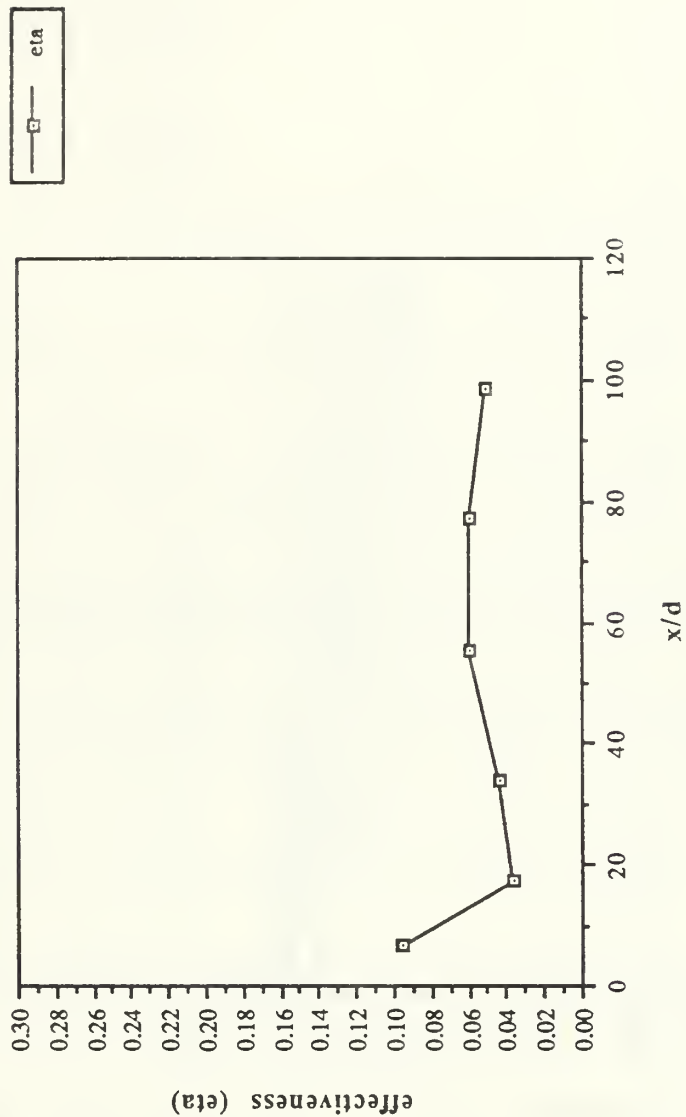


Figure 76. $\bar{\eta}$ Versus x/d , Compound Angle, 1 Row, $m=4.0$, Spanwise Average

Reynolds vs Stanton nr. for 1 row $m=4.0$

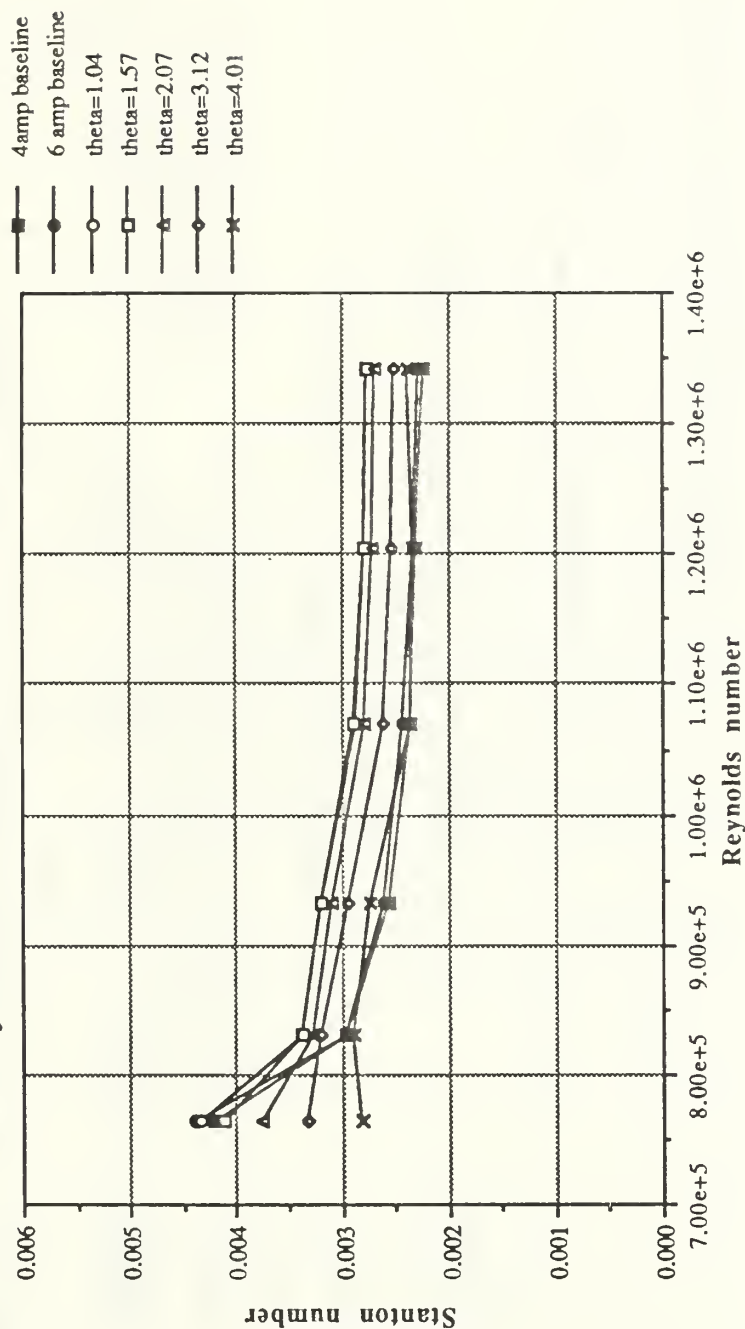


Figure 78. Spanwise Averaged Stanton Number Versus Reynolds Number, Comparison of Different θ Values and Baselines, 1 Row, $m=4.0$

FILM-COOLING EFFECTIVENESS

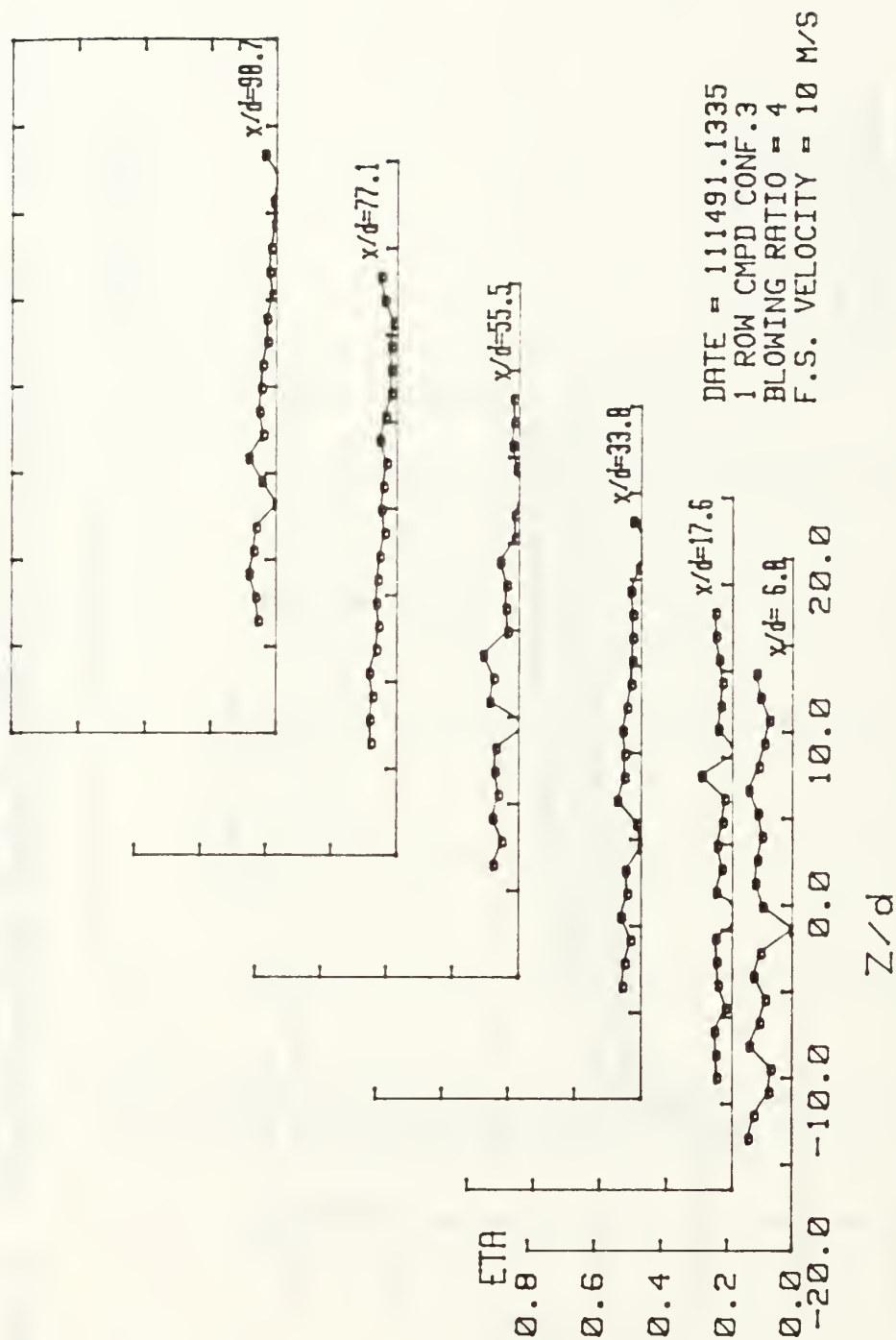


Figure 79. Spanwise Variation of η , Compound Angle, 1 Row, $m=4.0$

ISO-ENERGETIC STANTON # RATIO

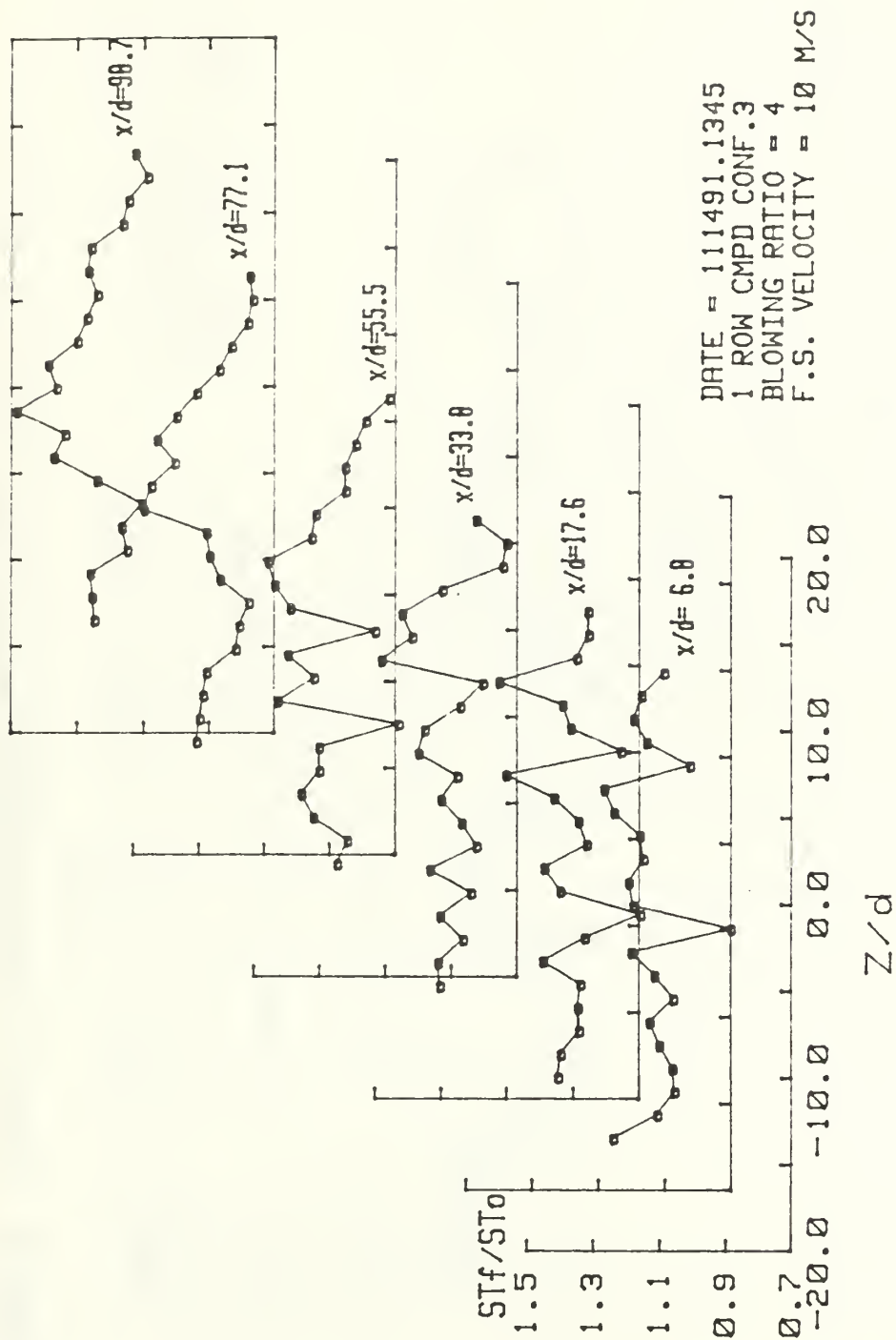


Figure 80. Spanwise Variation of St_f/St_0 , Compound Angle, 1 Row, $m=4.0$

STANTON NUMBER RATIOS

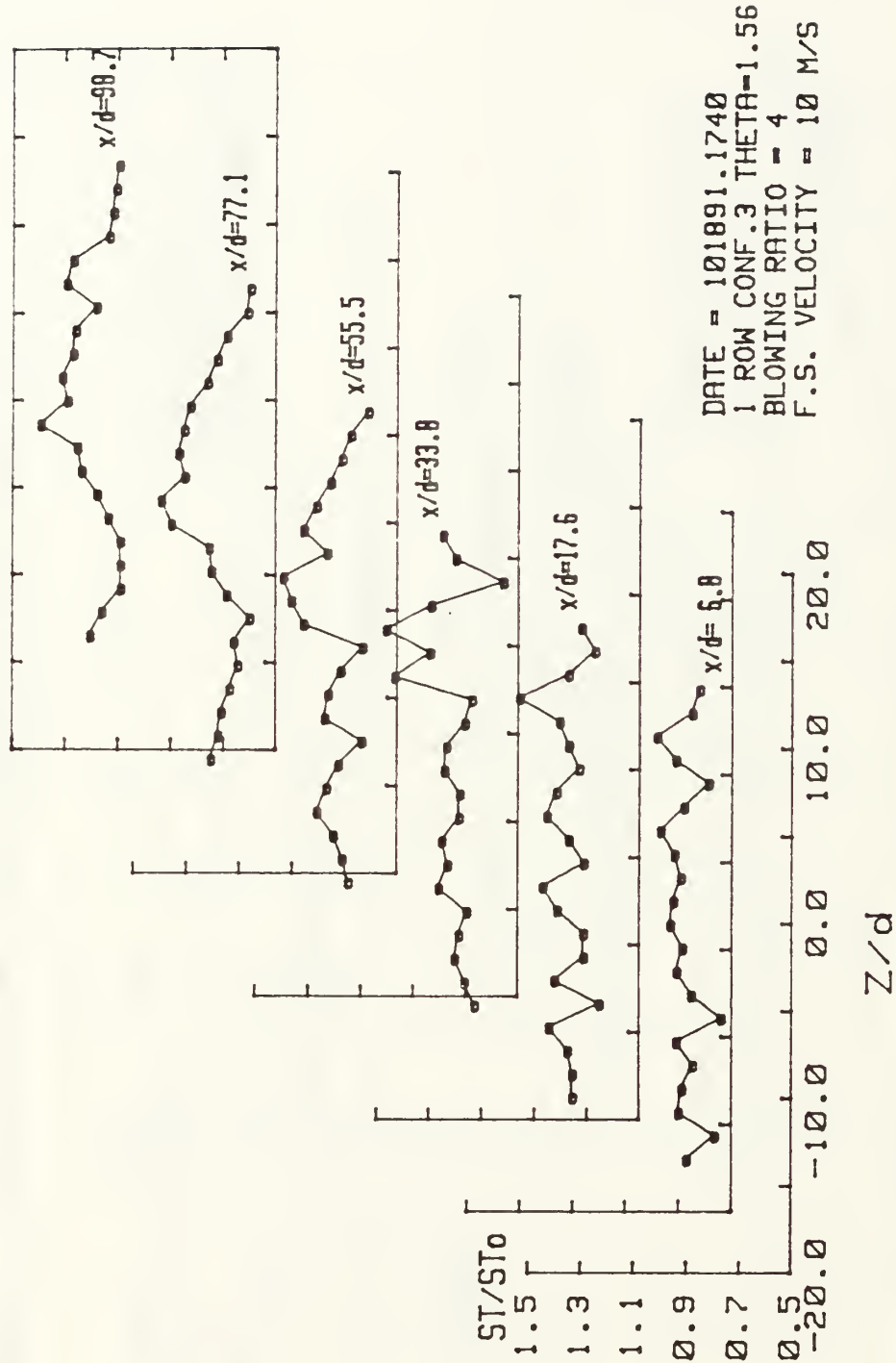
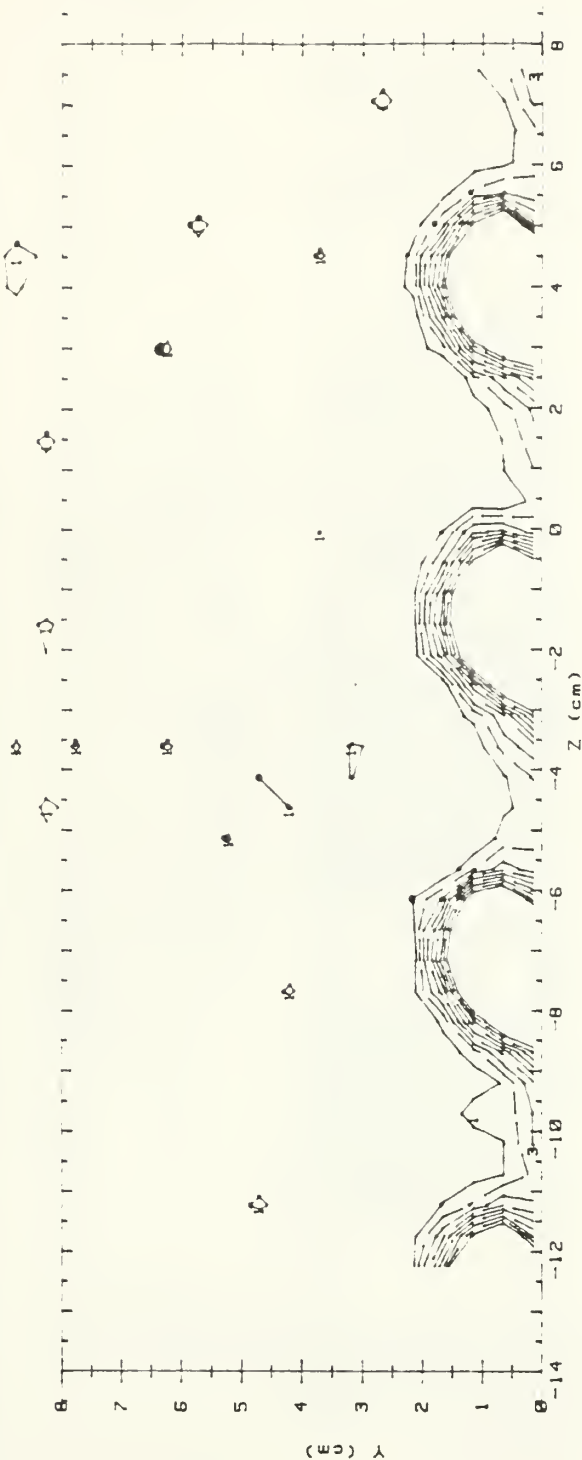


Figure 81. Spanwise Variation of St/St_0 , Compound Angle, 1 Row, $m=4.0$, $\theta=1.56$

RUN #92291.1355

T - Tfs



T - Tfs (CELCIUS) RANGES 1 ROW M=1.5 X/D=9.9

0 :	< .5	5 :	2.5 < 3
1 :	.5 < 1	6 :	3 < 3.5
2 :	1 < 1.5	7 :	3.5 < 4
3 :	1.5 < 2	8 :	4 < 4.5
4 :	2 < 2.5	9 :	4.5

Figure 82. Streamwise Injectant Distribution, Compound Angle, 1 Row, $m=1.5$, $x/d=9.9$

RUN #92291.0935

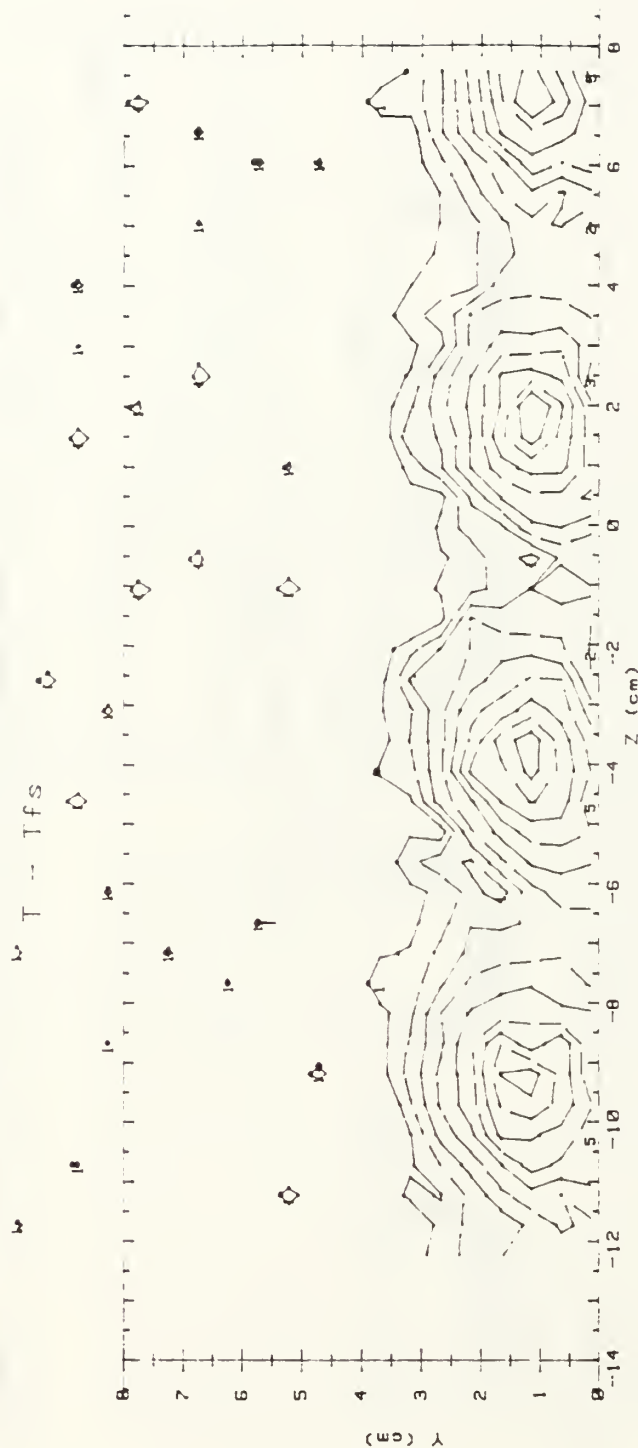
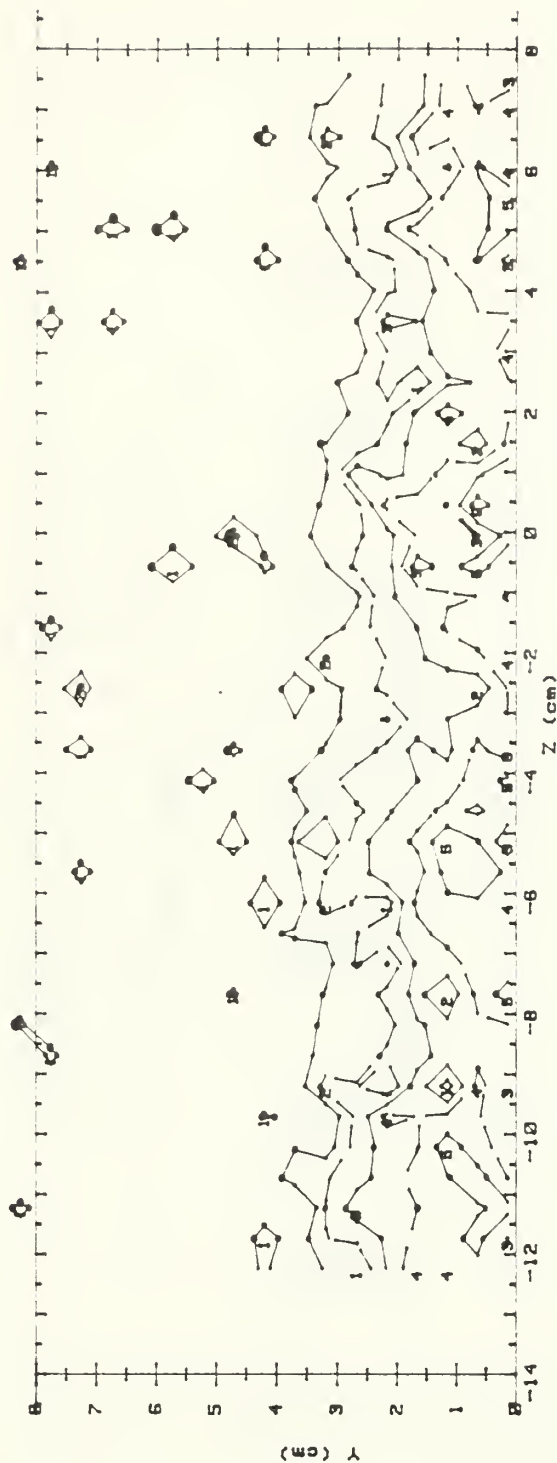


Figure 83. Streamwise Injectant Distribution, Compound Angle, 1 Row, $m=1.5$, $x/d=44.3$

RUN #91691.175

Tfs



T - Tfs (CELCIUS) RANGES 1 ROW m=1.5 x/d = 86.3

0 1	< .5	5 1	> 2.5	< 3	
1 1	> .5	< 1	6 1	> 3	< 3.5
2 1	> 1	< 1.5	7 1	> 3.5	< 4
3 1	> 1.5	< 2	8 1	> 4	< 4.5
4 1	> 2	< 2.5	8 1	> 4.5	

Figure 84. Streamwise Injectant Distribution, Compound Angle, 1 Row, m=1.5, x/d=86.3

RUN #92291.1825

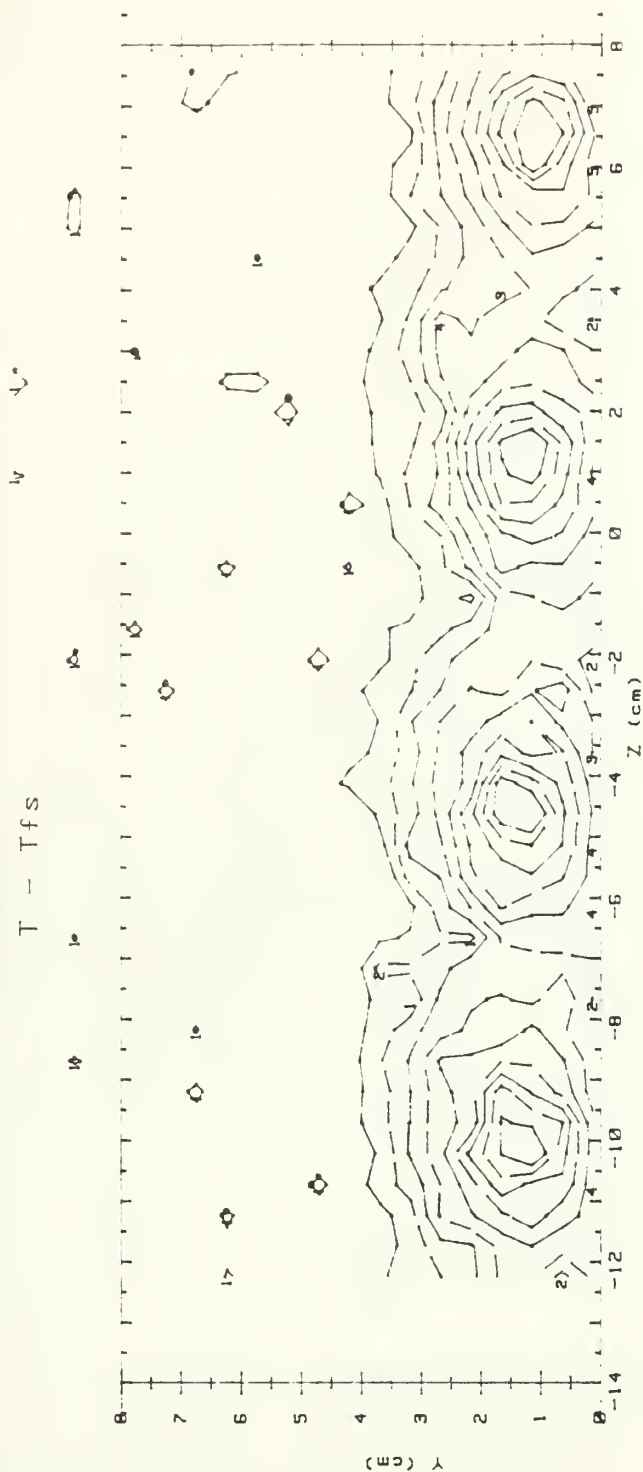
T - Tfs



T - Tfs (CELCIUS) RANGES				ROW	M=2.0	X/D=9.9
0 :	< .5			5 :	2.5 < 3	
1 :	.5 < 1			6 :	3 < 3.5	
2 :	1 < 1.5			7 :	3.5 < 4	
3 :	1.5 < 2			8 :	4 < 4.5	
4 :	2 < 2.5			9 :	4.5	

Figure 85. Streamwise Injectant Distribution, Compound Angle, 1 Row, $m=2.0$, $x/d=9.9$

RUN #92191.204



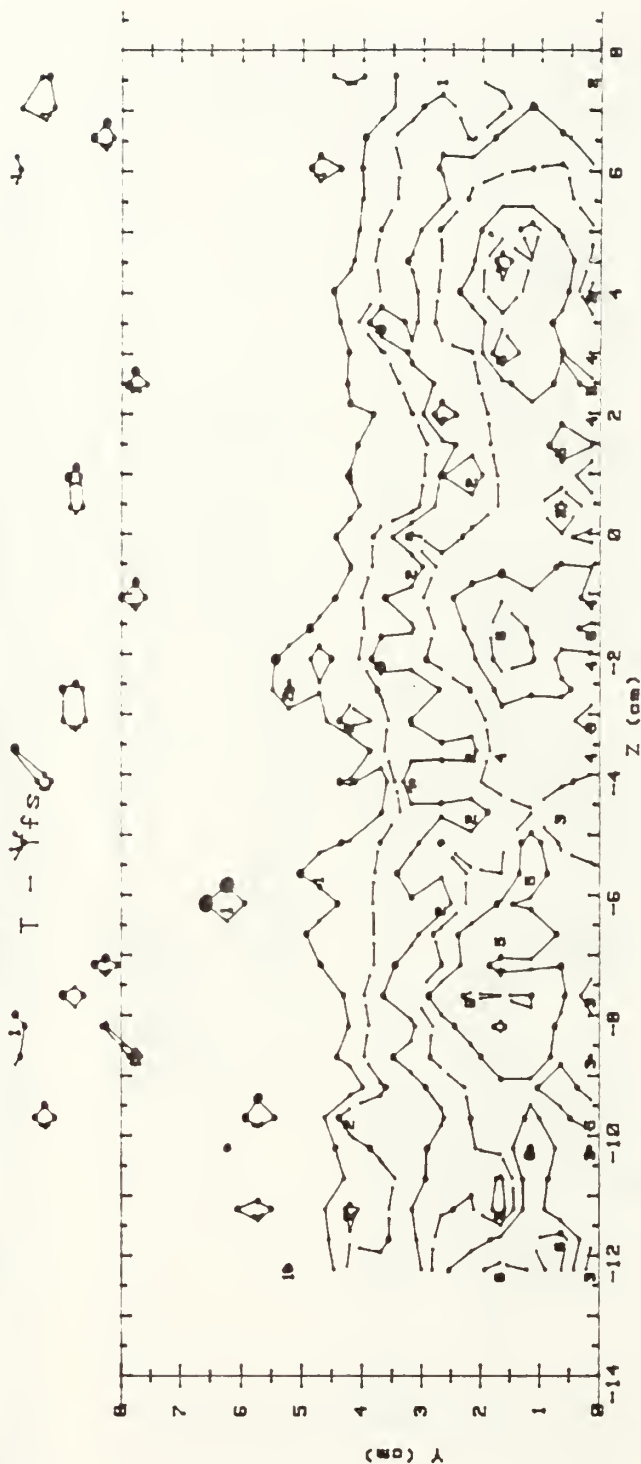
T - Tfs (CELCIUS) RANGES 1 ROW M=2.0 X/D=44.3

0 :	< .5	5 :	2.5 < 3
1 :	.5 < 1	6 :	3 < 3.5
2 :	1 < 1.5	7 :	3.5 < 4
3 :	1.5 < 2	8 :	4 < 4.5
4 :	2 < 2.5	9 :	4.5

Figure 86. Streamwise Injectant Distribution, Compound Angle, 1 Row, $m=2.0$, $x/d=44.3$

RUN #91791.1155

T - γ_{fs}



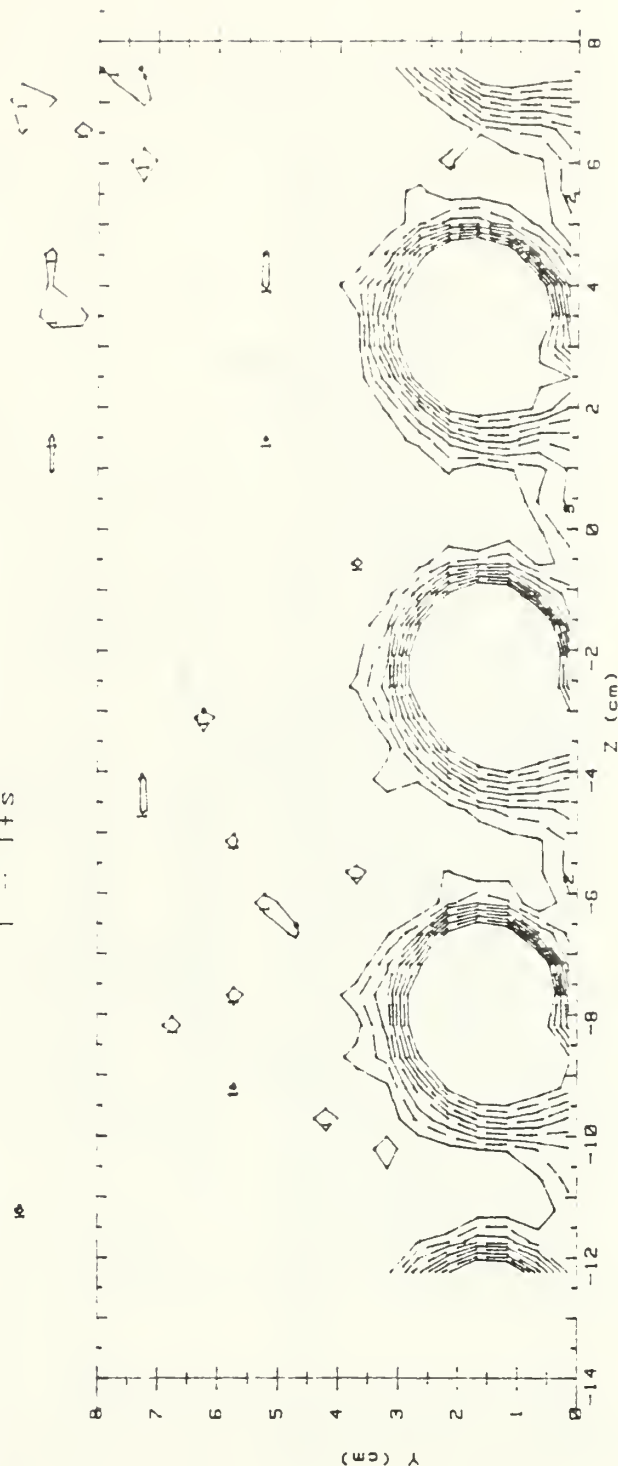
T - Tfe(CELCIUS) RANGES 1 ROW m=2.0 x/d = 86.3

0 1	< .5	5 1	2.5 < 3
1 1	.5 < 1	6 1	3 < 3.5
2 1	1 < 1.5	7 1	3.5 < 4
3 1	1.5 < 2	8 1	4 < 4.5
4 1	2 < 2.5	8 1	4.5

Figure 87. Streamwise Injectant Distribution, Compound Angle, 1 Row, $m=2.0$, $x/d=86.3$

RUN #92391.0915

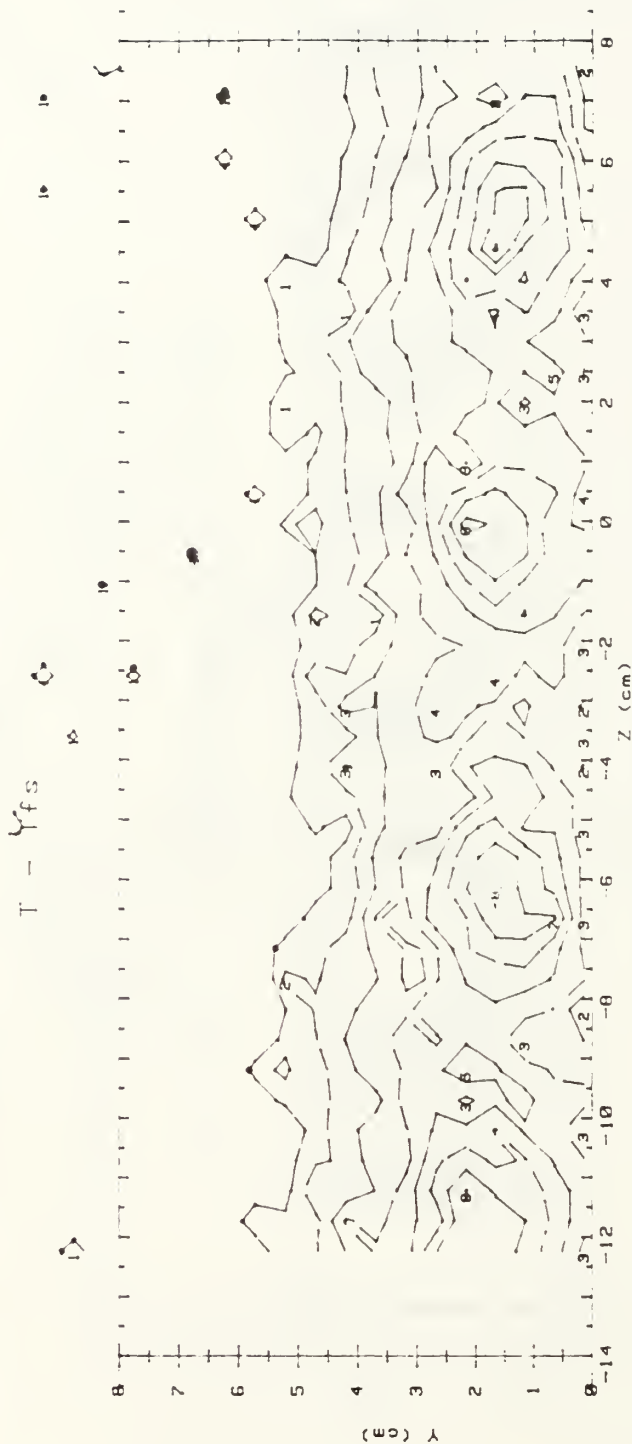
T - Tfs



T - Tfs (CELCIUS) RANGES					1	ROW	M=3.0	X/D=9.9
0 :		< .5			5 :	2.5	< 3	
1 :	.5	< 1			6 :	3	< 3.5	
2 :	1	< 1.5			7 :	3.5	< 4	
3 :	1.5	< 2			8 :	4	< 4.5	
4 :	2	< 2.5			9 :	4.5		

Figure 88. Streamwise Injectant Distribution, Compound Angle, 1 Row, $m=3.0$, $x/d=9.9$

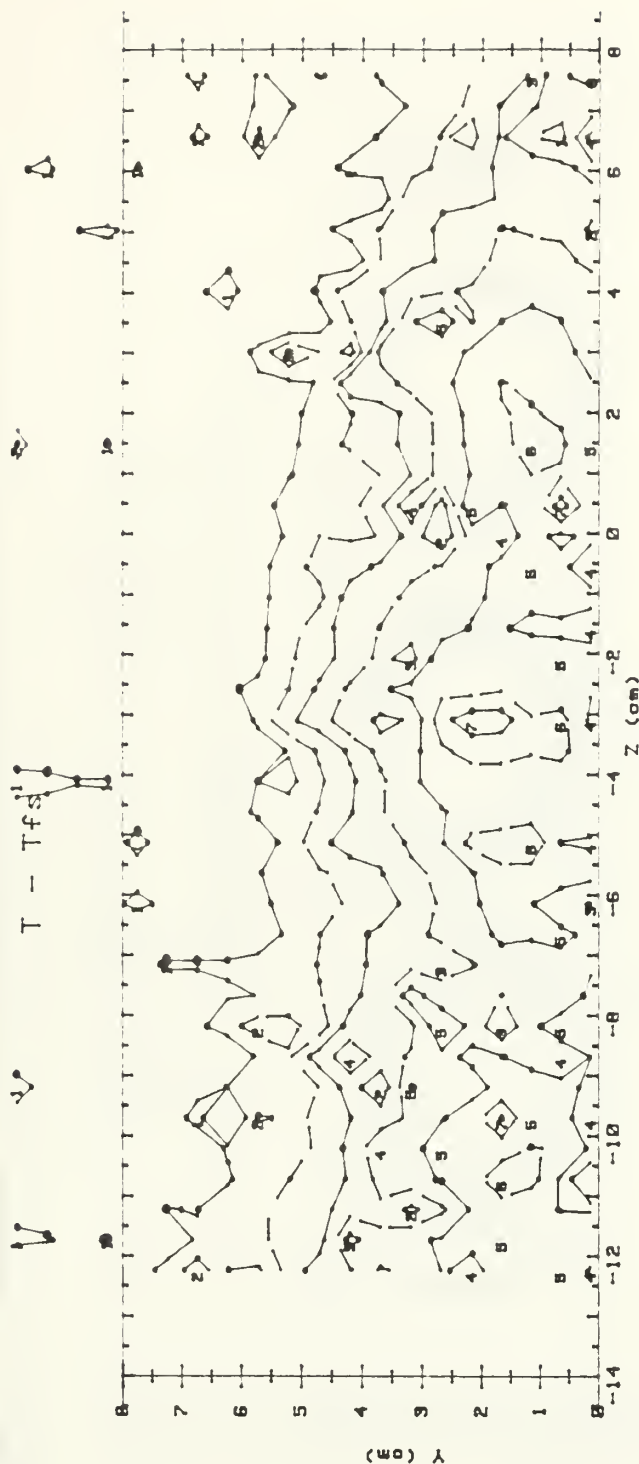
RUN #92191.15



$T - T_{fs}(\text{CELCIUS})$ RANGES			
0 :	< .5	5 :	> 2.5 < 3
1 :	.5 < 1	6 :	> 3 < 3.5
2 :	1 < 1.5	7 :	> 3.5 < 4
3 :	1.5 < 2	8 :	> 4 < 4.5
4 :	2 < 2.5	9 :	> 4.5

Figure 89. Streamwise Injectant Distribution, Compound Angle, 1 Row, $m=3.0$, $x/d=44.3$

RUN #91891.11



T - Tfs (CELCIUS) RANGES 1 ROW M=9.0 X/D=86.3

0 :	< .5	5 :	2.5 < 3
1 :	.5 < 1	6 :	3 < 3.5
2 :	1 < 1.5	7 :	3.5 < 4
3 :	1.5 < 2	8 :	4 < 4.5
4 :	2 < 2.5	9 :	4.5

Figure 90. Streamwise Injectant Distribution, Compound Angle, 1 Row, $m=3.0$, $x/d=86.3$

RUN #92391.152

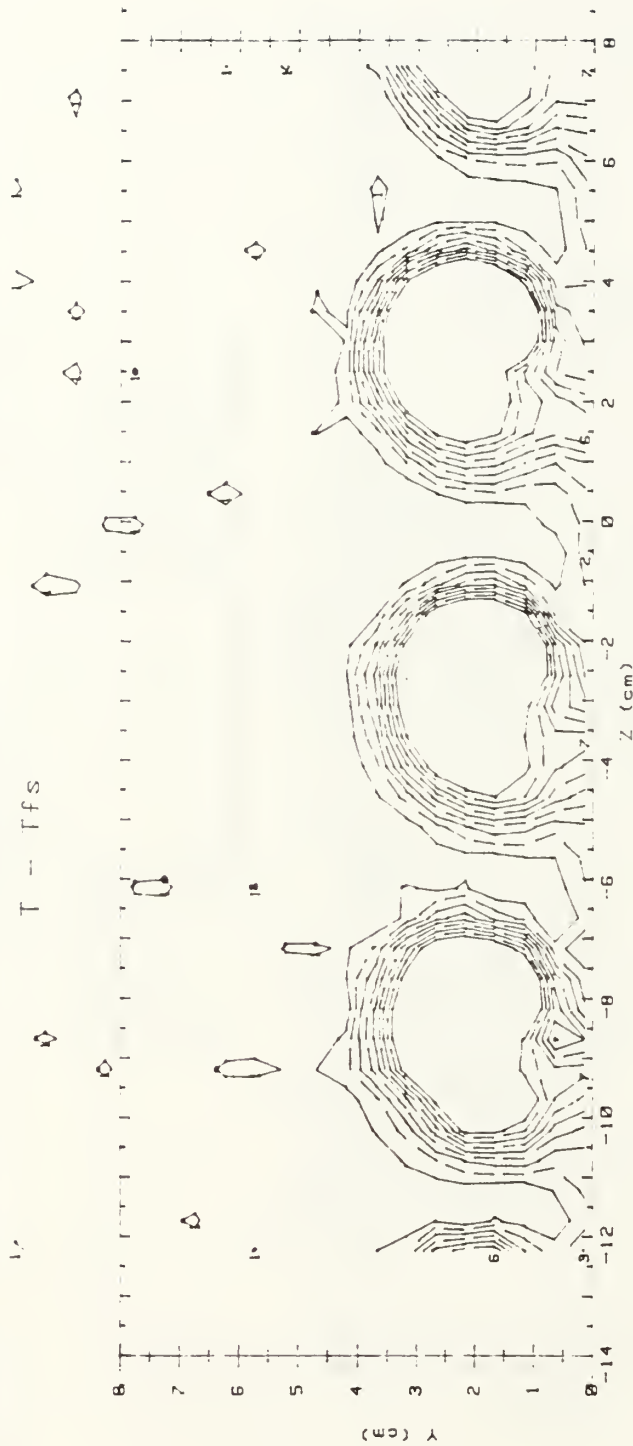
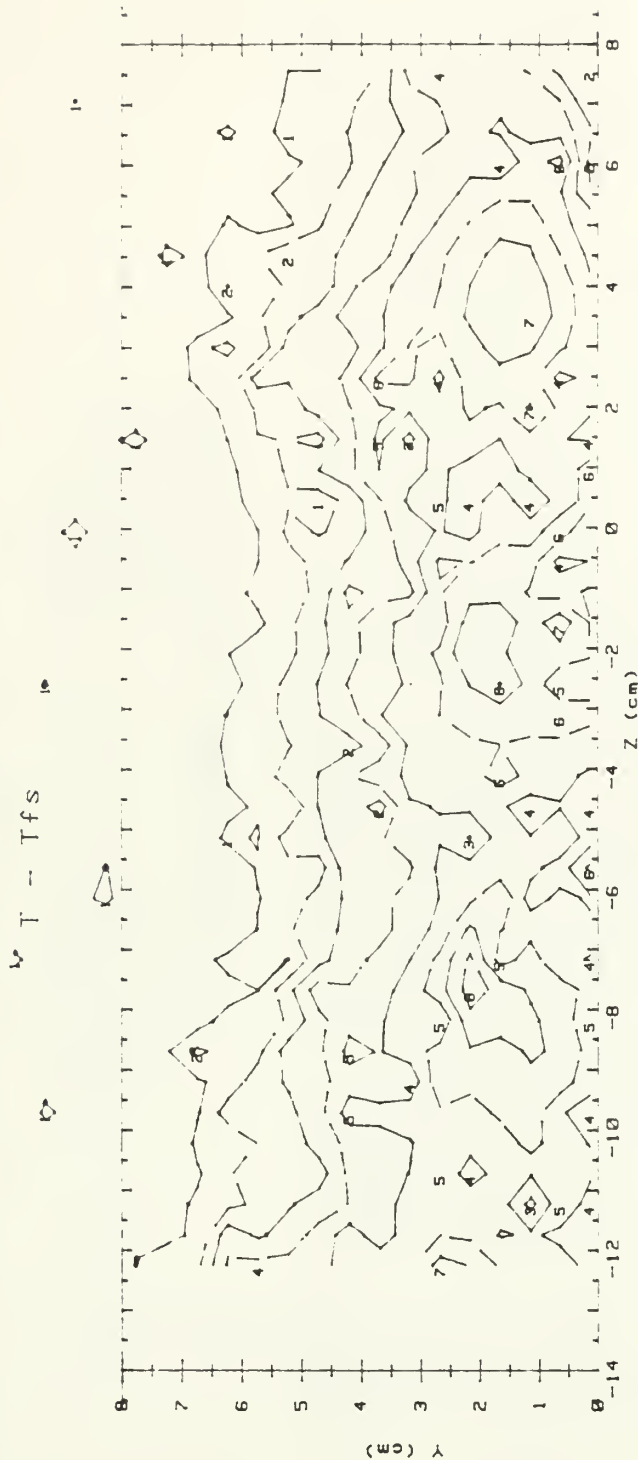


Figure 91. Streamwise Injectant Distribution, Compound Angle, 1 Row, $m=4.0$, $x/d=9.9$

RUN #92191.0945

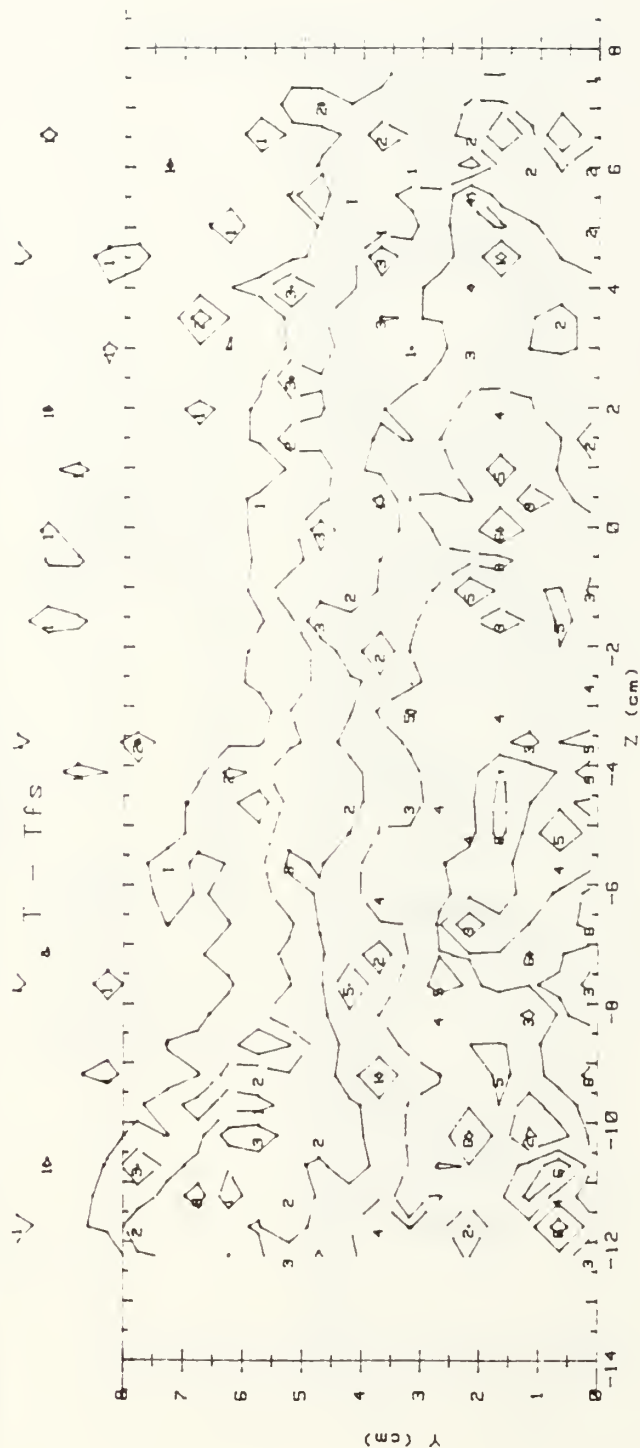


T - Tfs (CELCIUS) RANGES 1 ROW M=4.0 X/D=44.3

0 :	< .5	5 :	2.5 < 3
1 :	.5 < 1	6 :	3 < 3.5
2 :	1 < 1.5	7 :	3.5 < 4
3 :	1.5 < 2	8 :	4 < 4.5
4 :	2 < 2.5	9 :	4.5

Figure 92. Streamwise Injectant Distribution, Compound Angle, 1 Row, $m=4.0$, $x/d=44.3$

RUN #91891.1905



T - Tfs (CELCIUS) RANGES 1 ROW M=4.0 X/D=86.3

0 :	< .5	5 :	2.5 < 3
1 :	.5 < 1	6 :	3 < 3.5
2 :	1 < 1.5	7 :	3.5 < 4
3 :	1.5 < 2	8 :	4 < 4.5
4 :	2 < 2.5	9 :	4.5

Figure 93. Streamwise Injectant Distribution, Compound Angle, 1 Row, $m=4.0$, $x/d=86.3$

RUN #101391.19

Ux



Figure 94. Streamwise Velocity Field, Compound Angle, 1 Row, $m=1.5$, $x/d=9.9$



Figure 95. Streamwise Velocity Field, Compound Angle, 1 Row, $m=1.5$, $x/d=44.3$

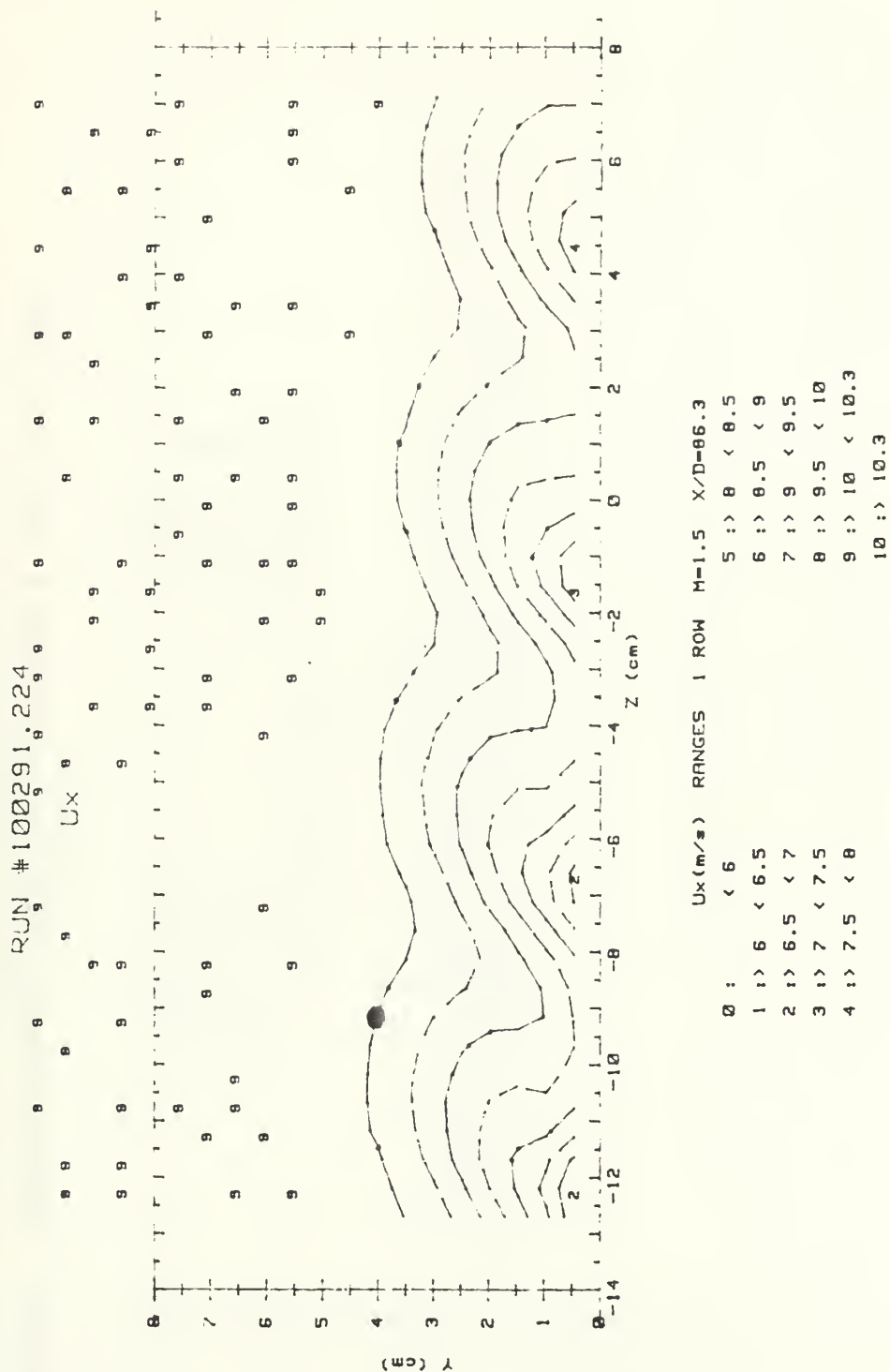


Figure 96. Streamwise Velocity Field, Compound Angle, 1 Row, $m=1.5$, $x/d=86.3$

RUN #101391.19

Ptotal

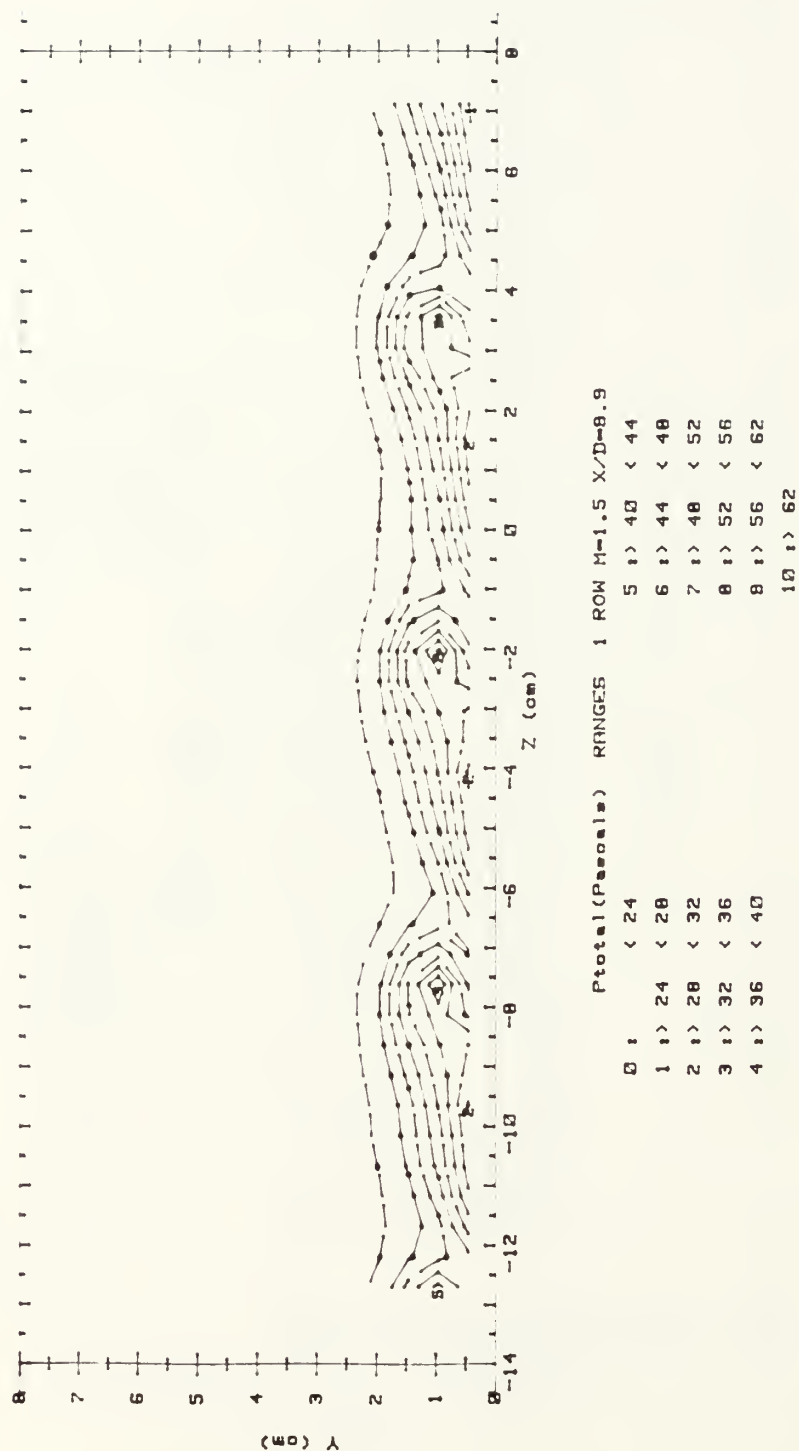


Figure 97. Streamwise Pressure Field, Compound Angle, 1 Row, $m=1.5$, $x/d=9.9$

RUN #100891.21

Ptotal

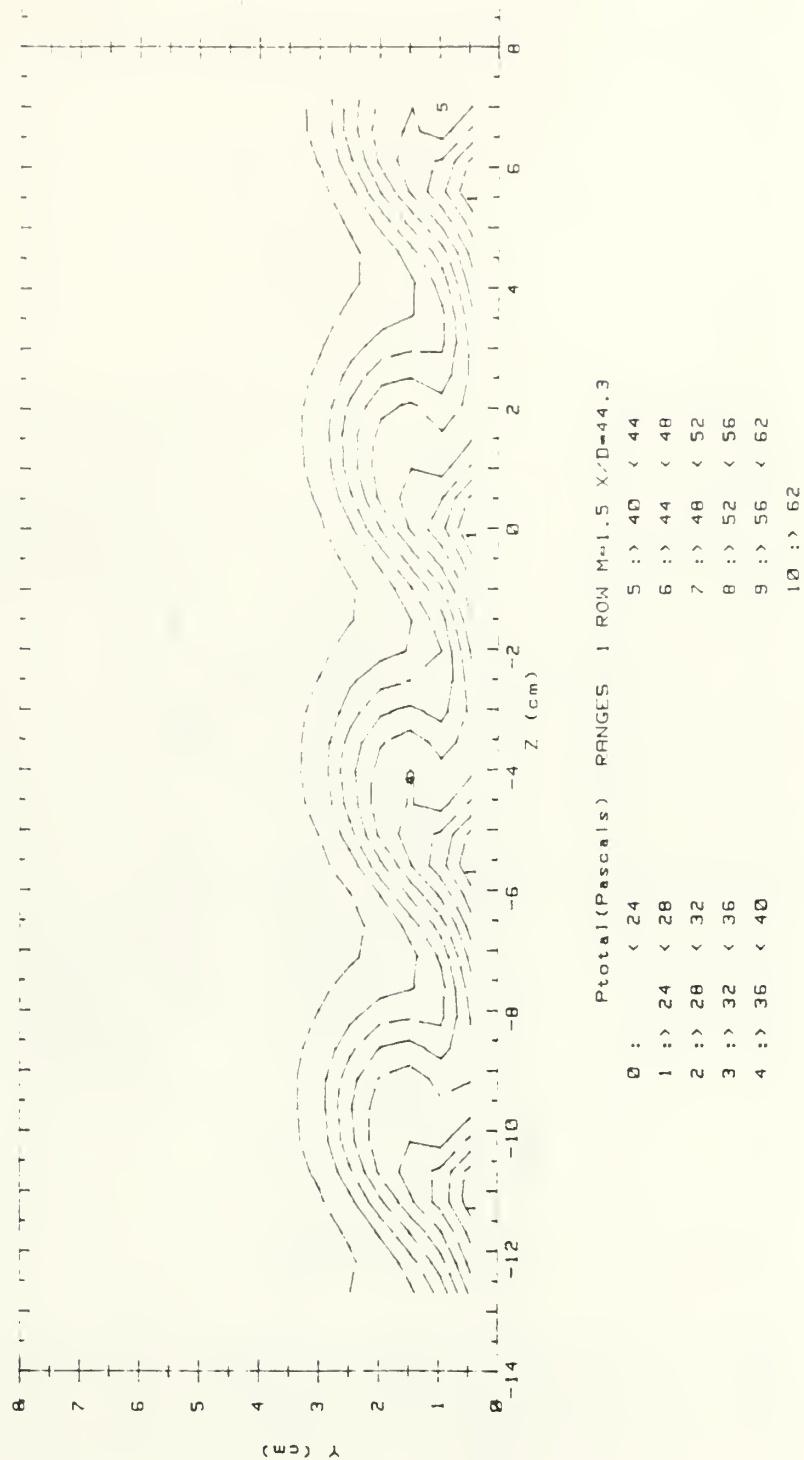


Figure 98. Streamwise Pressure Field, Compound Angle, 1 Row, $m=1.5$, $x/d=44.3$

RUN #100291.224

Ptotal

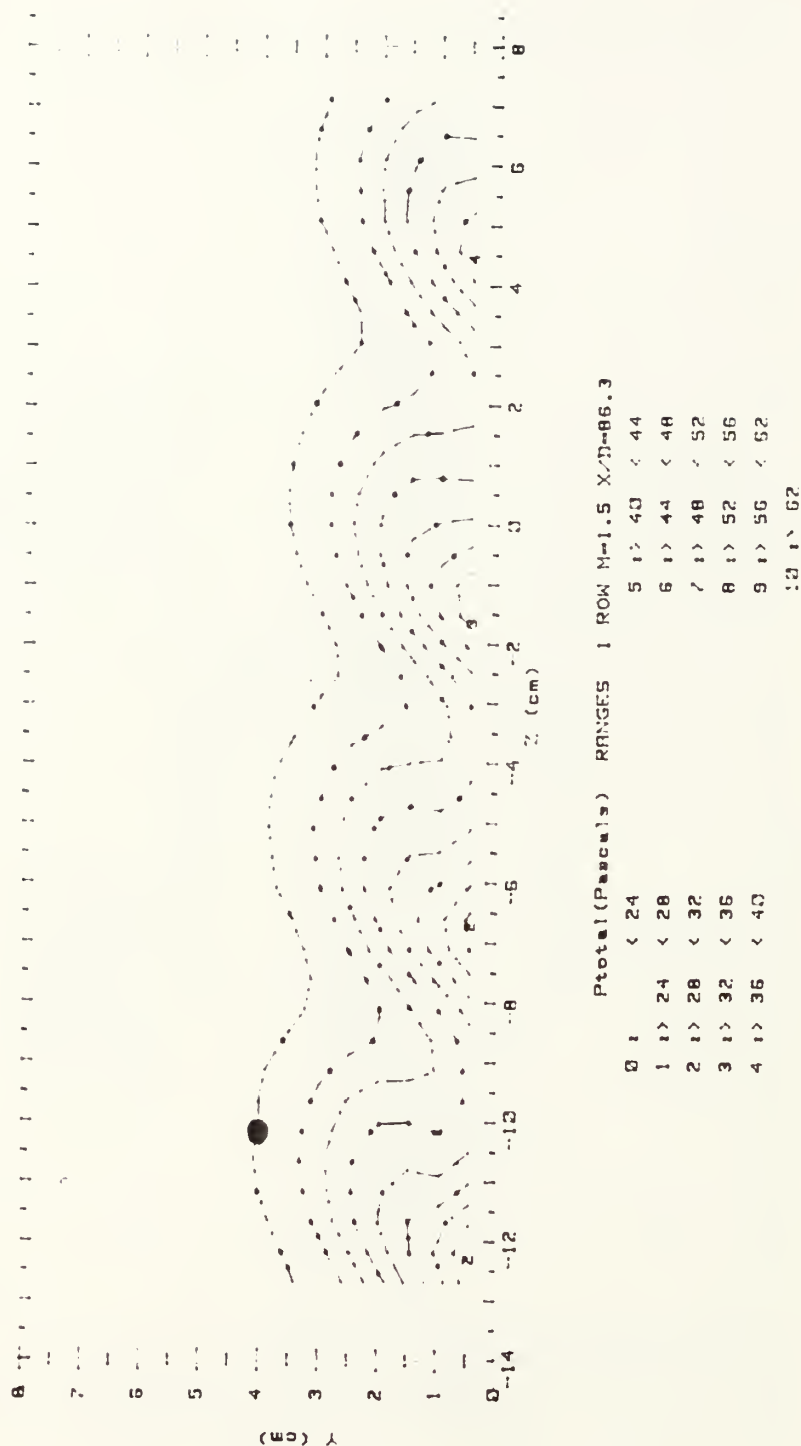


Figure 99. Streamwise Pressure Field, Compound Angle, 1 Row, $m=1.5$, $x/d=86.3$

2001 101391.082

Ux



Figure 100. Streamwise Velocity Field, Compound Angle, 1 Row, $m=2.0$, $x/d=9.9$

RUN #100991.095

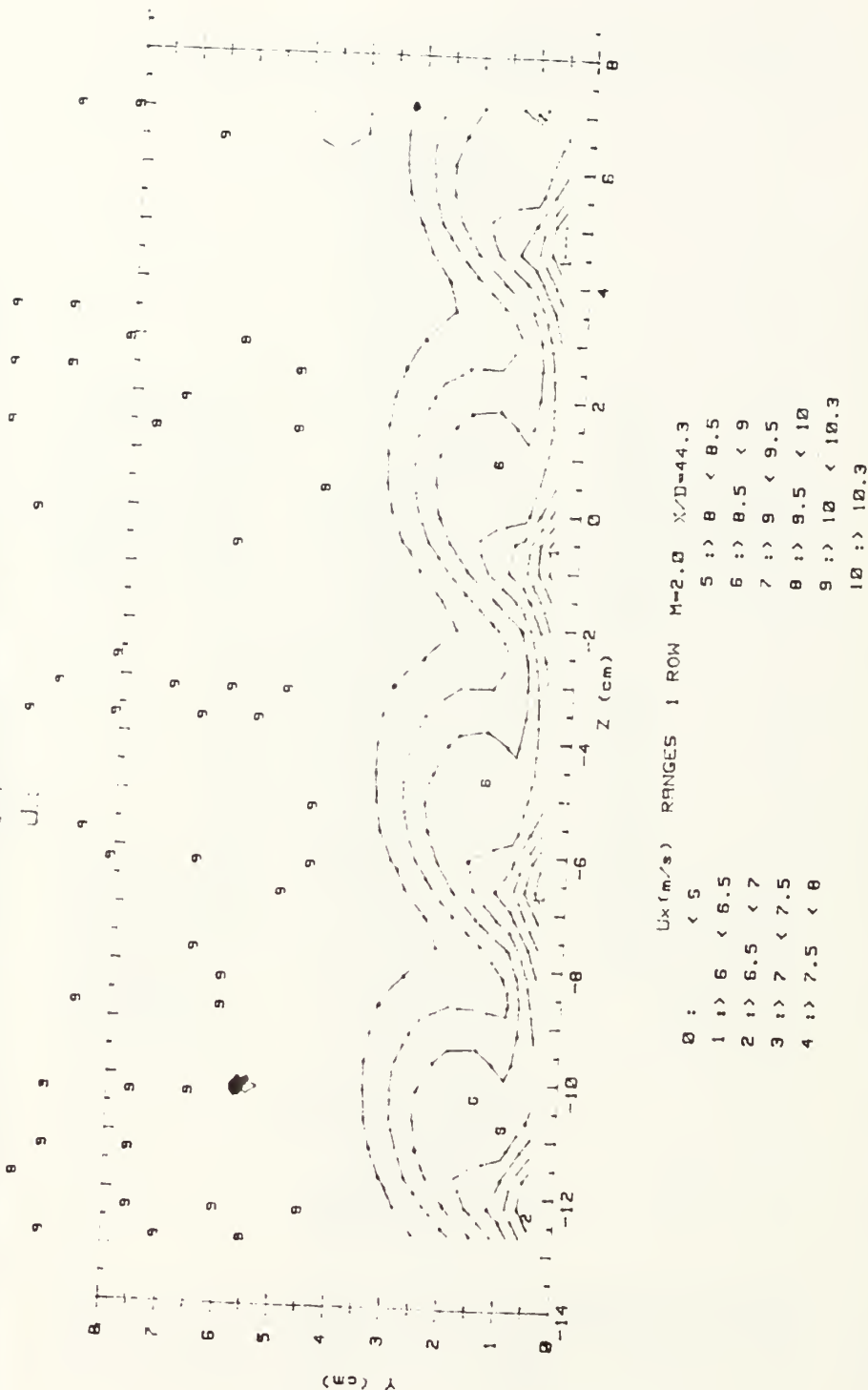
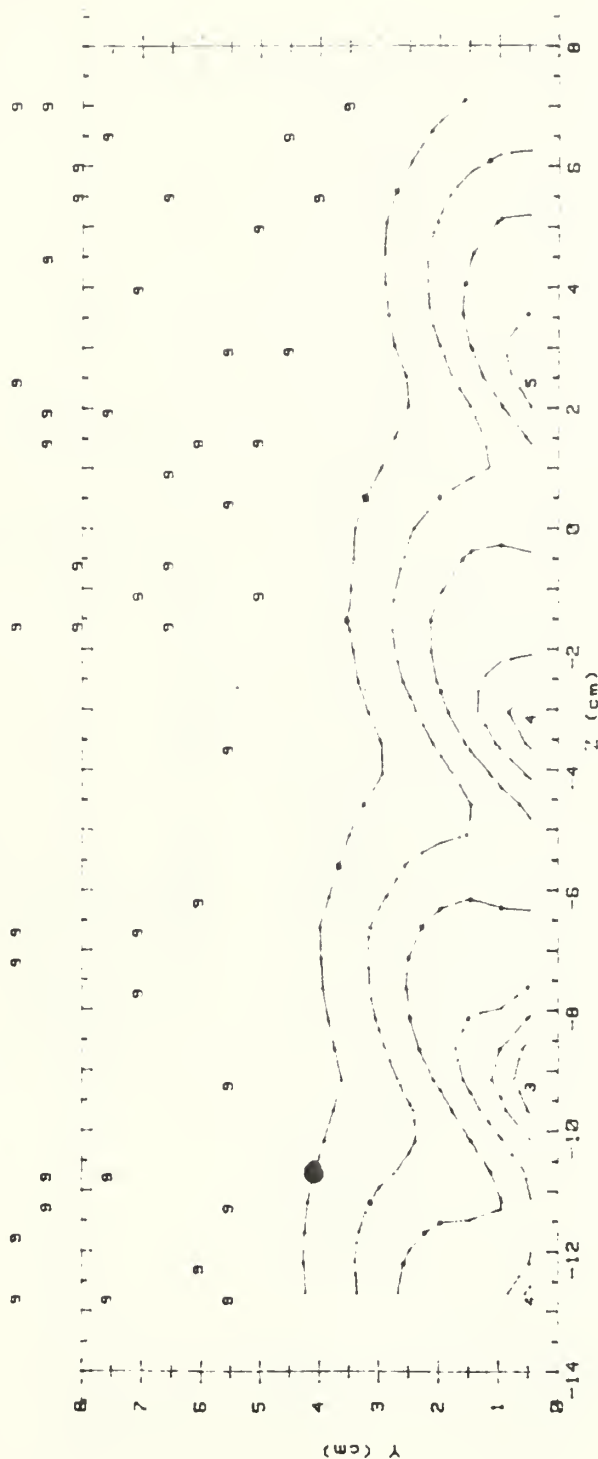


Figure 101. Streamwise Velocity Field, Compound Angle, 1 Row, $m=2.0$, $x/d=44.3$

RUN #100391.1015

UX



U_x (m/s) RANGES 1 ROW $M=2.0$ $X/D=86.3$
 0 : < 6
 1 : 6 < 6.5
 2 : 6.5 < 7
 3 : 7 < 7.5
 4 : 7.5 < 8
 5 : 8 < 8.5
 6 : 8.5 < 9
 7 : 9 < 9.5
 8 : 9.5 < 10
 9 : 10 < 10.3
 10 : > 10.3

Figure 102. Streamwise Velocity Field, Compound Angle, 1 Row, $m=2.0$, $x/d=86.3$

RUN #101391.082

Ptotal

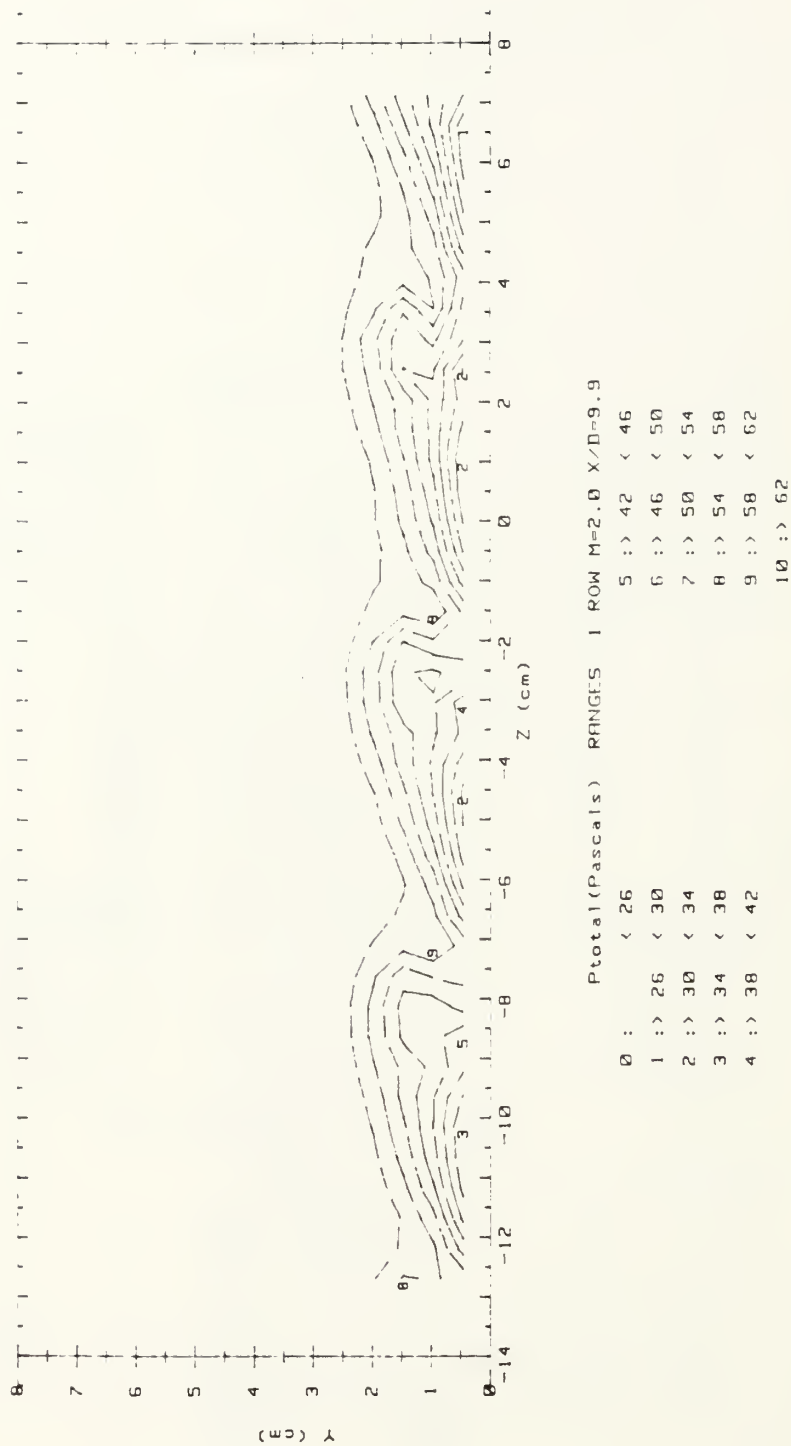


Figure 103. Streamwise Pressure Field, Compound Angle, 1 Row, $m=2.0$, $x/d=9.9$

RUN #100991.095

Ptotal

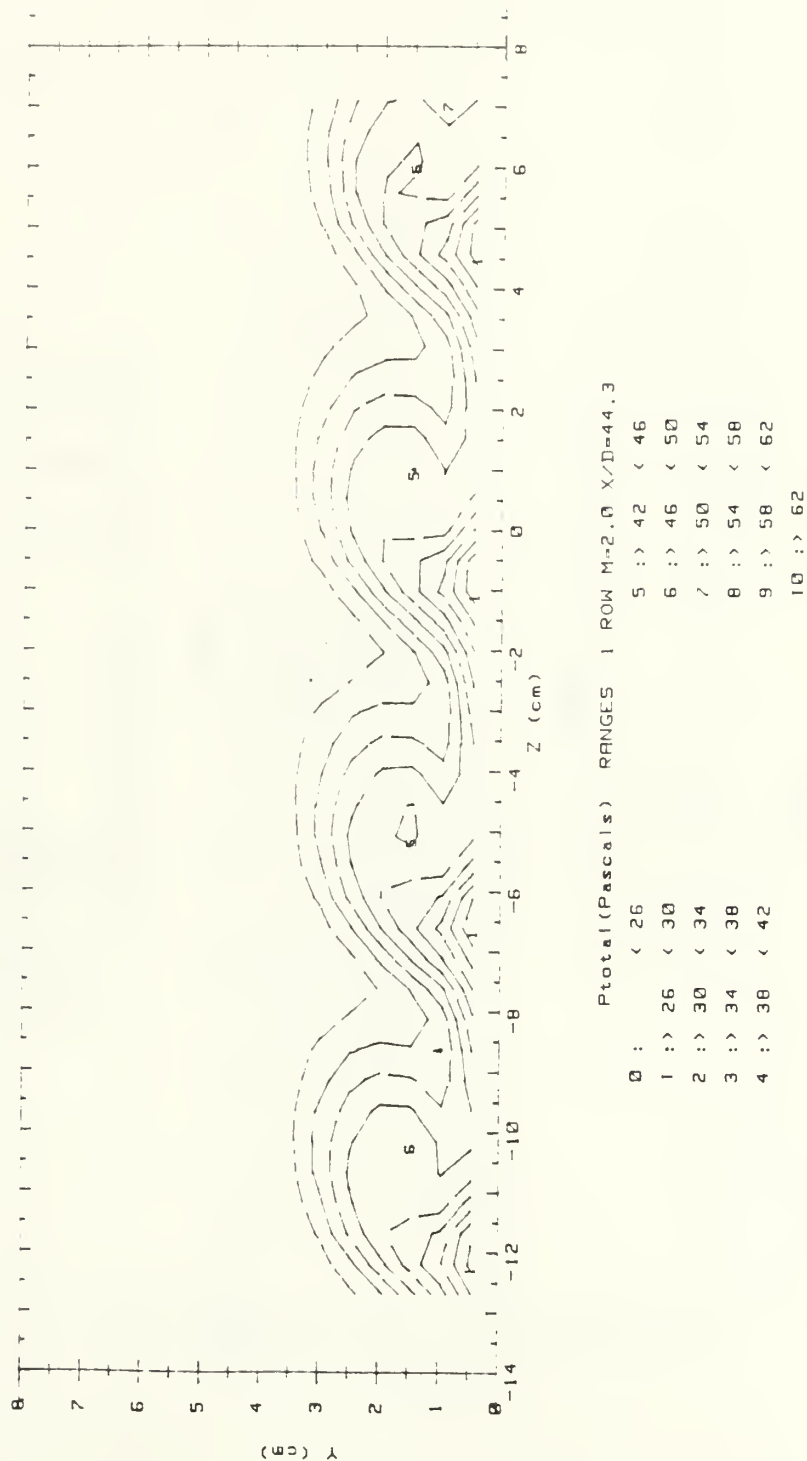


Figure 104. Streamwise Pressure Field, Compound Angle, 1 Row, $m=2.0$, $x/d=44.3$

RUN #100391.1015

Ptotal

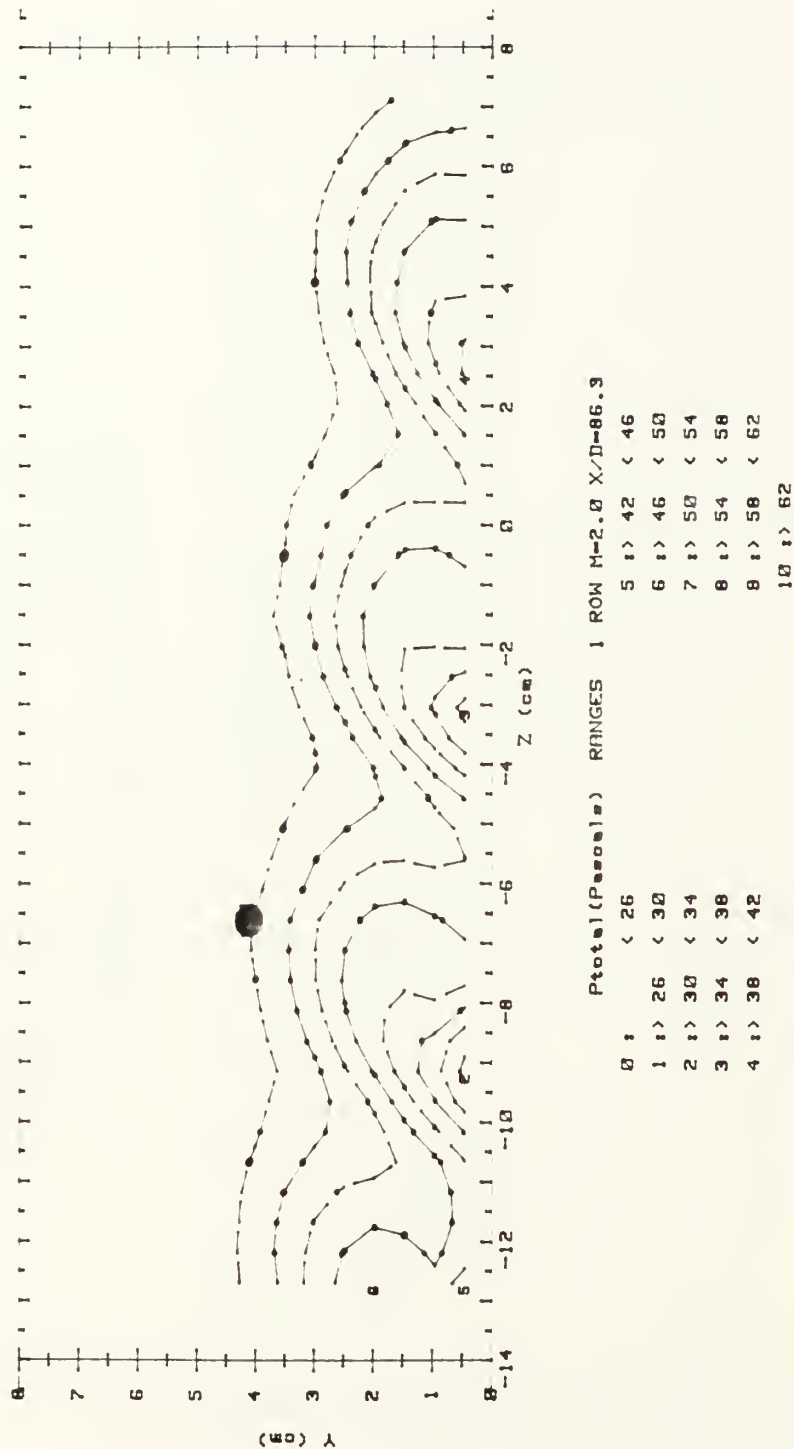


Figure 105. Streamwise Pressure Field, Compound Angle, 1 Row, $m=2.0$, $x/d=86.3$

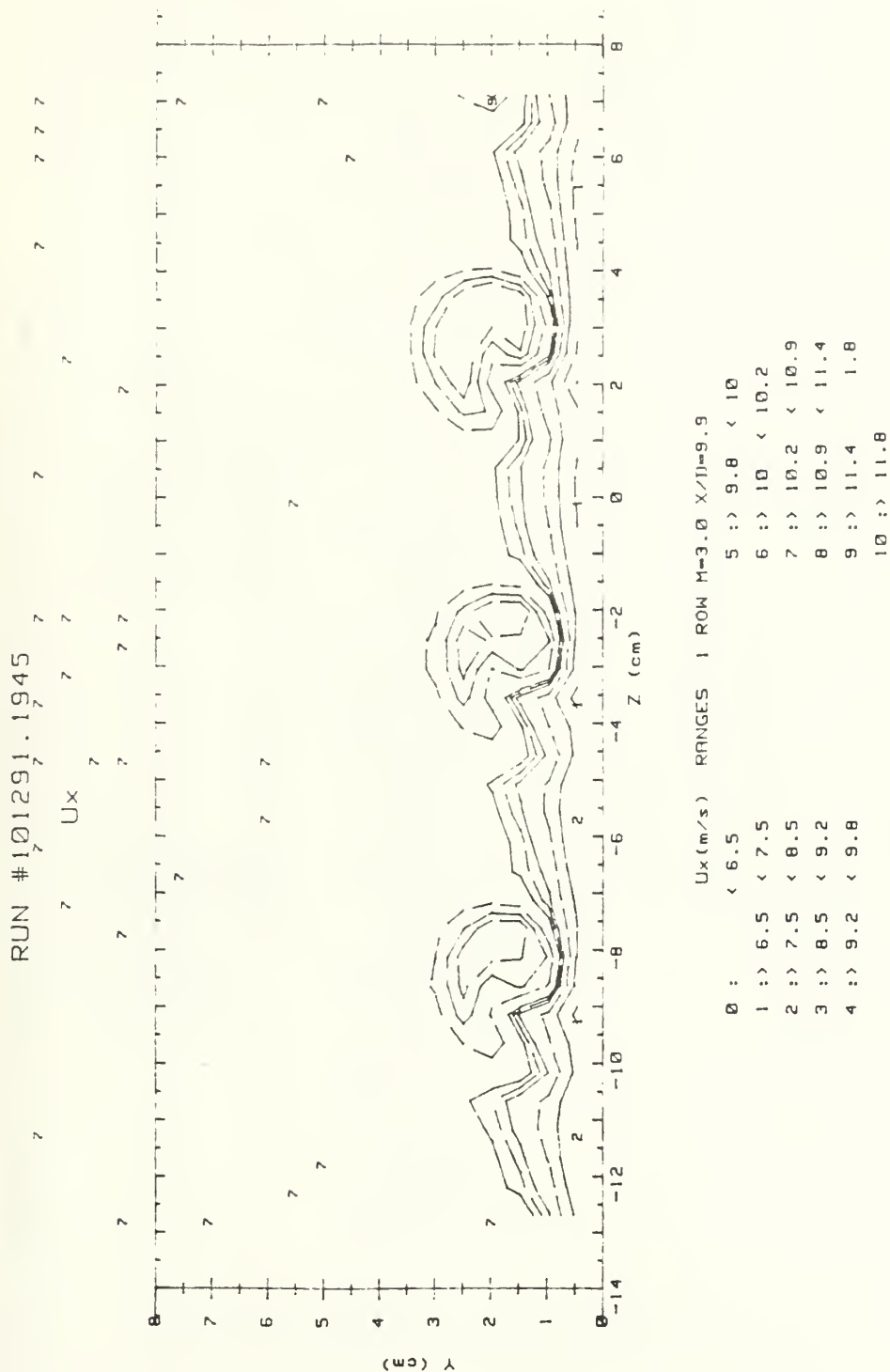
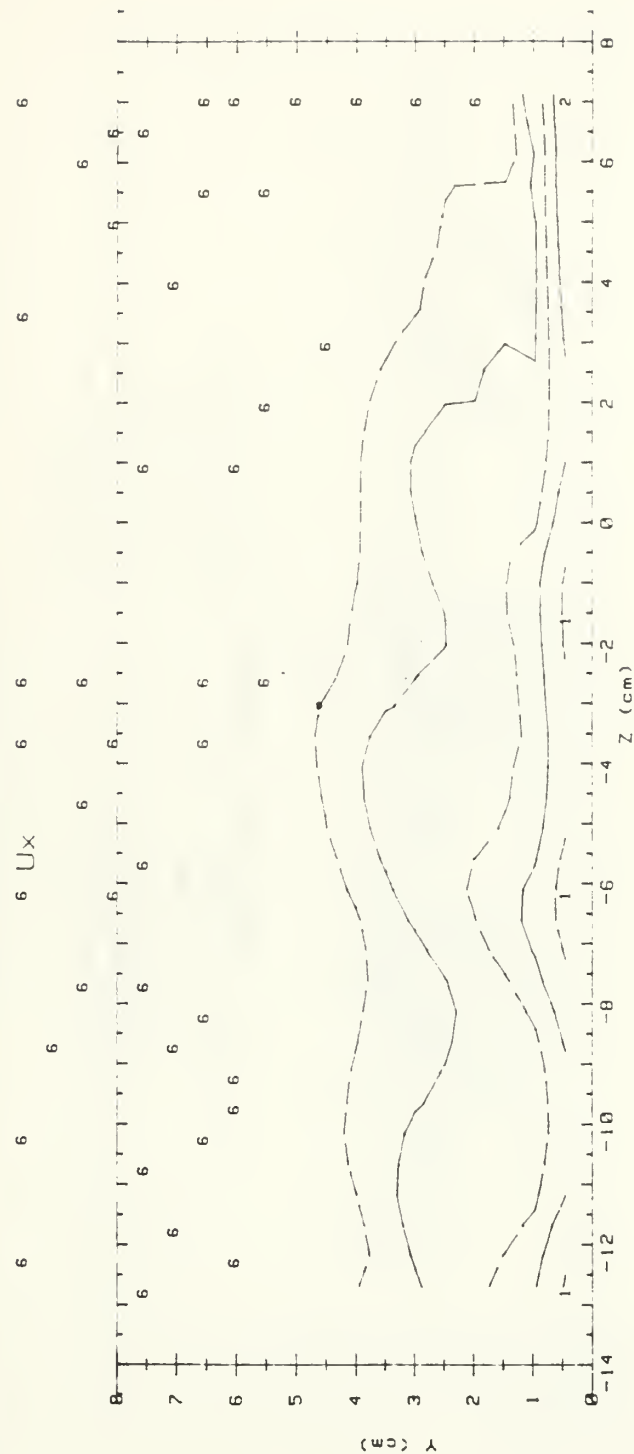


Figure 106. Streamwise Velocity Field, Compound Angle, 1 Row, $m=3.0$, $x/d=9.9$



Figure 107. Streamwise Velocity Field, Compound Angle, 1 Row, $m=3.0$, $x/d=44.3$

RUN #100891-0925



U_x (m/s) RANGES 1 ROW $M=3.0$ $X/D=86.3$

- 0 : < 6.5
- 1 :> 6.5 < 7.5
- 2 :> 7.5 < 8.5
- 3 :> 8.5 < 9.2
- 4 :> 9.2 < 9.8
- 5 :> 9.8 < 10
- 6 :> 10 < 10.2
- 7 :> 10.2 < 10.9
- 8 :> 10.9 < 11.4
- 9 :> 11.4 < 11.8
- 10 :> 11.8

Figure 108. Streamwise Velocity Field, Compound Angle, 1 Row, $m=3.0$, $x/d=86.3$

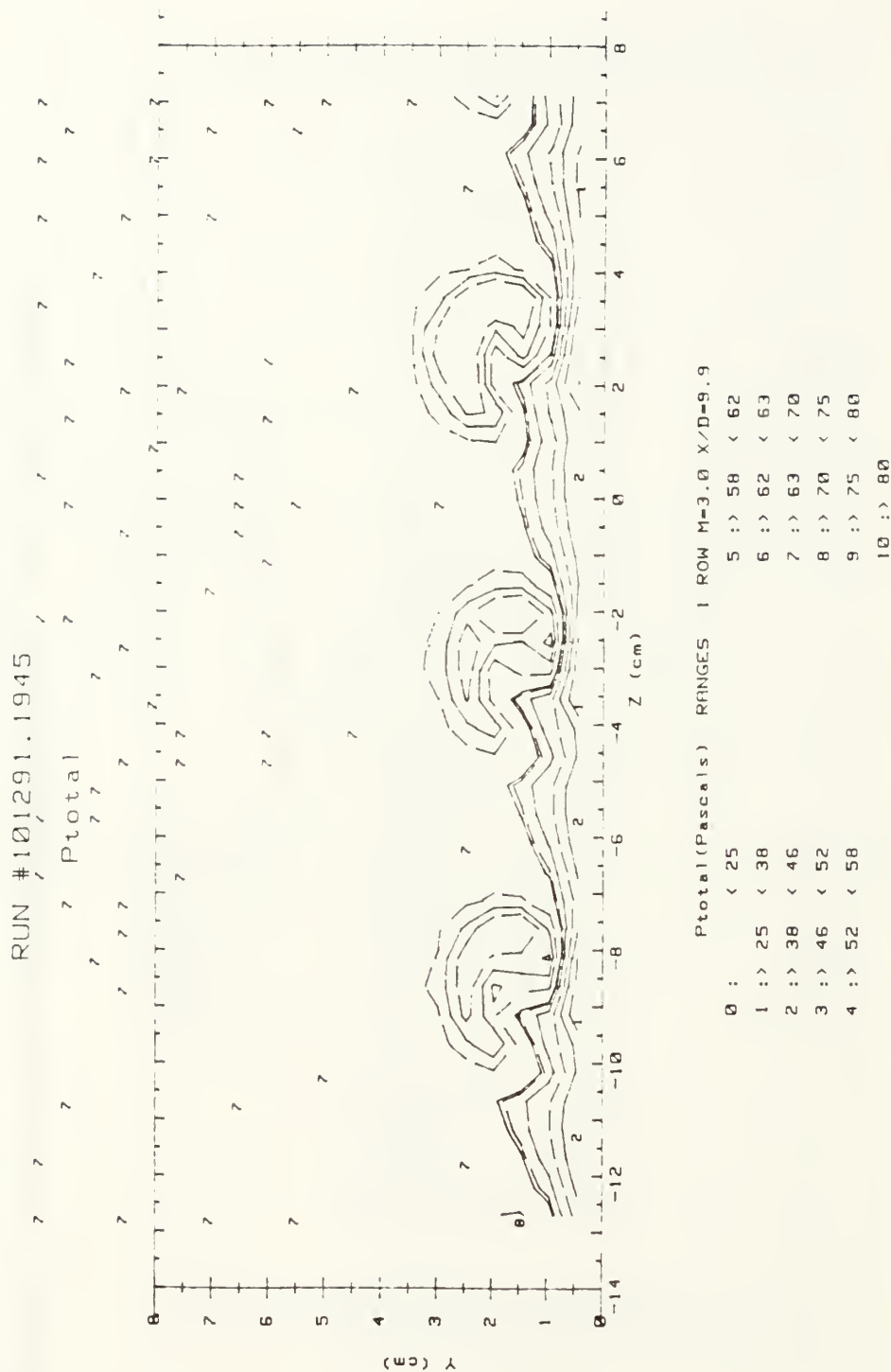


Figure 109. Streamwise Pressure Field, Compound Angle, 1 Row, $m=3.0$, $x/d=9.9$

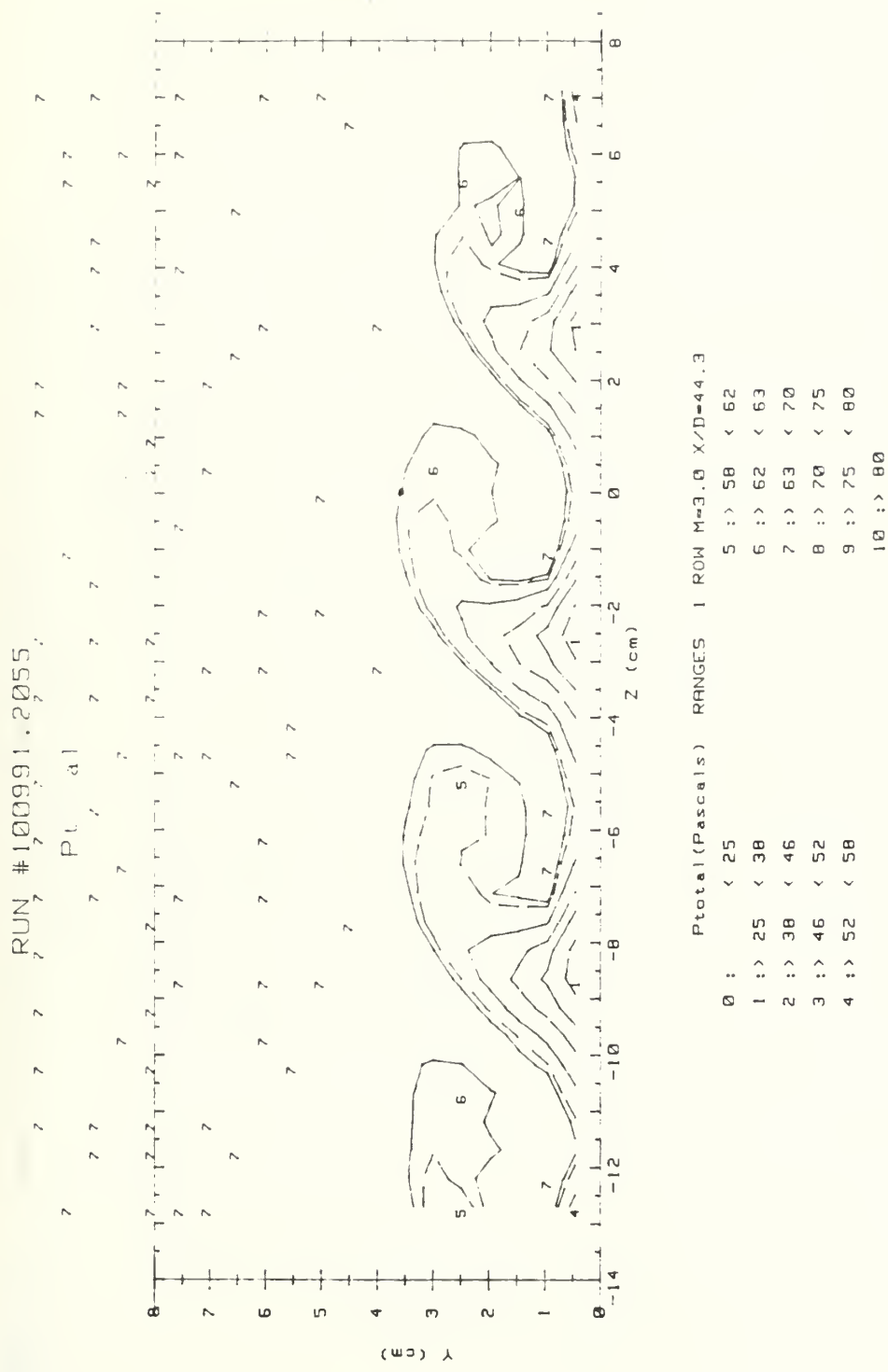


Figure 110. Streamwise Pressure Field, Compound Angle, 1 Row, $m=3.0$, $x/d=44.3$

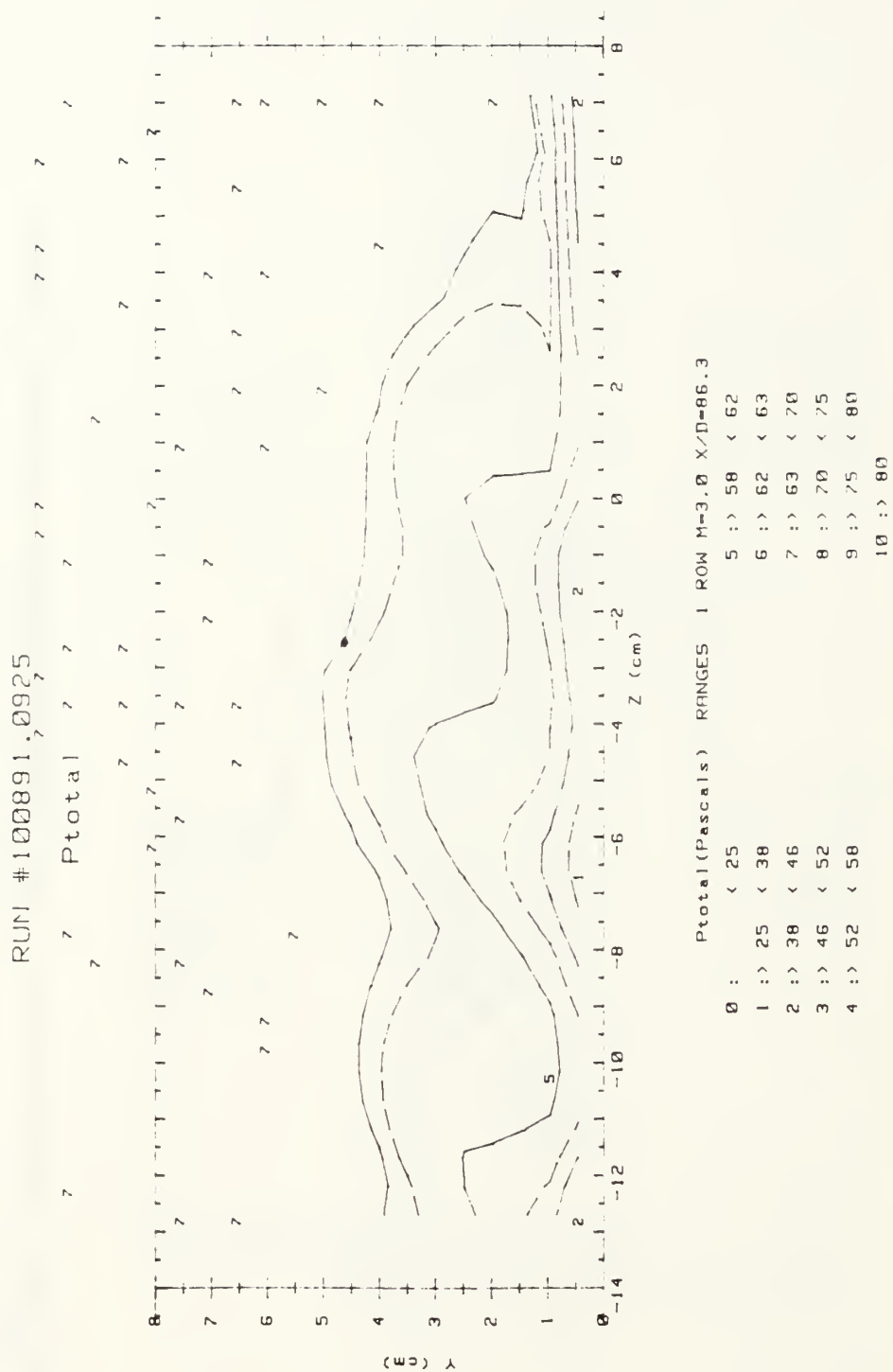


Figure 111. Streamwise Pressure Field, Compound Angle, 1 Row, $m=3.0$, $x/d=86.3$

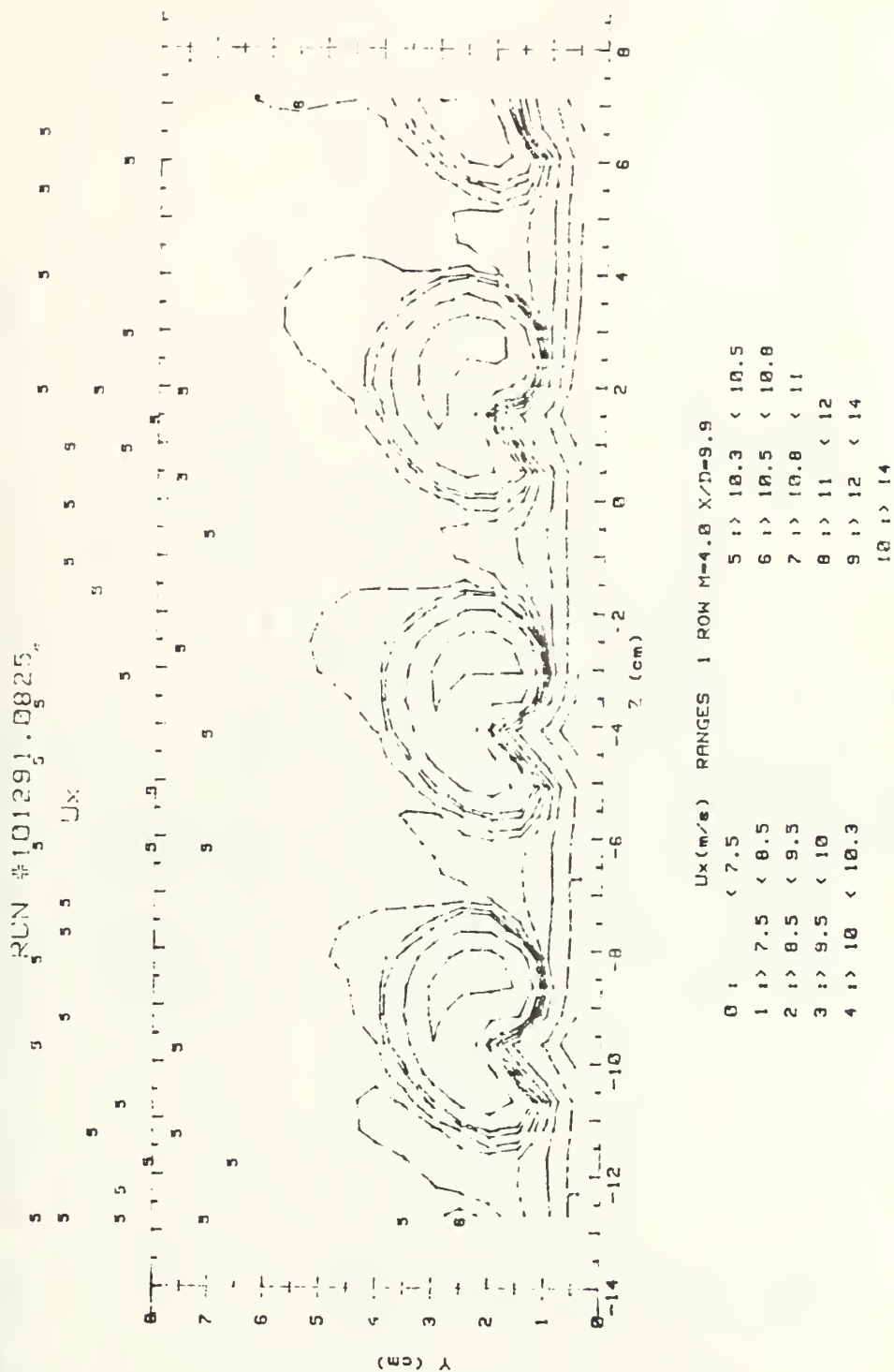


Figure 112. Streamwise Velocity Field, Compound Angle, 1 Row, $m=4.0$, $x/d=9.9$

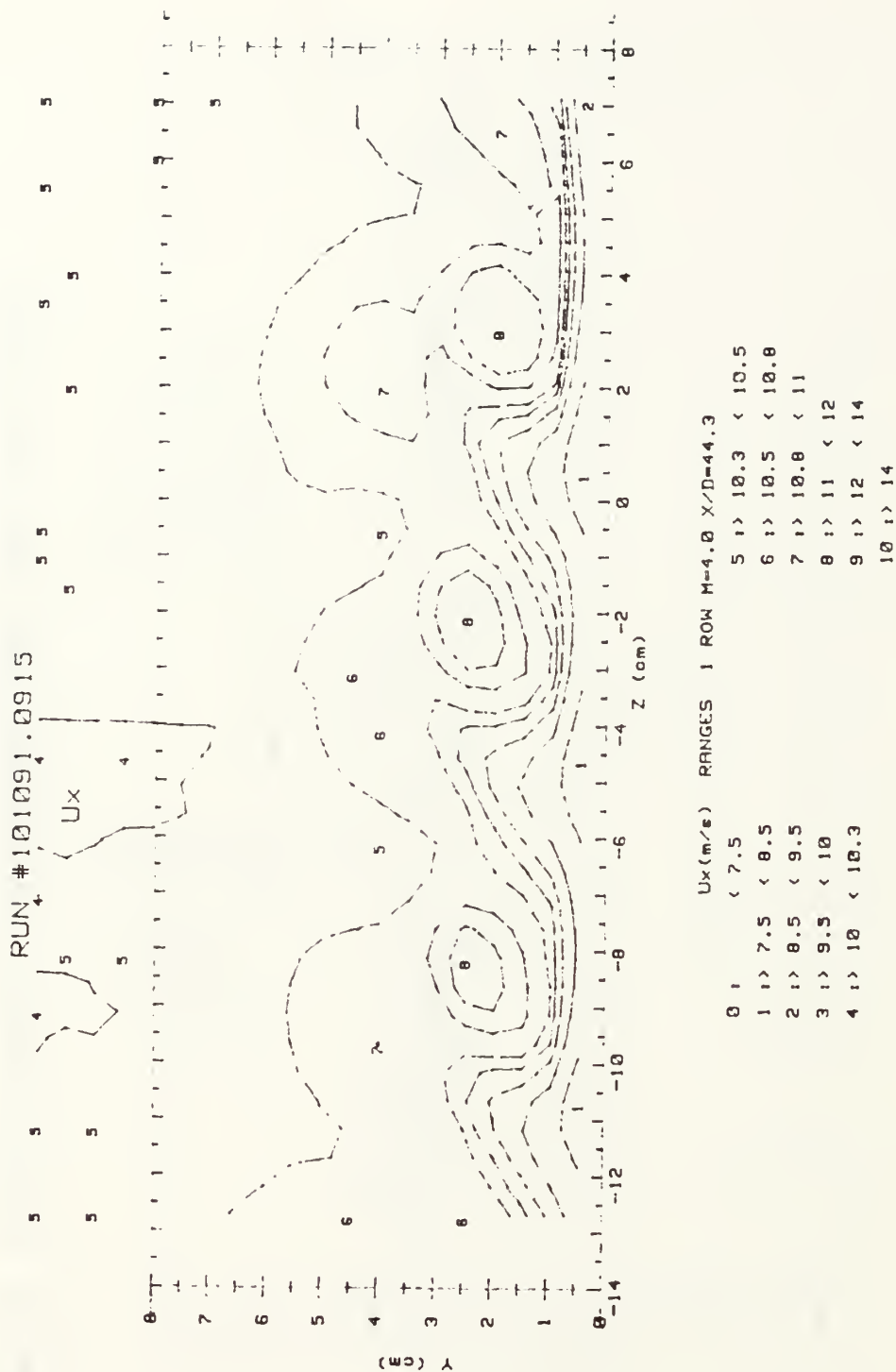


Figure 113. Streamwise Velocity Field, Compound Angle, 1 Row, $m=4.0$, $x/d=44.3$

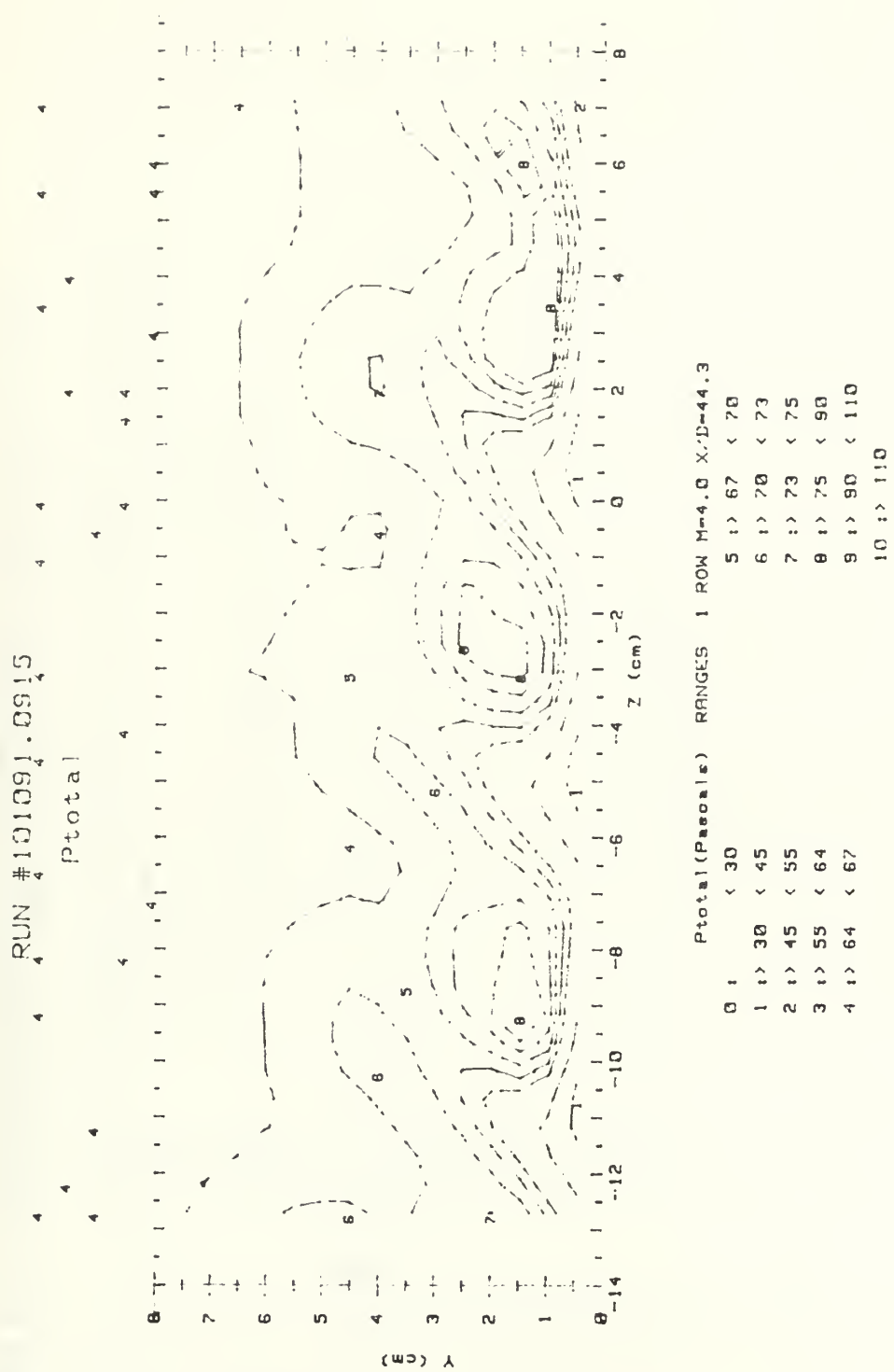


Figure 116. Streamwise Pressure Field, Compound Angle, 1 Row, $m=4.0$, $x/d=44.3$

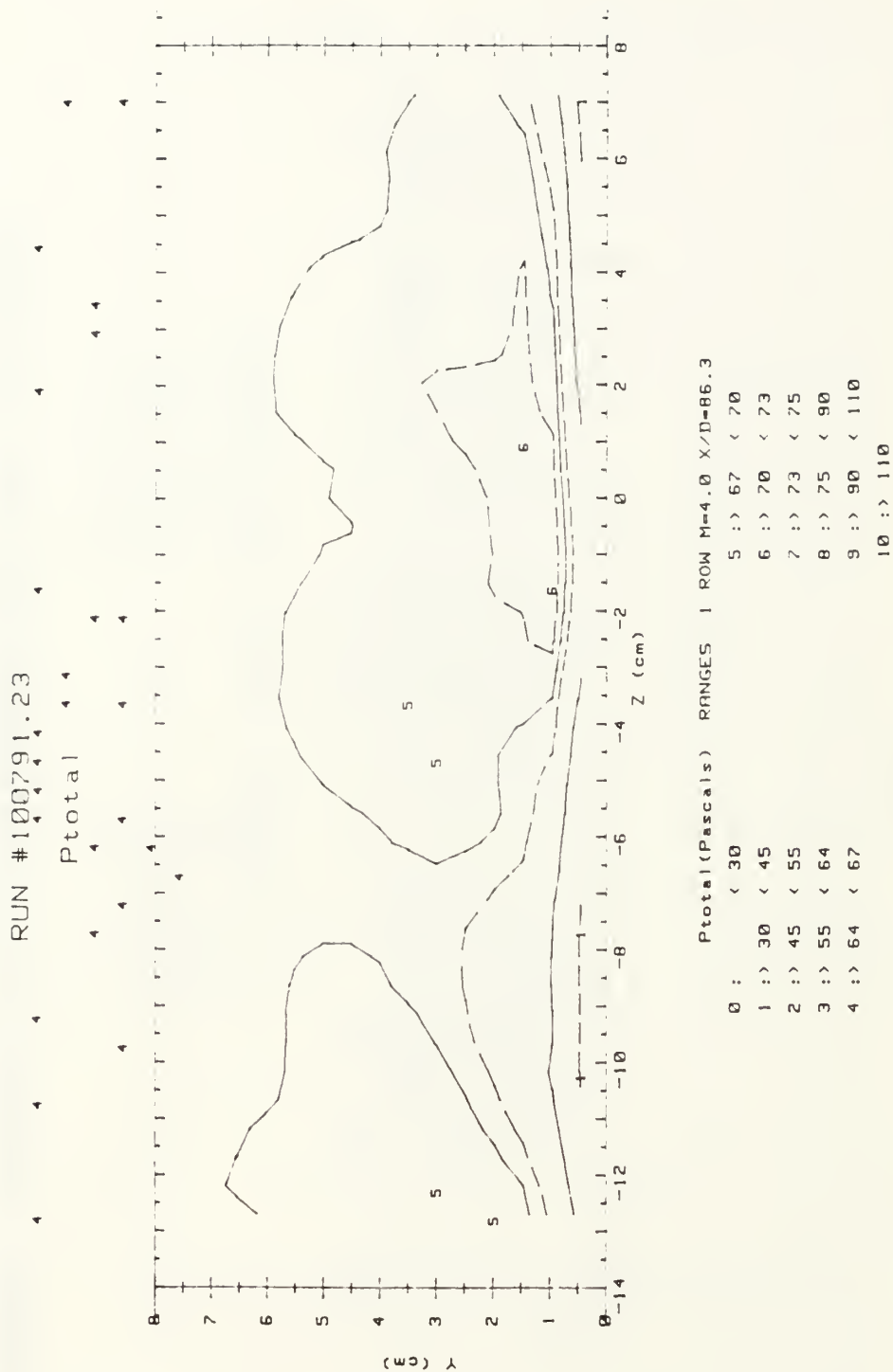


Figure 117. Streamwise Pressure Field, Compound Angle, 1 Row, $m=4.0$, $x/d=86.3$

2 row $m=2.0$ Theta vs St/St_0 for $z=-2.54$ cm

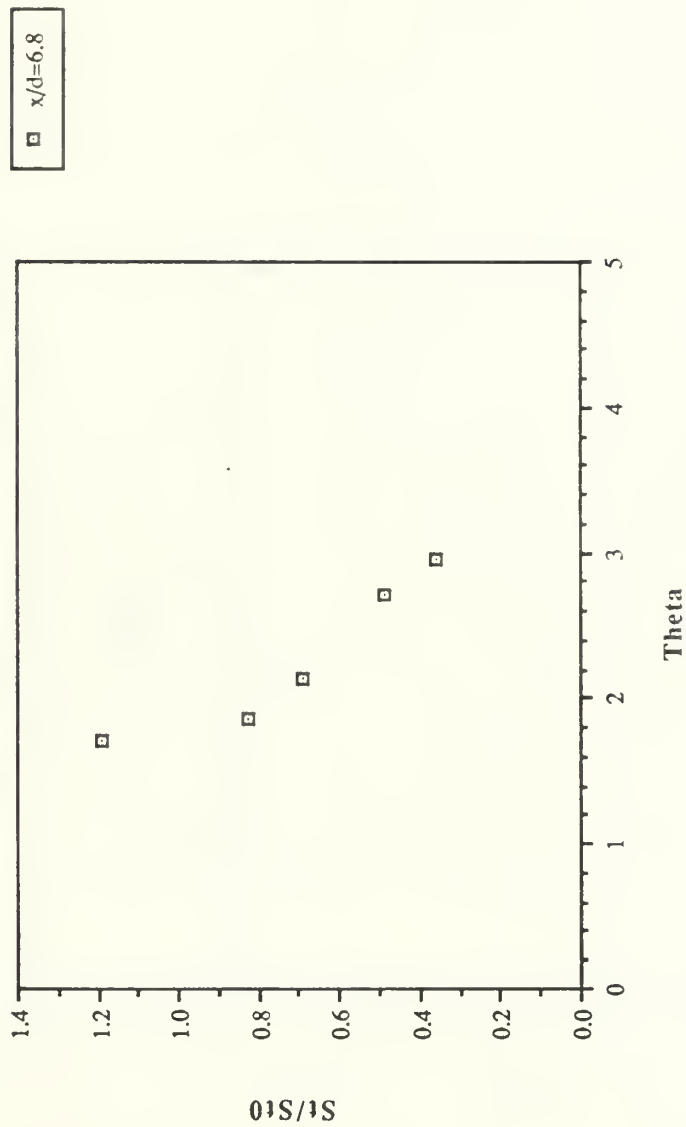


Figure 118. St/St_0 Versus θ , Compound Angle, 2 Rows, $m=2.0$, $x/d=6.8$, $Z=-2.54$ cm

2 row $m=2.0$ Theta vs St/St_0 for $z=-2.54$ cm

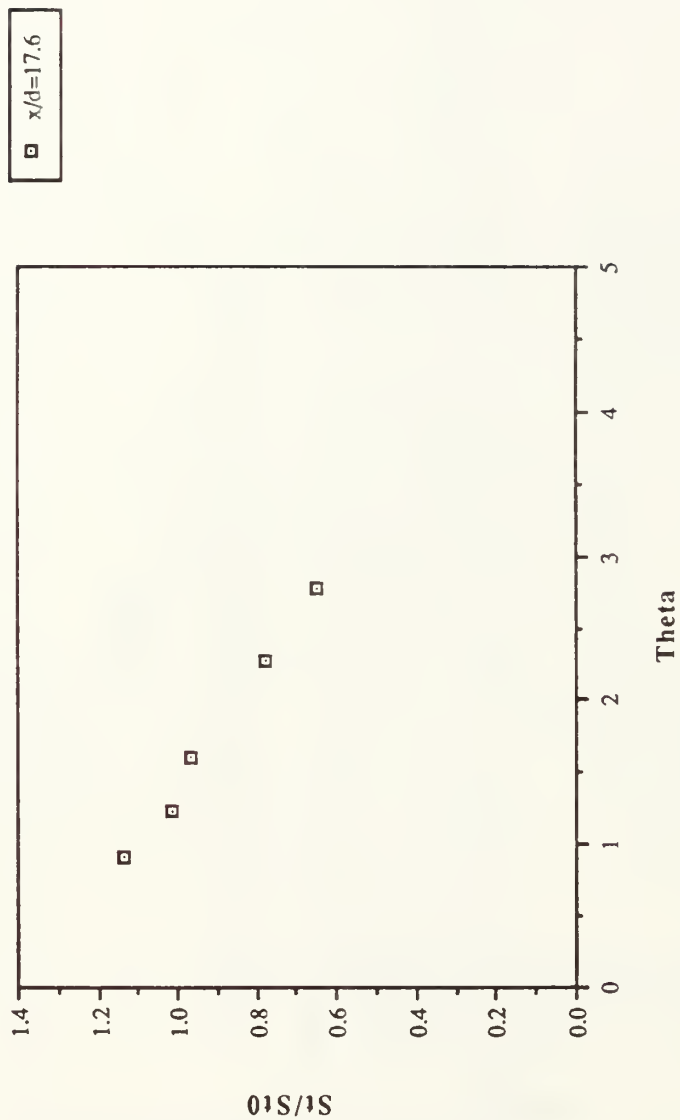


Figure 119. St/St_0 Versus θ , Compound Angle, 2 Rows, $m=2.0$, $x/d=17.6$, $Z=-2.54$ cm

2 row $m=2.0$ Theta vs St/St_0 for $z=-2.54$ cm

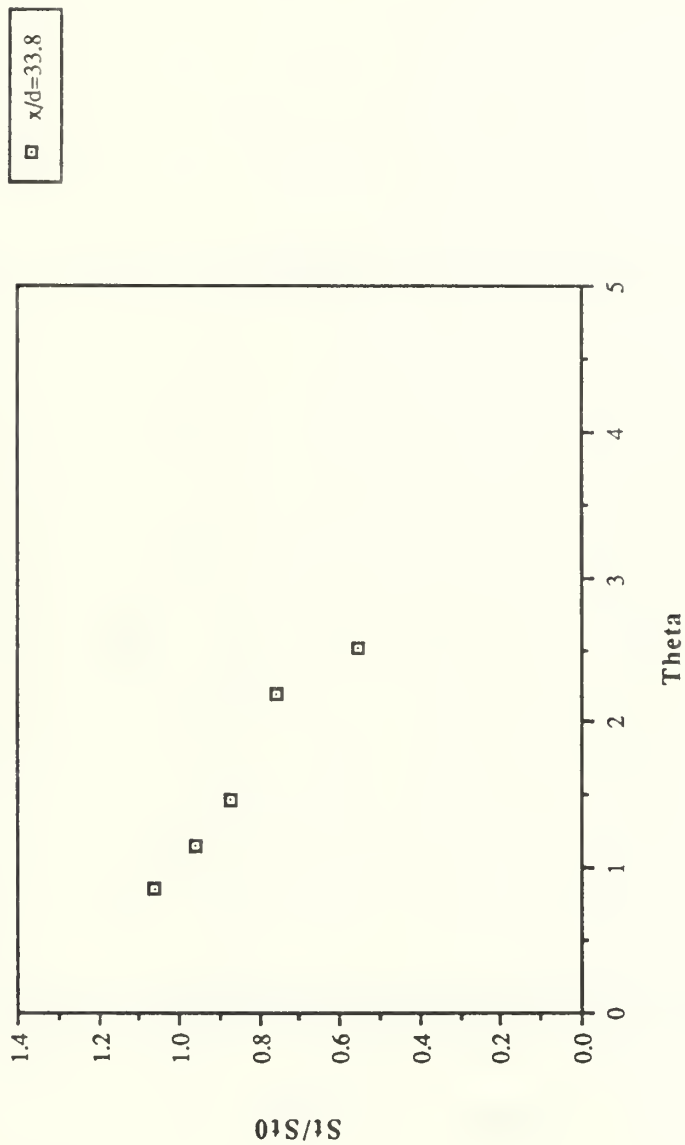


Figure 120. St/St_0 Versus θ , Compound Angle, 2 Rows, $m=2.0$, $x/d=33.8$, $Z=-2.54$ cm

2 row $m=2.0$ Theta vs St/St_0 for $z=-2.54$ cm

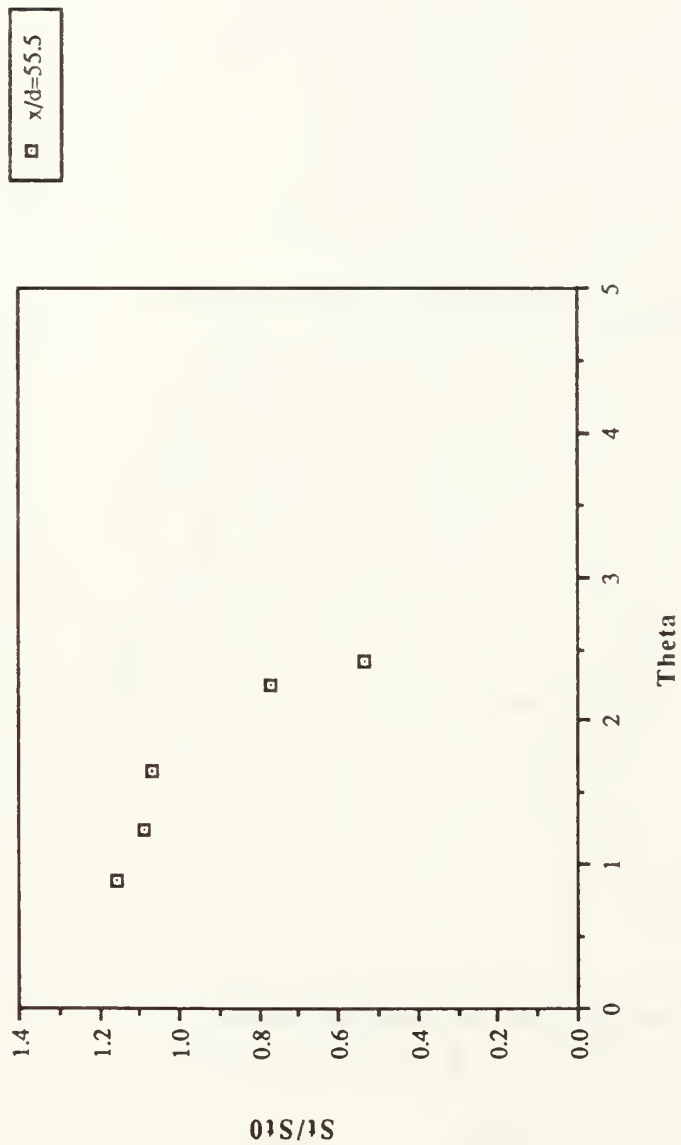


Figure 121. St/St_0 Versus θ , Compound Angle, 2 Rows, $m=2.0$, $x/d=55.5$, $Z=-2.54$ cm

2 row $m=2.0$ Theta vs St/St_0 for $z=-2.54$ cm

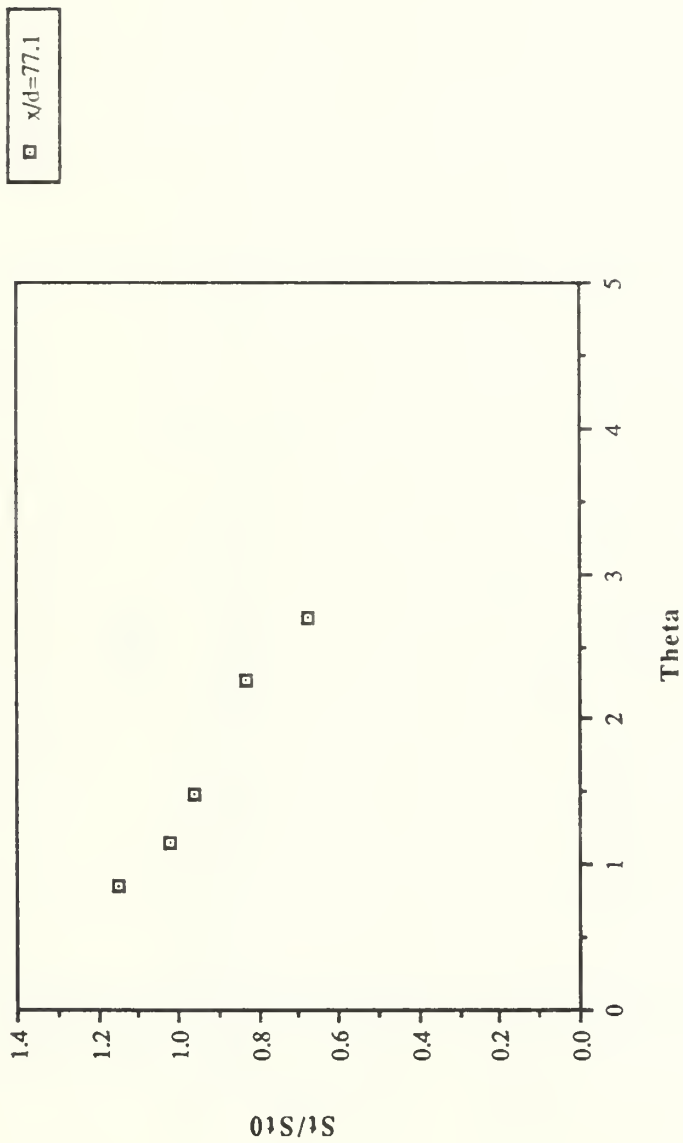


Figure 122. St/St_0 Versus θ , Compound Angle, 2 Rows, $m=2.0$, $x/d=77.1$, $Z=-2.54$ cm

2 row $m=2.0$ Theta vs St/St_0 for $z=-2.54$ cm



Figure 123. St/St_0 Versus θ , Compound Angle, 2 Rows, $m=2.0$, $x/d=98.7$, $Z=-2.54$ cm

spanwise avg. η vs x/d for 2 rows $m=2.0$

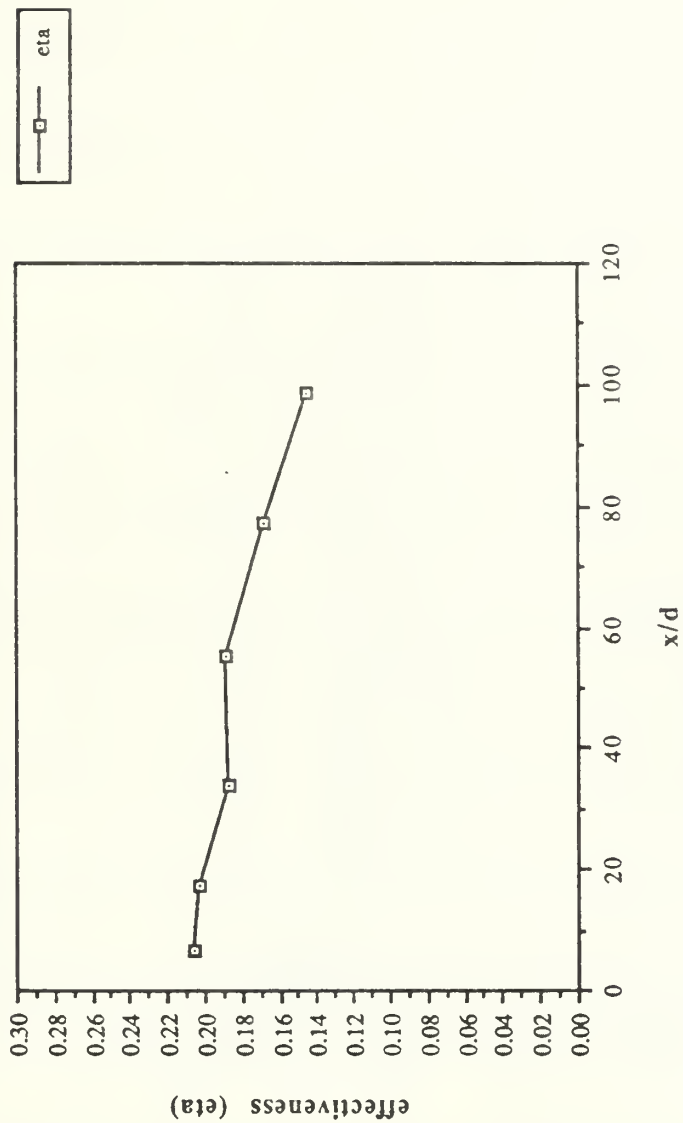


Figure 124. $\bar{\eta}$ Versus x/d , Compound Angle, 2 Rows, $m=2.0$, Spanwise Average

spanwise avg. St_f/St_0 vs x/d for 2 rows $m=2.0$

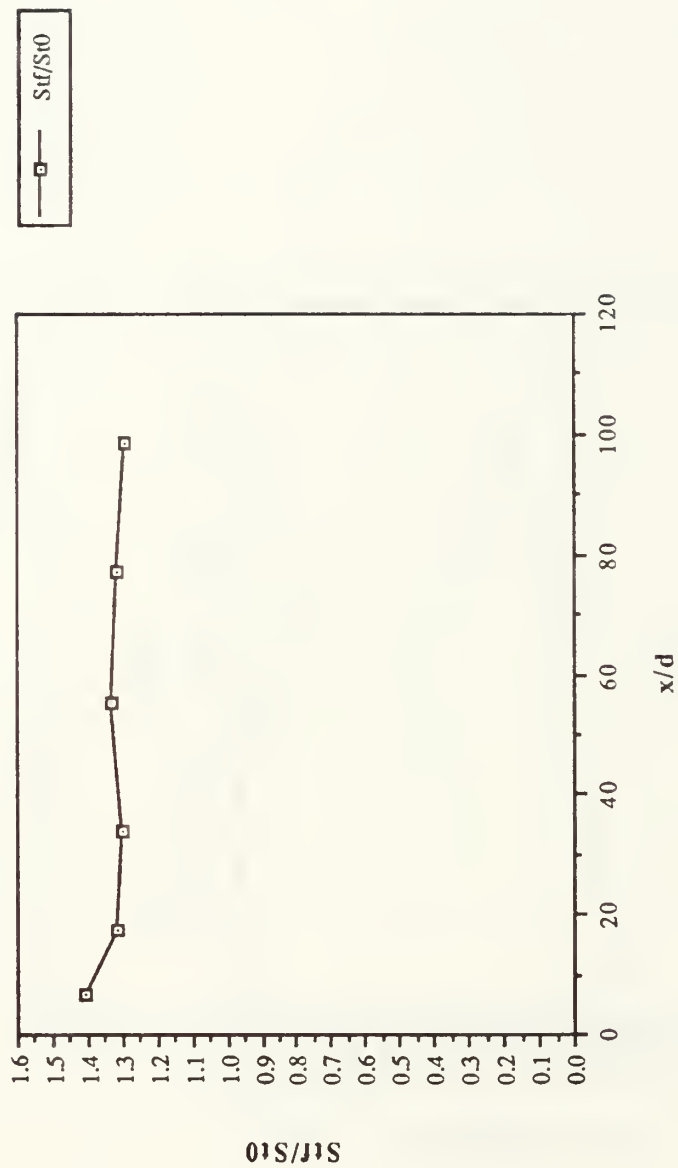


Figure 125. St_f/St_0 Versus x/d , Compound Angle, 2 Rows, $m=2.0$, Spanwise Average

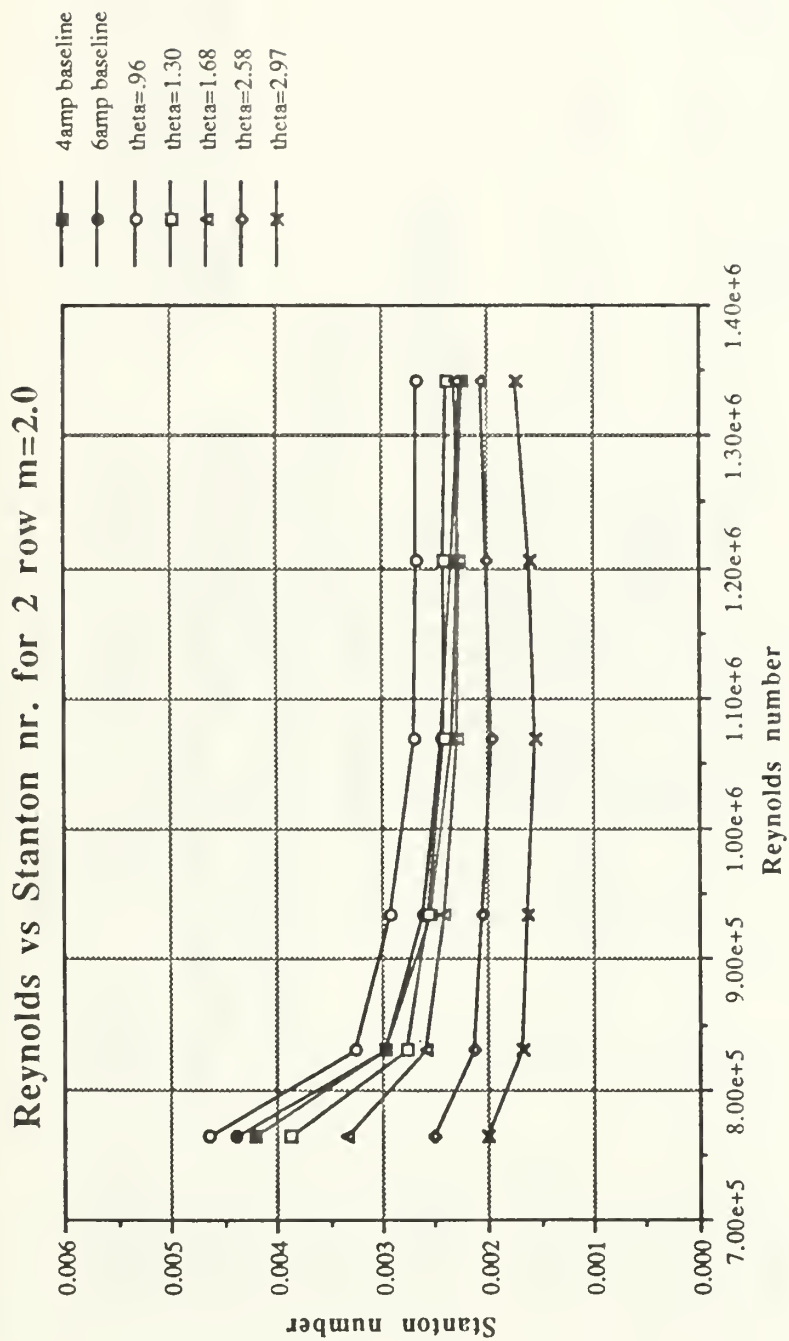


Figure 126. Spanwise Averaged Stanton Number Versus Reynolds Number, Comparison of Different θ Values and Baselines, 2 Rows, $m=2.0$

FILM-COOLING EFFECTIVENESS

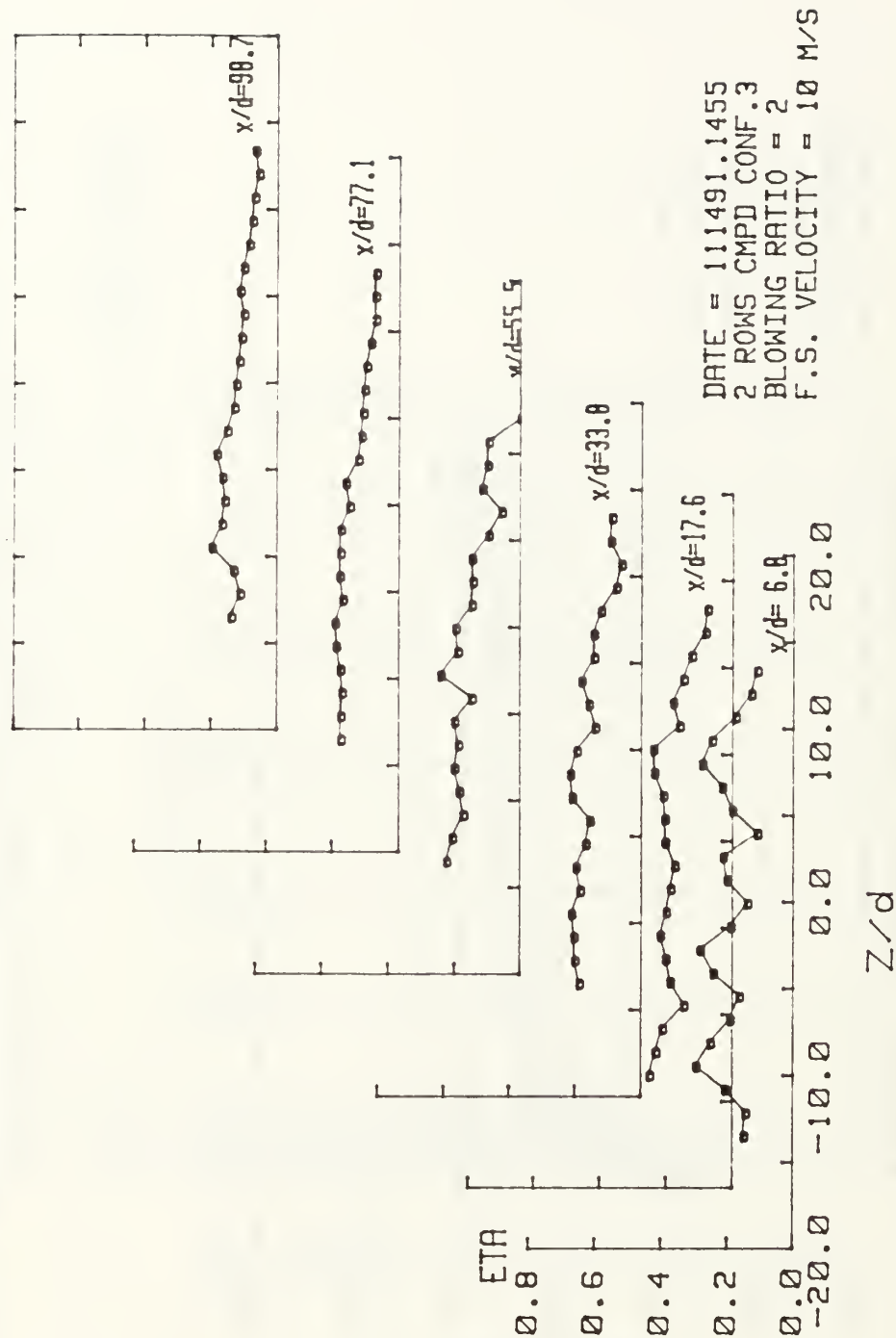


Figure 127. Spanwise Variation of η , Compound Angle, 2 Rows, $m=2.0$

ISO-ENERGETIC STANTON # RATIO

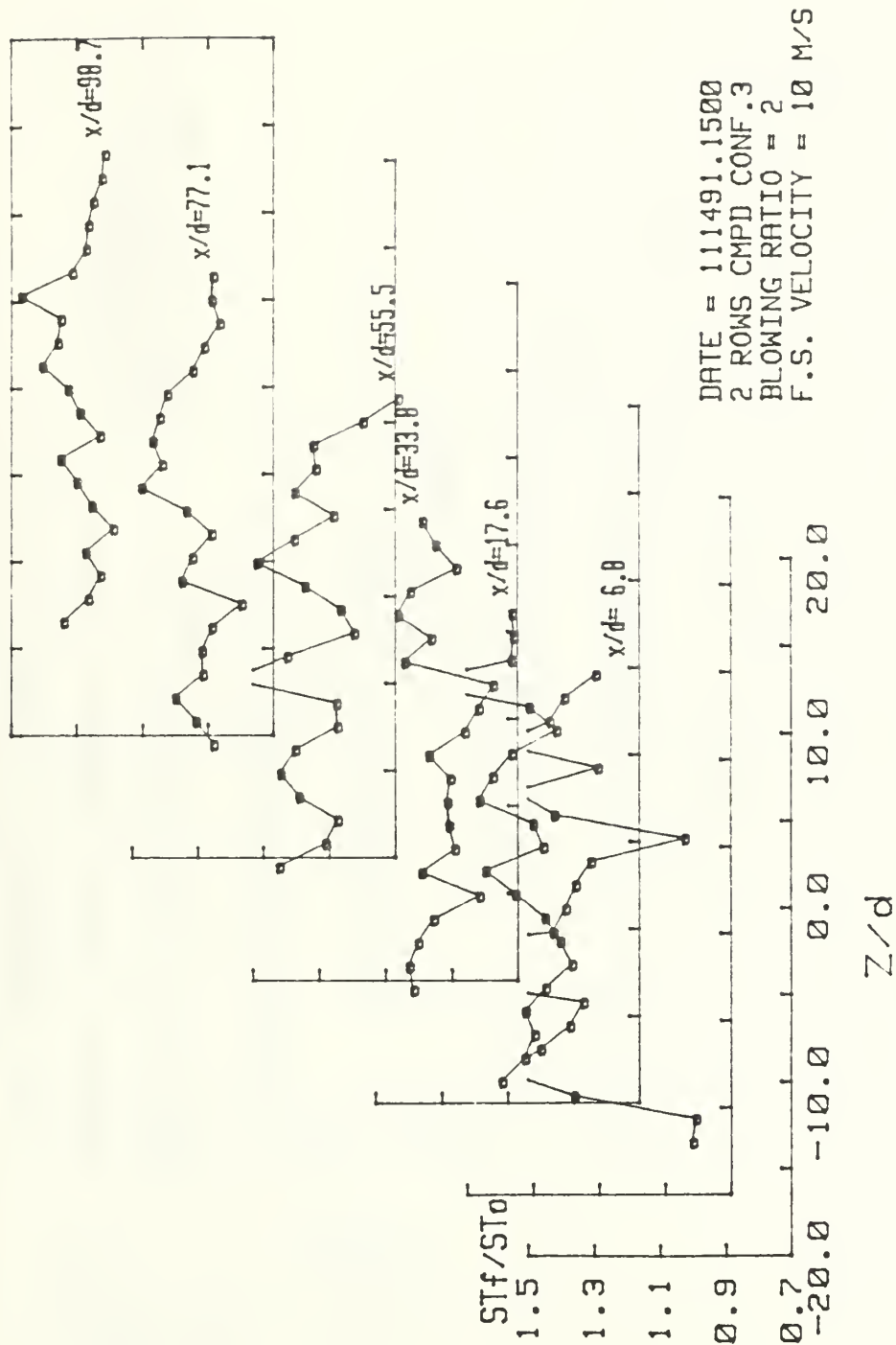


Figure 128. Spanwise Variation of St_f/St_0 , Compound Angle, 2 Rows, $m=2.0$

STANTON NUMBER RATIOS

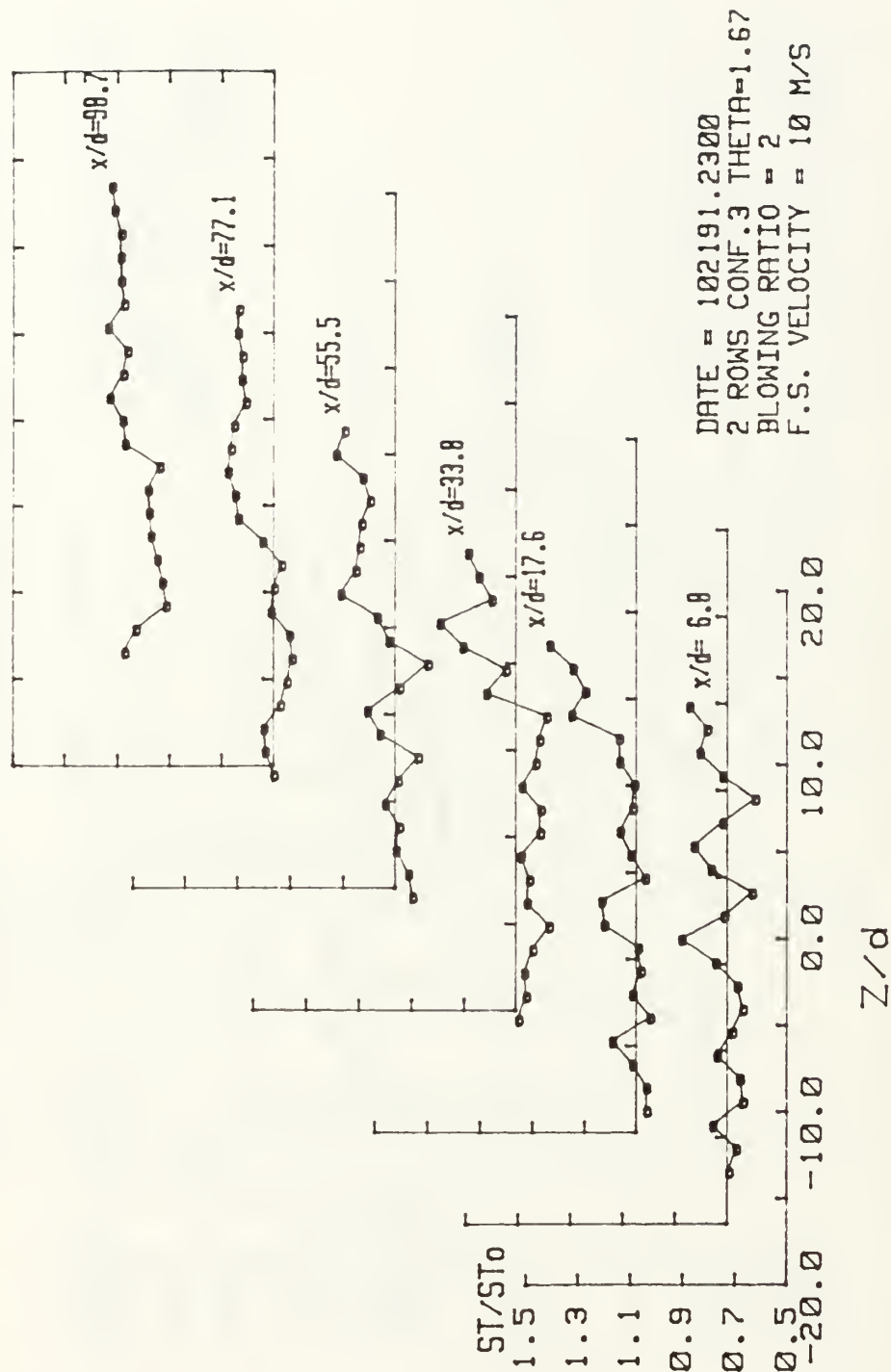


Figure 129. Spanwise Variation of St/St_0 , Compound Angle, 2 Rows, $m=2.0$, $\theta=1.67$

2 row $m=3.0$ Theta vs St/St_0 for $z=-1.27$ cm

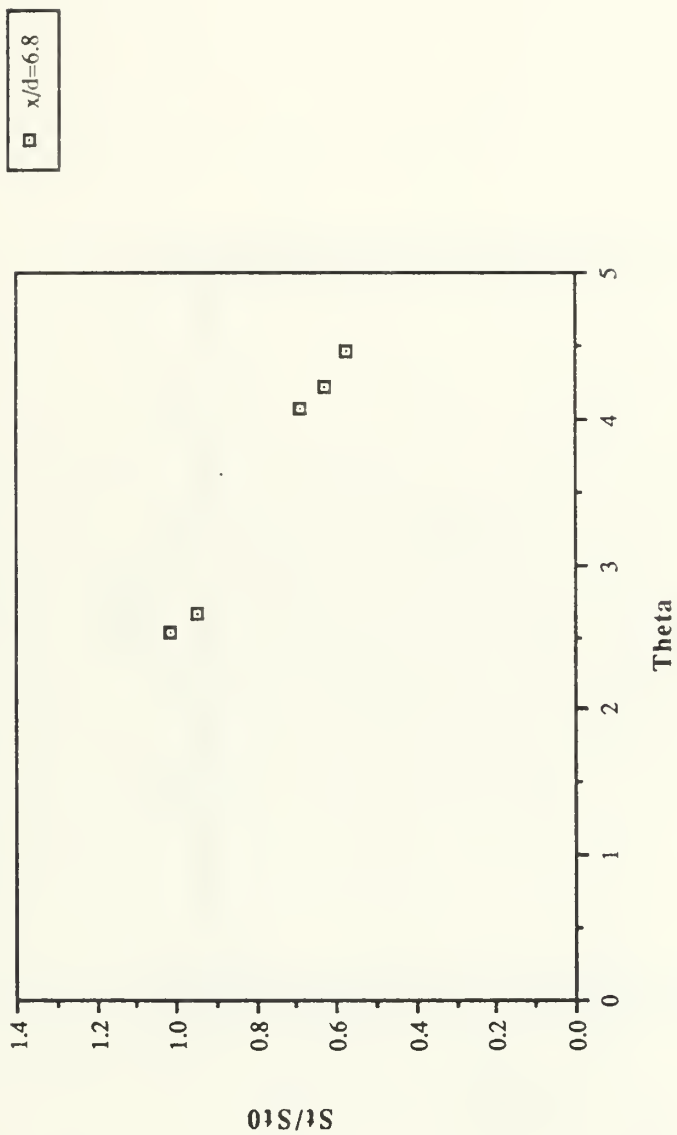


Figure 130. St/St_0 Versus θ , Compound Angle, 2 Rows $m=3.0$, $x/d=6.8$, $Z=-1.27$ cm

2 row $m=3.0$ Theta vs St/St_0 for $z=-1.27$ cm

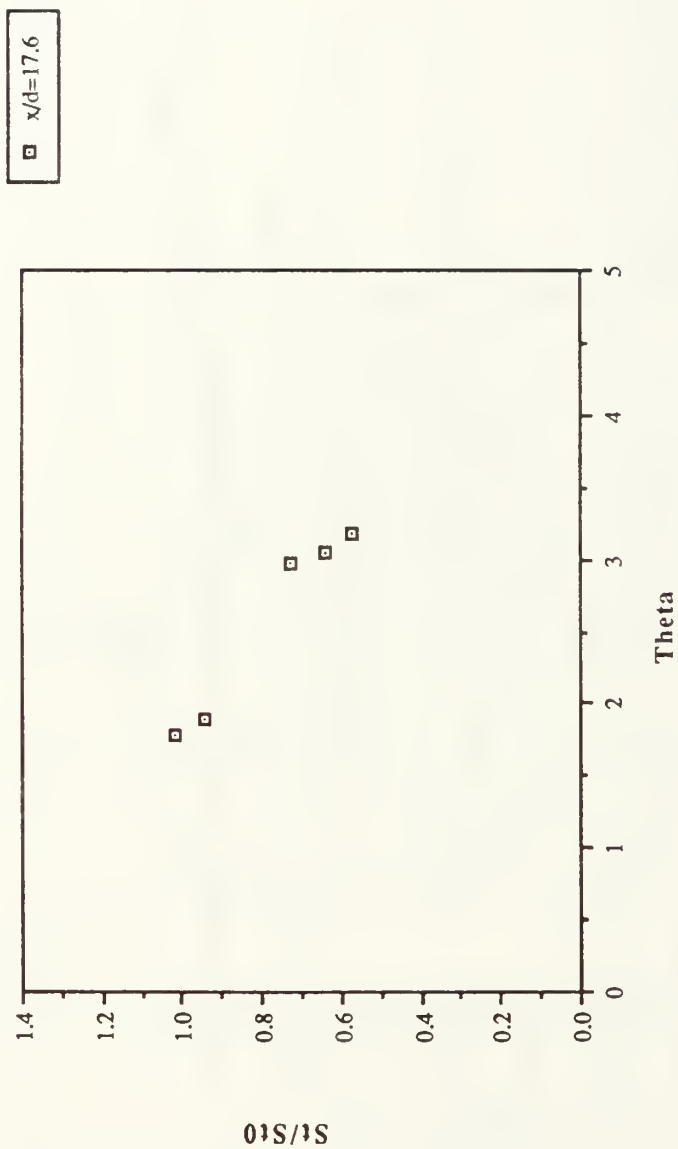


Figure 131. St/St_0 Versus θ , Compound Angle, 2 Rows, $m=3.0$, $x/d=17.6$, $Z=-1.27$ cm

2 row $m=3.0$ Theta vs St/St_0 for $z=-1.27$ cm

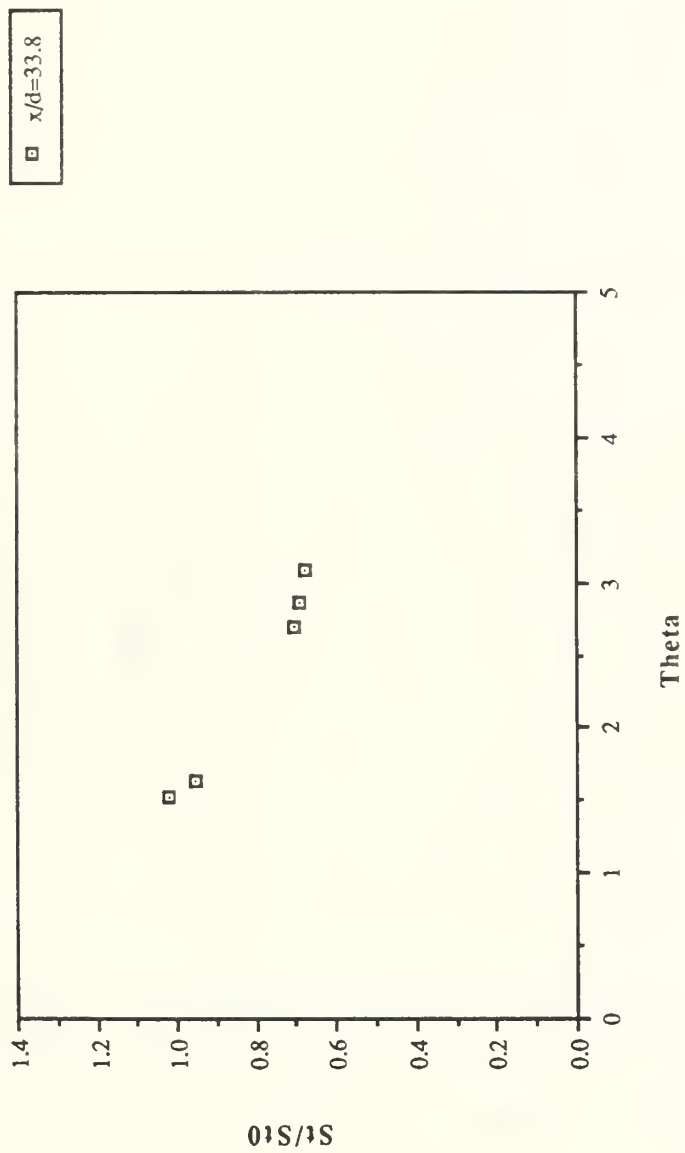


Figure 132. St/St_0 Versus θ , Compound Angle, 2 Rows, $m=3.0$, $x/d=33.8$, $Z=-1.27$ cm

2 row $m=3.0$ Theta vs St/St_0 for $z=-1.27$ cm

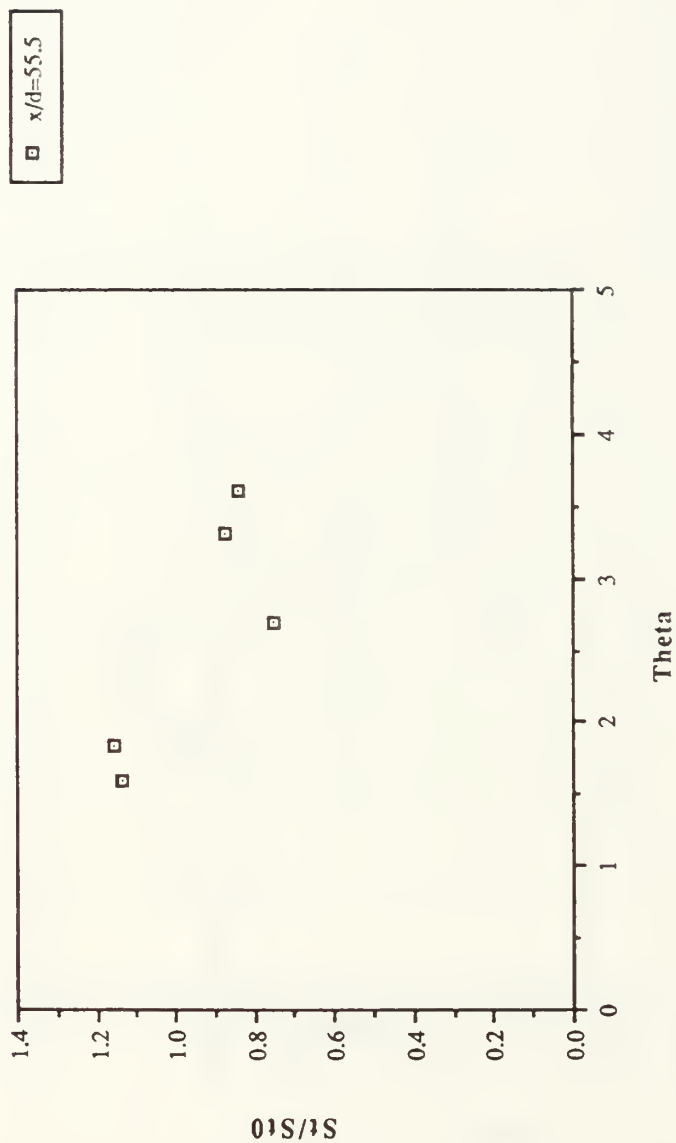


Figure 133. St/St_0 Versus θ , Compound Angle, 2 Rows, $m=4.0$, $x/d=55.5$, $Z=-1.27$ cm

2 row $m=3.0$ Theta vs St/St_0 for $z=-1.27$ cm

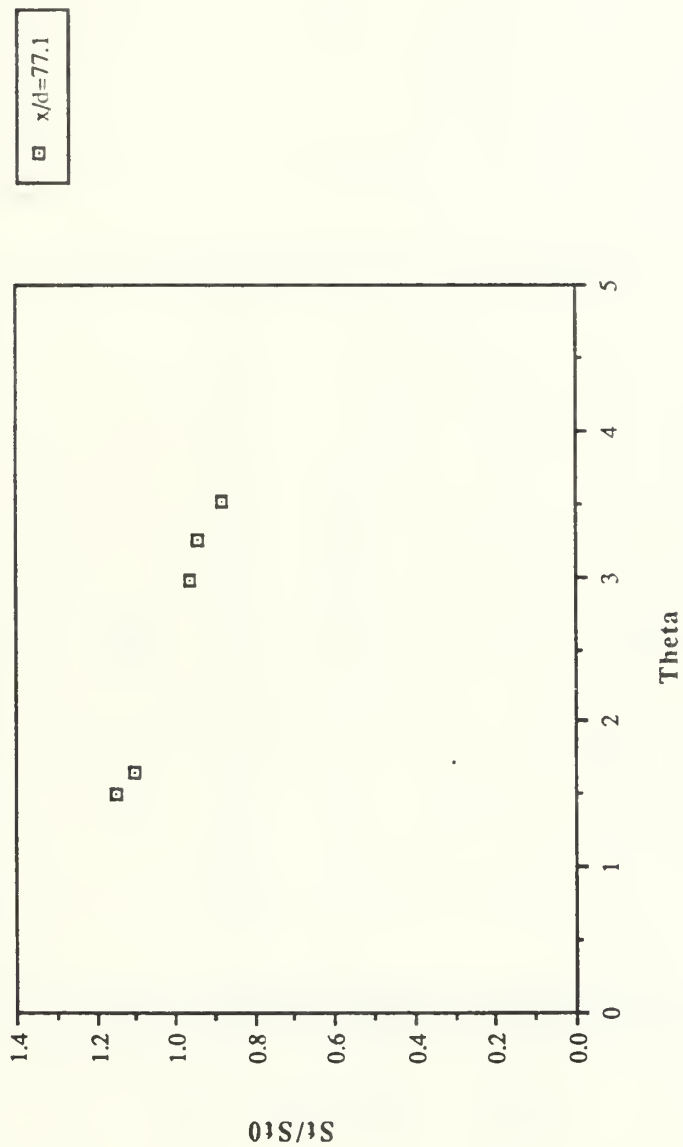


Figure 134. St/St_0 Versus θ , Compound Angle, 2 Rows, $m=3.0$, $x/d=77.1$, $Z=-1.27$ cm

2 row $m=3.0$ Theta vs St/St_0 for $z=-1.27$ cm

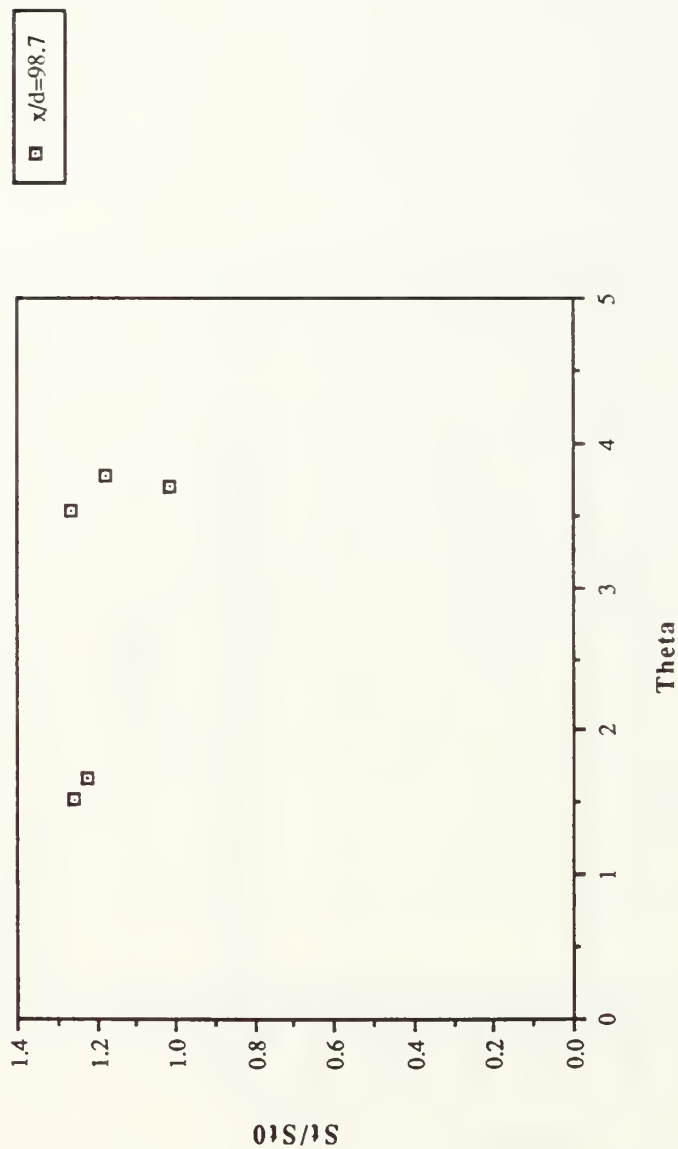


Figure 135. St/St_0 Versus θ , Compound Angle, 2 Rows, $m=3.0$, $x/d=98.7$, $Z=-1.27$ cm

spanwise avg. η vs x/d for 2 rows $m=3.0$

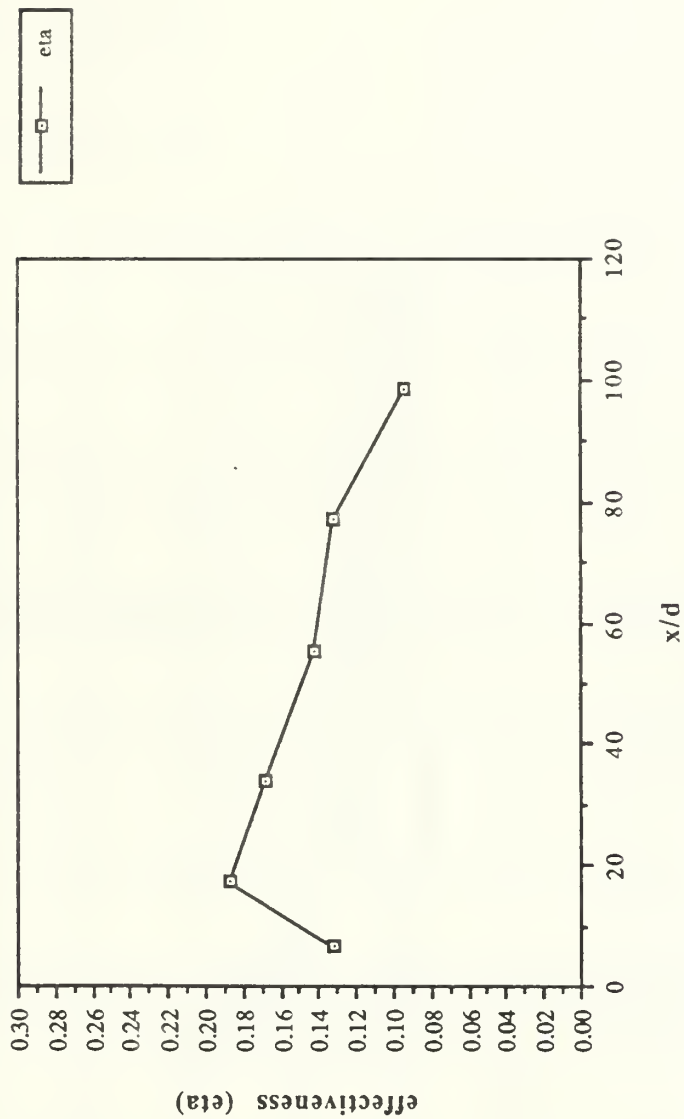


Figure 136. $\bar{\eta}$ Versus x/d , Compound Angle, 2 Rows, $m=3.0$, Spanwise Average

spanwise avg. St_f/St_0 vs x/d for 2 rows $m=3.0$

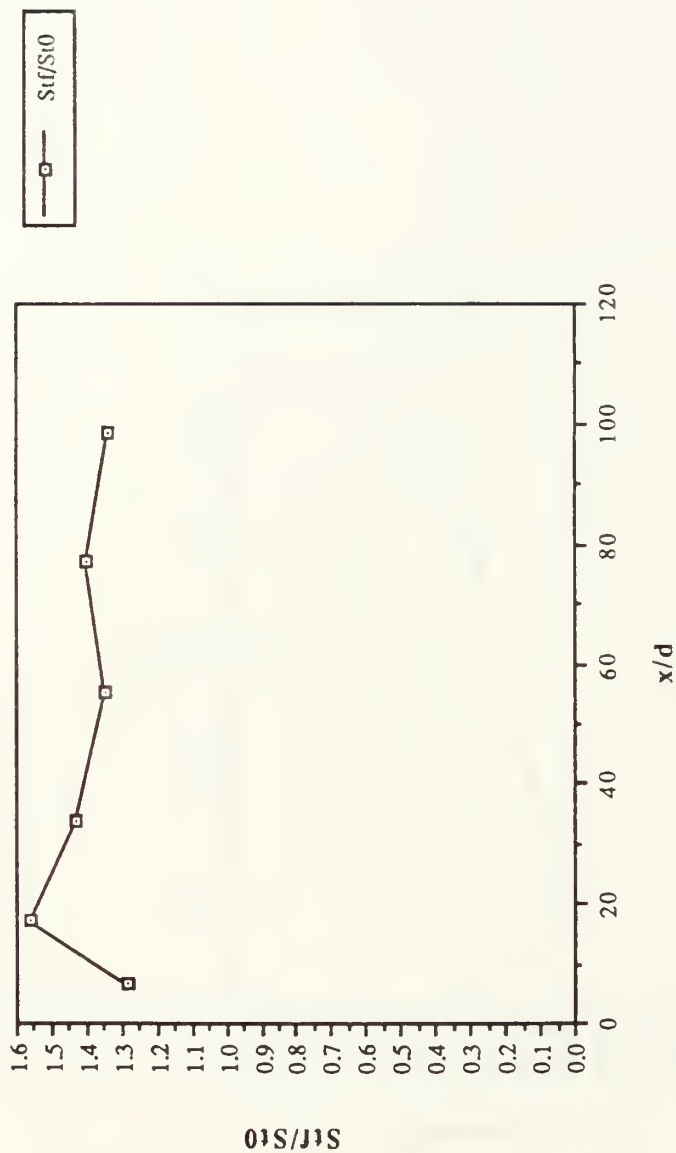


Figure 137. St_f/St_0 Versus x/d , Compound Angle, 2 Rows, $m=3.0$, Spanwise Average

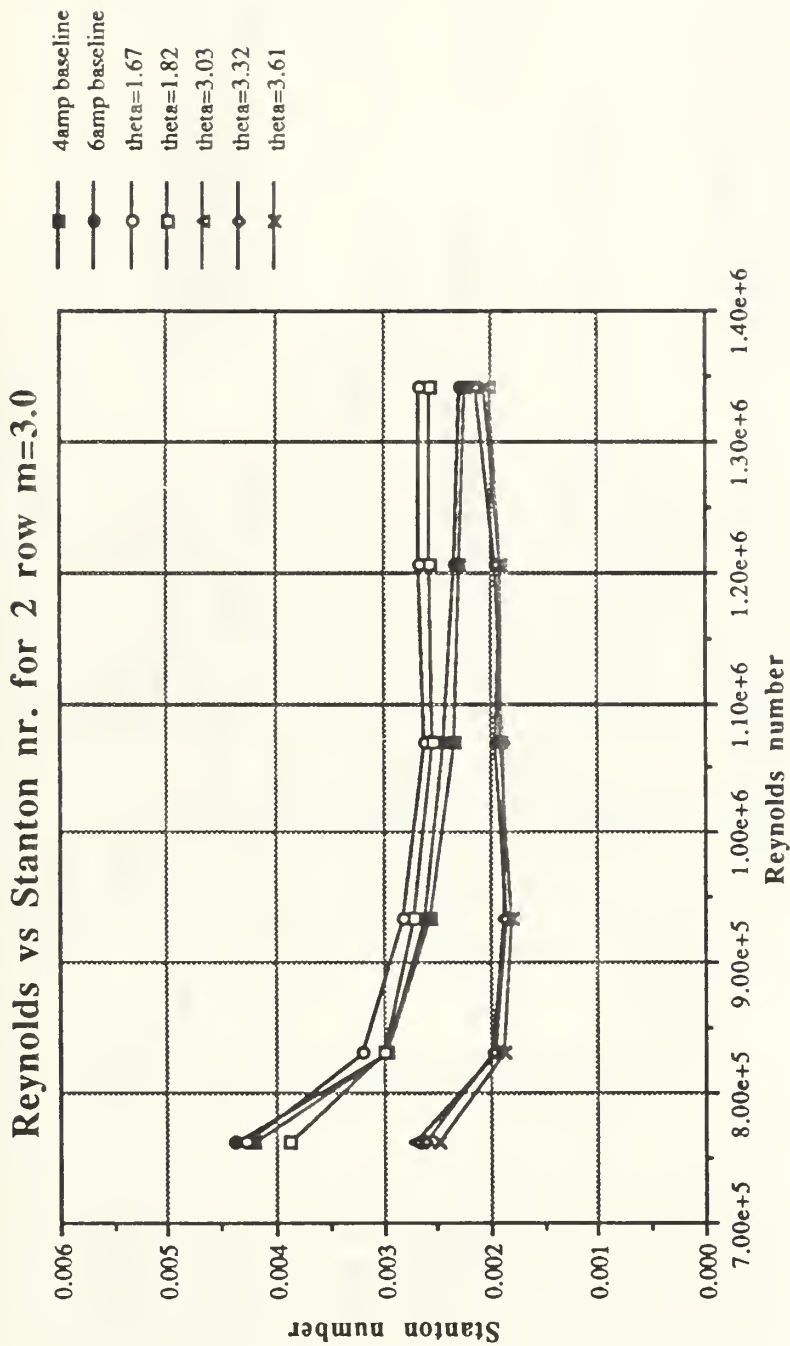


Figure 138. Spanwise Averaged Stanton Number Versus Reynolds Number, Comparison of Different θ Values and Baselines, 2 Rows, $m=3.0$

FILM-COOLING EFFECTIVENESS

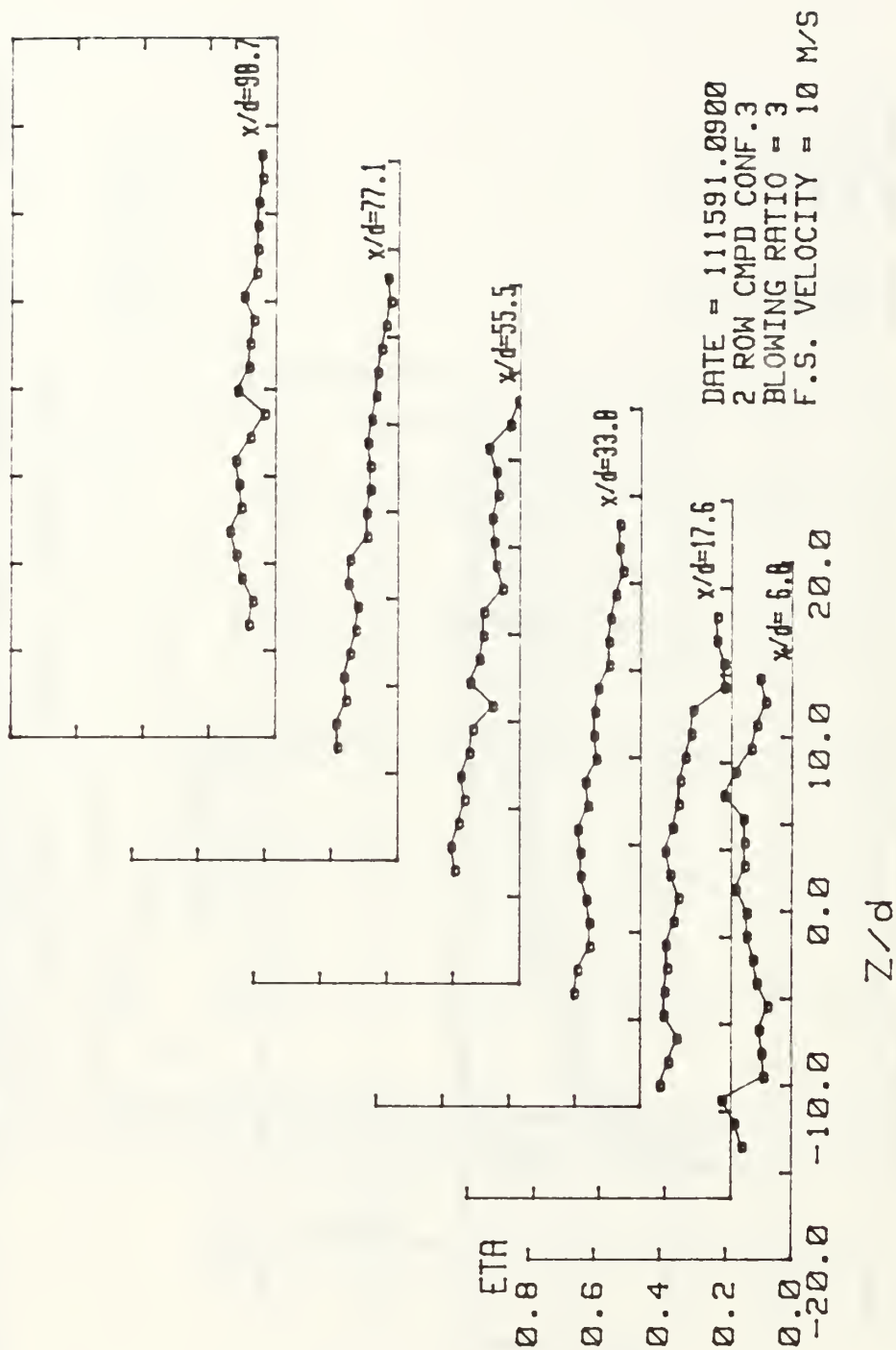


Figure 139. Spanwise Variation of η , Compound Angle, 2 Rows, $m=3.0$

ISO-ENERGETIC STANTON # RATIO

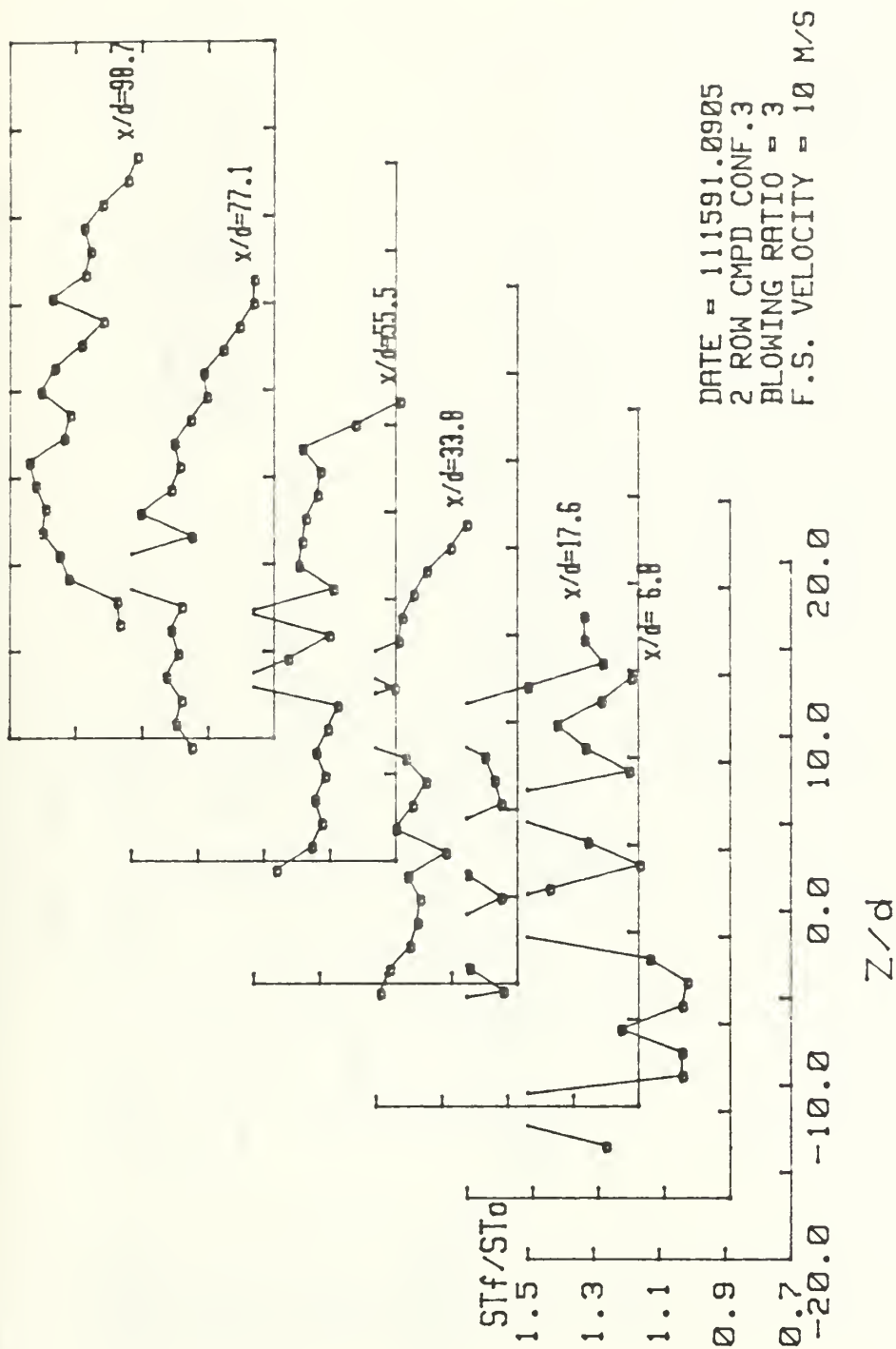


Figure 140. Spanwise Variation of St_f/St_0 , Compound Angle, 2 Rows, $m=3.0$

STANTON NUMBER RATIOS

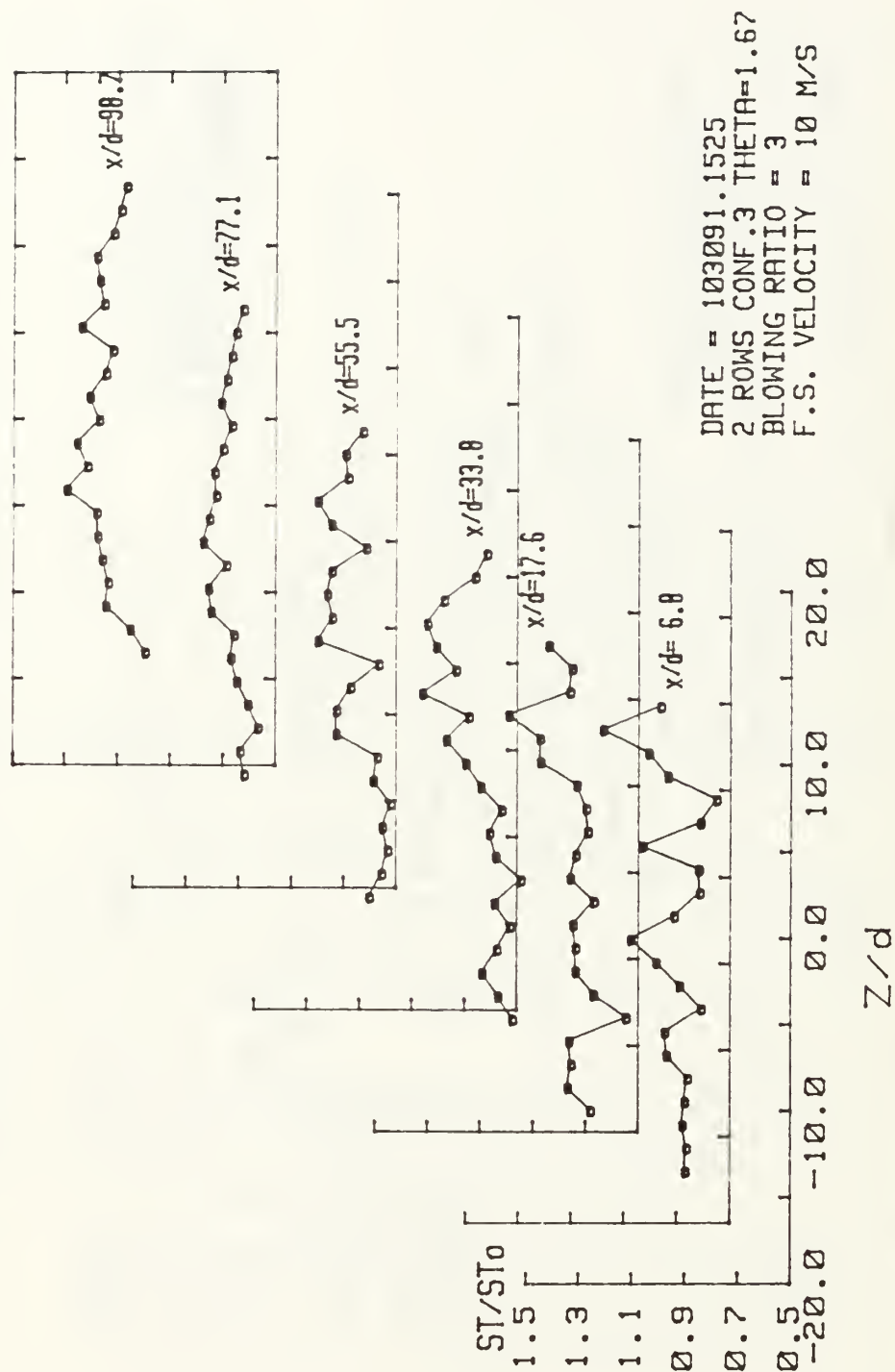


Figure 141. Spanwise Variation of St/St_0 , Compound Angle, 2 Rows, $m=3.0$, $\theta=1.67$

RUN #92391.201

T - Tfs

~ 1/

1/ 1/



T - Tfs(CELCIUS) RANGES 2 ROWS M=2.0 X/D=9.9

0 :	< .5	5 :	2.5 < 3
1 :	.5 < 1	6 :	3 < 3.5
2 :	1 < 1.5	7 :	3.5 < 4
3 :	1.5 < 2	8 :	4 < 4.5
4 :	2 < 2.5	9 :	4.5

Figure 142. Streamwise Injectant Distribution, Compound Angles, 2 Rows, $m=2.0$, $x/d=9.9$

RUN #92091.2225

T -- Tfs

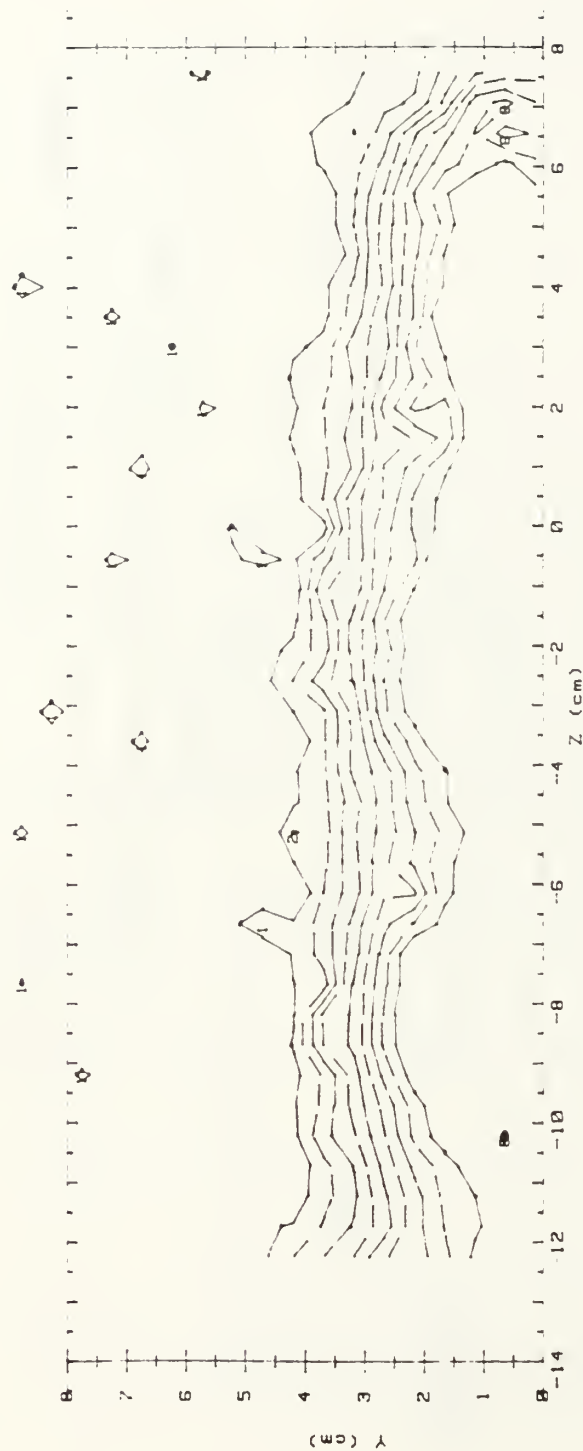
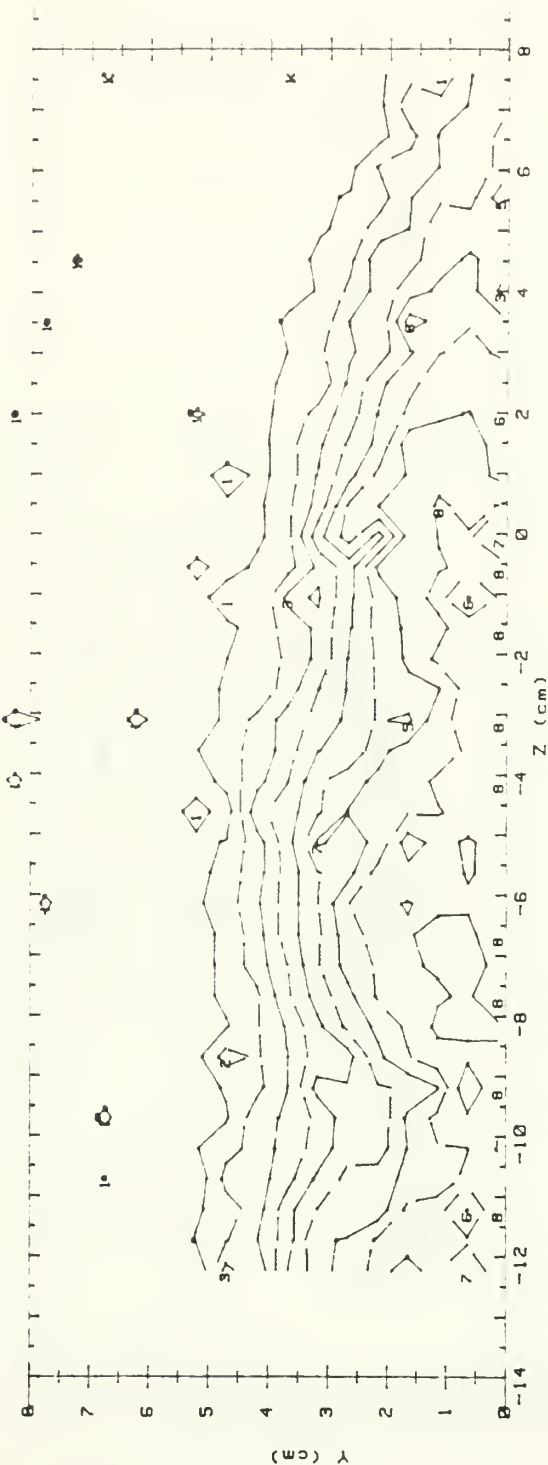


Figure 143. Streamwise Injectant Distribution, Compound Angles, 2 Rows, $m=2.0$, $x/d=44.3$

RUN #91991.1315

T - Tfs

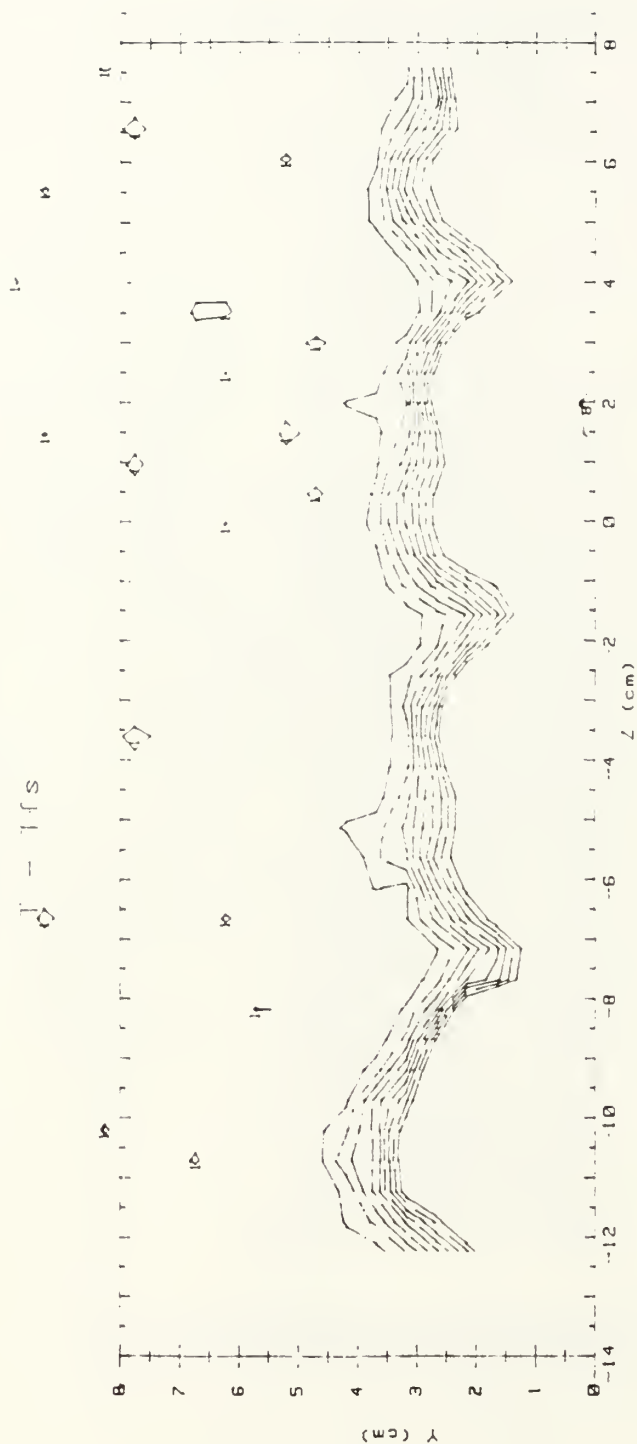


T - Tfs(CELCIUS) RANGES 2 ROWS M=2.0 X/D=86.3

0 :	< .5	5 :	2.5 < 3
1 :	.5 < 1	6 :	3 < 3.5
2 :	1 < 1.5	7 :	3.5 < 4
3 :	1.5 < 2	8 :	4 < 4.5
4 :	2 < 2.5	9 :	4.5

Figure 144. Streamwise Injectant Distribution, Compound Angles, 2 Rows, $m=2.0$, $x/d=86.3$

RUN #92491.0915

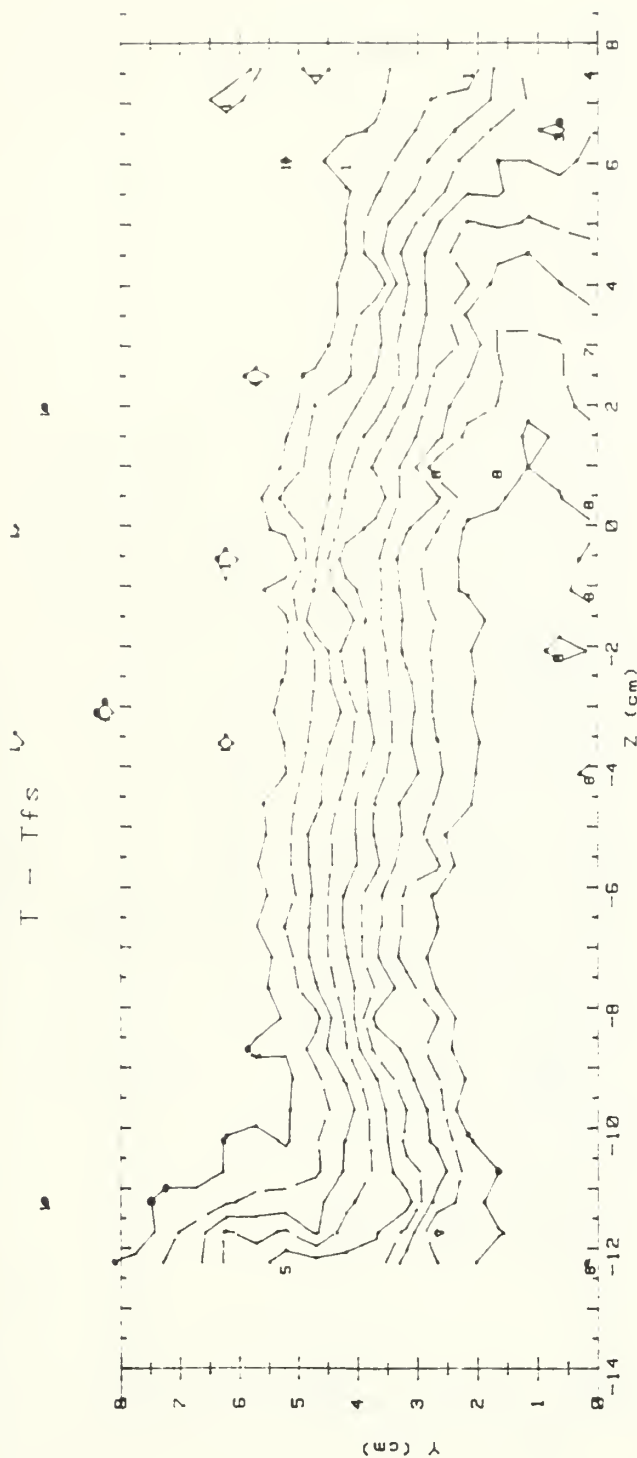


T - Tfs (CELCIUS) RANGES 2 ROWS M=3.0 X/D=9.9

0 :	< .5	5 :	2.5 < 3
1 :	.5 < 1	6 :	3 < 3.5
2 :	1 < 1.5	7 :	3.5 < 4
3 :	1.5 < 2	8 :	4 < 4.5
4 :	2 < 2.5	9 :	4.5

Figure 145. Streamwise Injectant Distribution, Compound Angles, 2 Rows, $m=3.0$, $x/d=9.9$

RUN #92091.151

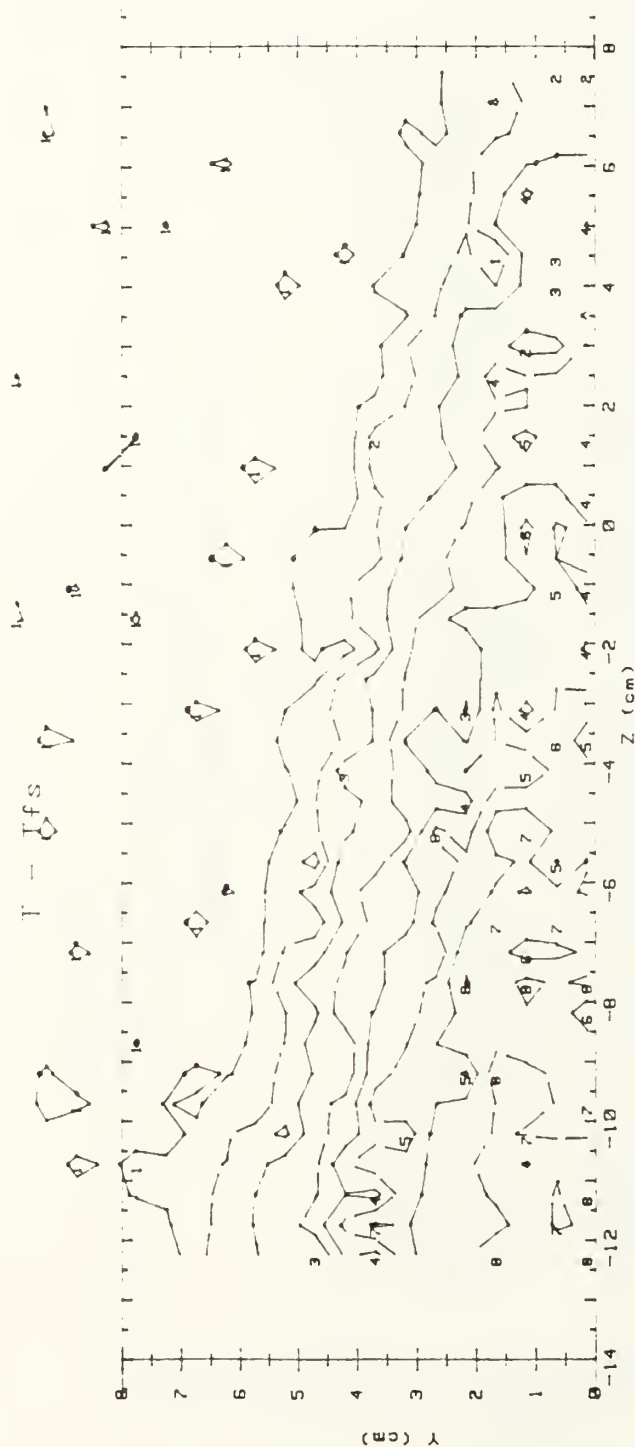


T - Tfs(CELCIUS) RANGES 2 ROWS M=3.0 X/D=44.3

0 :	< .5	5 :	2.5 < 3
1 :	.5 < 1	6 :	3 < 3.5
2 :	1 < 1.5	7 :	3.5 < 4
3 :	1.5 < 2	8 :	4 < 4.5
4 :	2 < 2.5	9 :	4.5

Figure 146. Streamwise Injectant Distribution, Compound Angles, 2 Rows, $m=3.0$, $x/d=44.3$

RUN #91991.19



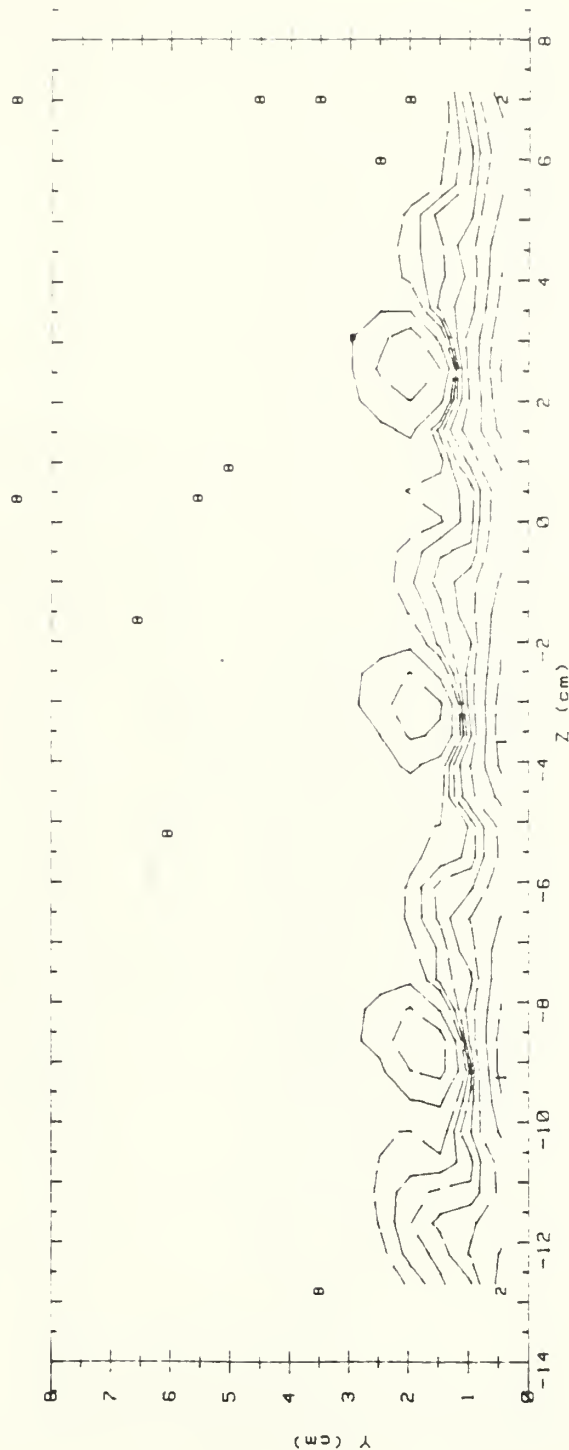
T = Ifs(CELCIUS) RANGES 2 ROWS M=3.0 X/D=86.3

- | | | | |
|-----|---------|-----|---------|
| 0 : | < .5 | 5 : | 2.5 < 3 |
| 1 : | .5 < 1 | 6 : | 3 < 3.5 |
| 2 : | 1 < 1.5 | 7 : | 3.5 < 4 |
| 3 : | 1.5 < 2 | 8 : | 4 < 4.5 |
| 4 : | 2 < 2.5 | 9 : | 4.5 |

Figure 147. Streamwise Injectant Distribution, Compound Angles, 2 Rows, $m=3.0$, $x/d=86.3$

RUN #101191.0905

Ux



Ux (m/s) RANGES 2 ROWS M=2.0 X/D=9.9

0 :	< 6	5 :	9.5 < 9.8
1 :	6 < 7	6 :	9.8 < 10
2 :	7 < 8	7 :	10 < 10.2
3 :	8 < 9	8 :	10.2 < 10.7
4 :	9 < 9.5	9 :	10.7 < 11.5
		10 :	> 11.5

Figure 148. Streamwise Velocity Field, Compound Angle, 2 Rows, $m=2.0$, $x/d=9.9$



Figure 149. Streamwise Velocity Field, Compound Angle, 2 Rows, $m=2.0$, $x/d=44.3$

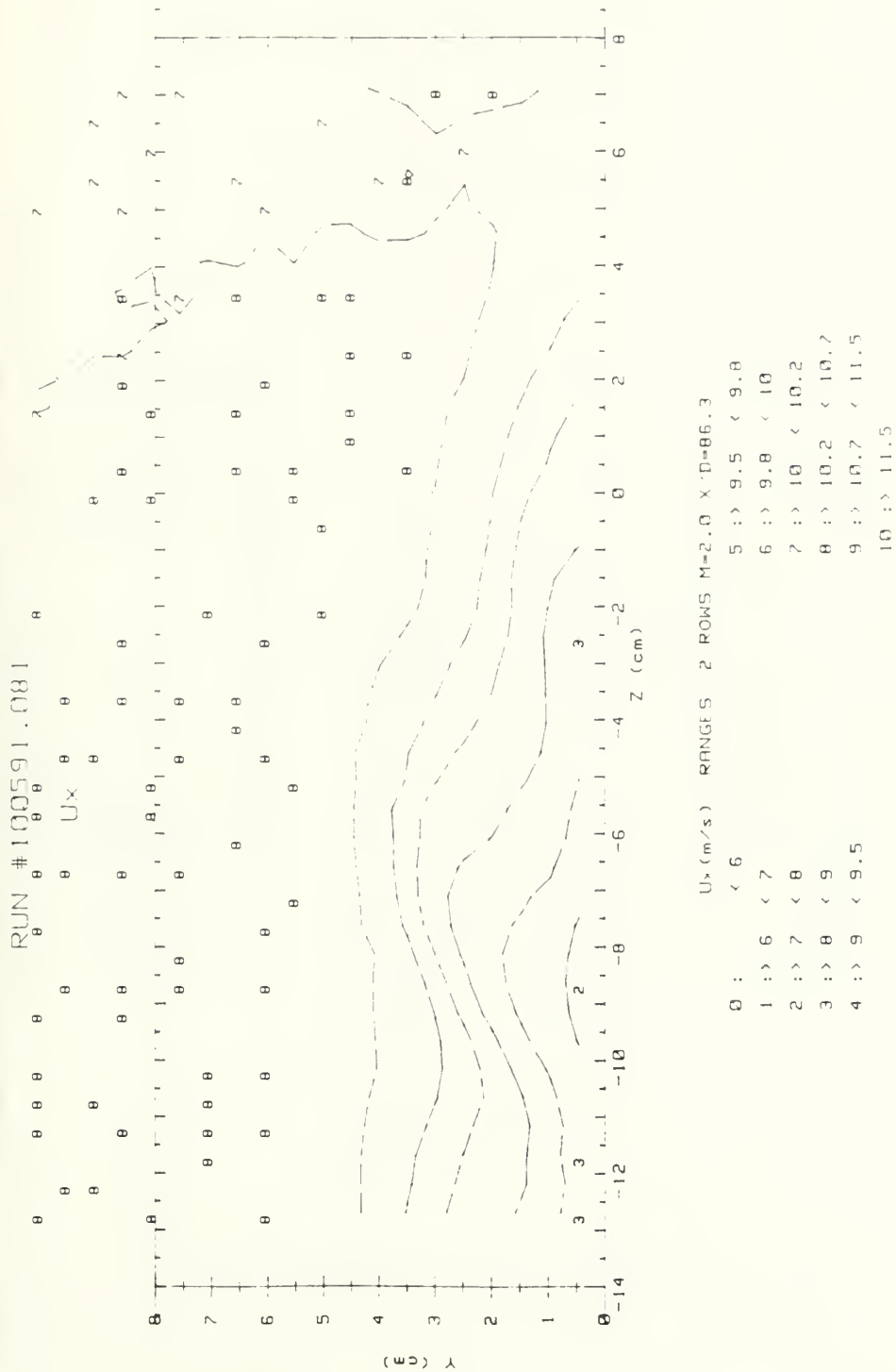


Figure 150. Streamwise Velocity Field, Compound Angle, 2 Rows, $m=2.0$, $x/d=86.3$

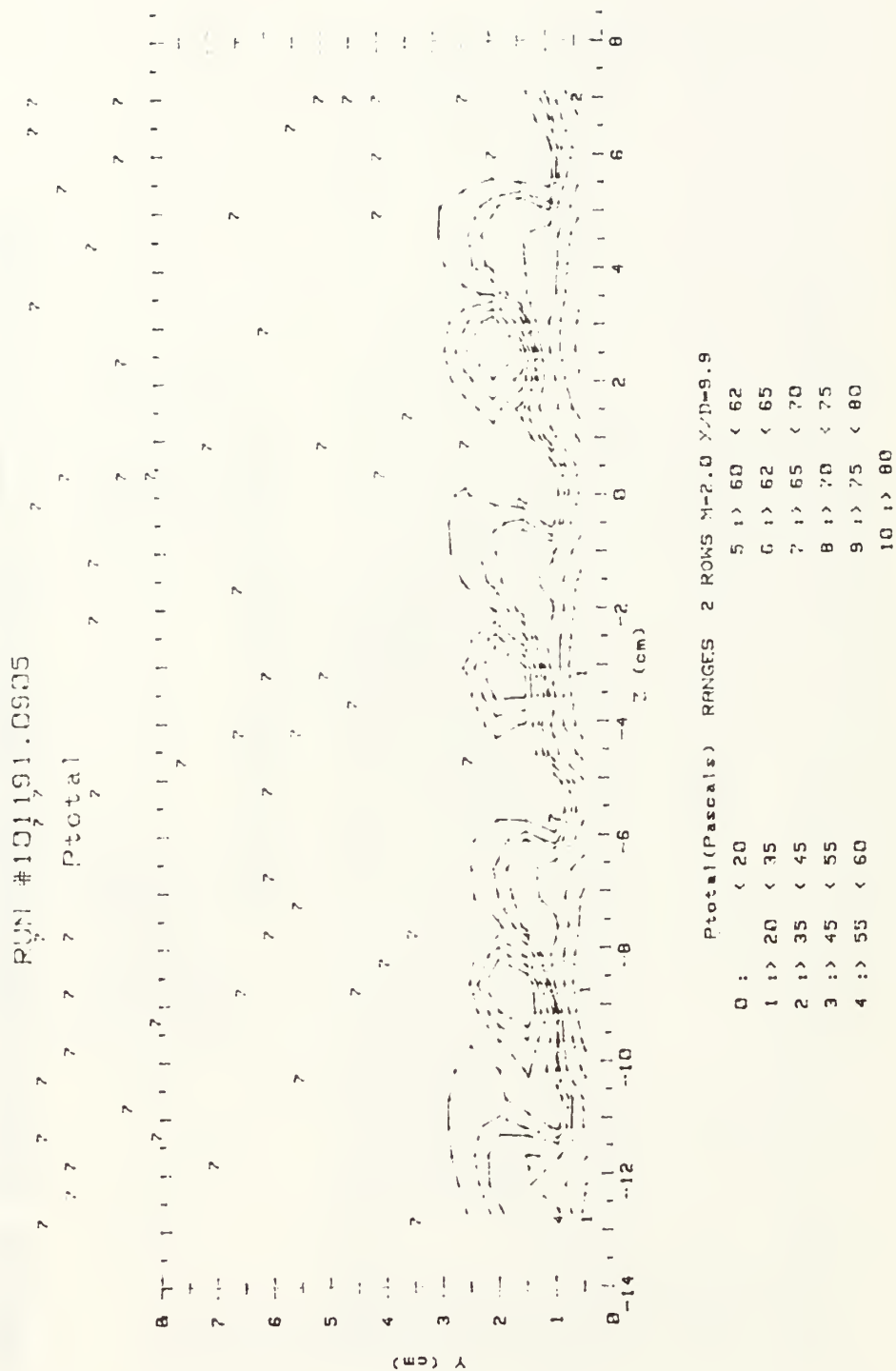


Figure 151. Streamwise Pressure Field, Compound Angle, 2 Rows, $m=2.0$, $x/d=9.9$

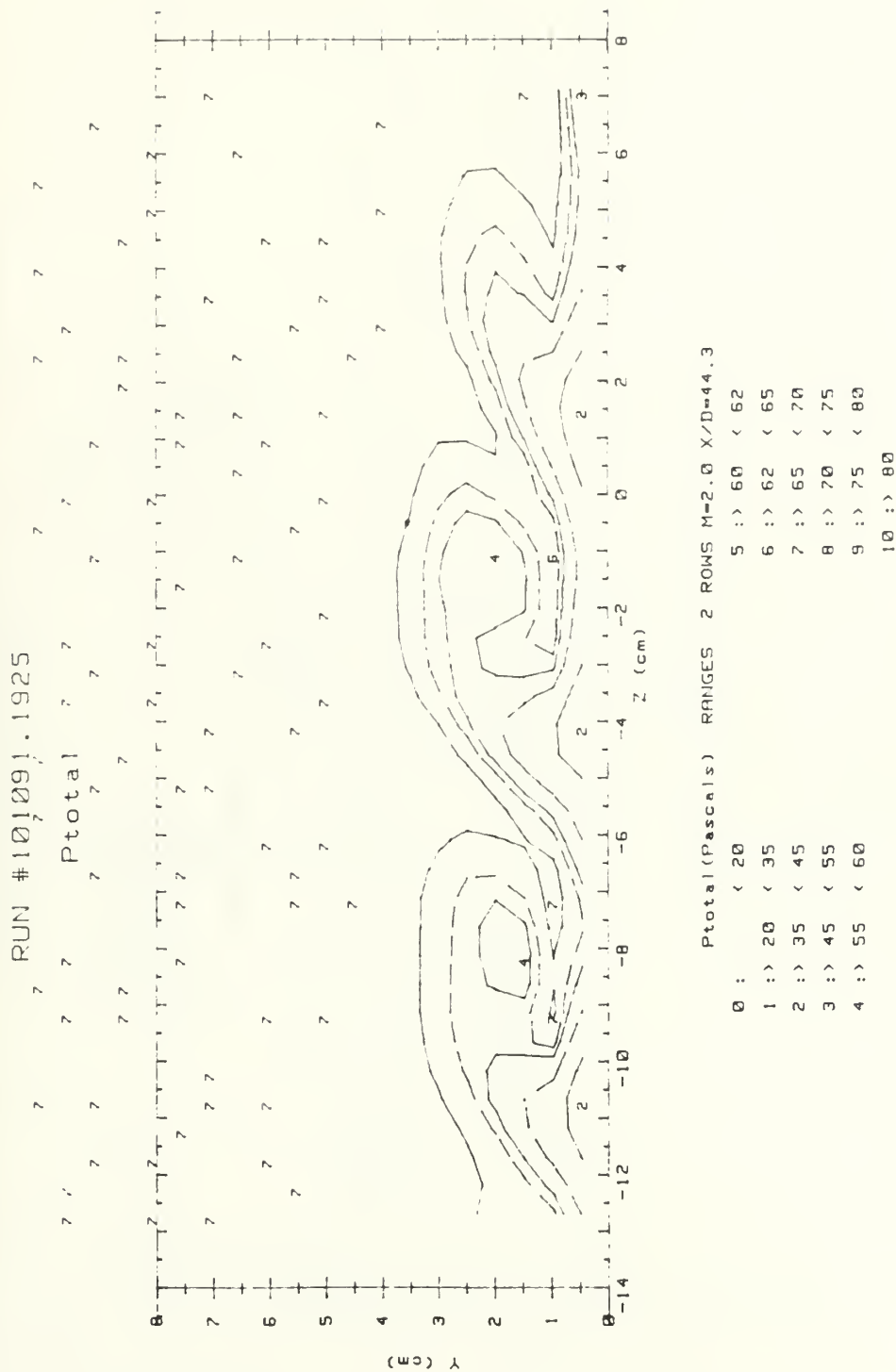
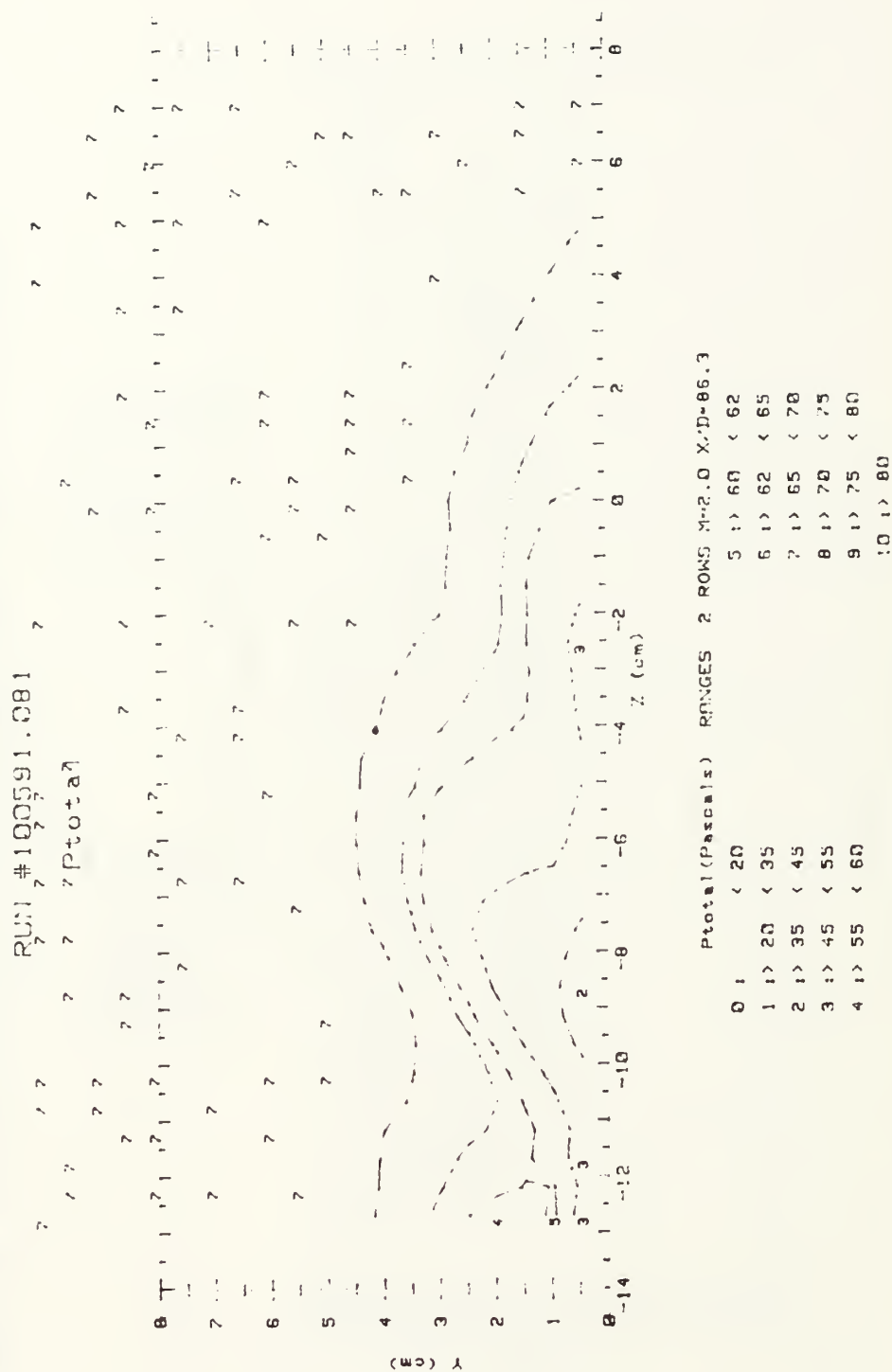


Figure 152. Streamwise Pressure Field, Compound Angle, 2 Rows, $m=2.0$, $x/d=44.3$



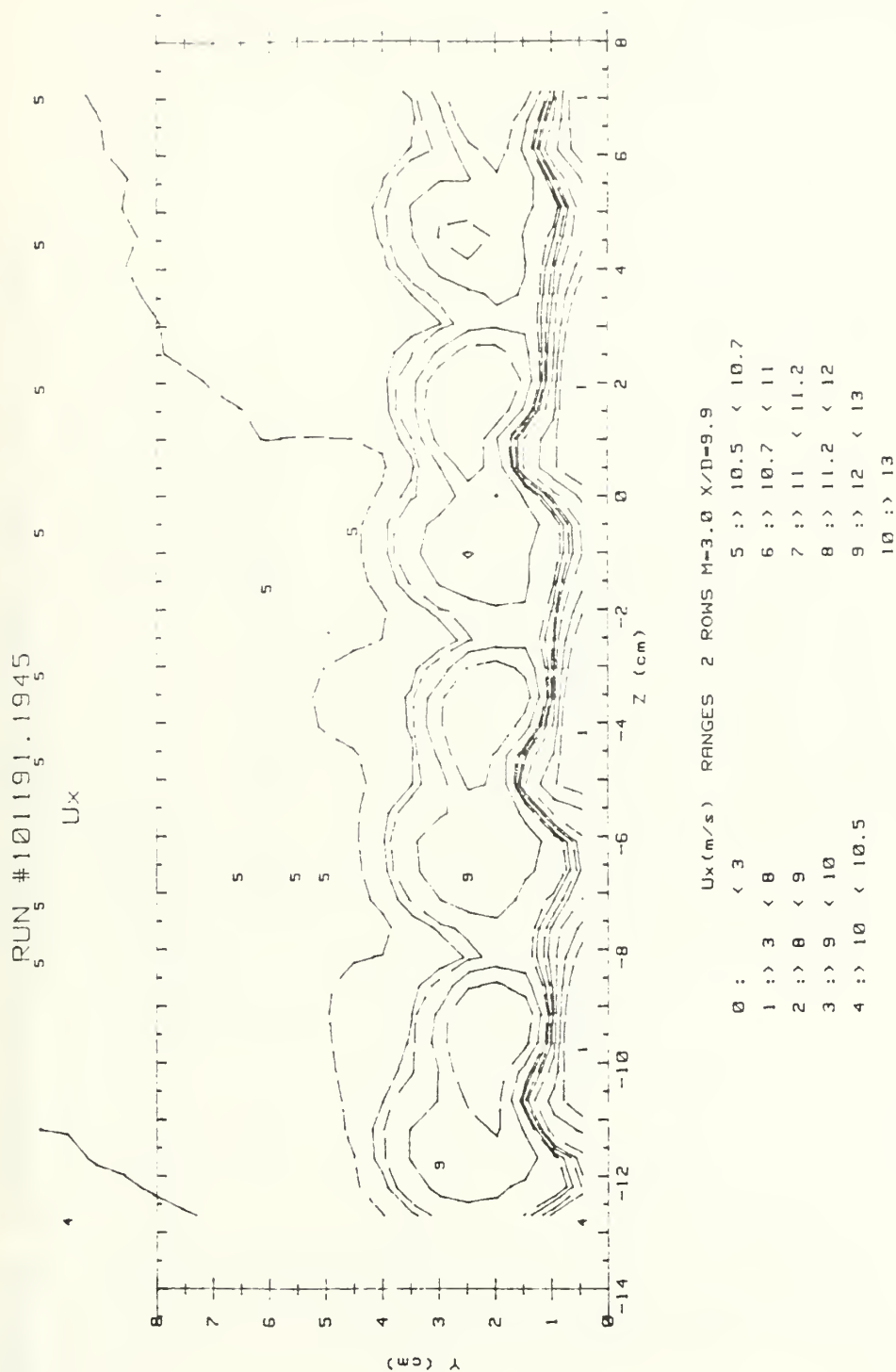
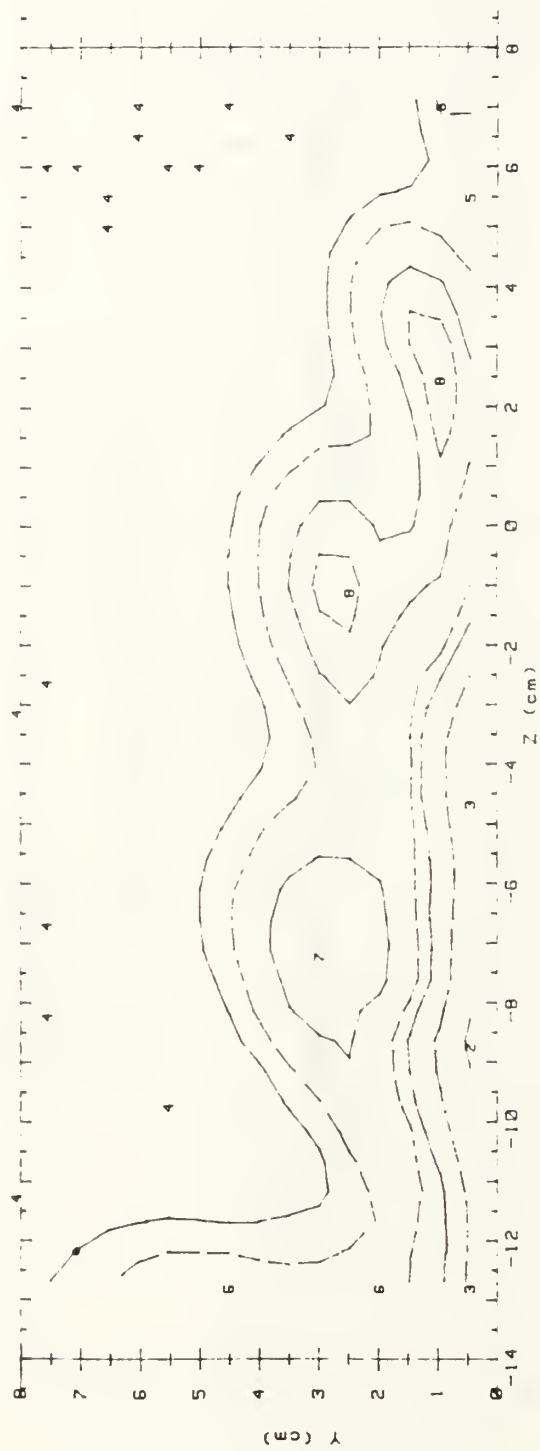


Figure 154. Streamwise Velocity Field, Compound Angle, 2 Rows, $m=3.0$, $x/d=9.9$

RUN #100691.0935

Ux



Ux (m/s) RANGES 2 ROWS M=3.0 X/D=44.3

0 :	< 3	5 :	10.5 < 10.7
1 :	3 < 8	6 :	10.7 < 11
2 :	8 < 9	7 :	11 < 11.2
3 :	9 < 10	8 :	11.2 < 12
4 :	10 < 10.5	9 :	12 < 13
		10 :	13

Figure 155. Streamwise Velocity Field, Compound Angle, 2 Rows, $m=3.0$, $x/d=44.3$

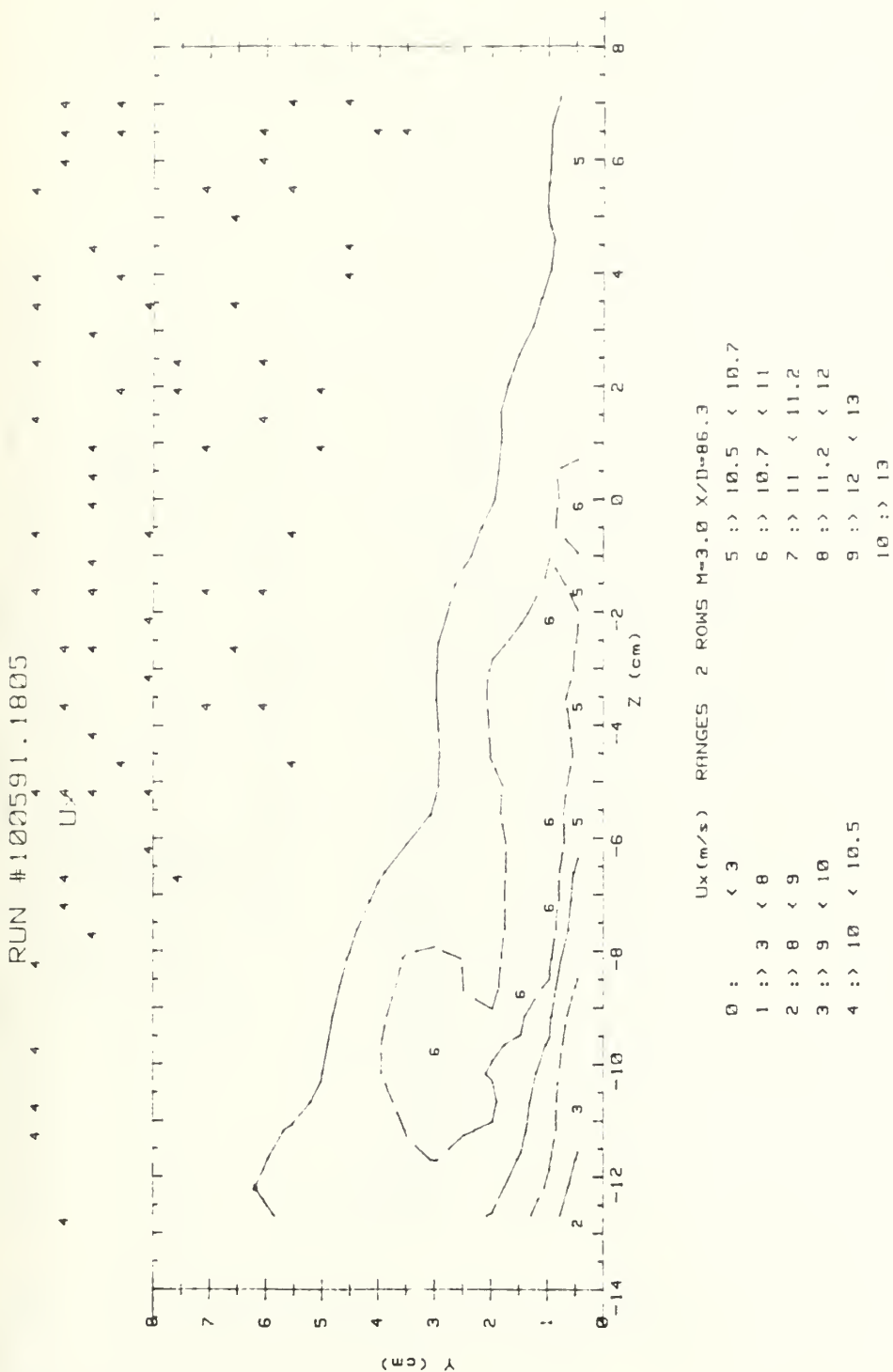


Figure 156. Streamwise Velocity Field, Compound Angle, 2 Rows, $m=3.0$, $x/d=86.3$

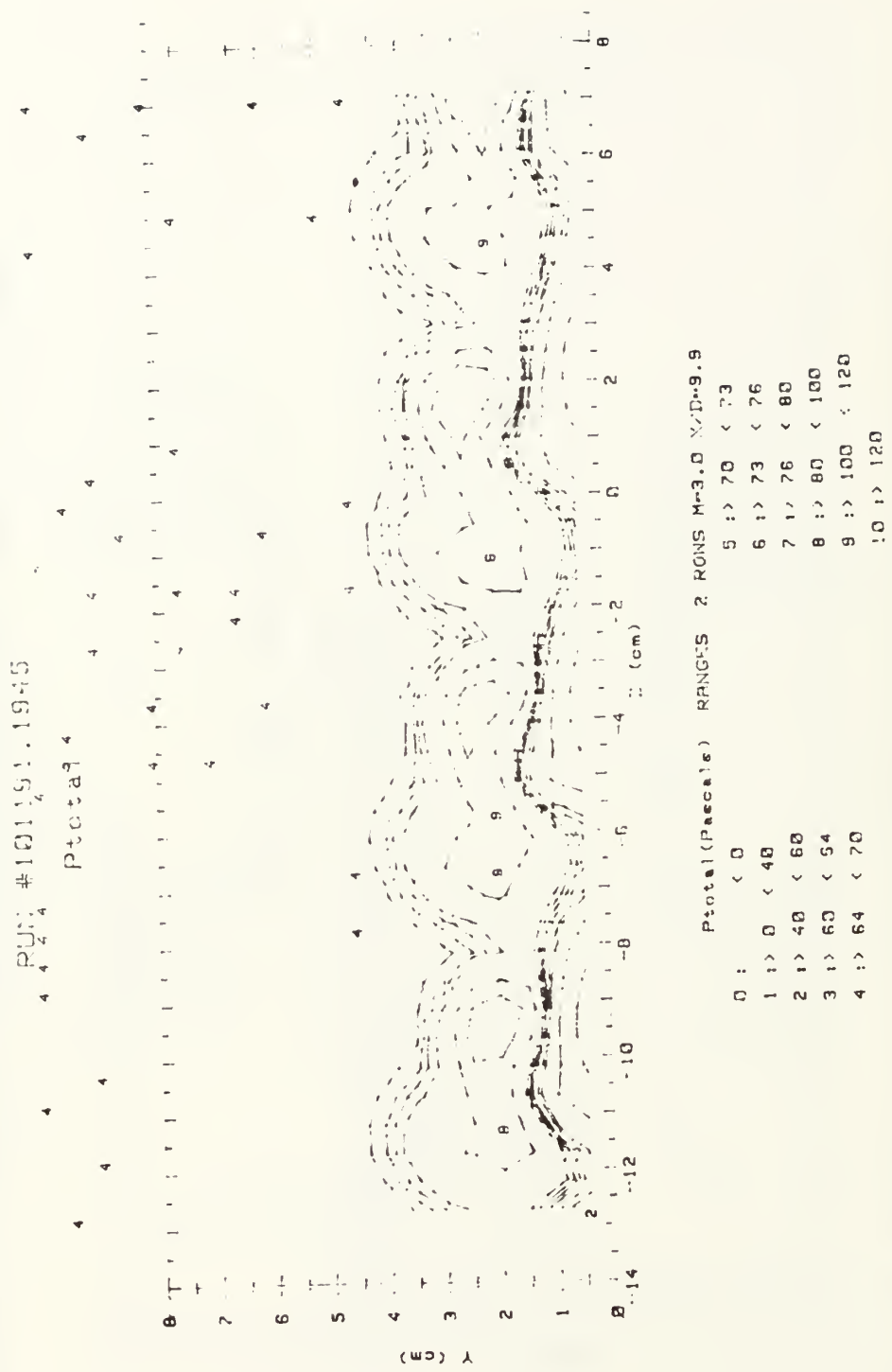


Figure 157. Streamwise Pressure Field, Compound Angle, 2 Rows, $m=3.0$, $x/d=9.9$

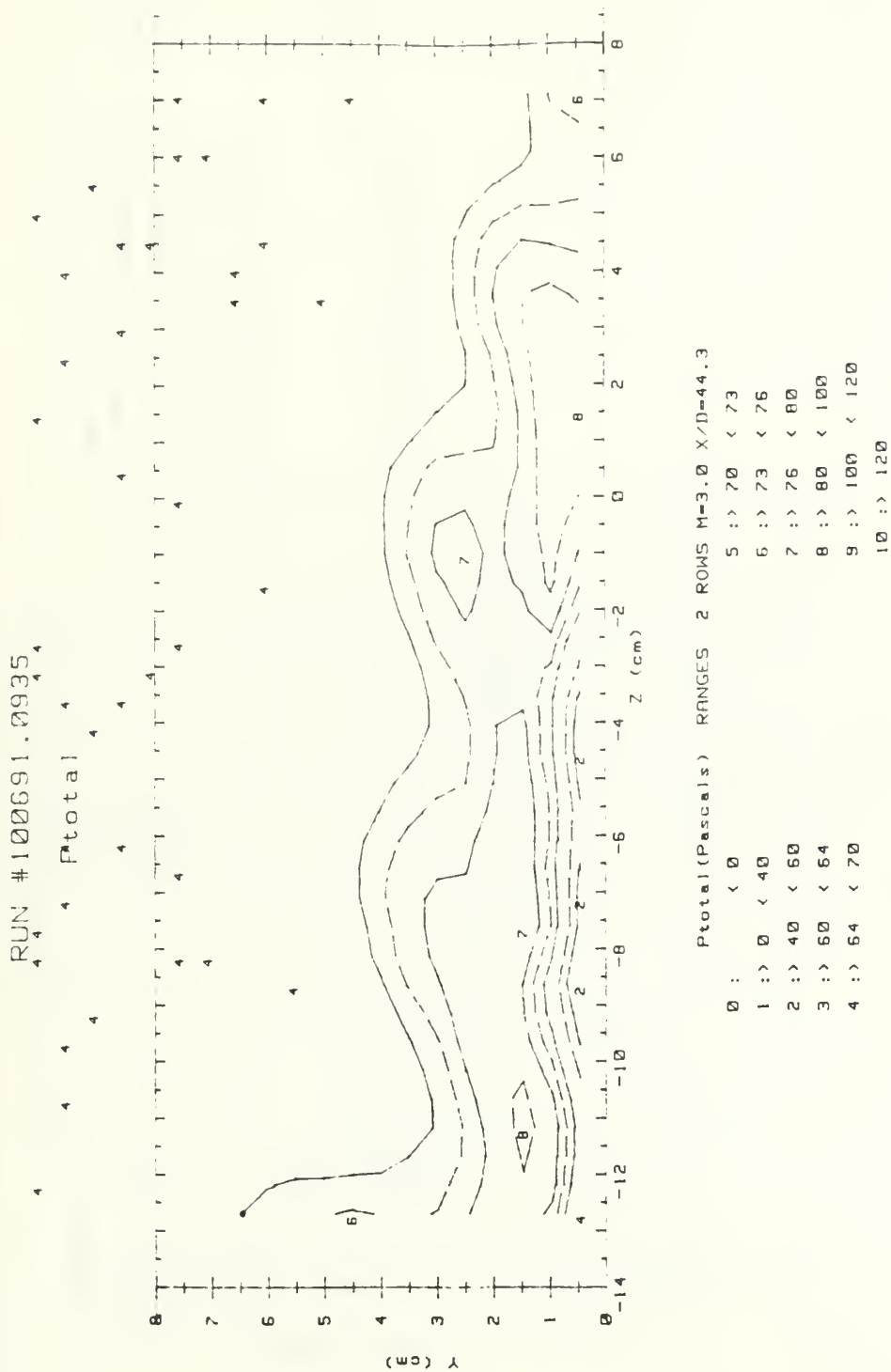
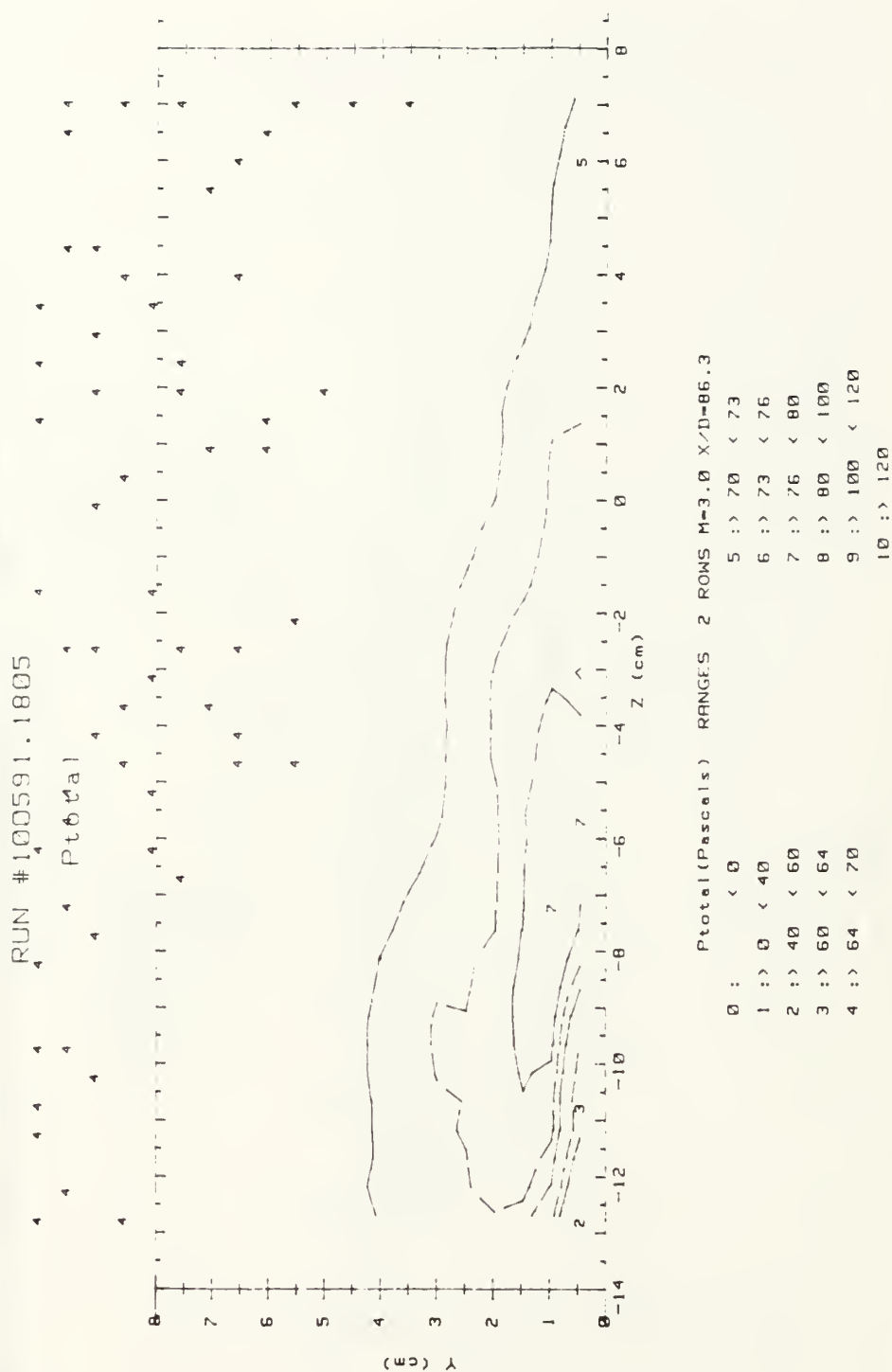


Figure 158. Streamwise Pressure Field, Compound Angle, 2 Rows, $m=3.0$, $x/d=44.3$



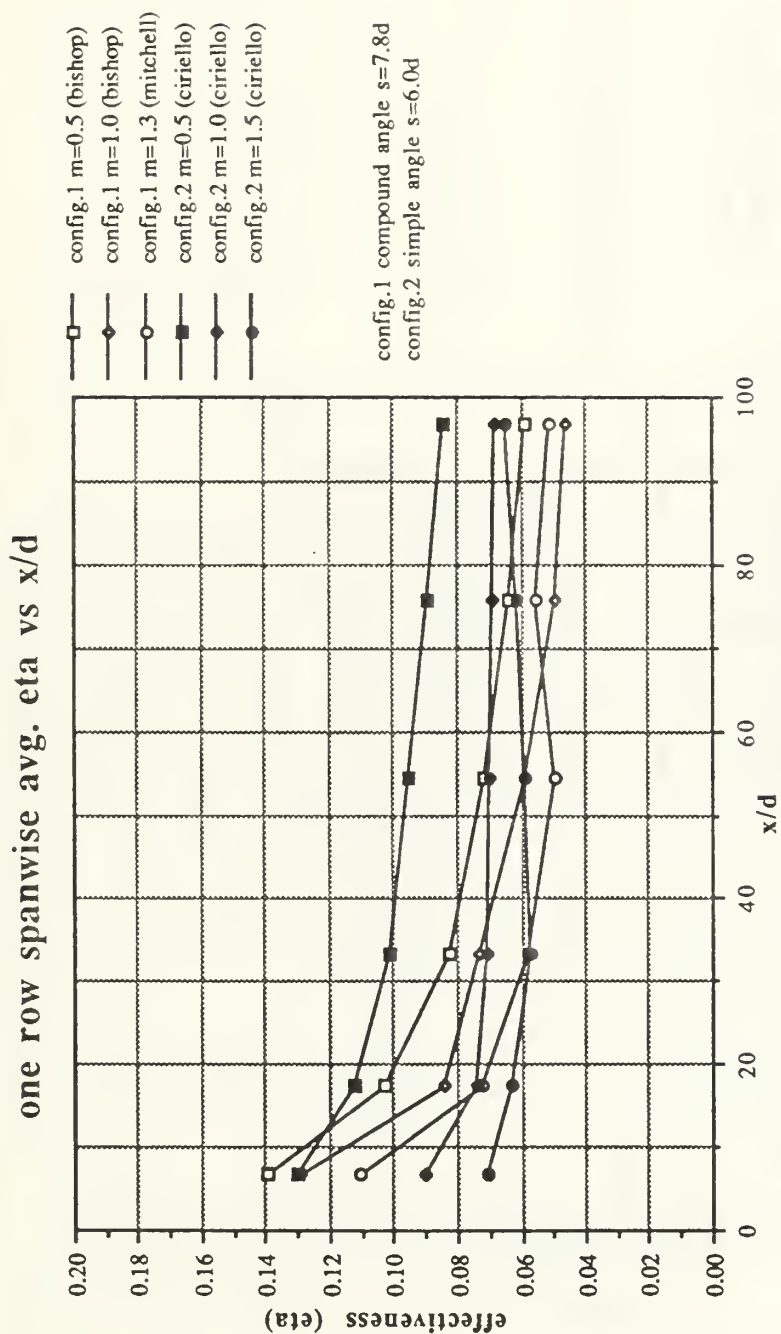


Figure 160. Spanwise Averaged $\bar{\eta}$ Versus x/d , Comparison of Configuration 1 to Configuration 2, $m=0.5$, 1.0, and 1.5, 1 Row

one row spanwise avg. St_f/St_0 vs x/d

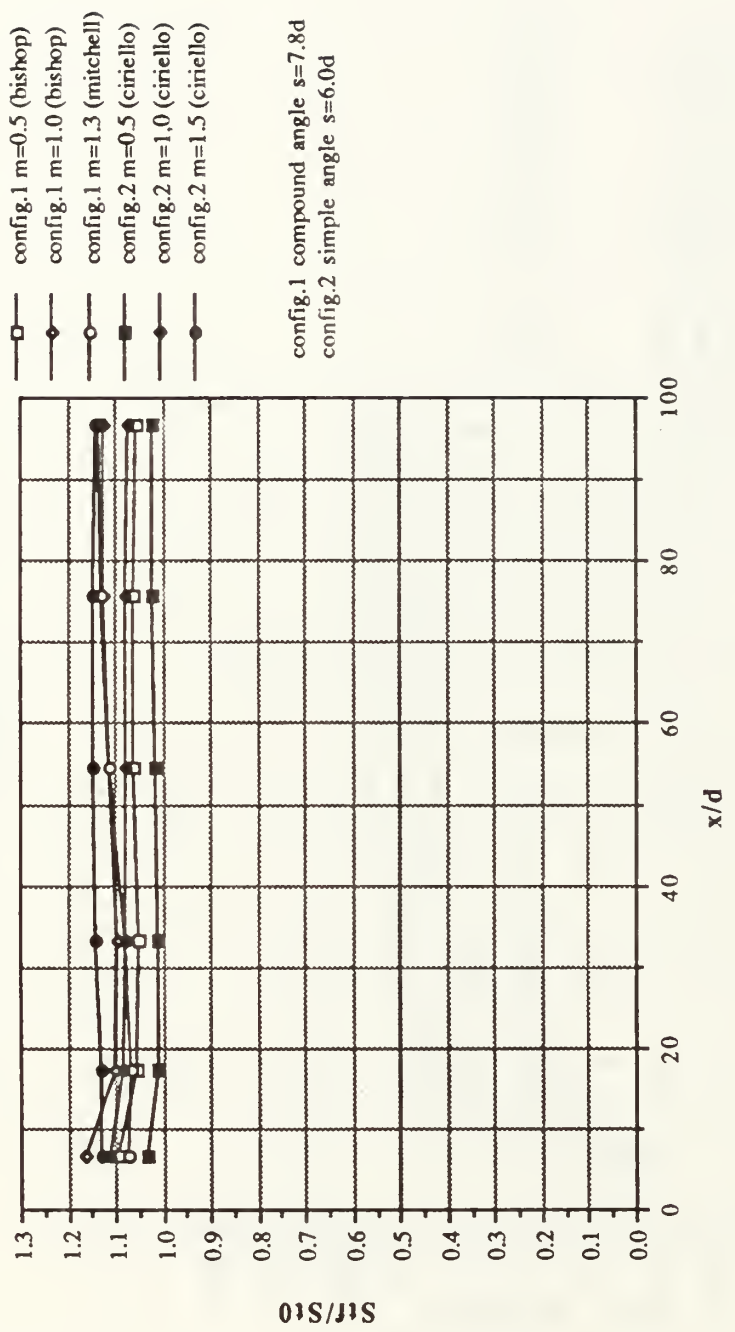


Figure 161. Spanwise Averaged St_f/St_0 Versus x/d , Comparison of Configuration 1 to Configuration 2, $m=0.5, 1.0$, and 1.5 , 1 Row

two row spanwise avg. η vs x/d

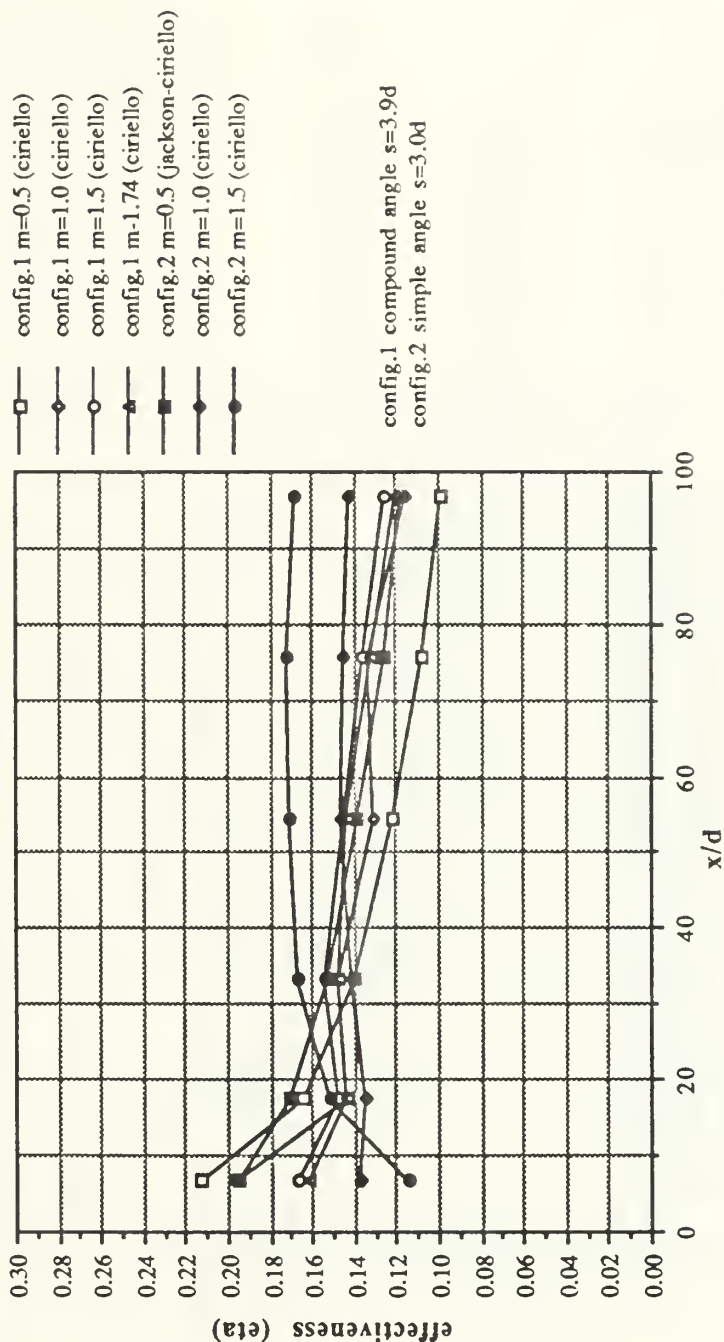


Figure 162. Spanwise Averaged $\bar{\eta}$ Versus x/d , Comparison of Configuration 1 to Configuration 2, $m=0.5$, 1.0, and 1.5, 2 Rows

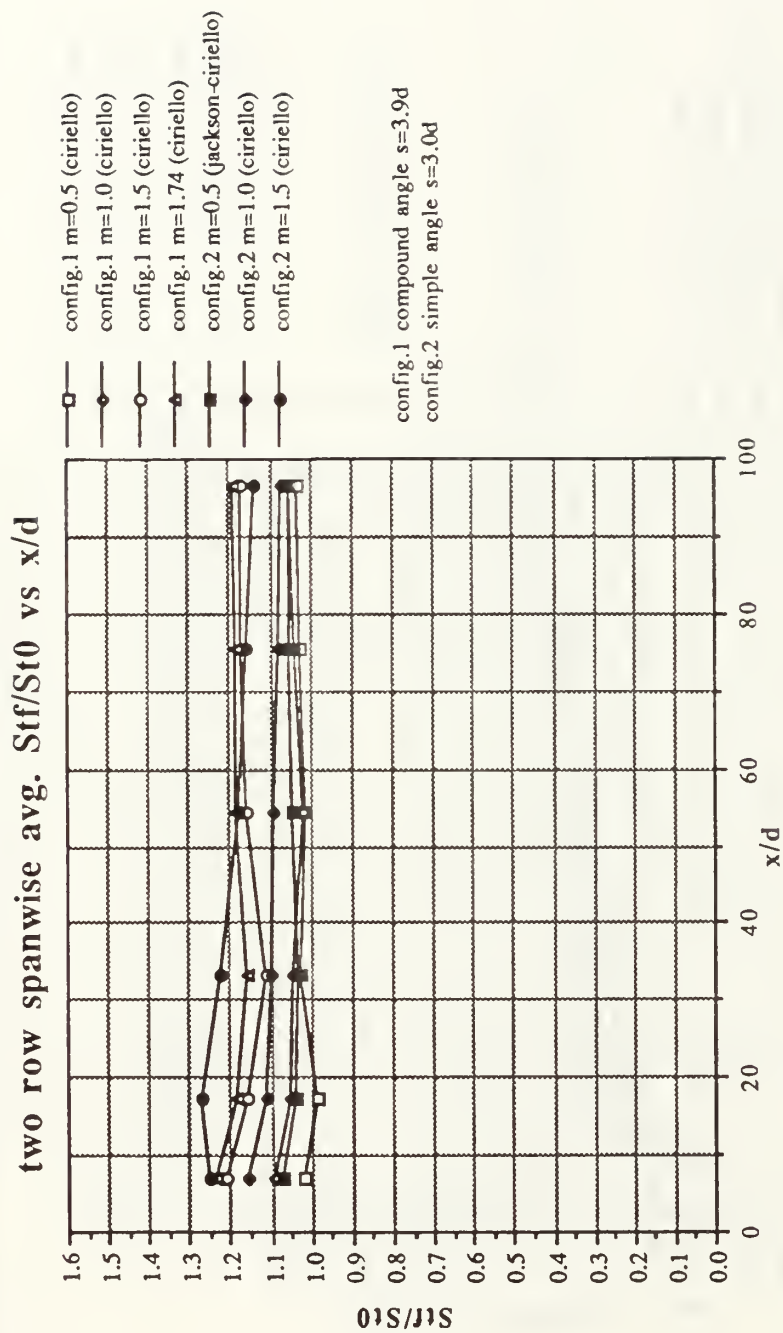


Figure 163. Spanwise Averaged St_f/St_0 Versus x/d , Comparison of Configuration 1 to Configuration 2, $m=0.5$, 1.0, and 1.5, 2 Rows

one row spanwise avg. η vs x/d

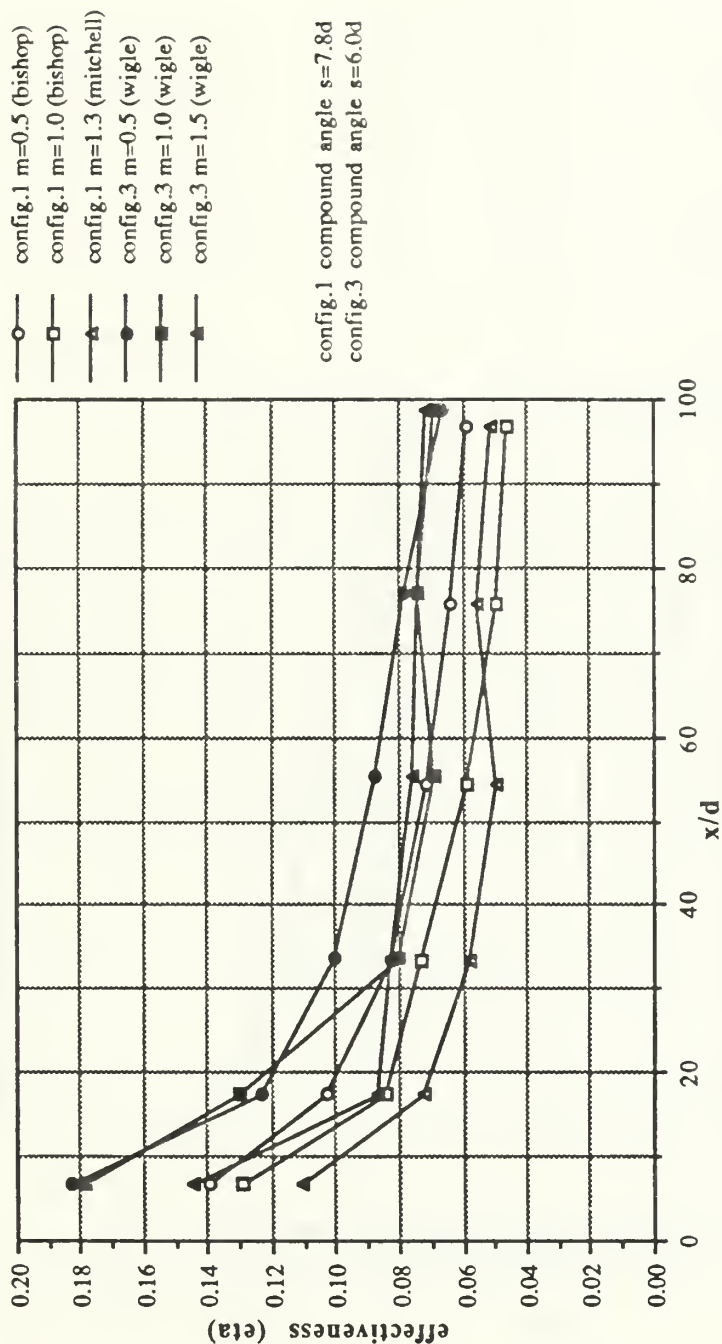


Figure 164. Spanwise Averaged $\bar{\eta}$ Versus x/d , Comparison of Configuration 1 to Configuration 3, $m=0.5$, 1.0, and 1.5, 1 Row

one row spanwise avg. St_f/St_0 vs x/d

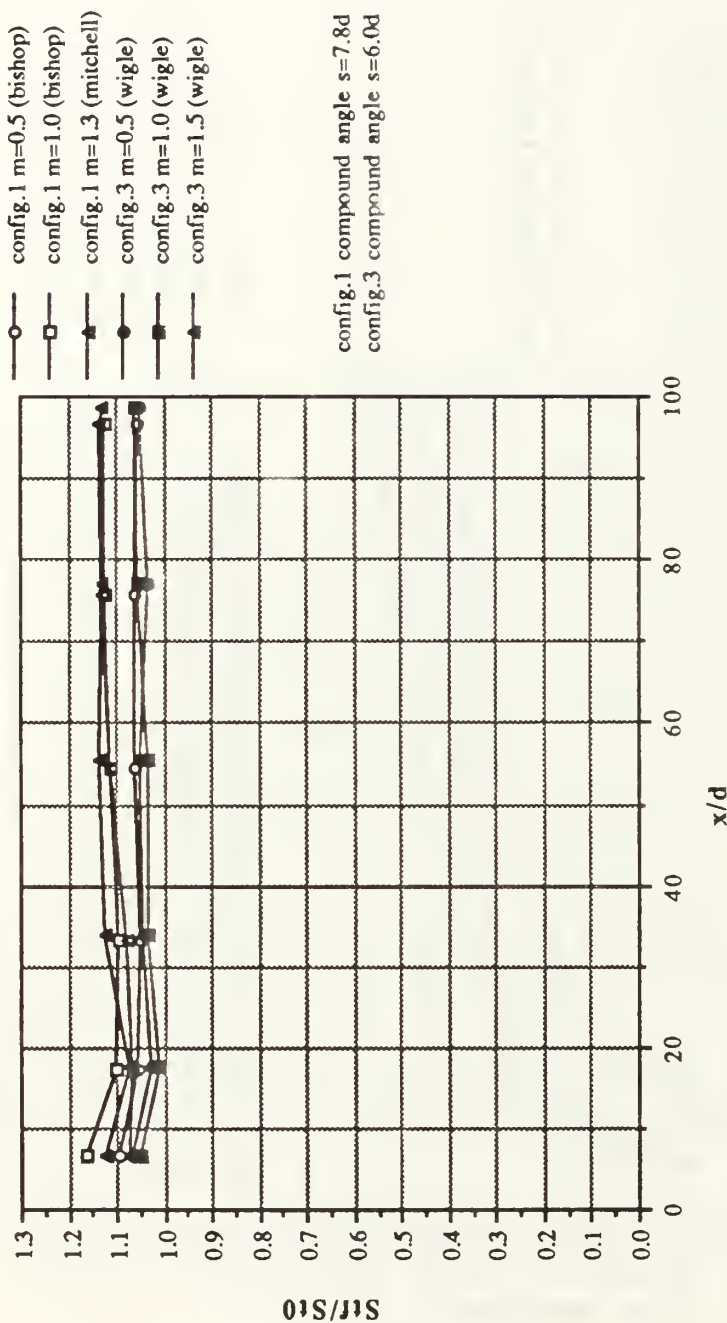


Figure 165. Spanwise Averaged St_f/St_0 Versus x/d , Comparison of Configuration 1 to Configuration 3, $m=0.5, 1.0$, and 1.5 , 1 Row

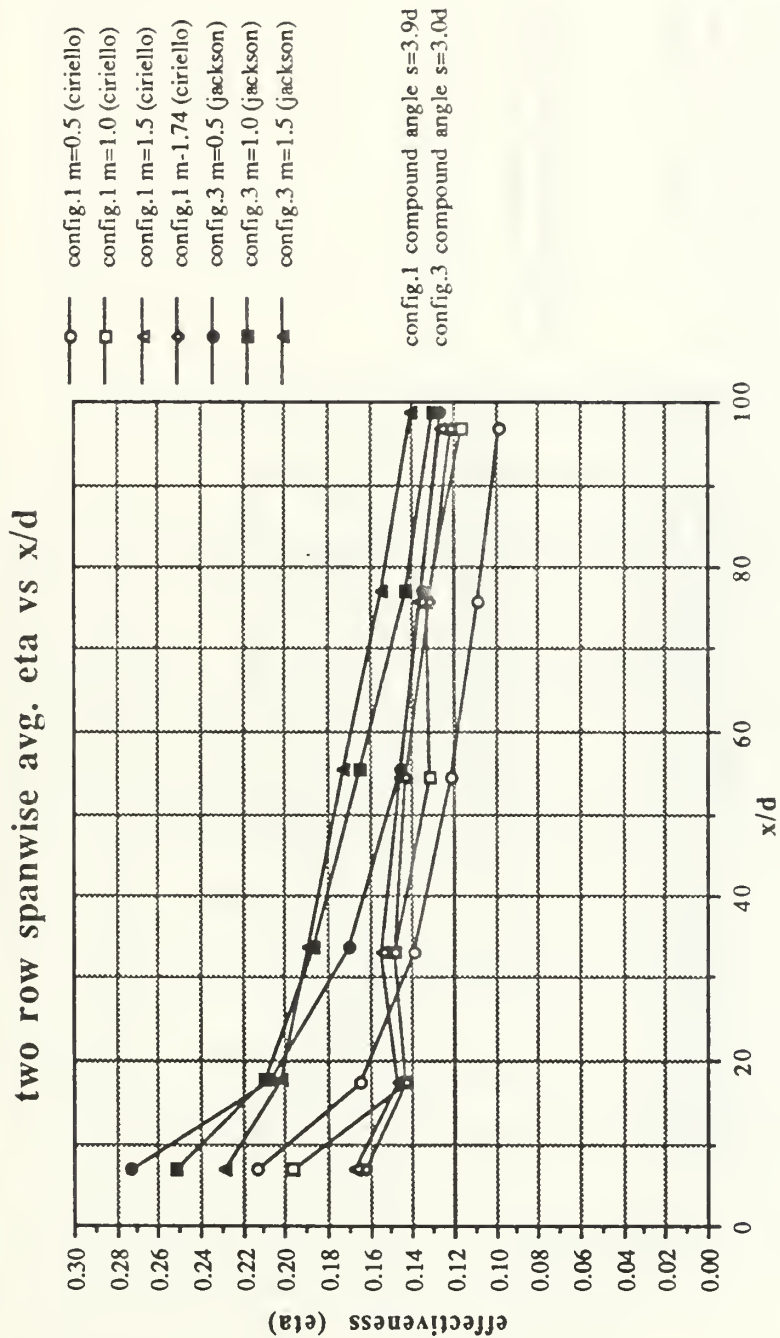


Figure 166. Spanwise Averaged $\bar{\eta}$ Versus x/d , Comparison of Configuration 1 to Configuration 3, $m=0.5$, 1.0, and 1.5, 2 Rows

two row spanwise avg. St_f/St_0 vs x/d

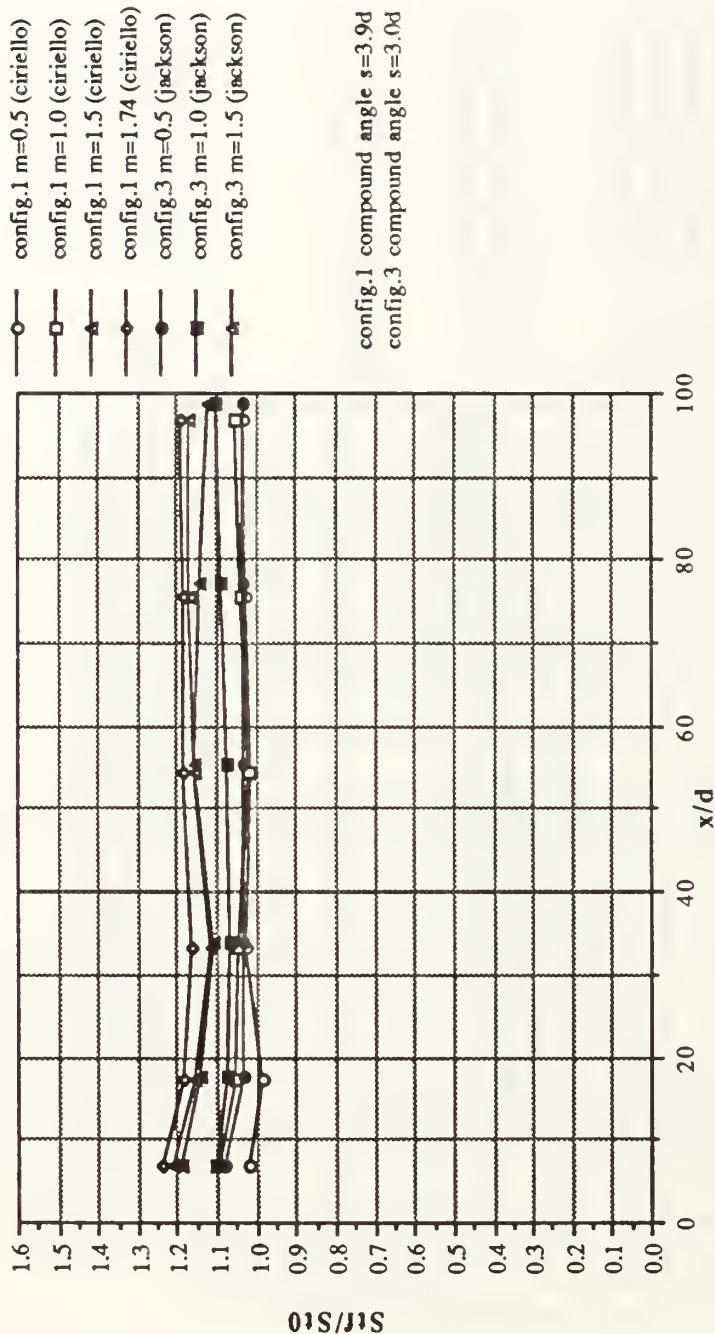


Figure 167. Spanwise Averaged St_f/St_0 Versus x/d , Comparison of Configuration 1 to Configuration 3, $m=0.5$, 1.0, and 1.5, 2 Rows

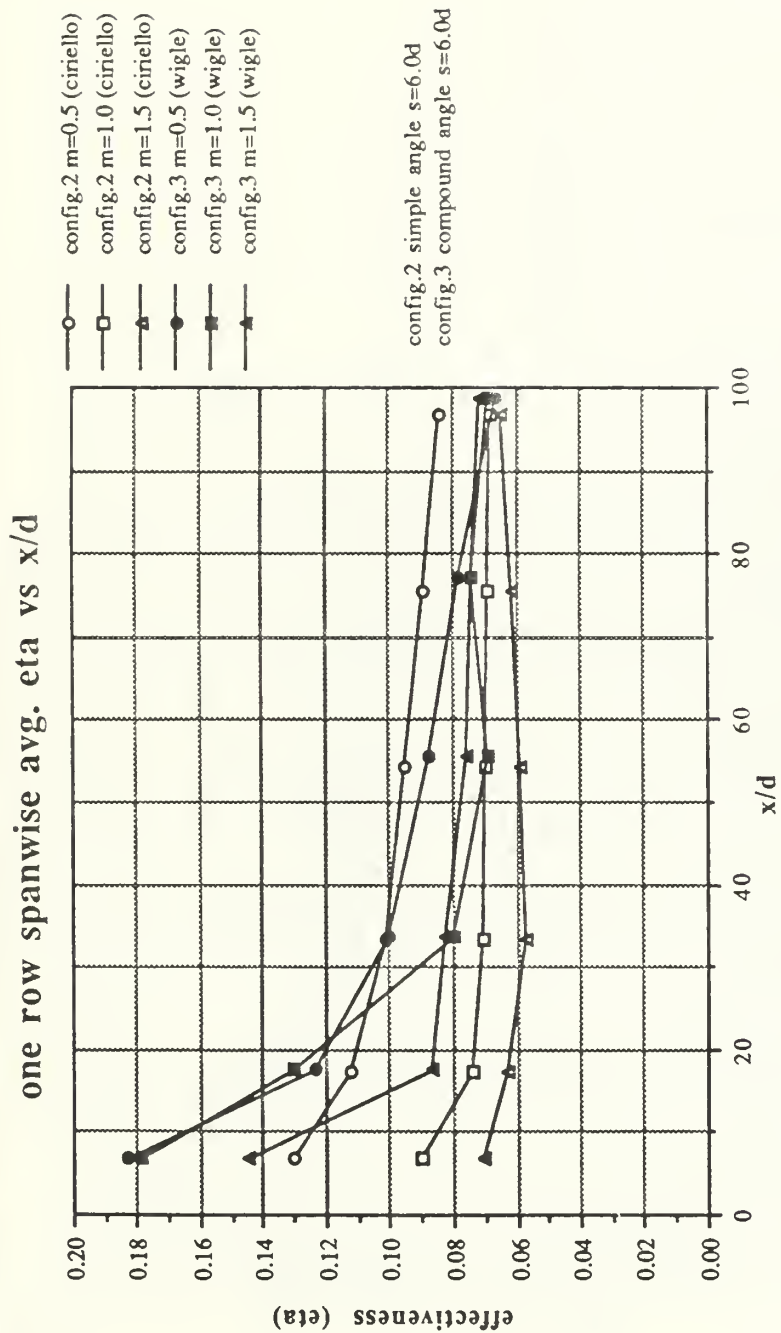


Figure 168. Spanwise Averaged $\bar{\eta}$ Versus x/d , Comparison of Configuration 2 to Configuration 3, $m=0.5$, 1.0, and 1.5, 1 Row

one row spanwise avg. St_f/St_0 vs x/d

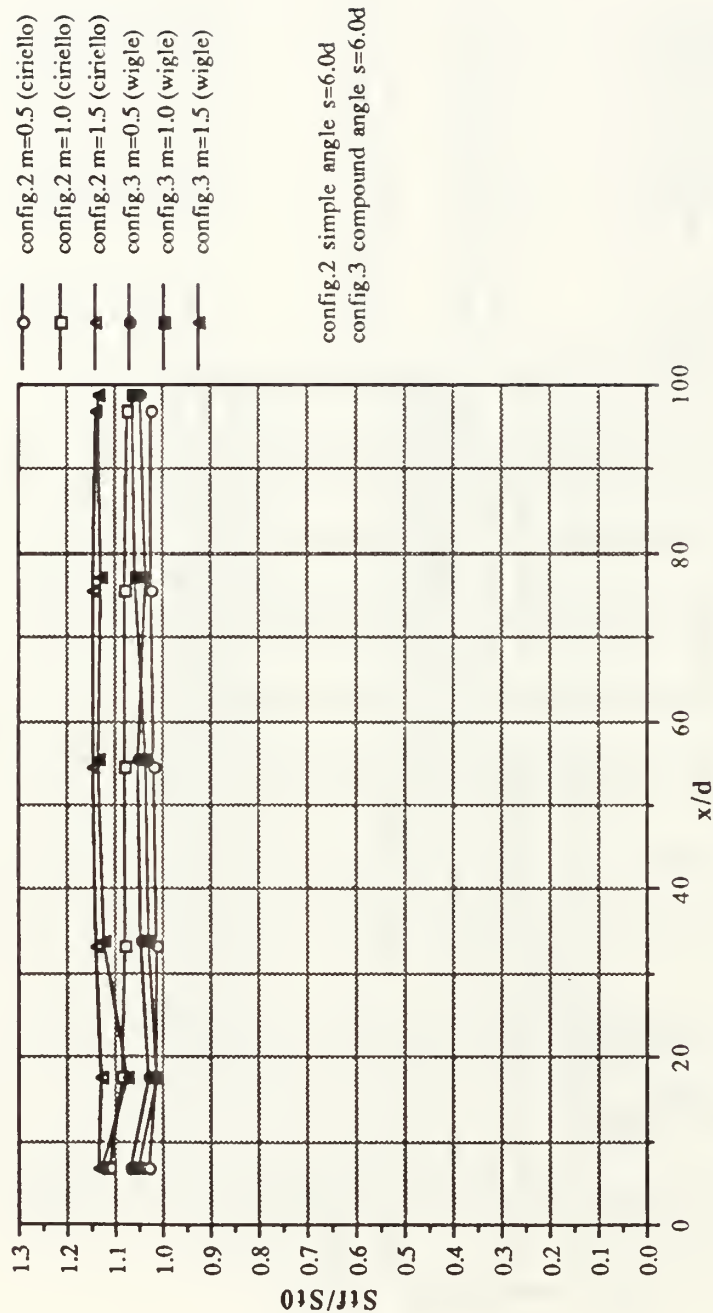


Figure 169. Spanwise Averaged St_f/St_0 Versus x/d , Comparison of Configuration 2 to Configuration 3, $m=0.5, 1.0$, and 1.5 , 1 Row

two row spanwise avg. eta vs x/d

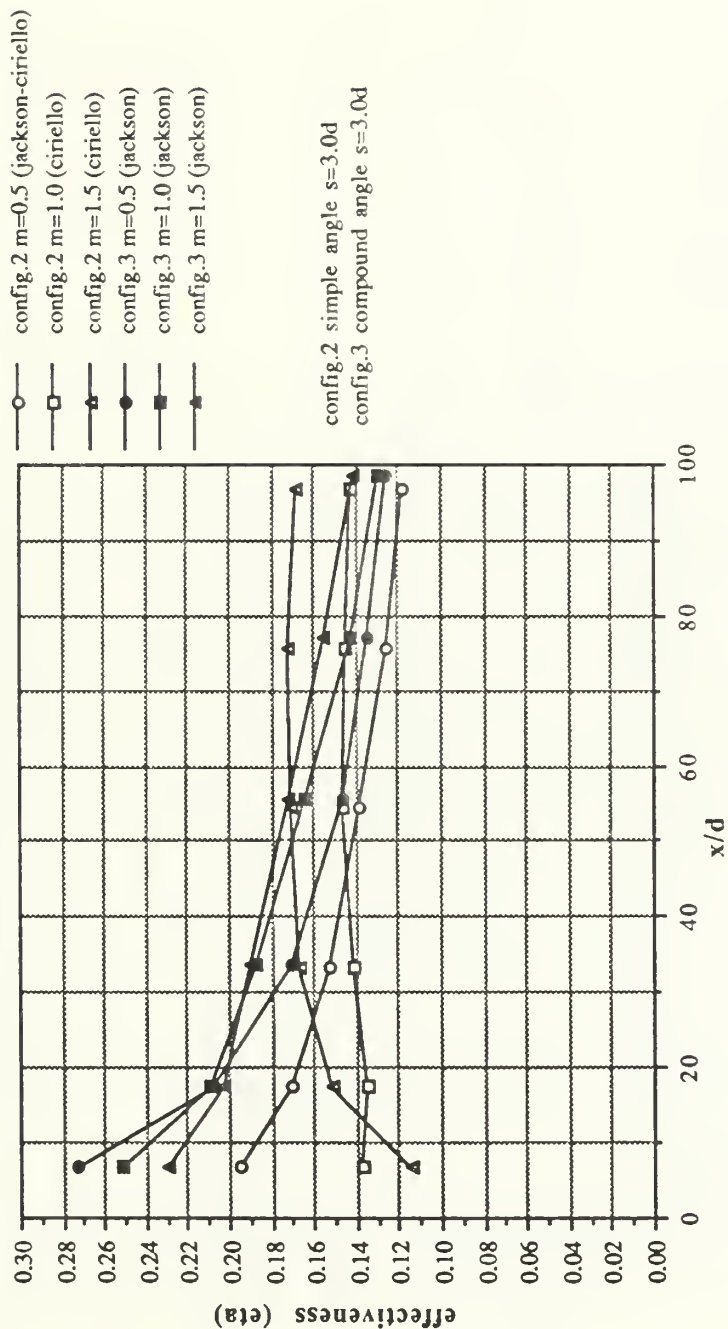


Figure 170. Spanwise Averaged $\bar{\eta}$ Versus x/d , Comparison of Configuration 2 to Configuration 3, $m=0.5, 1.0$, and 1.5 , 2 Rows

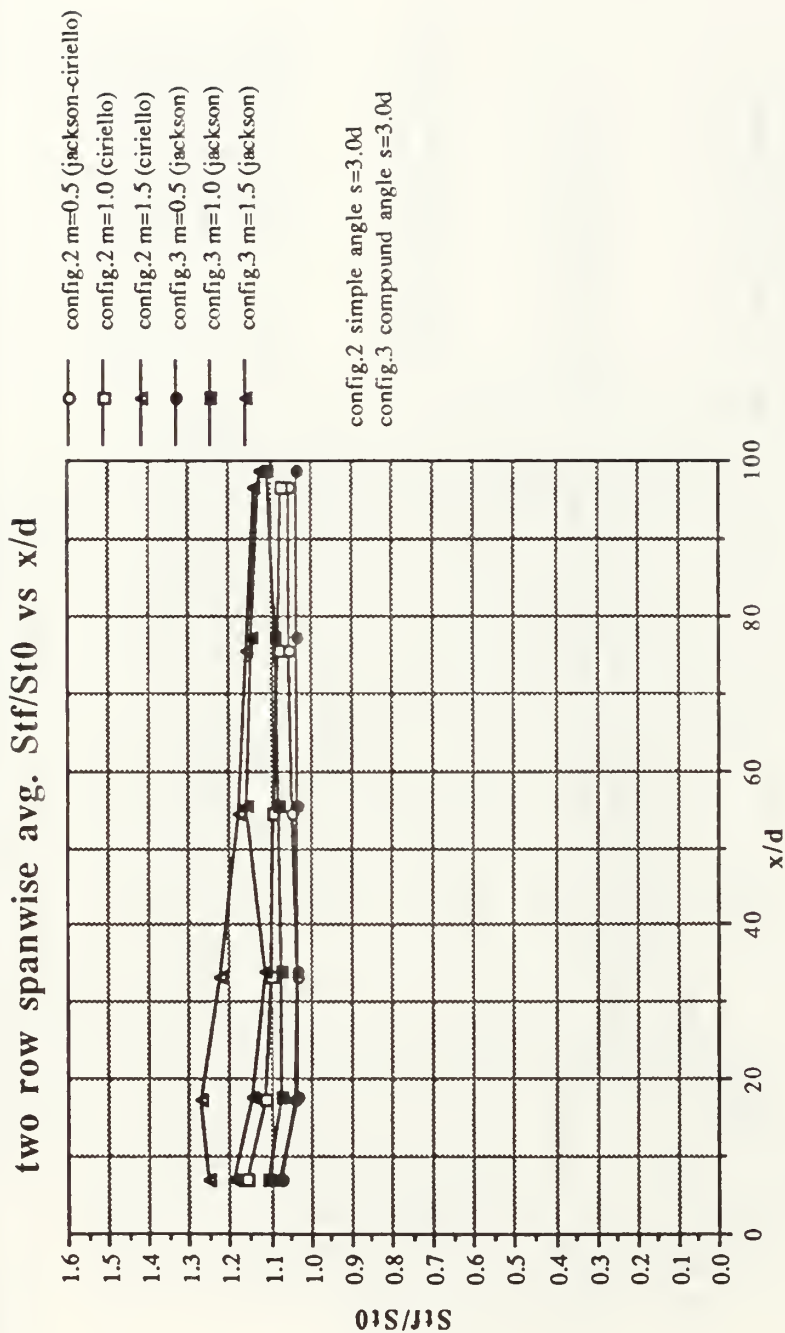


Figure 171. Spanwise Averaged St_f/St_0 Versus x/d , Comparison of Configuration 2 to Configuration 3, $m=0.5$, 1.0, and 1.5, 2 Rows

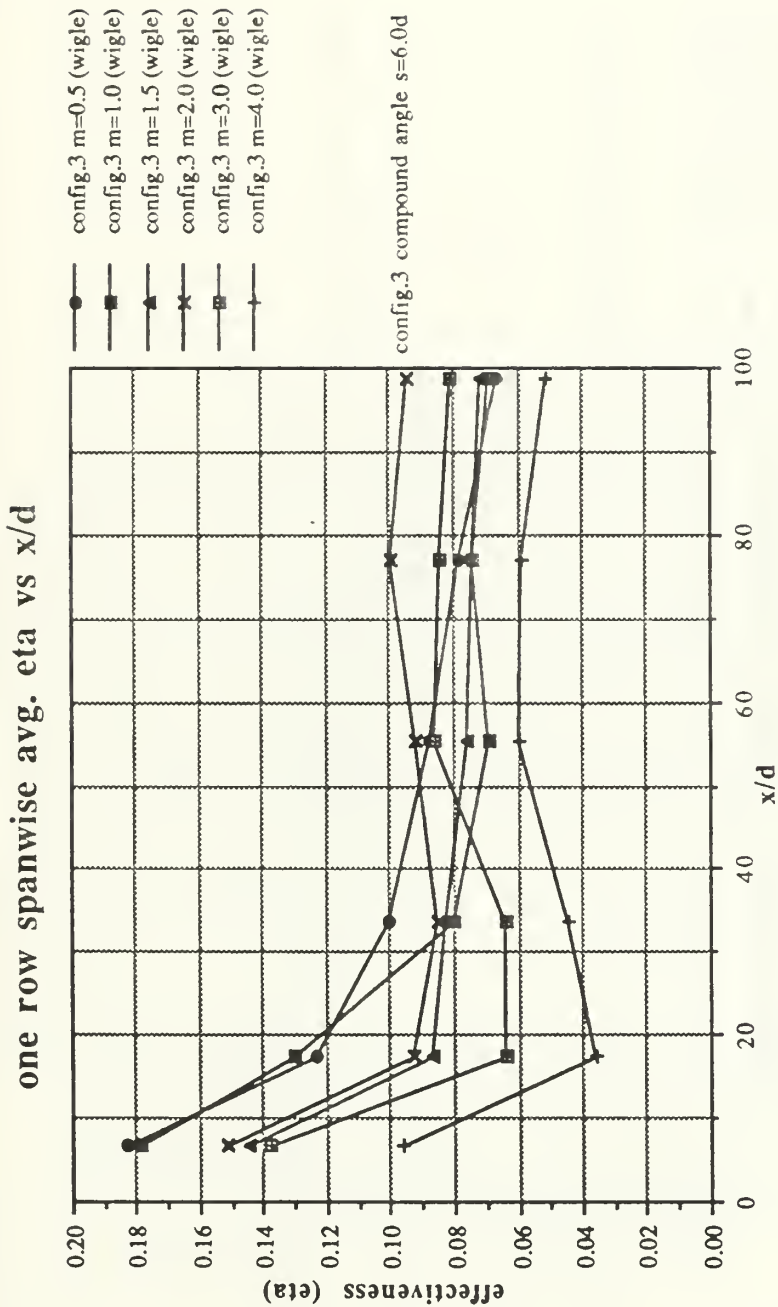


Figure 172. Spanwise Averaged $\bar{\eta}$ Versus x/d , Comparison of Different Blowing Ratios for Configuration 3, 1 Row

one row spanwise avg. St_f/St_0 vs x/d

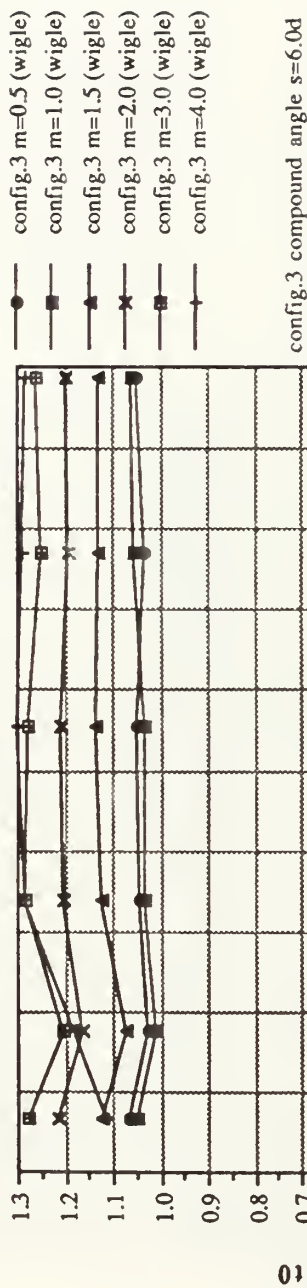


Figure 173. Spanwise Averaged St_f/St_0 Versus x/d , Comparison of Different Blowing Ratios for Configuration 3, 1 Row

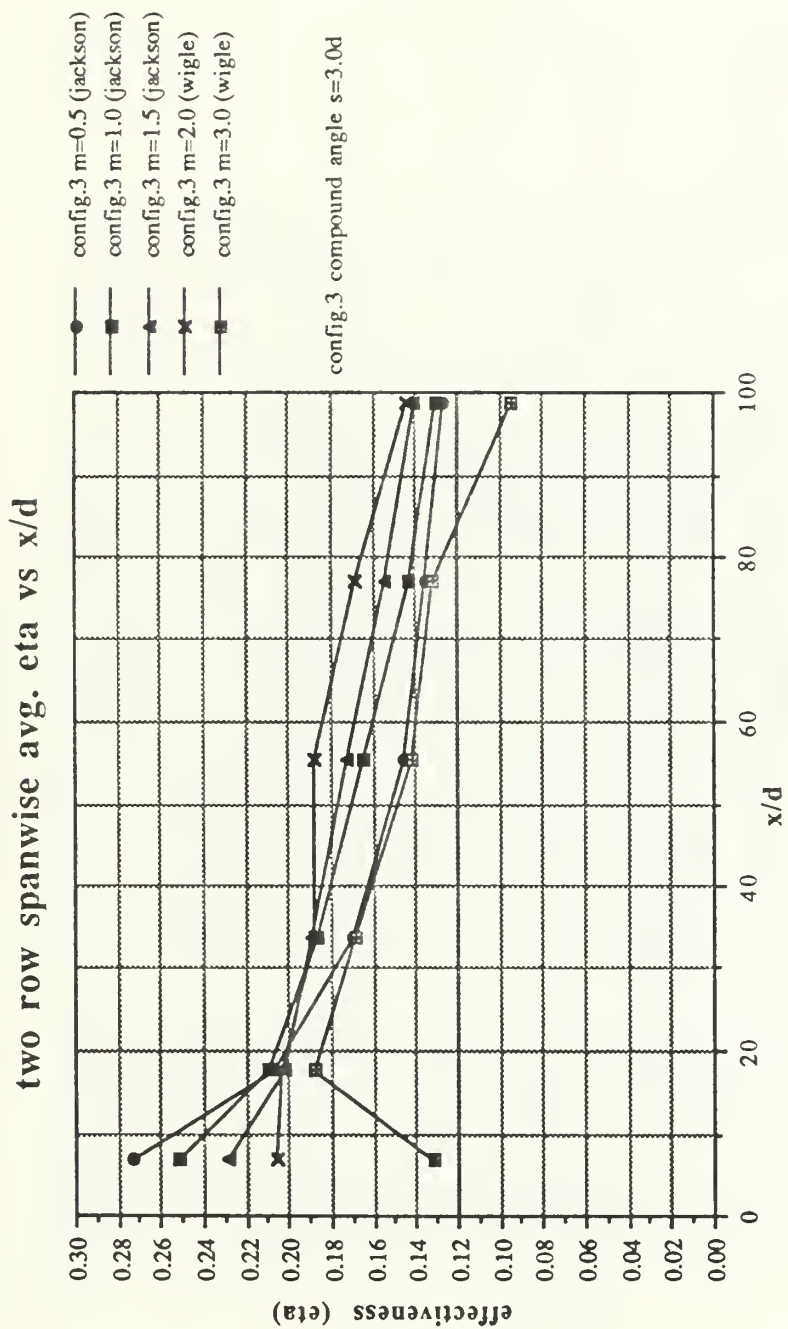


Figure 174. Spanwise Averaged $\bar{\eta}$ Versus x/d , Comparison of Different Blowing Ratios for Configuration 3, 2 Rows

two row spanwise avg. St_f/St_0 vs x/d

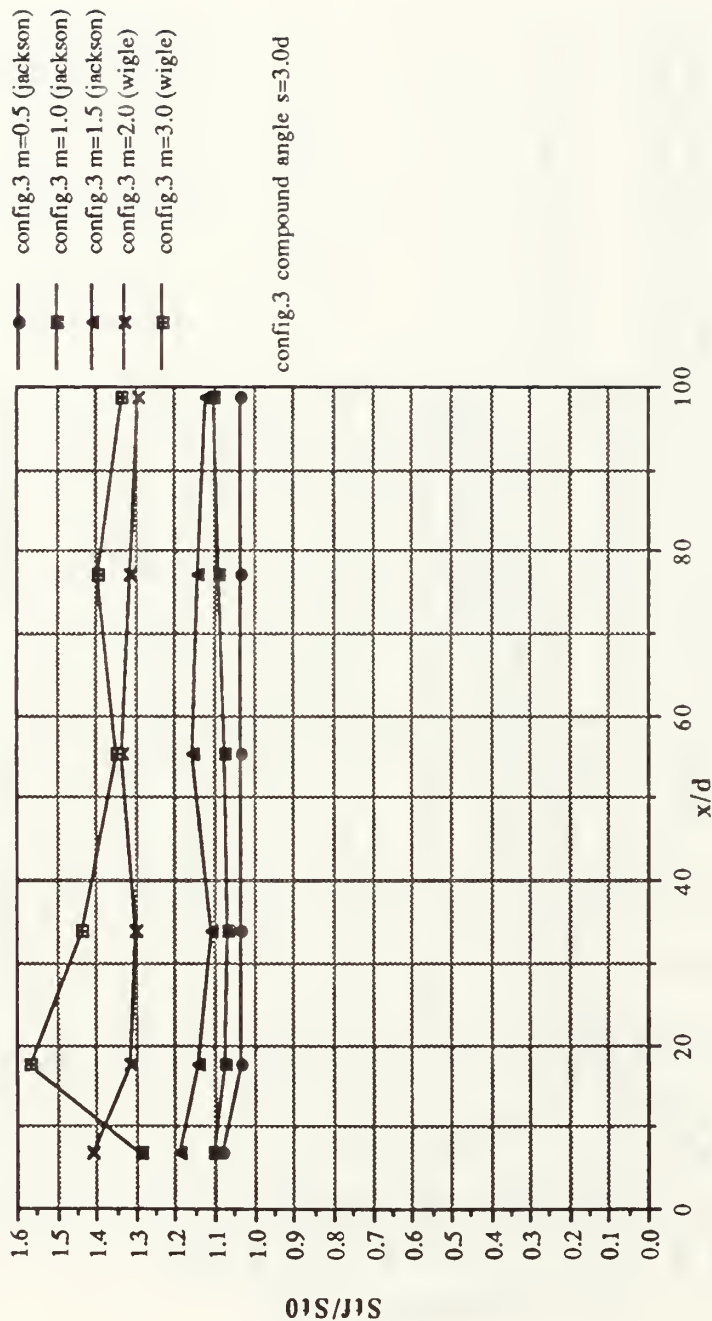


Figure 175. Spanwise Averaged St_f/St_0 Versus x/d , Comparison of Different Blowing Ratios for Configuration 3, 2 Rows

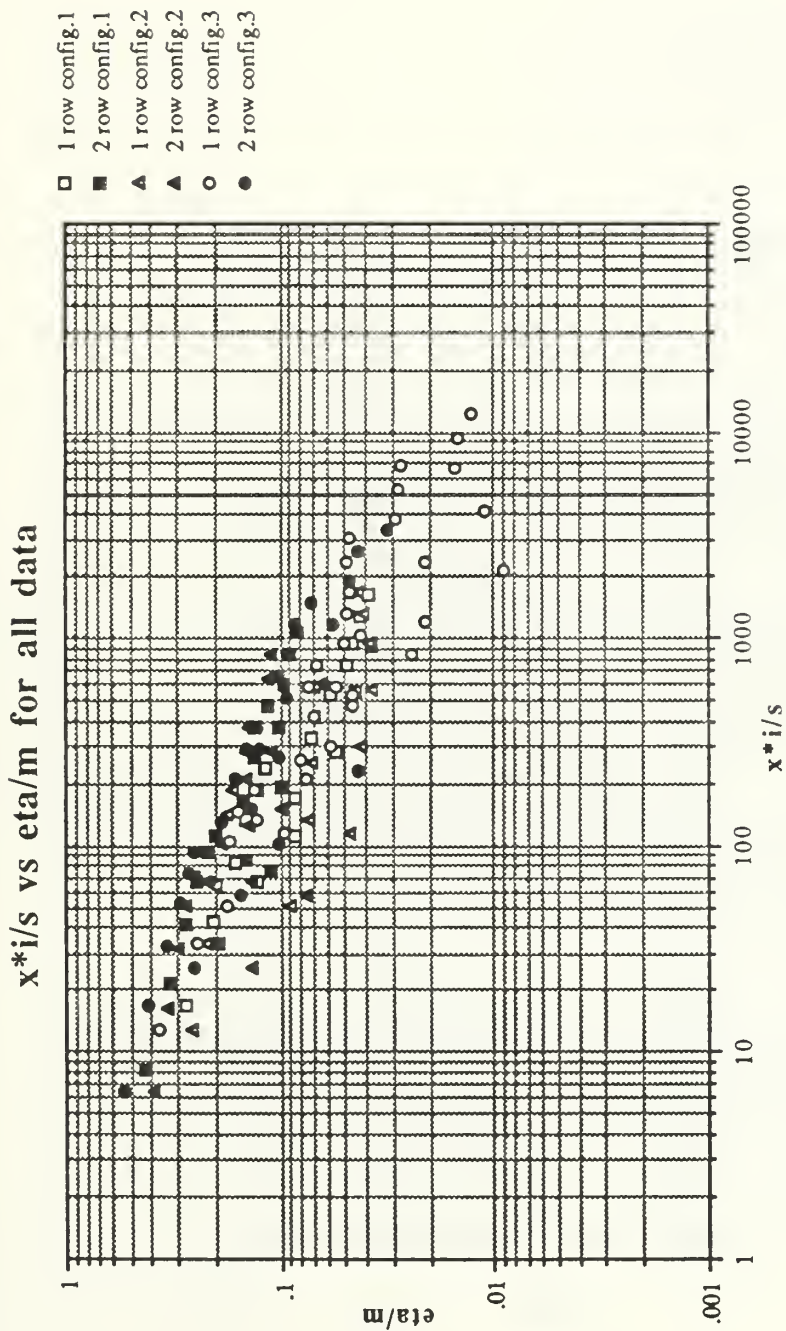


Figure 176. $\bar{\eta}/m$ Versus x^*l/s , Correlation Plot of Configurations 1, 2, and 3, All Blowing Ratios, 1 Row and 2 Rows

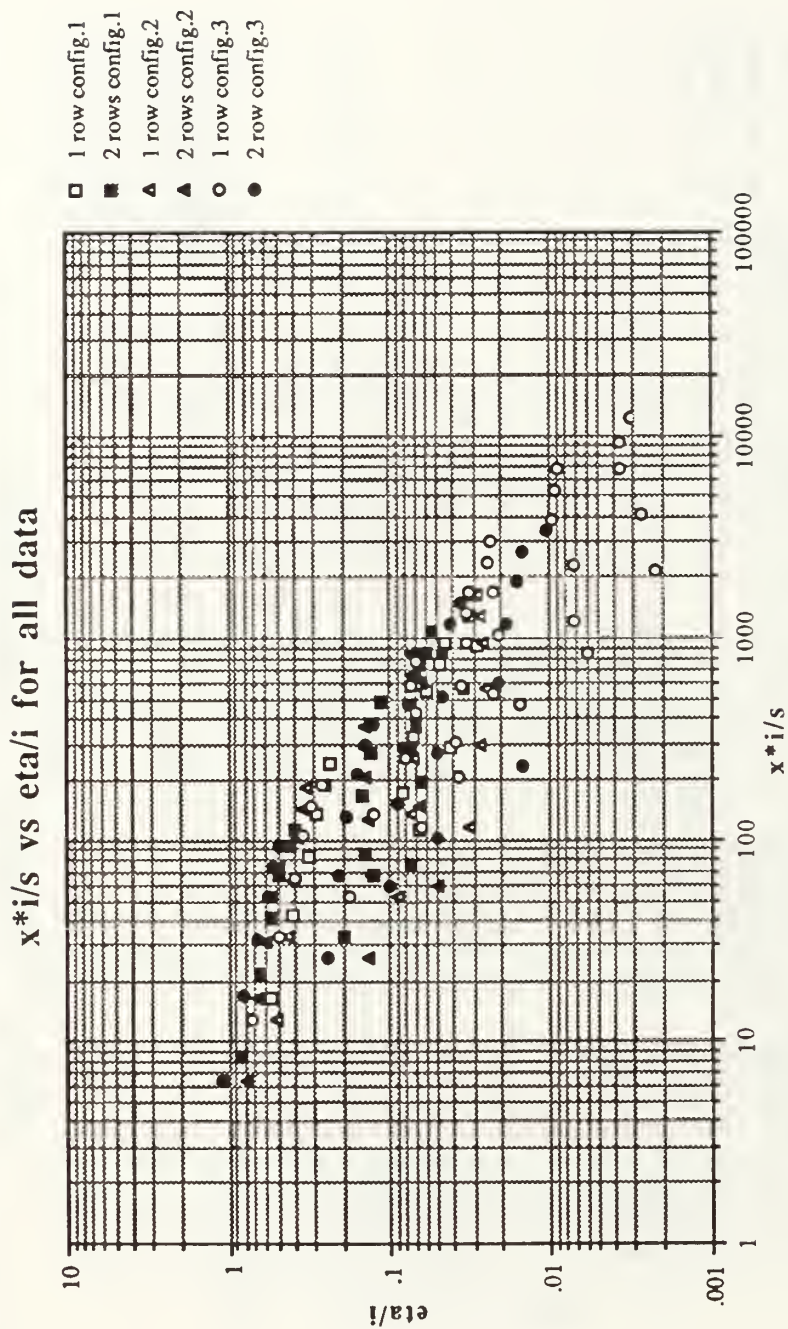


Figure 177. $\bar{\eta}/I$ Versus x^*I/s , Correlation Plot of Configurations 1, 2, and 3, All Blowing Ratios, 1 Row and 2 Rows

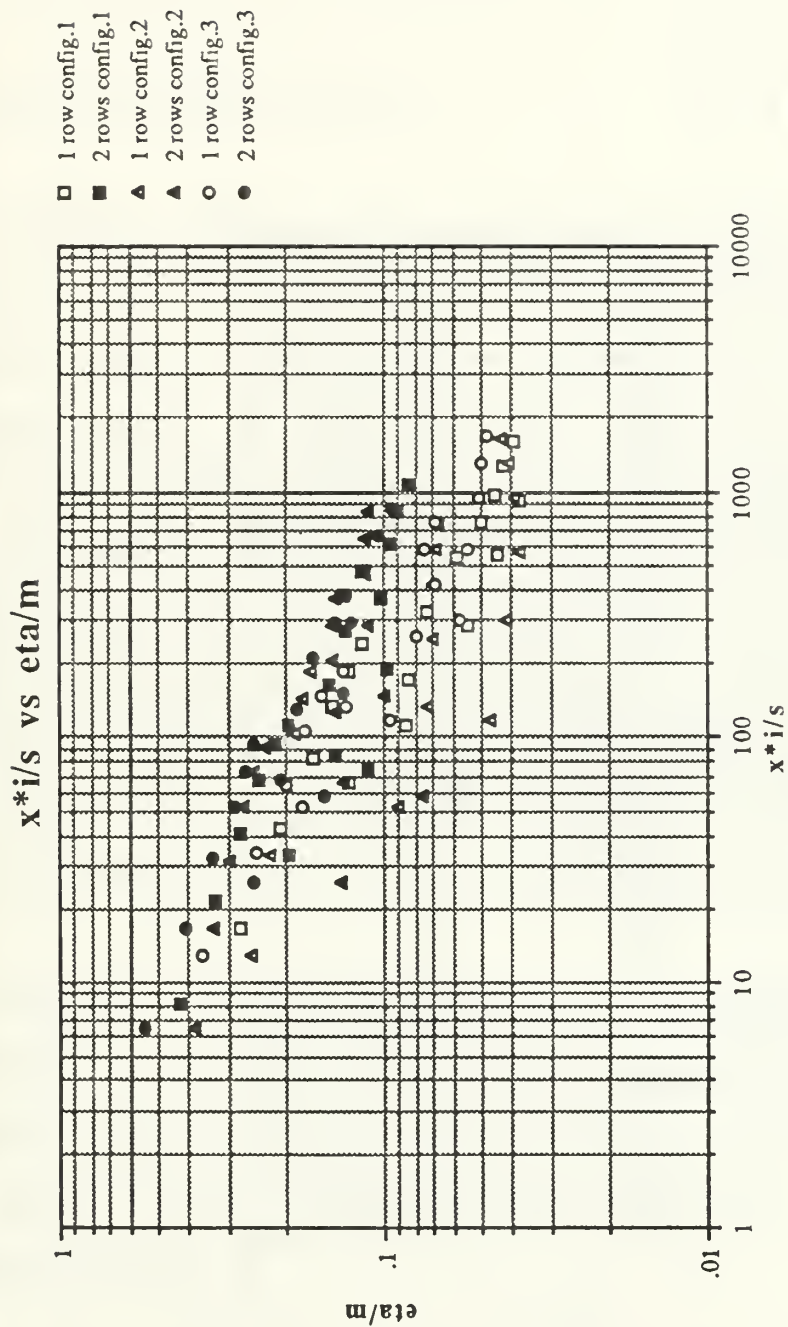


Figure 178. $\bar{\eta}/m$ Versus $x \cdot l/s$, Correlation Plot of Configurations 1, 2, and 3, $m=0.5, 1.0$ and 1.5 ,
1 Row and 2 Rows

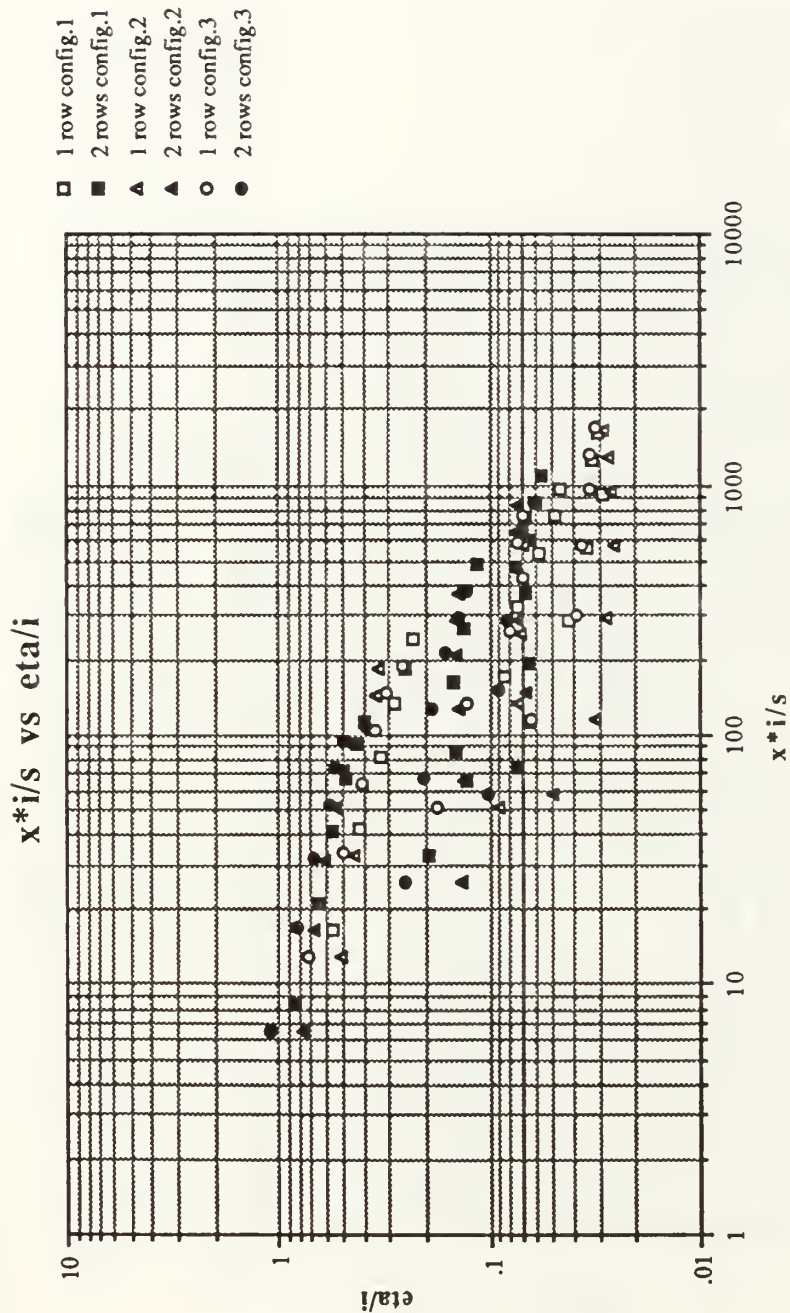


Figure 179. $\bar{\eta}/I$ Versus $x \cdot I/s$, Correlation Plot of Configurations 1, 2, and 3, $m=0.5, 1.0$, and 1.5 , 1 Row and 2 Rows

APPENDIX B

DATA ACQUISITION, PROCESSING AND PLOTTING PROGRAMS

1. Mean Velocity Survey Software :

FIVEHOLE1 : This program acquires pressure data from each of the five transducers associated with the five hole pressure probe. The FIVEHOLE1 program controls the MITAS motor controller which, in turn, controls the automatic traversing device on which the five hole probe is mounted. An 800 point pressure survey is conducted in the Y-Z plane normal to the freestream flow. Two data files, FIVx and FIVPx, are created. The FIVx data file consists of mean velocity, center port pressure, average pressure of the four peripheral ports, and the yaw and pitch coefficients for each of the 800 locations sampled. The FIVx data file consists of the pressures P1 through P5 sensed by each of the five pressure probe sensing ports, the average pressure of the four peripheral ports and the mean velocity, for each of the 800 survey locations.

PADJUST : This program accesses the FIVPx data file created by FIVEHOLE1 and adjusts the pressures to account for spatial resolution problems. Pressure correction is performed using a curve fit to move the measurement location to the center sensing port location. The output file of PADJUST is FIVxA.

VELOCITY : This program accesses FIVxA, the data file created by

PADJUST, and computes U_x , U_y and U_z velocity components. The output file of VELOCITY is V_x .

UXJ : This program accesses V_x , the data file created by VELOCITY, and plots streamwise velocity (U_x) contours of the Y-Z plane surveyed by the five hole pressure probe.

PTOTJ : This program accesses V_x , data file created by VELOCITY, and plots total pressure contours of the surveyed Y-Z plane.

2. Mean Temperature Survey Software :

ROVER1 : This program acquires flow temperature data from the "roving" thermocouple mounted on the automatic traversing device. The traversing device is controlled by the MITAS controller which is, in turn, controlled by this program. The output data file consists of differential temperatures ($T_{\text{ROVER}} - T_{\infty}$) for each of the 800 survey locations in the Y-Z plane. The output file of ROVER1 is TEM_x .

PLTMPJ : This program uses the differential temperature data file TEM_x , created by ROVER1 and plots differential temperature contours of the surveyed Y-Z plane.

3. Heat Transfer Measurement Software (No Film Cooling) :

STANTON3 : This program acquires multiple channel thermocouple data for heat transfer measurements with no film cooling. It creates two output data files, TDATA and IDATA. The TDATA file consists of the 126 test plate thermocouple temperatures. The IDATA file records run number, test plate voltage and current, ambient pressure, pressure differential, ambient temperature, freestream velocity, air density and freestream temperature.

STANTONJ : STANTONJ uses as input TDATA and IDATA files created by STANTON3 and calculates heat transfer coefficients and Stanton numbers for each of the 126 thermocouple locations. The calculations of the local heat transfer coefficient and local Stanton number are updated using an energy balance which includes spanwise/streamwise conduction and the modified radiation heat flux calculations. STANTONJ creates a output file, the name of which is designated by the user, which consists of the Stanton number for each thermocouple. A printout is also produced which includes the local heat transfer coefficient, the Stanton number and the X and Z coordinates for each of the 126 test plate thermocouples.

4. Heat Transfer Measurement Software (with Film Cooling) :

SETCONDJ: This program is used to set conditions for heat transfer data acquisition when film cooling is employed. SETCONDJ determines injection velocity, Reynolds number, blowing ratio (m) and non-dimensional temperature (θ). It requires user input from the terminal of freestream conditions, rotometer percent flow and injection plenum differential pressure. This version is updated

to include three different sized rotometers.

STANFC1J : This program is used when film cooling is employed to acquire multiple channel thermocouple data for heat transfer measurements. STANFC1J creates three data files : a temperature data file (Tx), a terminal input data file (Ix), and a film cooling data file (FCx). The temperature data file consists of the 126 test plate thermocouple temperatures. The terminal input data file records the identical information contained in the IDATA file of STANTON3, as discussed earlier. The film cooling data file contains the injection rotometer percent flow and the injection plenum differential pressure. This version is updated to include the larger sized rotometer.

STANFC2J : This program accesses the temperature, terminal input and film cooling data files created by STANFC1J. The program calculates Stanton number values for the 126 thermocouple locations and creates a single output file (FCx) containing these values. This version is updated to calculate the local heat transfer coefficients and Stanton numbers using an energy balance which includes spanwise/streamwise conduction and a modified radiation heat flux calculation.

STANR1 : This program reads two Stanton number data files and creates a single output file containing Stanton number ratios for each of the 126 thermocouple locations for a particular θ . The required input data files are : The user designated file created by STANTONJ containing baseline Stanton numbers for no film cooling and the FCx data file created by STANFC2J containing Stanton numbers with film cooling for a particular value of θ . The

output file of STANR1 is STRx.

FLMEFFJ : This program processes Stanton number data and calculates the local and spanwise averaged film cooling effectiveness and iso-energetic Stanton number ratios. The program reads the output file created by STANTONJ which contains the baseline Stanton numbers for no film cooling, and up to six FCx, Tx and Ix files created by STANFC!J and STANFC2J. One of the two output data files contains the local effectiveness and iso-energetic Stanton number ratios and the other output file contains the spanwise averaged effectiveness and iso-energetic Stanton number ratios. This version of the program accounts for the use of two different baseline inputs (4 amp and 6 amp) and corrects the local θ calculation to account for convective heat flux when applying the thermal contact resistance to calculate the local plate surface temperature.

3DSTGETA : This program accesses the files created by FLMEFFJ and plots the spanwise variation of effectiveness in three-dimensional form.

3DSTGSTRIS : This program accesses the files created by FLMEFFJ and plots the spanwise variation of the iso-energetic Stanton number ratio in three-dimensional form.

3DSTRST : This program accesses STRx, the Stanton number ratio file created by STANR1, and plots the spanwise variations of the Stanton number ratios for a particular θ in three-dimensional form.

APPENDIX C

DATA FILE DIRECTORY

1. Heat Transfer Data:

A. STANTON3 / STANTONJ data files -- (no film cooling) :

xTDATA ---- temperature data file

xIDATA ---- user terminal input data file

xABL ---- local Stanton number data file

<u>Data Run #</u>	<u>Data File</u>	<u>Experimental Conditions</u>
101691.1155	6TDATA 6IDATA 6ABL	Compound Angle Tp-Tf=21.6 deg C no film-cooling
101691.1440	4TDATA 4IDATA 4ABL	Compound Angle Tp-Tf=9.6 deg C no film cooling

B. STANFC1J/ STANFC2J data files -- (film-cooling)

pTxx ---- temperature data file

pIxx ---- user terminal input data file

pFCxx ---- film-cooling parameters data file

pSTxx ---- local Stanton number data file

COMPOUND ANGLE, 1 ROW

<u>Data Run #</u>	<u>Data File</u>	<u>Experimental Conditions</u>
072991.1715	3T14 3I14 3FC14 3ST14A	Compound Angle 1 row, m=0.5, theta=-0.04
072991.1940	3T15 3I15 3FC15 3ST15A	Compound Angle 1 row, m=0.5, theta=0.96
073091.0750	3T16 3I16 3FC16 3ST16B	Compound Angle 1 row, m=0.5, theta=1.39
073091.1045	3T17 3I17 3FC17 3ST17	Compound Angle 1 row, m=0.5, theta=2.27
073091.1750	3T18 3I18 3FC18 3ST18A	Compound Angle 1 row, m=0.5, theta=2.79
073091.1615	3T19 3I19 3FC19 3ST19A	Compound Angle 1 row, m=0.5, theta=3.07
072691.1845	3T7 3I7 3FC7 3ST7A	Compound Angle 1 row, m=1.0, theta=0.62

072791.0735	3T8 3I8 3FC8 3ST8	Compound Angle 1 row, $m=1.0$, $\theta=0.96$
072791.1050	3T9 3I9 3FC9 3ST9B	Compound Angle 1 row, $m=1.0$, $\theta=1.16$
072791.1355	3T10A 3I10A 3FC10A 3ST10A	Compound Angle 1 row, $m=1.0$, $\theta=1.71$
072791.1735	3T11B 3I11B 3FC11B 3ST11B	Compound Angle 1 row, $m=1.0$, $\theta=1.90$
072991.1205	3T12 3I12 3FC12 3ST12A	Compound Angle 1 row, $m=1.0$, $\theta=2.45$
072891.1245	3T13 3I13 3FC13 3ST13A	Compound Angle 1 row, $m=1.0$, $\theta=3.23$
072591.1140	3T1 3I1 3FC1 3ST1A	Compound Angle 1 row, $m=1.5$, $\theta=0.12$

072591.1448	3T2 3I2 3FC2 3ST2A	Compound Angle 1 row, m=1.5, theta=0.94
072591.1740	3T3 3I3 3FC3 3ST3A	Compound Angle 1 row, m=1.5, theta=1.30
072691.0818	3T4 3I4 3FC4 3ST4A	Compound Angle 1row, m=1.5, theta=2.00
072691.1100	3T5 3I5 3FC5 3ST5A	Compound Angle 1 row, m=1.5, theta=2.71
072691.1400	3T6 3I6 3FC6 3ST6A	Compound Angle 1 row, m=1.5, theta=3.37
101491.1340	3T20 3I20 3FC20 3ST20A	Compound Angle 1 row, m=2.0, theta=0.35
101491.1700	3T21 3I21 3FC21 3ST21A	Compound Angle 1 row, m=2.0, theta=0.94

101491.2100	3T22 3I22 3FC22 3ST22	Compound Angle 1 row, m=2.0, theta=1.30
101591.1210	3T23 3I23 3FC23 3ST23A	Compound Angle 1 row, m=2.0, theta=2.29
101591.1505	3T24 3I24 3FC24 3ST24A	Compound Angle 1 row, m=2.0, theta=2.71
101591.1935	3T25 3I25 3FC25 3ST25A	Compound Angle 1 row, m=2.0, theta=3.40
101691.0840	3T26 3I26 3FC26 3ST26A	Compound Angle 1 row, m=2.0, theta=1.83
101691.1755	3T27 3I27 3FC27 3ST27A	Compound Angle 1 row, m=3.0, theta=0.55
101791.0835	3T28 3I28 3FC28 3ST28A	Compound Angle 1 row, m=3.0, theta=1.375

101791.1315	3T29 3I29 3FC29 3ST29A	Compound Angle 1 row, $m=3.0$, $\theta=1.785$
101791.1710	3T30 3I30 3FC30 3ST30A	Compound Angle 1 row, $m=3.0$, $\theta=2.58$
101791.2105	3T31 3I31 3FC31 3ST31A	Compound Angle 1 row, $m=3.0$, $\theta=3.23$
101891.0930	3T32 3I32 3FC32 3ST32A	Compound Angle 1 row, $m=3.0$, $\theta=3.74$
101891.1435	3T33 3I33 3FC33 3ST33A	Compound Angle 1 row, $m=4.0$, $\theta=1.04$
101891.1740	3T34 3I34 3FC34 3ST34A	Compound Angle 1 row, $m=4.0$, $\theta=1.57$
101991.0850	3T35 3I35 3FC35 3ST35A	Compound Angle 1 row, $m=4.0$, $\theta=2.07$

191991.1150	3T36 3I36 3FC36 3ST36A	Compound Angle 1 row, m=4.0, theta=2.57
101991.1515	3T37 3I37 3FC37 3ST37A	Compound Angle 1 row, m=4.0, theta=3.12
102091.0810	3T38 3I38 3FC38 3ST38A	Compound Angle 1 row, m=4.0, theta=4.01

COMPOUND ANGLE, 2 ROWS

102191.1415	3T39 3I39 3FC39 3ST39A	Compound Angle 2 rows, m=2.0, theta=0.96
102191.1745	3T40 3I40 3FC40 3ST40A	Compound Angle 2 rows, m=2.0, theta=1.30
102191.2300	3T41 3I41 3FC41 3ST41A	Compound Angle 2 rows, m=2.0, theta=1.68
102291.0820	3T42 3I42 3FC42 3ST42A	Compound Angle 2 rows, m=2.0, theta=2.58

102291.1215	3T43 3I43 3FC43 3ST43A	Compound Angle 2 rows, m=2.0, theta=2.97
102291.1525	3T44 3I44 3FC44 3ST44A	Compound Angle 2 rows, m=2.0, theta=2.14
103091.1525	3T45 3I45 3FC45 3ST45A	Compound Angle 2 rows, m=3.0, theta=1.67
103091.1840	3T46 3I46 3FC46 3ST46A	Compound Angle 2 rows, m=3.0, theta=1.82
103091.2300	3T47 3I47 3FC47 3ST47A	Compound Angle 2 rows, m=3.0, theta=2.13
103191.0840	3T48 3I48 3FC48 3ST48A	Compound Angle 2 rows, m=3.0, theta=3.04
103191.1515	3T49 3I49 3FC49 3ST49A	Compound Angle 2 rows, m=3.0, theta=3.32

103191.1750	3T50 3I50 3FC50 3ST50A	Compound Angle 2 rows, m=3.0, theta=3.61
110191.1420	3T51 3I51 3FC51 3ST51A	Compound Angle 2 rows, m=3.0, theta=3.07

C. FILM EFFECTIVENESS DATA

Generating Program : FLMEFFJ

pFLMxxx ---- local effectiveness data file
pFLMAxxx ---- spanwise average effectiveness data file

COMPOUND ANGLE, 1 ROW

<u>Data Run #</u>	<u>Data File</u>	<u>Experimental Conditions</u>
072991.1715	3FLM15A	Compound Angle.
072991.1940	3FLMA15A	1 row, m=0.5
073091.0750		
073091.1750		
073091.1615		
072691.1845	3FLM11A	Compound Angle
072791.1050	3FLMA11A	1 row, m=1.0
072791.1735		
072991.1205		
072891.1245		

072591.1140	3FLM115A	Compound Angle
072591.1448	3FLMA115A	1 row, m=1.5
072591.1740		
072691.0818		
072691.1100		
072691.1400		

101491.1340	3FLM12B	Compound Angle
101491.1700	3FLMA12B	1 row, m=2.0
101491.2100		
101591.1210		
101591.1505		
101691.0840		

101691.1755	3FLM13A	Compound Angle
101791.0835	3FLMA13A	1 row, m=3.0
101791.1315		
101791.1710		
101791.2105		
101891.0930		

101891.1435	3FLM14A	Compound Angle
101891.1740	3FLMA14A	1 row, m=4.0
101991.0850		
101991.1515		
102091.0810		

COMPOUND ANGLE, 2 ROWS

102191.1415	3FLM22B	Compound Angle
102191.1745	3FLMA22B	2 rows, m=2.0
102191.2300		
102291.0820		
102291.1215		

103191.1525	3FLM23B	Compound Angle
103091.1840	3FLMA23B	2 rows, m=3.0
103191.1515		
103191.1750		
110191.1420		

D. STANTON NUMBER RATIO FILES

Generating Program : STANR1

pSTRxx ---- Film-cooling data file

COMPOUND ANGLE, 1 ROW

<u>Data Run #</u>	<u>Data File</u>	<u>Experimental Conditions</u>
073091.0750	3STR15	1 row, m=0.5, theta=1.39
072791.1050	3STR11	1 row, m=1.0, theta=1.16
072591.1740	3STR115	1 row, m=1.5, theta=1.30
101491.2100	3STR12	1 row, m=2.0, theta=1.30
101791.1315	3STR13	1 row, m=3.0, theta=1.76
101891.1740	3STR14	1 row, m=4.0, theta=1.55

COMPOUND ANGLE, 2 ROWS

<u>Data Run #</u>	<u>Data File</u>	<u>Experimental Conditions</u>
102191.2300	3STR22	2 rows, m=2.0, theta=1.67
103091.1525	3STR23	2 rows, m=3.0, theta=1.67

E. MEAN VELOCITY DATA :

COMPOUND ANGLE, 1 ROW

<u>Data Run #</u>	<u>Data File</u>	<u>Generating Program</u>	<u>Experimental Conditions</u>
101391.1900	FIV1 FIVP1 FIV19 V19 Data Disc 7	FIVEHOLE1 FIVEHOLE1 PADJUST VELOCITY	1 row, m=1.5 x/d = 9.9
100891.2100	FIV1 FIVP1 FIV09 V9 Data Disc 4	FIVEHOLE1 FIVEHOLE1 PADJUST VELOCITY	1 row, m=1.5 x/d = 44.3
100291.2240	FIV0 FIVP0 FIV00 V0 Data Disc 1	FIVEHOLE1 FIVEHOLE1 PADJUST VELOCITY	1 row, m=1.5 x/d = 86.3
101391.0820	FIV0 FIVP0 FIV18 V18 Data Disc 7	FIVEHOLE1 FIVEHOLE1 PADJUST VELOCITY	1 row, m=2.0 x/d = 9.9
100991.0950	FIV2 FIVP2 FIV10 V10 Data Disc 3	FIVEHOLE1 FIVEHOLE1 PADJUST VELOCITY	1 row, m=2.0 x/d = 44.3

100391.1015	FIV0 FIVP0 FIV01 V1 Data Disc 2	FIVEHOLE1 FIVEHOLE1 PADJUST VELOCITY	1 row, m=2.0 x/d = 86.3
101291.1945	FIV2 FIVP2 FIV17 V17 Data Disc 6	FIVEHOLE1 FIVEHOLE1 PADJUST VELOCITY	1 row, m=3.0 x/d = 9.9
100991.2055	FIV2 FIVP2 FIV11 V11 Data Disc 4	FIVEHOLE1 FIVEHOLE1 PADJUST VELOCITY	1 row, m=3.0 x/d = 44.3
100891.0925	FIV1 FIVP1 FIV08 V8 Data Disc 3	FIVEHOLE1 FIVEHOLE1 PADJUST VELOCITY	1 row, m=3.0 x/d = 86.3
101291.0825	FIV2 FIVP2 FIV16 V16 Data Disc 5	FIVEHOLE1 FIVEHOLE1 PADJUST VELOCITY	1 row, m=4.0 x/d = 9.9
101091.0915	FIV0 FIVP0 FIV12 V12 Data Disc 5	FIVEHOLE1 FIVEHOLE1 PADJUST VELOCITY	1 row, m=4.0 x/d = 44.3

100791.2300	FIV0 FIVP0 FIV07 V7 Data Disc 4	FIVEHOLE1 FIVEHOLE1 PADJUST VELOCITY	1 row, m=4.0 x/d = 86.3
-------------	---	---	----------------------------

COMPOUND ANGLE, 2 ROWS

<u>Data Run #</u>	<u>Data File</u>	<u>Generating Program</u>	<u>Experimental Conditions</u>
101191.0905	FIV1 FIVP1 FIV14 V14 Data Disc 5	FIVEHOLE1 FIVEHOLE1 PADJUST VELOCITY	2 rows, m=2.0 x/d = 9.9
101091.1925	FIV0 FIVP0 FIV13 V13 Data Disc 6	FIVEHOLE1 FIVEHOLE1 PADJUST VELOCITY	2 rows, m=2.0 x/d = 44.3
100591.0810	FIV2 FIVP2 FIV04 V4 Data Disc 1	FIVEHOLE1 FIVEHOLE1 PADJUST VELOCITY	2 rows, m=2.0 x/d = 86.3
101191.1945	FIV1 FIVP1 FIV15 V15 Data Disc 6	FIVEHOLE1 FIVEHOLE1 PADJUST VELOCITY	2 rows, m=3.0 x/d = 9.9

100691.0935	FIV0 FIVP0 FIV06 V6 Data Disc 3	FIVEHOLE1 FIVEHOLE1 PADJUST VELOCITY	2 rows, m=3.0 x/d = 44.3
100591.1605	FIV2 FIVP2 FIV05 V5 Data Disc 2	FIVEHOLE1 FIVEHOLE1 PADJUST VELOCITY	2 rows, m=3.0 x/d = 86.3

F. Mean Temperature Survey Data :

Generating Program : ROVER1

COMPOUND ANGLE

<u>Data Run #</u>	<u>Data File</u>	<u>Experimental Conditions</u>
092291.1355	TEM12	1 row, m=1.5, x/d=9.9
092291.0935	TEM11	1 row, m=1.5, x/d=44.3
091691.1750	TEM0	1 row, m=1.5, x/d=86.3
092291.1825	TEM13	1 row, m=2.0, x/d=9.9
092191.2040	TEM10	1 row, m=2.0, x/d=44.3
091791.1155	TEM1	1 row, m=2.0, x/d=86.3
092391.0915	TEM14	1 row, m=3.0, x/d=9.9
092191.1500	TEM9	1 row, m=3.0, x/d=44.3
091891.1100	TEM2	1 row, m=3.0, x/d=86.3

092391.1520	TEM15	1 row, m=4.0, x/d=9.9
092191.0945	TEM8	1 row, m=4.0, x/d=44.3
091891.1905	TEM3	1 row, m=4.0, x/d=86.3

COMPOUND ANGLE, 2 ROW

<u>Data Run #</u>	<u>Data File</u>	<u>Experimental Conditions</u>
092391.2010	TEM16	2 rows, m=2.0, x/d=9.9
092091.2225	TEM7	2 rows, m=2.0, x/d=44.3
091991.1315	TEM4	2 rows, m=2.0, x/d=86.3
092491.0915	TEM17	2 rows, m=3.0, x/d=9.9
092091.1510	TEM6	2 rows, m=3.0, x/d=44.3
091991.1900	TEM5	2 rows, m=3.0, x/d=86.3

REFERENCES

1. Jackson, S. A., *Heat Transfer, Adiabatic Effectiveness and Injectant Distributions Downstream of a Single Row and Two Staggered Rows of Film-Cooling Holes with Simple and Compound Angles*, M.S. Thesis, Naval Postgraduate School, Monterey, California, December 1991.
2. Metzger, D. E., Carper, H. J., and Swank, L. R., "Heat Transfer With Film Cooling Near Nontangential Injection Slots," *ASME Transactions-Journal of Engineering for Power*, pp. 157-163, April, 1968.
3. Ligrani, P. M., and Camci, C., "Adiabatic Film Cooling Effectiveness from Heat Transfer Measurements in Compressible, Variable Property Flow," *ASME Transactions-Journal of Heat Transfer*, Vol. 107, No. 2, pp. 313-320, 1985.
4. Ligrani, P. M., "Comment on Behavior of a Coolant Film With Two Rows of Holes Along the Pressure Side of a High Pressure Nozzle Guide Vane," *ASME Transactions-Journal of Turbomachinery*, Vol. 112, No. 3, pp. 520-521, 1990.
5. Ligrani, P. M., Ortiz, A., Joseph, S. L., and Evans, D. L., "Effects of Embedded Vortices on Film-Cooled Turbulent Boundary Layers," *ASME Transactions-Journal of Turbomachinery*, Vol. 111, No. 1, pp. 71-77, 1989.
6. Ligrani, P. M., Subramanian, C. S., Craig, D. W. and Kaisuwan, P., "Effect of Vortices with Different Circulations on Heat Transfer and Injectant Downstream of a Row of Film-Cooling Holes in a Turbulent Boundary Layer," *ASME Transactions-Journal of Heat Transfer*, Vol. 113, No. 1, pp.79-90, 1991.
7. Bishop, D. T., *Heat Transfer, Adiabatic Effectiveness and Injectant Distributions Downstream of Single and Double Rows of Film-Cooling Holes With Compound Angles*, M. S. Thesis, Naval Postgraduate School, Monterey, California, September 1990.

8. Ciriello, S., *Heat Transfer, Adiabatic Effectiveness and Injectant Distributions Downstream of Single and Double Rows of Film-Cooling Holes With Simple and Compound Angles*, M. S. Thesis, Naval Postgraduate School, Monterey, California, March 1991.
9. Ortiz, A., *The Thermal Behavior of Film Cooled Turbulent Boundary Layers as Affected by Longitudinal Vortices*, M. E. Thesis, Naval Postgraduate School, Monterey, California, September 1987.
10. Joseph, S. L., *The Effects of an Embedded Vortex on a Film-Cooled Turbulent Boundary Layer*, M. E. Thesis, Naval Postgraduate School, Monterey, California, December 1986.
11. Williams, W., *Effects of an Embedded Vortex on a Single Film-Cooling Jet in a Turbulent Boundary Layer*, M. S. Thesis, Naval Postgraduate School, Monterey, California, June 1988.
12. Incropera, F. P., and Dewitt, D. P., *Introduction to Heat Transfer*, Second Edition, pp. 748-771, Appendix A, John Wiley and Sons Inc., 1990.
13. Avallone, E. A., and Baumeister, T., *Mark's Standard Handbook for Mechanical Engineers*, Ninth Edition, pp. 4-79 - 4-81, McGraw-Hill Book Company, 1987.
14. Gerald, C. F., *Applied Numerical Analysis*, Second Edition, pp. 504-507, Addison-Wesley Publishing Company, 1978.
15. Kays, W. M., and Crawford, M. E., *Convective Heat and Mass Transfer*, Second Edition, p.216, McGraw-Hill Book Company, 1980.

INITIAL DISTRIBUTION LIST

	No. Copies
1. Defense Technical Information Center Cameron Station Alexandria, Virginia 22304-6145	2
2. Library, Code 52 Naval Postgraduate School Monterey, California 93943-5002	2
3. Professor P.M. Ligrani, Code ME/Li Department of Mechanical Engineering Naval Postgraduate School Monterey, California 93943-5000	3
4. Department Chairman, Code ME Department of Mechanical Engineering Naval Postgraduate School Monterey, California 93943-5000	1
5. Dr. Dan Groghan Naval Sea Systems Command Code 56X3 Washington, D.C. 20362	4
6. Naval Engineering Curricular Officer, Code 34 Department of Mechanical Engineering Naval Postgraduate School Monterey, California 93943-5000	1
7. Professor C.S. Subramanian, Code ME/Su Department of Mechanical Engineering Naval Postgraduate School Monterey, California 93943-5000	1
8. LCDR. James M. Wigle 522 Rushville St. La Jolla, California 92037	1

144-403

Thesis

W58375 Wigle

c.1 Heat transfer, adiabatic effectiveness and injectant distributions downstream of single and double rows of film-cooling holes with compound angles.

Thesis

W58375 Wigle

c.1 Heat transfer, adiabatic effectiveness and injectant distributions downstream of single and double rows of film-cooling holes with compound angles.

DUDLEY KNOX LIBRARY



3 2768 00018424 6